TiO_2 Nanorod Polymer Composite Materials

By

Uroš Vukičević

Department of Chemistry
Imperial College London
South Kensington Campus
London, SW7 2AZ

June 2008

A dissertation submitted to the University of London for the degree of Doctor of Philosophy and the Diploma of Imperial College London



Declaration

The work described in this thesis was carried out in the Department of Chemistry and the Department of Chemical Engineering, Imperial College London between January 2005 and December 2007. Except where acknowledged, the material is the original work of the author and no part of it has been submitted for a degree at this or any other university.

Acknowledgments

I would first like to thank my supervisors, Dr. Milo Shaffer and Dr. Alexander Bismarck for their guidance, encouragement and support during my studies. Special thanks go to Dr. Sabina Chyła for helpful discussions and ideas on the synthesis of TiO_2 nanorods. I am very grateful to Dr. Ben Cottam, Richard Winchester and Johann Cho for carrying out various measurements. I would like to thank Jonathan James for his work on TiO_2 nanorod synthesis as part of his final year undergraduate project. I must also acknowledge all the people from the Department of Chemistry and the Department of Chemical Engineering at Imperial College who have helped me during my studies. In particular, I would like to express my gratitude to the members of the PaCE and Electronic Materials groups for all their helpful suggestions.

I must also thank Advance Nanotech Inc. and Overseas Student Research Award Scheme for their financial support.

This thesis is dedicated to my parents, Marija and Dušan, and my wife, Jelena, for their endless support and encouragement during my studies.

Abstract

The remarkable characteristics of TiO_2 are widely used, from everyday life applications (pigments, food/cosmetics additives) to more specialised systems, including photovoltaics and structural composites. Use in polymers is substantial (25% of all TiO_2 produced), but most applications and research focus on commercial powders. A new generation of TiO_2 nanoparticles has emerged, based on very small, single-crystals, with well-defined morphology and phase. A limited number of papers report the use of this new nanoscale TiO_2 in polymer nanocomposites, and indicate improved properties. Although the synthesis of anisotropic nanoparticles (e.g. nanorods) has been well-reported, use in polymer nanocomposites remains largely unreported. This thesis broadly covers three topics: (1) synthesis of TiO_2 nanorods using different sol-gel routes in presence of structure directing agents, (2) modification of the nanorod surface chemistry in order to control dispersion and surface properties and (3) fabrication of titania nanorod-polymer composites. Single-crystal anatase nanorods were produced with variable aspect ratio (3-12), depending on the specific structure directing agent (SDA) used during synthesis. Due to organic functionalisation at the nanorod surface, nanorods could be well dispersed in chloroform. A new procedure, based on the self-cleaning ability of TiO_2 under UV, was developed for removal of organics from the nanorod surface, without compromising the nanorod morphology, crystallinity or dispersibility. This powerful tool can be used to change the surface character of the nanorods to generate aqueous TNR dispersions. Stable dispersions were achieved using quaternary ammonium hydroxides to modify the surface electrostatically and sterically. Once dispersed individually, the surface can be further modified by sol-gel chemistry. Composite work involved blending both organic and water-soluble polymers with nanorod dispersions in chloroform and water, respectively, to produce composite films of exceptional optical transparency, even for nanorod loadings up to 30 wt%. The films possess very strong, wavelength-tuneable UV absorbance, which could be used in UV filters and optical limiting. The presence of SDAs or dispersants at the nanorod-polymer interface hinders strong adhesion, as evidenced by marginally lower tensile strength and thermal stability of the nanocomposites. The photo-stability of the nanorod composites is comparable to that of the pure polymer and better than that of composites with commercial equiaxed TiO_2 nanoparticles.

Contents

List of figures **9**

List of tables **16**

List of symbols **17**

List of abbreviations **18**

1. Project motivation and aims **21**

1.1 Scientific objectives **24**

2. Introduction and background literature **25**

2.1 Introduction **25**

2.2 Synthesis of TiO_2 nanomaterials **28**

2.2.1 Sol-gel methods for synthesis of TiO_2 nanostructures 29

2.2.2 Synthesis of TiO_2 nanostructures in reverse micelles 36

2.2.3 Hydrothermal and solvothermal routes for the synthesis of TiO_2 nanostructures 37

2.2.4 Synthesis of TiO_2 nanostructures using direct oxidation methods 40

2.2.5 Chemical and physical vapour deposition (CVD/PVD) of TiO_2 nanostructures 41

2.2.6 Electrodeposition of TiO_2 nanostructures 42

2.2.7 Synthesis of TiO_2 nanostructures using sonochemical methods 42

2.2.8 Synthesis of TiO_2 nanostructures using microwave method 43

2.3 Summary of the TiO_2 synthesis state-of-the-art **43**

2.4 Nanocomposite materials **44**

2.5 TiO_2 nanocomposite materials **46**

2.5.1 TiO_2-polymer composites for photocatalytic and electronic applications 47

2.5.1.1 Background of TiO_2 photocatalysis 47

2.5.1.2 Improving / suppressing the photocatalytic activity of TiO_2 49

2.5.1.3 Nano-TiO_2 photocatalysis for environmental, self-cleaning and medical applications 54

2.5.1.4 Electronic and electrochemical devices with nano-TiO_2 59

2.5.2 TiO_2 nanocomposites for optical applications 65

2.5.3 TiO_2 structural composites 68

2.5.4 TiO_2 nanocomposites for biomedical applications 71

2.6 Concluding remarks 76

3. Materials and Methods 78

3.1 Materials 78

3.2 Preparation of TiO_2 nanorods (TNR) 80

3.2.1 General synthesis setup and equipment 80

3.2.2 Hydrolytic synthesis of TiO_2 nanorods 82

3.2.3 Nonhydrolytic synthesis of TiO_2 nanorods using TOPO / dodecylamine ligands (TNR_{TOPO}) 83

3.2.4 Nonhydrolytic synthesis of TiO_2 nanorods using OA ligand (TNR_{OA}) 85

3.3 UV-assisted removal of structure directing agents ("stripping") and stabilisation of aqueous dispersions 86

3.4 Silanisation of "stripped" TNR_{TOPO} and effect on nanorod photocatalytic activity 88

3.5 Composite preparation 92

3.5.1 Processing of the PDLLA and PMMA composites 92

3.5.2 Processing of the PVA composites 96

3.6 Analytical techniques used for materials characterisation 98

3.6.1 Analysis of the nanomaterial morphology using Transmission Electron Microscopy (TEM) 98

3.6.2 Analysis of the composite morphology using Scanning Electron Microscopy (SEM) 98

3.6.3 Powder X-ray Diffraction (XRD) for structural, crystallinity and phase identification of TiO_2 nanomaterials 99

3.6.4 Structural and phase identification analysis of TiO_2 nanomaterials using Raman spectroscopy 99

3.6.5 Analysis of the particle dispersion in the nanocomposites using optical microscopy 100

3.6.6 Analysis of optical properties of titania dispersions and composites using UV-Vis spectroscopy 100

3.6.7 Measurement of composition of TiO_2 nanorod powders and composite films using Thermo-Gravimetric Analysis (TGA) 101

3.6.8 Measurement of the glass transition temperature of the composites using Differential Scanning Calorimetry (DSC) 102

3.6.9 Measurement of the storage modulus and the glass transition temperature of the nanocomposites using the Dynamic Mechanical Thermal Analysis (DMTA) 103

3.6.10 Characterisation of the wetting behaviour of the composite films using Drop Shape Analysis (DSA) 104

3.6.11 Surface chemistry of TNR in aqueous dispersions - ζ-potential from electrophoretic mobility measurements 105

3.6.12 Mechanical properties of the composites 105

3.6.13 pH measurements of the aqueous titania dispersions 106

4. Synthesis and modification of TiO_2 nanorods 107

4.1 Introduction 107

4.2 Results and discussion 108

4.2.1 Hydrolytic synthesis of TiO_2 nanorods 108

4.2.2 Non-hydrolytic synthesis of TiO_2 nanorods – trioctylphosphine oxide and dodecylamine ligands 111

4.2.3 UV-assisted removal of surface organics and stabilisation of TNR_{TOPO} dispersions in water 120

4.2.4 Reduction in photocatalytic activity of TNR_{TOPO} in aqueous dispersions through silica coating 129

4.2.5 Non-hydrolytic synthesis of TiO_2 nanorods – OA ligand 134

4.2.5.1 UV-assisted removal of surface organics and stabilisation of TNR_{OA} dispersions in water 139

4.2 Concluding remarks 143

5. TiO_2 nanorod – polymer composites 145

5.1 Introduction 145

5.2 TNR – PDLLA and TNR – PMMA nanocomposite films 146

5.2.1 TNR-PMMA composites made with TNR_{OA} [09/2007 batch] 163

5.3 TNR – PVA composites 167

5.3.1 Photochemical degradation of composites 178

5.4 Concluding remarks 182

6. Conclusions and future research 184

6.1 Summary of contributions 184

6.1.1 Synthesis and modification of TiO_2 nanorods 184

6.1.2 TiO_2 nanorod – polymer nanocomposites 185

6.2 Summary of collaboration work 186

6.3 Future research 188

7. Appendix 189

7.1 DMTA results for TNR – PDLLA and TNR – PMMA nanocomposite films, at 10 Hz 189

7.2 Typical DSC scan 193

7.3 TGA curves for PVA nanocomposite films 194

7.4 DMTA results for PVA nanocomposite films, at 1 Hz 196

7.4 DMTA results for PVA nanocomposite films, at 10 Hz 200

7.5 Work on thermosetting nanocomposites 204

8. List of references 206

List of figures

Figure 1 – Transmission Electron Microscopy (TEM) micrographs of the: (a) commercial Degussa P25 TiO_2 Aeroxide® and (b, c) TiO_2 nanorods synthesised in relation to the current project..... 22

Figure 2 – TEM images of: (a, b) nanoparticles, (c) nanorods and (d) superlattice self-assemblies synthesised by hydrolysis of $Ti(OR)_4$ in presence of TMAH, from Chemseddine et al.[54] 30

Figure 3 – TEM images of TiO_2 (a, b) nanorods and (c) nanospheres synthesised by hydrolysis of TTIP in aqueous basic solutions, using OA as a surface modifier, from Cozzoli et al.[6]..... 31

Figure 4 – TEM micrographs of TiO_2 (a) nanorods and (b, c) nanotubes grown using AAM dipped into a TiF_4 sol, from Imai et al.[56]..... 32

Figure 5 – TEM image of TiO_2 nanoparticles synthesised using $TiCl_4$-$Ti(OPr)_4$ in TOPO/heptadecane, from Trentler et al.[72]. The top left inset is a selected-area electron diffraction pattern, indicating anatase and high-resolution TEM (HRTEM) of a single particle is shown in top right. 34

Figure 6 – TEM images of TiO_2 nanorods grown using $Ti(OPr)_4$ and following ligands: (a, b) 1-hexadecylamine and OA, from Joo et al.[77]; (c-g) lauric acid and TOPO, (c→f) increasing the relative ratio of lauric acid to $Ti(OPr)_4$ results in longer rods (scale bar 25 nm), from Jun et al.[75]..... 35

Figure 7 – TEM images of anatase TiO_2 (a) nanodots and (b) nanorods formed by nonhydrolytic aminolysis of $Ti(OPr)_4$, from Zhang et al.[7] 36

Figure 8 – TEM images of TiO_2 nanoshuttles and nanopetals formed by hydrolysis of $Ti(OBu)_4$ in reverse micelles, after: (a) 5 days (b) 10 days and (c) 20 days of synthesis; from Zhang et al.[83] 37

Figure 9 – TEM images of TiO_2 nanotubes grown by hydrothermal treatment of titania precursors or powders by (a) Kasuga et al.[84]; (b) Wang et al.[89] and (c) Chen et al.[88]..... 38

Figure 10 – (a) Nanotube formation routes according to Bavykin et al.[95]; (b, c) variation of hydrothermal conditions to produce (b) short rods and (c) nanowires, from hydrolyzed $TiCl_4$ sols, from Zhang and Gao[93] 39

Figure 11 – TEM images of TiO_2 (a) equiaxed nanoparticles and (b) nanorods, grown using the solvothermal route with $Ti(OBu)_4$ as precursor and NH_4HCO_3 / linoleic acid / triethylamine as surfactants in cyclohexane, from Li et al.[100] 40

Figure 12 – Cross-sectional SEM image of porous TiO_2 nanotube array grown by anodization of titanium in NH_4F solution, from Macak et al.[105] 40

Figure 13 – TEM images of TiO_2 (a) nanorod and (b) nanowire arrays, grown by CVD (from Wu and Yu[106]) and PVD (from Wu et al.[107]), respectively 41

Figure 14 – SEM images of the (a) as-prepared and (b) annealed TiO_2 nanotube arrays prepared by $TiCl_3$ electrodeposition onto a polymer template, from Hoyer[4] 42

Figure 15 – TEM images of TiO_2 (a) nanotubes and (b) nanowires produced by the sonochemical route from TiO_2 powder treated with NaOH and HNO_3, from Zhu et al.[110] 43

Figure 16 – Different types of polymer-clay composites, from LeBaron et al.[114] 45

Figure 17 – UV-Vis spectra of (a) N-doped[167] and (b) S-doped TiO_2[173], showing a red-shift in absorbance with respect to pristine TiO_2 51

Figure 18 – TEM images showing silica coated (a) TiO_2 nanorod grown by nonhydrolytic route, from Yang and Chen[193] and (b) commercial TiO_2 equiaxed nanoparticles, from El-Toni and Sato[188] 52

Figure 19 – (a) Absorption spectra and (b) free radical generation rates of Mn-doped titania compared with appropriate surface-treated commercial powders, from Wakefield et al.[195] 53

Figure 20 – (a) Hydrophobic glass surface covered by water droplets transforming into a hydrophilic film, (b) upon UV exposure; (c) fogging of glass under normal conditions and (d) anti-fogging surface upon UV exposure, from Fujishima et al.[202] 54

Figure 21 – Niche applications of photocatalytic water treatment, from[144] 57

Figure 22 – HRTEM micrograph of a TiO_2-PTh nanocomposite particle, from Vu et al.[239] 62

Figure 23 – Structure of P3HT-TiO_2 based solar cell, from Kwong et al.[241] 62

Figure 24 – Experimental setup for assessing the anisotropic photocatalytic behaviour of TiO_2 nanorods, from Dessombz et al.[296] 68

Figure 25 – Schematic and a photograph of the experimental setup for the nonhydrolytic synthesis of TNR 81

Figure 26 – Stages in the synthesis of TNR_{TOPO}: (a) TOPO + dodecylamine + heptadecane, (b) after adding $TiCl_4$, (c) after adding TTIP, (d) after 20 h at 300°C and (e) product supernatant (waste) 84

Figure 27 – Schematic for the stripping setup 87

Figure 28 – Photograph of the stripping setup inside a boxed enclosure 87

Figure 29 – Schematic for the silane addition setup 89

Figure 30 – Structure of Brilliant Blue R 90

Figure 31 – Fabrication of TiO_2 – PDLLA / PMMA composites 95

Figure 32 – Fabrication of TiO_2 – PVA composites 97

Figure 33 – (a) Contact angle diagram and (b) DSA experimental setup 104

Figure 34 – TEM of TiO_2 nanorods prepared by fast hydrolysis route 108

Figure 35 – XRD pattern of TiO_2 nanorods prepared by fast hydrolysis route and standard TiO_2 anatase diffraction lines 109

Figure 36 – Raman spectrum of TiO_2 nanorods prepared by fast hydrolysis route .. 109

Figure 37 – TGA of the as-prepared TiO_2 nanorods and after purification by dialysis 110

Figure 38 – Dispersion of TNR_{TOPO} in $CHCl_3$ (5 mg ml^{-1} TiO_2) 111

Figure 39 – TEM of TiO_2 nanorods synthesised using nonhydrolytic route with TOPO / dodecylamine ligands: (a) low resolution and (b) high resolution 112

Figure 40 – XRD pattern of TNR_{TOPO} 113

Figure 41 – Raman spectrum of TNR_{TOPO} 113

Figure 42 – Reaction yield of TNR_{TOPO} – overview 114

Figure 43 – Purity of TNR_{TOPO} (wt % TiO_2) – overview 114

Figure 44 – Typical TGA curve for the TNR_{TOPO} sample..... 115

Figure 45 – Reaction yield of TNR_{TOPO} as a function of reaction time 116

Figure 46 – XRD pattern of TNR_{TOPO} as a function of synthesis time 116

Figure 47 – Raman spectra of TNR_{TOPO} as a function of reaction time 117

Figure 48 – Raman spectra of TNR_{TOPO} for variable TOPO content (X denotes ratio of TOPO to other reactants in the reactant composition 1:1:6:X) 118

Figure 49 – Raman spectra of TNR_{TOPO} - effect of TOPO alkyl chain length..... 119

Figure 50 – Water-$CHCl_3$ mixture with TiO_2 nanorods:..... 121

Figure 51 – TEM of stripped TNR_{TOPO} 122

Figure 52 – Comparison of the XRD data between the as-prepared and stripped TNR_{TOPO} 122

Figure 53 – Comparison of the Raman spectra between the as-prepared and stripped TNR_{TOPO} 123

Figure 54 – TGA comparison between the as-prepared and UV-treated TNR_{TOPO} .. 123

Figure 55 – TNR_{TOPO} dispersions in water (5mg ml^{-1} TiO_2):..... 124

Figure 56 – Stability and optical transparency of stripped TNR_{TOPO} dispersions (5 mg ml^{-1} TiO_2) as a function of concentration of stabilising agent:..... 125

Figure 57 – UV-Vis spectra of aqueous TNR_{TOPO} dispersions (10 mg ml^{-1}) as function of TMAH concentration 128

Figure 58 – UV-Vis spectra of aqueous TNR_{TOPO} dispersions as function of TNR_{TOPO} concentration for fixed TMAH concentration [41.1 mM]..... 128

Figure 59 – ζ-potential as a function of pH for: (a) stripped and (b) APTS-coated aqueous TNR dispersions [10 mg ml^{-1} TNR_{TOPO}; 1 mM KCl background electrolyte, 20°C]..... 130

Figure 60 – UV-Vis spectra of Brilliant Blue R solutions in water at (a) basic pH 12-13 and (b) acidic pH ≤ 2, as a function of UV-exposure time..... 132

Figure 61 – UV-Vis spectra of the dye solutions containing (a) pristine, stripped TiO_2 nanorods (3 mg ml^{-1}) and (b) APTS-coated TiO_2 nanorods (3 mg ml^{-1}) as a function of irradiation time 133

Figure 62 – Half-life values for the dye concentration in: pH 12-13 and <2 references, uncoated and coated TiO_2 dispersions 134

Figure 63 – TEM of TNR_{OA}: (a) low-resolution micrograph and (b) high-resolution micrograph 135

Figure 64 – XRD pattern of TNR_{OA} 136

Figure 65 – Raman spectrum of TNR_{OA} 136

Figure 66 – TGA curve of TNR_{OA} 137

Figure 67 – TNR_{OA} nanorod dispersion in $CHCl_3$ (~ 60 mg ml^{-1}) 138

Figure 68 – UV-Vis spectra of TNR_{OA} dispersions in chloroform - function of concentration 138

Figure 69 – TNR_{OA} dispersions in water (1 mg ml^{-1} TiO_2): (a) stripped (b) stripped with 200 mM TMAH 140

Figure 70 – TGA curves for TNR_{OA} - effect of UV irradiation time 140

Figure 71 – TEM of stripped TNR_{OA}: (a) low-resolution and (b) high resolution micrograph 141

Figure 72 – Raman spectrum of stripped TNR_{OA} 142

Figure 73 – Scanned images of the as-prepared composite films and pure polymer controls: (a) TNR – PDLLA and (b) P25 TiO_2 – PDLLA 147

Figure 74 – Scanned images of the as-prepared composite films and pure polymer controls: (a) TNR – PMMA and (b) P25 TiO_2 – PMMA 148

Figure 75 – Optical microscope images of the PDLLA composite films: (a) pure PDLLA; (b, d, f) 0.1 wt%, 1 wt% and 2.5 wt% TNR-PDLLA; (c, e, g) 0.1 wt%, 1 wt% and 2.5 wt% P25 TiO_2-PDLLA 150

Figure 76 – UV-Vis spectra of the PDLLA composites filled with: (a) TNR and (b) P25 TiO_2 152

Figure 77 – UV-Vis spectra of the PMMA composites filled with: (a) TNR and (b) P25 TiO_2 153

Figure 78 – Contact angles for TNR-PDLLA composite films measured by DSA .. 155

Figure 79 – DMTA results for low loading TNR – PDLLA composites at 1 Hz: (a) Storage modulus and (b) tan δ as a function of temperature 157

Figure 80 – DMTA results for low loading TNR – PMMA composites at 1 Hz: (a) Storage modulus and (b) tan δ as a function of temperature 158

Figure 81 – DMTA results for high loading TNR – PDLLA composites at 1 Hz: (a) Storage modulus and (b) tan δ as a function of temperature 160

Figure 82 – DMTA results for high loading TNR – PMMA composites at 1 Hz: (a) Storage modulus and (b) tan δ as a function of temperature 161

Figure 83 – Summary of T_g measured by DSC for PDDLA and PMMA composite films 163

Figure 84 – Images of the as-prepared TNR – $PMMA_{09/2007}$ composites on glass slides 164

Figure 85 – UV-Vis spectra of the TNR – $PMMA_{09/2007}$ composites..... 165

Figure 86 – Thermogravimetric analysis of PMMA and $TNR_{09/2007}$ composites..... 166

Figure 87 – Images of the as-prepared composites on glass slides: (a) TNR_{TOPO}-PVA and (b) 5 nm anatase – PVA and (c) TNR_{OA}-PVA 168

Figure 88 – UV-Vis spectra of PVA and composites (a) 5 nm anatase – PVA (b) TNR_{TOPO} – PVA and (c) TNR_{OA} - PVA..... 170

Figure 89 – UV onset wavelength of PVA composites – function of TiO_2 loading . 171

Figure 90 – Measured TiO_2 content in the composites, compared against expected values (dashed line) 171

Figure 91 – Young's modulus of PVA and the composites: 174

Figure 92 – Maximum tensile strength of PVA and the composites:..... 175

Figure 93 – Elongation at break of PVA and the composites: 176

Figure 94 – Fracture surface of the 10 wt% TNR_{OA} - PVA composite under SEM.. 177

Figure 95 – Fractional weight loss of the pure PVA and the composites, after 300 h of UV (λ = 365 nm, power = 19 ± 1 $W \cdot m^{-2}$)..... 178

Figure 96 – UV-Vis spectra of PVA and the composites during UV degradation: (a) 1 wt% TNR_{TOPO} – PVA; (b) 5 wt% TNR_{TOPO} – PVA 180

Figure 97 – UV-Vis spectra of PVA with 10 wt% TMAH, at room temperature and after heating at 70°C for 15 min [*no UV treatment*] 180

Figure 98 – UV-Vis spectra of PVA and the composites during UV degradation: (a) 1 wt% 5 nm anatase – PVA; (b) 5 wt% 5 nm anatase – PVA 181

Figure 99 – DMTA results for low loading TNR – PDLLA composites at 10 Hz: (a) Storage modulus and (b) tan δ as a function of temperature 189

Figure 100 – DMTA results for low loading TNR – PMMA composites at 10 Hz: (a) Storage modulus and (b) tan δ as a function of temperature 190

Figure 101 – DMTA results for high loading TNR–PDLLA composites at 10 Hz: (a) Storage modulus and (b) tan δ as a function of temperature 191

Figure 102 – DMTA results for high loading TNR – PMMA composites at 10 Hz: (a) Storage modulus and (b) tan δ as a function of temperature 192

Figure 103 – DSC curve for the pure PMMA, showing three individual heating cycles and the regions associated with the glass transition temperature 193

Figure 104 – Thermogravimetric analysis of PVA and the composites (a) TNR_{TOPO} – PVA (b) TNR_{OA} – PVA 194

Figure 105 – Thermogravimetric analysis of PVA and composites (a) PVA with TMAH and (b) 5 nm anatase - PVA 195

Figure 106 – DMTA results for TNR_{TOPO}-PVA nanocomposites at 1 Hz: (a) Storage modulus and (b) tan δ as a function of temperature 196

Figure 107 – DMTA results for TNR_{OA}-PVA nanocomposites at 1 Hz: (a) Storage modulus and (b) tan δ as a function of temperature 197

Figure 108 – DMTA results for PVA films with TMAH at 1 Hz: (a) Storage modulus and (b) tan δ as a function of temperature 198

Figure 109 – DMTA results for 5 nm anatase-PVA nanocomposites at 1 Hz: (a) Storage modulus and (b) tan δ as a function of temperature 199

Figure 110 – DMTA results for TNR_{TOPO}-PVA nanocomposites at 10 Hz: (a) Storage modulus and (b) tan δ as a function of temperature 200

Figure 111 – DMTA results for TNR_{OA}-PVA nanocomposites at 10 Hz: (a) Storage modulus and (b) tan δ as a function of temperature 201

Figure 112 – DMTA results for PVA films with TMAH at 10 Hz: (a) Storage modulus and (b) tan δ as a function of temperature 202

Figure 113 – DMTA results for 5 nm anatase - PVA nanocomposites at 10 Hz: (a) Storage modulus and (b) tan δ as a function of temperature 203

Figure 114 – TNR – epoxy samples (top to bottom): pure epoxy, 1 wt% TNR - epoxy (dried nanorod powder added), 1 wt% TNR - epoxy (nanorod dispersion in $CHCl_3$ added) 205

List of tables

Table 1 – Oxidative potentials of various oxidants, values obtained from Threebond publication146.....
…49

Table 2 – Chemicals used in experimental work..... 79

Table 3 – Properties of organic dyes considered for evaluation of TiO2 photocatalytic activity..... 90

Table 4 – Tg values measured by DSC for TNR-PMMA composite films.....166

Table 5 – Notched fracture toughness results for pure epoxy and TNR-epoxy nanocomposites.....205

List of symbols

Dimensions		Units
A	– Absorbance	-
E	– Band gap energy	eV
A	– Cross-sectional area	m^2
C	– Concentration	$mg \cdot ml^{-1}$ / M ($mol \cdot l^{-1}$)
	– Centrifugal force	g
ρ	– Density	$g \cdot cm^{-3}$
D	– Diameter	m
ε	– Electrical permittivity	$F \cdot m^{-1}$
μ	– Electrophoretic mobility	$\mu m \cdot s^{-1}$
ε	– Extinction coefficient	$mol \cdot m^{-2}$
F	– Force	N
I_0 / I	– Incident / detected light intensity	$W \cdot m^{-2}$
L	– Length	m
M_w	– Molecular weight	$g \cdot mol^{-1}$
P	– Power	W
η	– Power conversion efficiency	%
P	– Pressure	bar
k	– Reaction constant	
A’	– Specific surface area	$m^2 \cdot g^{-1}$
ε	– Strain	-
T	– Temperature	K / °C
T_g	– Glass transition temperature	K / °C
σ	– Tensile Strength	Pa
t	– Time	s
η	– Viscosity	Pa·s
V	– Volume	dm^3 / l
λ	– Wavelength	nm
	– Weight fraction	wt%
E	– Young’s modulus	Pa
ζ	– ζ-potential	mV

List of abbreviations

Abbreviations

AAM	– Anodic alumina membrane
AM 1.5	– Air mass 1.5 standard
APTS	– 3-aminopropyl trimethoxysilane
CCD	– Charge coupled device
CEP-68	– Chondrocyte expressed protein-68
CNT	– Carbon nanotube
CVD / PVD	– Chemical vapour deposition / Physical vapour deposition
DSC	– Differential Scanning Calorimetry
DSA	– Drop Shape Analysis
DSSC	– Dye-sensitized solar cell
DMTA	– Dynamic Mechanical Thermal Analysis
EQE	– External quantum efficiency
GlOPS	– Glycidoxypropyl trimethoxysilane
IPA	– Isopropanol / isopropyl alcohol
IR	– Infra-red
LED	– Light emitting diode
OA	– Oleic acid
P25 TiO_2	– Commercial P25 TiO_2 Aeroxide® nanopowder
PL	– Photoluminescent
PANI	– Polyaniline
PCL	– Polycaprolactone
PDLLA	– Poly (D, L lactide)
PE	– Polyethylene
PET	– Poly (ethylene phthalate)
PEI	– Poly (ether imide)
PEN	– Poly (arylene ether nitrile)
PEO	– Poly (ethylene oxide)
PGA	– Polyglycolic acid
PHB	– Polyhydroxybutyrate

PI – Polyimide

PLGA – Polylactic-co-glycolic acid

PMMA – Poly (methyl methacrylate)

PPCO – Polypropylene-co-polymer

PPV – Poly (p-phenylenevinylene)

MEH-PPV – Poly [2-methoxy-5-(2'-ethylhexyloxy)-*p*-phenylenevinylene]

PPy – Polypyrrole

PS – Polystyrene

PSMA – Poly (styrene maleic anhydride)

PTh – Polythiophene

P3HT – Poly ((3-hexyl) thiophene)

P3OT – Poly ((3-octyl) thiophene)

PTFE – Poly (tetrafluoroethylene)

PVA – Poly (vinyl alcohol)

PVB – Poly (vinyl butyral)

PVC – Poly (vinyl chloride)

PVdF – Poly (vinyldene fluoride)

PVP – Poly (vinyl pyrrolidone)

RH – Relative humidity

SEM – Scanning Electron Microscopy

TBAH – Tetrabutylammonium hydroxide

TBPO – Tributylphosphine oxide

(HR)TEM – (High-Resolution) Transmission Electron Microscopy

TEPO – Triethylphosphine oxide

TGA – Thermogravimetric Analysis

THAH – Tetrahexylammonium hydroxide

TMAH – Tetramethylammonium hydroxide

TNR – TiO_2 nanorods

TNR_{TOPO} – TiO_2 nanorods from nonhydrolytic synthesis with trioctylphosphine oxide - dodecylamine ligands

TNR_{OA} – TiO_2 nanorods from nonhydrolytic synthesis with oleic acid ligand

TOPO – Trioctylphosphine oxide

TTIP – Titanium tetraisopropoxide

UV – Ultraviolet

UV-A	– 'Near' ultraviolet (315 – 400 nm)
UV-B	– 'Far' ultraviolet (200 – 320 nm)
UV-Vis	– Ultraviolet - visible
XRD	– X-ray Diffraction

1. Project motivation and aims

Titanium dioxide (TiO_2) or titania is an extremely versatile material, due to its high refractive index, brightness, stability, non-flammability and non-toxicity. Anatase, rutile and brookite are the three known crystal polymorphs of TiO_2, but only anatase and rutile are of wider academic and industrial interest. Because of its unique properties, titania is produced and used on a very large scale – 5 million tonnes in 2006, with a total worth of US$ 9 billion p.a. with a consistent annual market increase of 2-3%[1]. Major applications of TiO_2 include use in paints, fillers in plastics, paper, cosmetics and even food colouring (E171). A vast range of Dulux® paints, Nivea® sunscreens, Colgate® toothpaste, Vicks VapoRub®, McDonald's Toasted Deli Spicy Veggie® and styptic pencil are only a few of omnipresent products that contain titanium dioxide. TiO_2 is produced principally from the mineral ilmenite (90% of supply, theoretical formula $FeTiO_3$) and the mineral rutile, rarer but higher purity ore. Perhaps surprisingly, only 7% of titanium contained in the mined ores is actually used for the production of titanium metal, an extremely high strength- to-weight ratio and corrosion-resistant material; the remaining 93% is used in the production of TiO_2. Commercial production of TiO_2 is carried out through two routes – the sulphate and the chloride process, both of which are very energy intensive and involve a large number of unit operations[2]. The technologically simpler sulphate process uses ilmenite as the feedstock and can produce both anatase and rutile, while the chloride route is more suited for rutile production and generally gives a purer product. The leading manufacturers, to name but a few, according to a 2004 report are[3]: DuPont (25% market share), Millennium Chemicals (15%), Kerr-McGee (14%), Huntsman (13%) and Kronos (11%).

The use of TiO_2 in polymers is significant (20-25%[1]), however, the extent to which the majority of commercial powders can improve features of current polymeric composites is already reaching its limit. These fillers are often aggregated (despite the fact that the primary particle size is marketed as in the nanometre range), mixed phase, polycrystalline and polydispersed in size and shape (Figure 1A).

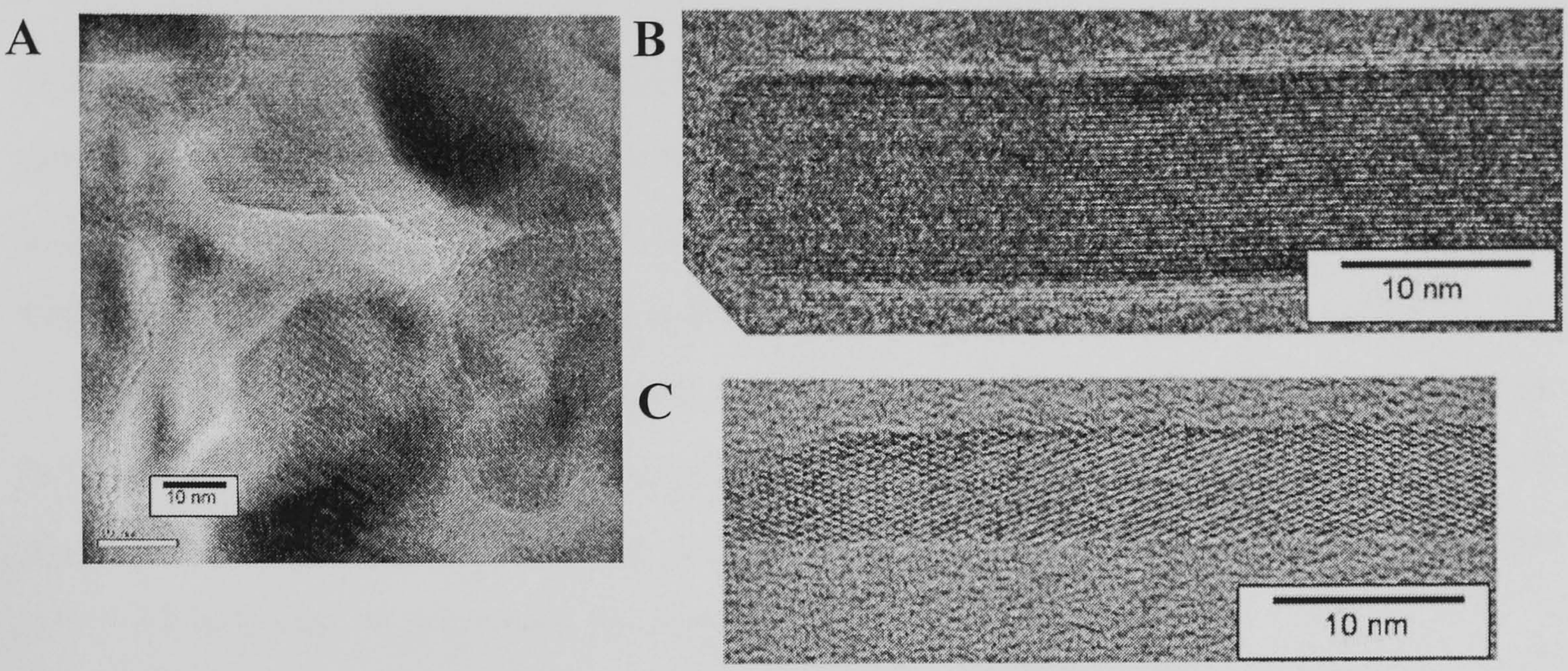


Figure 1 – Transmission Electron Microscopy (TEM) micrographs of the: (a) commercial Degussa P25 TiO_2 Aeroxide® and (b, c) TiO_2 nanorods synthesised in relation to the current project

The last two decades have seen an explosion of interest into the synthesis of nanoscale particles, with a whole spectrum of fascinating properties, potentially advantageous in many technological applications. In the present work, we turn our attention towards a new generation of titania nanoparticles, with a particular focus on anisotropic, single crystalline anatase nanorods (Figure 1B-C). The synthesis of anisotropic TiO_2 single crystals has been extensively reported for different morphologies – nanotubes[4,5], nanorods[6,7], nanowires[8,9], etc. Synthesis procedures, although still at gram-scale at best, allow much better control over shape and size of particles, as well as giving rise to single-crystal, single-phase product.

Due to quantum confinement on the nanoscale[10], the surface area-to-volume ratio of nanocrystals is higher than for micron-sized powders and even equiaxed nanoparticles, which translates into higher density of surface sites available for surface reactions, allowing better load-transfer and higher interfacial charge carrier transfer rates, important for example in photocatalysis and photovoltaics. High aspect ratio nanorods

could be induced to form oriented arrays under the effects of electric field or extensional flow. Anisotropy could be beneficial in optical and electronic devices with improved conductivity resulting from the formation of electron percolation networks. Aligned reinforcement also has potential for enhancement of mechanical properties.

Several distinct groups of processing methods have been reported to produce TiO_2 nanoparticles of various shapes, sizes, crystallinity and degree of alignment, which will be considered in the next Chapter. Research efforts into fabrication and characterisation of nano-TiO_2-polymer composites are also on the rise; however, the vast majority of publications pertain to equiaxed particles and indicate improved properties[11,12]. Only a small number of publications focus on anisotropic materials and almost exclusively on applications in electronic devices[13-15]. The literature review of this field will also be presented in Chapter 2.

The primary objective of this project was to fabricate TiO_2-nanorod polymer composites and characterise their optical, mechanical and thermal behaviour in contrast to pure polymers and composites reinforced with the most promising commercial powders. Chapter 3 will briefly address the experimental conditions used in the synthesis and modification of TiO_2 nanorods, fabrication of polymer nanocomposites and ultimately, analytical techniques used to characterise both the nanorods and the nanocomposites.

Synthesis of highly crystalline single-crystal anatase nanorods, and their subsequent surface modification, will be discussed in detail in Chapter 4. By changing the surface character of the nanorods, it becomes possible to achieve excellent dispersion in either aqueous or organic solvents, which is a prerequisite for successful fabrication of composites, or indeed many other applications. In this work, nanocomposite samples of outstanding optical quality have been fabricated using poly (vinyl alcohol) (PVA), poly (methyl methacrylate) (PMMA) and poly (D,L lactide) (PDLLA) matrices, which will be presented together with other composite-related findings in Chapter 5.

In the course of this work, synthesised TiO_2 nanorods were provided to other research groups within Imperial College for fabrication of novel materials. A brief summary of the relevant findings will be presented in Chapter 6, to demonstrate the scope and versatility of our material. This Chapter will also provide a critical summary of the findings of this project as well as an outlook for subsequent research potential.

1.1 Scientific objectives

The scope of this thesis is to address several fundamental scientific issues:

- The effect of the nanoparticle aspect ratio on nanocomposite properties – what are the advantages offered by introducing nanorods rather than equiaxed nanoparticles? Can the anisotropic properties of nanorods be conveyed through to the nanocomposites to yield materials with superior or novel properties?

- Investigation of the nanorod surface chemistry – prospect of modifying the titania surface in order to allow nanorod dispersion in different solvents and, consequently, polymer matrices. Different surface functionalities could be also useful to control the adhesion at nanorod-polymer interface or to control the activity of the titania surface (e.g. reduction in photocatalytic activity of TiO_2). An important requirement is that the modification procedures do not affect the particle morphology or the crystal phase.

2. Introduction and background literature

2.1 Introduction

Materials with a characteristic dimension at the nanometre scale have been the subject of extensive research for several decades, but the interest in the fields of nanomaterial science and nanotechnology has surged with the discovery of C_{60} fullerene in 1985 by Kroto et al.[16] and carbon nanotubes (CNTs) in 1991 by Iijima[17]. Although the formal structural determination has been credited to Iijima, CNTs have been extensively encountered in the past (refer to Monthioux and Kuznetsov[18] for a comprehensive historical review). For instance, it has been recently reported that CNTs have been inadvertently formed during forging of the Damascus sabres, which were famous in medieval ages for their extremely high strength, most likely due to CNT reinforcement[19]. Formation of CNTs was also reported in 1890 by thermal decomposition of methane and more recently, CNT-like, sub-microscopic carbonaceous filaments in the tubes of catalytic steam reformers have been a major problem in the production of synthetic gas[20].

Although much of current nanomaterials research is directed at the properties and possible applications of CNTs (nearly 40,000 relevant publications to date, 05/2008, Web of Knowledge database), considerable efforts have also been directed towards other inorganic nanostructures. Several comprehensive reviews have been publicised in the past few years, providing critical summaries of some currently known inorganic nanotubes, synthesis methods and some relevant applications[21-23]. Chronologically, the first inorganic nanotubes[24] (WS_2) were discovered, in 1992, only a year after Iijima's report of CNTs. Following this discovery, many other types of inorganic nanotubes were reported subsequently[23]: 1993 – MoS_2[25]; 1995 – BN[26], SiO_2[27]; 1996 – TiO_2[4]; 1998 – VO_x[28]; $NiCl_2$[29]; 2000 – $NbSe_2$[30], Au[31], Co and Fe[32]; 2001 – CdS[33], CdSe[34], ZnS[35], NiS[36], $Cu_{5.5}FeS_{6.5}$[37], Al_2O_3[38], In_2O_3 and Ga_2O_3[39], GaN[40]; 2002 – ZrS_2 and HfS_2[41], NbS_2 and TaS_2[42], (Er, Tm, Yb, Lu) oxide[43], ZnO[44], $BaTiO_3$ and $PbTiO_3$[45], Cu and Ni[46], Te[47], ReS_2[48], silicon nanotubes[49], etc.

Inorganic nanotubes can be classified into six categories:

- *Transition metal chalcogenides*: MoS_2, $MoSe_2$, WS_2, WSe_2, NbS_2, $NbSe_2$, TaS_2, ZrS_2, HfS_2, TiS_2, ZnS, NiS, CdSe, CdS
- *Oxides:* TiO_2, ZnO, GaO/ZnO, VO_x, $W_{18}O_{49}$, V_2O_5, Al_2O_3, In_2O_3, Ga_2O_3, $BaTiO_3$, $PbTiO_3$, SiO_2, MoO_3, RuO_2, rare earth oxide nanotubes
- *Transition metal halogenides*: $NiCl_2$
- *Mixed-phase and metal-doped nanotubes:* $PbNb_nS_{2n+1}$, $Mo_{1-x}WS_2$, Nb–WS_2, $W_xMo_yC_zS_z$;, WS_2–CNTs, NbS_2–CNTs, Au–MoS_2, Ag–WS_2, Ag–MoS_2
- *Boron and silicon based nanotubes*: BN, BCN, Si
- *Pure metal nanotubes*: Au, Co, Fe, Cu, Ni, Te, Bi

Inorganic nanotubes can be grown using different techniques, some of which are also utilised for CNT growth – decomposition of precursor crystals, template (both physical and chemical) growth, physical/chemical vapour deposition, sulphurisation, precursor-assisted pyrolysis, rolling of planar sheets, and precursor hydrolysis in presence of growth directing agents (surfactants). Each growth technique has a specific effect on the nanotube morphology, e.g. nanotubes prepared by direct growth from the vapour phase or sulphurisation of transitional metal oxides exhibit, on average, more perfect lattices than for instance nanotubes grown using templates. A defect-free structure, which is generally more difficult and costly to achieve, is not always required, especially for bulk applications, e.g. the use of nanotubes as sensors or catalysts with high surface aspect ratios.

We now turn our attention towards TiO_2 nanostructures, which are the main scope of this literature review, particularly focusing on promising novel methods for the synthesis of TiO_2 nanoparticles and current state-of-the-art of the TiO_2 polymer nanocomposites. The immense utilisation of TiO_2 powders produced by the commercial sulphate and chloride routes, for a wide range of purposes has been highlighted in Chapter 1, which in turn generates a large research interest in the development of nanoscale TiO_2. Specifically, the advantages offered by having a material with a characteristic dimension on the nanometre scale are quantum confinement, which in the case of semiconductor nanomaterials such as TiO_2 affects the electronic properties, e.g. band-gap, movement of electrons and holes, etc. The

surface-to-volume ratio of particles increases with decreasing size, clearly an advantage for photocatalytic and photoelectronic applications where interfacial area should be as large as possible. Lastly, nanoparticles with a size significantly lower than the visible light wavelength (i.e. several 100 nm) will not scatter light, provided that they are well-dispersed – a major opportunity for UV absorbing TiO_2 for fabrication of transparent UV filters.

It is very important, at this stage, to emphasise that dispersible, single-crystal, single-phase TiO_2 nanoparticles of well-defined morphology and size distribution are not yet available commercially. Indeed, many respectable companies advertise TiO_2 nanopowders, with primary particle sizes on the nanoscale (e.g. 5 nm, 21 nm, etc.), but most of the particles are fused into large agglomerates (>100 nm), which, due to agglomeration, cannot be broken down and properly re-dispersed. 'True' nano-TiO_2 synthesis procedures, although still gram-scale, allow much better control over shape and size of particles, as well as giving rise to single-crystal, single-phase products.

Particularly interesting to this work are anisotropic TiO_2 structures – nanotubes and nanorods. Again, the surface area-to-volume ratio of nanocrystals is higher than for micron-sized particles, which translates into higher availability of surface sites for surface reactions, allowing better load-transfer and higher interfacial charge carrier transfer rates. These potential advantages could be beneficial for enhanced catalysts, polymer nanocomposites, photovoltaic devices, etc. High aspect ratio nanorods could be induced to form oriented arrays under the effects of electric field or unidirectional flow. The nanorod alignment could be beneficial in optical devices or for enhancement of mechanical properties, for example in polymer nanocomposites. Although a lot of attention has been devoted to the development of synthesis methods for highly anisotropic titania nanotubes / nanorods, their use in polymer nanocomposite systems remains, perhaps surprisingly, almost unstudied so far.

2.2 Synthesis of TiO_2 nanomaterials

The synthesis of TiO_2 nanoparticles, with emphasis on anisotropic structures will be discussed and categorized according to the preparation method. Although two different methods are sometimes combined into a hybrid route to produce nano-TiO_2, the following synthesis routes can be generally distinguished:

- Sol-gel – hydrolytic and nonhydrolytic methods
- Reverse micelle method
- Hydrothermal and solvothermal methods
- Direct oxidation method
- Chemical and physical vapour deposition method
- Electrodeposition method
- Sonochemical method
- Microwave method

Each of these methods will be briefly discussed, with particular focus on the sol-gel route as it was used to synthesise the anatase nanorods. Key features of each route will be presented, with some most relevant references in the field. Transmission Electron Microscopy (TEM) micrographs from relevant publications will also be included, to give an appreciation of the potential of each method. The selection of publications included is by no means exhaustive; indeed, substantial number of papers, beyond the scope of this literature review has been published, which also extends to different TiO_2 structures – mesoporous materials, aerogels, opals, etc. A recent (2007) review[50] is an excellent resource for a detailed treatise on latter structures as well as for the methods discussed in the next section.

2.2.1 Sol-gel methods for synthesis of TiO_2 nanostructures

Sol-gel synthesis of TiO_2 nanomaterials has been extensively reported[6,7,51-79]. Sol-gel processing is a very versatile method, which allows control over a range of product parameters, including, but not limited to shape, crystallinity, size and size distribution. A suspension of colloids (i.e. *sol*) is formed either by hydrolytic[6,51-68] or nonhydrolytic[7,69-79] reactions from a range of precursors, most commonly inorganic titanium metal salts (e.g. TiF_4, $TiCl_4$) or organo-metallic compounds (e.g. alkoxides, $Ti(OPr)_4$ or $Ti(OBu)_4$). Complete polymerisation of the titanium precursors and loss of solvent will lead to a liquid to solid transition (i.e. *gel*).

In a typical hydrolytic synthesis, the growth of the Ti-O-Ti network proceeds via two reactions; hydrolysis (eq. 1) gives unstable hydroxyalkoxides, $Ti(OH)_x(OR)_{4-x}$, which react to eliminate water and alcohol and to produce a Ti-O-Ti bridge. This polycondensation (eq. 2) leads to the growth of the nanocrystalline network, which can be directed by using an appropriate structure directing agent (to be discussed shortly).

$$Ti(OR)_4 + x \cdot H_2O \rightarrow Ti(OH)_x(OR)_{4-x} + x \cdot ROH \qquad (1)$$

$$(OR)_{4-x}(OH)_{x-1}Ti - OH + XO - Ti(OH)_x(OR)_{3-x} \rightarrow (OR)_{4-x}(OH)_{x-1} - - (OR)_{3-x}(OH)_x + XOH \qquad (2) \qquad X = H, R$$

Hydrolytic reactions have been reported for synthesis of equiaxed[6,59-61] as well as anisotropic structures, specifically nanotubes[56,58,62], nanorods[6,54,63,65-68], and even nanoribbons[61]. Since the vast majority of hydrolytic processes utilise titanium alkoxides, the main challenge is to control the hydrolysis-condensation rates, which, due to the reactivity of the alkoxides, are generally too fast for satisfactory control over morphology. Indeed, very fast, uncontrolled hydrolysis results in the formation of precipitates with a high degree of micro-structural disorder. Modification of the precursor surface during synthesis with carboxylic acids (e.g. oleic acid)[6] or β-diketones (e.g. acetylacetone)[55,68] allows control over the rate of hydrolysis.

Anisotropic growth can be achieved by using structure directing ligands[6,54,61], which preferentially bind to certain crystal facets, thus preventing crystal growth in that

direction. The ligands can have a dual role, also leading to passivation of the titania surface, sterically preventing the agglomeration.

Chemseddine and co-workers[53,54] have reported the synthesis of highly crystalline anatase nanoparticles, with tuneable aspect ratio. Transmission electron microscopy (TEM) images of the produced particles are shown in Figure 2. Titanium alkoxides, in the presence of tetramethylammonium hydroxide react to produce equiaxed nanoparticles (~20 nm, Figure 2A-B), nanorods (~5x40 nm, Figure 2C), which in turn self-assemble into superlattices (Figure 2D). Tetramethylammonium hydroxide acts both as a catalyst for the polycondensation and provides an organic cation, which stabilises the titania nanocrystals in aqueous dispersions, which enhances the processability of the nanoparticles.

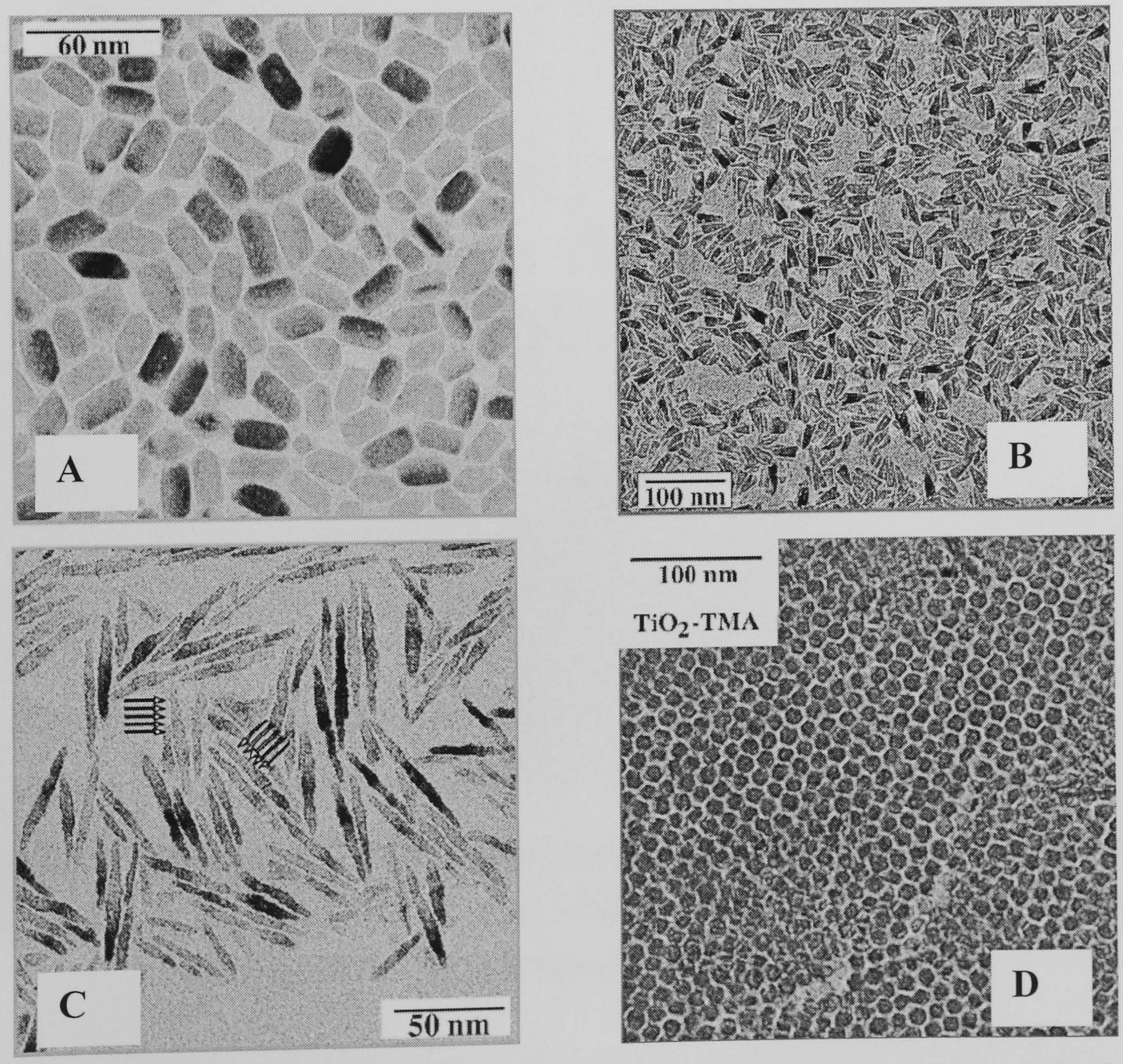


Figure 2 – TEM images of: (a, b) nanoparticles, (c) nanorods and (d) superlattice self-assemblies synthesised by hydrolysis of $Ti(OR)_4$ in presence of TMAH, from Chemseddine et al.[54]

In a more recent and highly cited paper, Cozzoli et al.[6] report the synthesis of highly crystalline anatase nanospheres and nanorods. Fast hydrolysis reactions favour the growth of nanorods (~4x40 nm, Figure 3A-B), while nanospheres (~10 nm, Figure 3C) are grown for slower hydrolysis rates. The hydrolysis rate of $Ti(OPr)_4$ is controlled by chemical modification with a long chain carboxylic acid, oleic acid (OA) in an aqueous base solution of tertiary amine oxides or quaternary ammonium hydroxides. The ratio of OA to $Ti(OPr)_4$ and the amount of amine oxides and ammonium hydroxides used during the synthesis directly affects the product morphology.

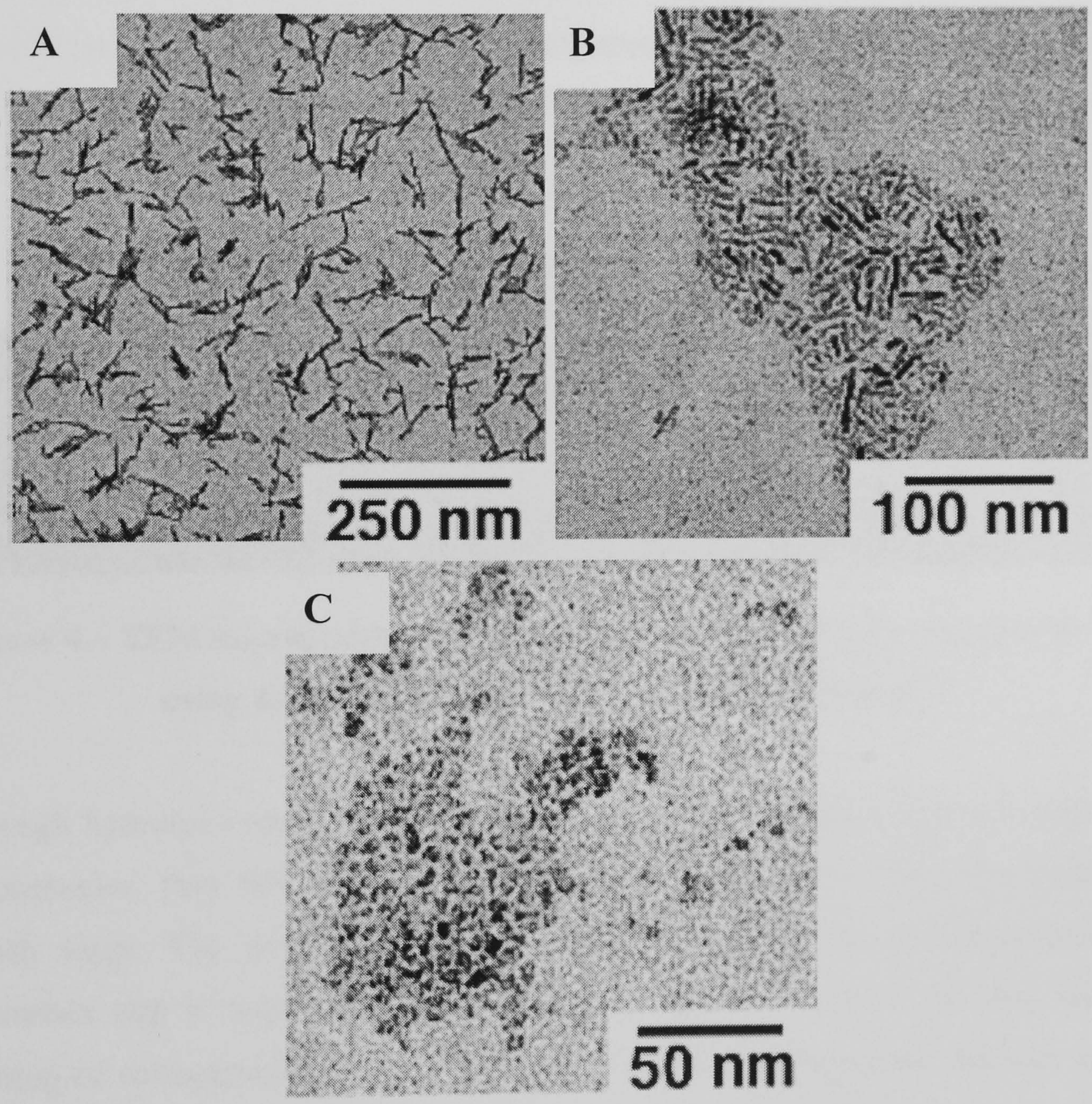


Figure 3 – TEM images of TiO_2 (a, b) nanorods and (c) nanospheres synthesised by hydrolysis of TTIP in aqueous basic solutions, using OA as a surface modifier, from Cozzoli et al.[6]

An alternative method has been frequently reported[56,58,62,68] for the synthesis of TiO_2 nanorods and nanotubes, which combines hydrolytic sol-gel processing with the use of growth directing templates. Typically, a precursor sol is prepared into which porous anodic alumina membranes (AAM) are dipped. The hydrolysis reaction takes place within the membrane pores. The products are usually calcined following the synthesis, at 400-600°C, with the temperature depending on the desired TiO_2 crystalline phase. The AAM is subsequently dissolved using an inorganic base (e.g. LiOH, NaOH) or acid (e.g. H_3PO_4) solution. Imai et al.[56] have used TiF_4 and AAM with tailored pore size (10-200 nm) to deposit anatase titania nanotubes and nanorods (100-150 nm internal diameter), scanning electron microscopy (SEM) micrographs of which are shown in Figure 4. Template growth yields only small amounts of product, but is advantageous in terms of producing well aligned arrays of nanotubes.

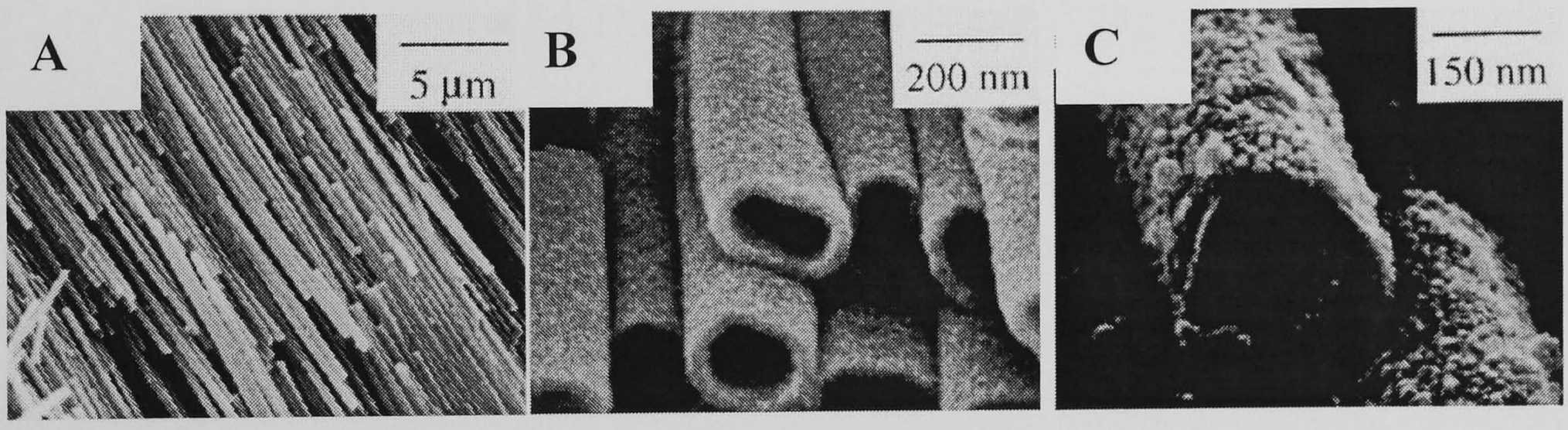


Figure 4 – TEM micrographs of TiO_2 (a) nanorods and (b, c) nanotubes grown using AAM dipped into a TiF_4 sol, from Imai et al.[56]

Although hydrolytic routes are facile and capable of producing intricate nanoparticle morphologies, they fall short in achieving high crystallinity during the hydrolytic growth stage. The products are sometimes amorphous and a high-temperature calcination step is required to improve crystallinity[57,58,68], which, in turn, leads to sintering of nanoparticles and loss of morphology and surface area. Another crucial problem is that the growth of nanoparticles inside templates leads to polycrystalline material.

Nonhydrolytic sol-gel routes are more advantageous and versatile since they are carried out in organic media, without the water presence, which permits synthesis at much higher temperatures, resulting in single-crystals with narrow size distribution and high crystallinity. Indeed, nonhydrolytic routes have been successfully used for synthesis of a whole range of metal oxide nanoparticles, which has been reviewed in the past by Vioux[71], Hay and Raval[80,81] and more recently by Niederberger and Garnweitner[79]. The nonhydrolytic reactions typically involve the reaction of titanium halide with either a titanium alkoxide (condensation reaction, eq. 3) or an organic anhydride (eq. 4), which act as oxygen donors. This results in TiO_2 formation and elimination of an alkyl halide (eq. 3) or an ester (eq. 4).

$$TiX_4 + Ti(OR)_4 \rightarrow 2 \cdot TiO_2 + 4 \cdot RX \qquad (3)$$

or

$$Ti(OR)_4 + 2 \cdot (R'C = O)_2 O \rightarrow TiO_2 + 4 \cdot R'COOR \qquad (4)$$

The actual reaction mechanism is much more complex than described above and most likely involves a series of reactions between equilibrated unstable intermediates (e.g. via $TiCl_{4-x}(OPr)_x$, $0 \leq x \leq 4$, for eq. 3).

Similar to hydrolytic synthesis, the high reactivity of the precursors can lead to very fast, uncontrolled crystal growth, which is clearly undesirable for the synthesis of single-crystal nanoparticles with well-defined morphology. Modification of the titanium precursors to control the rate of condensation has been reported by replacing one or more isopropoxide groups in $Ti(OPr)_4$, with amine-functionalised alkoxides[74]. More commonly, organic ligands are employed to passivate the titania surface (non-selective ligands) and to induce unidirectional growth for anisotropic nanostructures (selective ligands).

Synthesis of both equiaxed titania nanoparticles[72-74] and anisotropic titania nanorods[7,75-77] have been reported. Trentler et al.[72] used TiX_4-$Ti(OR)_4$ condensation in heptadecane at 300°C, with trioctylphosphine oxide (TOPO) as a non-selective ligand to grow equiaxed nanoparticles (Figure 5). The choice of X and R in the Ti-precursors was demonstrated to influence the particle size and rate of reaction, respectively, with larger X resulting in smaller particles, while highly branched alkoxides increased the reaction rate dramatically.

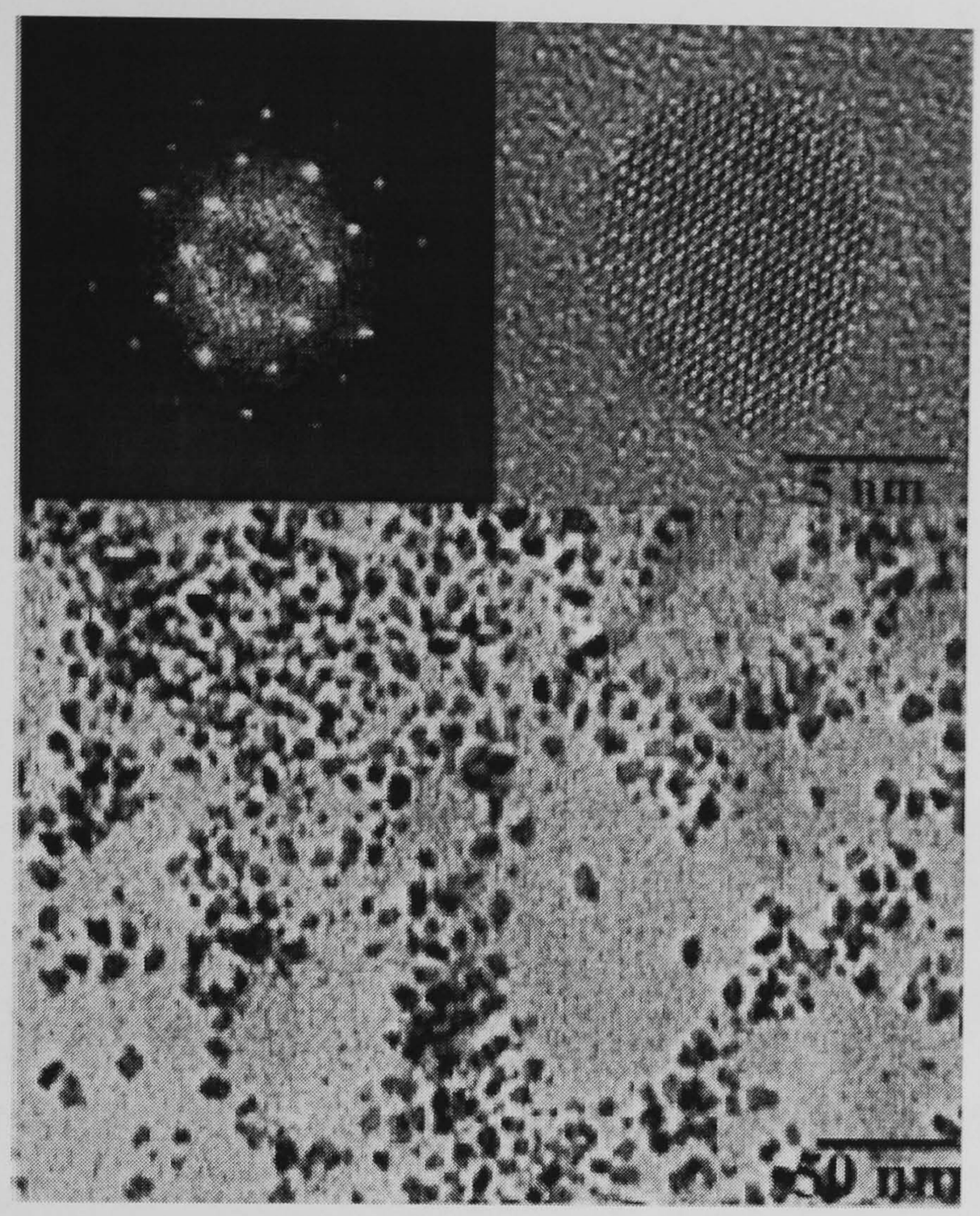


Figure 5 – TEM image of TiO_2 nanoparticles synthesised using $TiCl_4$-$Ti(OPr)_4$ in TOPO/heptadecane, from Trentler et al.[72]. The top left inset is a selected-area electron diffraction pattern, indicating anatase and high-resolution TEM (HRTEM) of a single particle is shown in top right.

Lauric acid[75], 2-amino-2-(hydroxymethyl)-1,3-propanediol[76], oleylamine / oleic acid[7] and hexadecylamine / oleic acid[77] are some of the selective ligands that have been used to affect nanorod growth under nonhydrolytic conditions. TEM micrographs of some of the nanorods are shown in Figure 6. Growth of nanostructures in the presence of different ligands is a simple and versatile technique to achieve control over particle size, shape and surface chemistry, all of which are of paramount importance in subsequent applications.

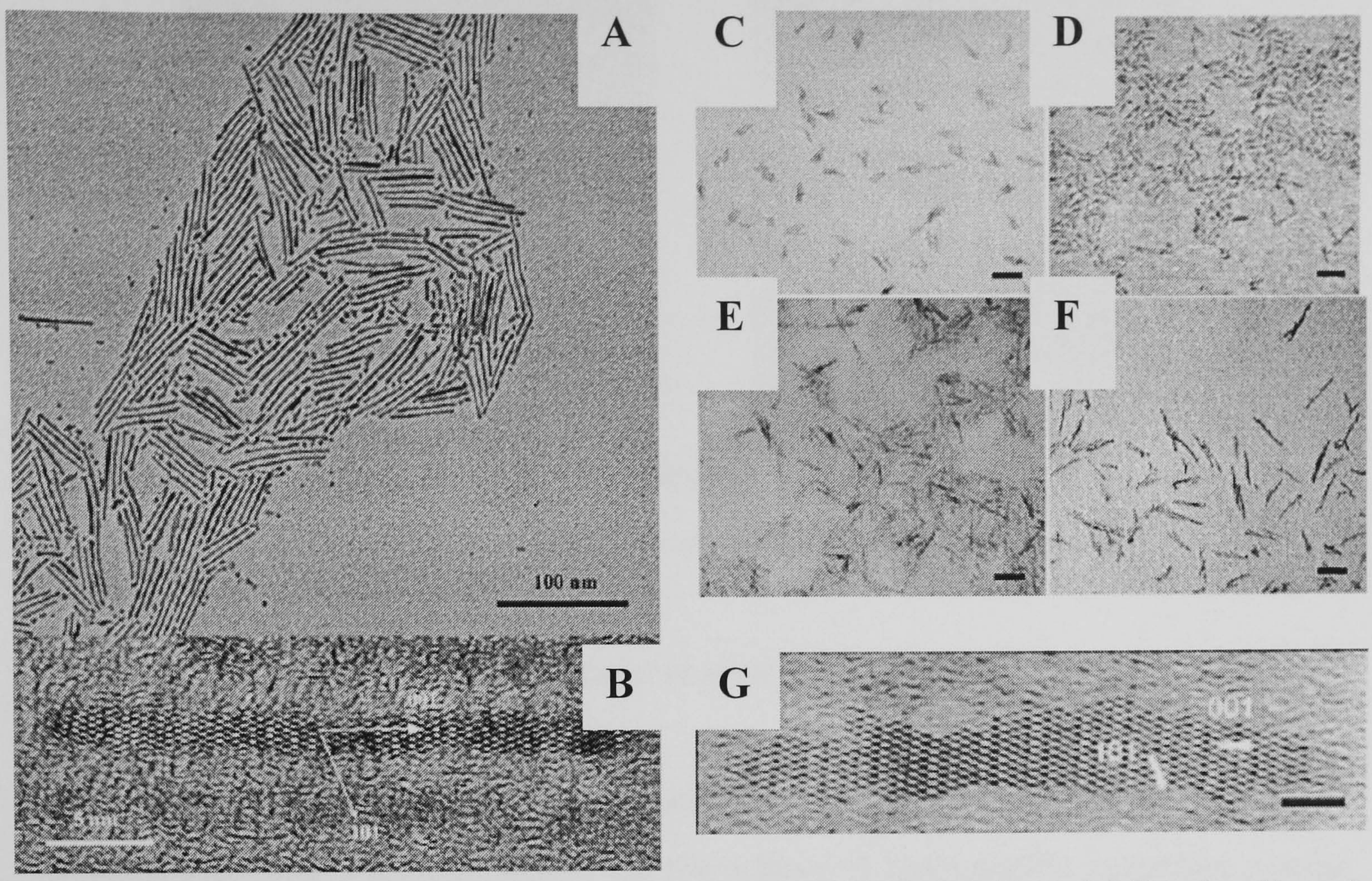


Figure 6 – TEM images of TiO_2 nanorods grown using $Ti(OPr)_4$ and following ligands: (a, b) 1-hexadecylamine and OA, from Joo et al.[77]; (c-g) lauric acid and TOPO, (c→f) increasing the relative ratio of lauric acid to $Ti(OPr)_4$ results in longer rods (scale bar 25 nm), from Jun et al.[75]

Nonhydrolytic condensation between TiX_4 and $Ti(OPr)_4$ has excellent potential for synthesis of highly crystalline single crystal TiO_2. However, a potential disadvantage of this route is the significant formation of environmentally harmful alkyl halides, which would need to be addressed for large-scale syntheses. Alkyl halides are highly volatile and flammable, so that removal could be achieved by, for example using absorption or more simply direct oxidation in an incinerator. An alternative, 'greener' mechanism for the synthesis of TiO_2 nanostructures has also been reported recently, which relies on aminolysis of $Ti(OPr)_4$-oleic acid complexes by a long alkyl chain primary amine, oleylamine[7]. Anatase nanodots and nanorods (Figure 7), with tuneable aspect ratio and diameter have been synthesised using this method.

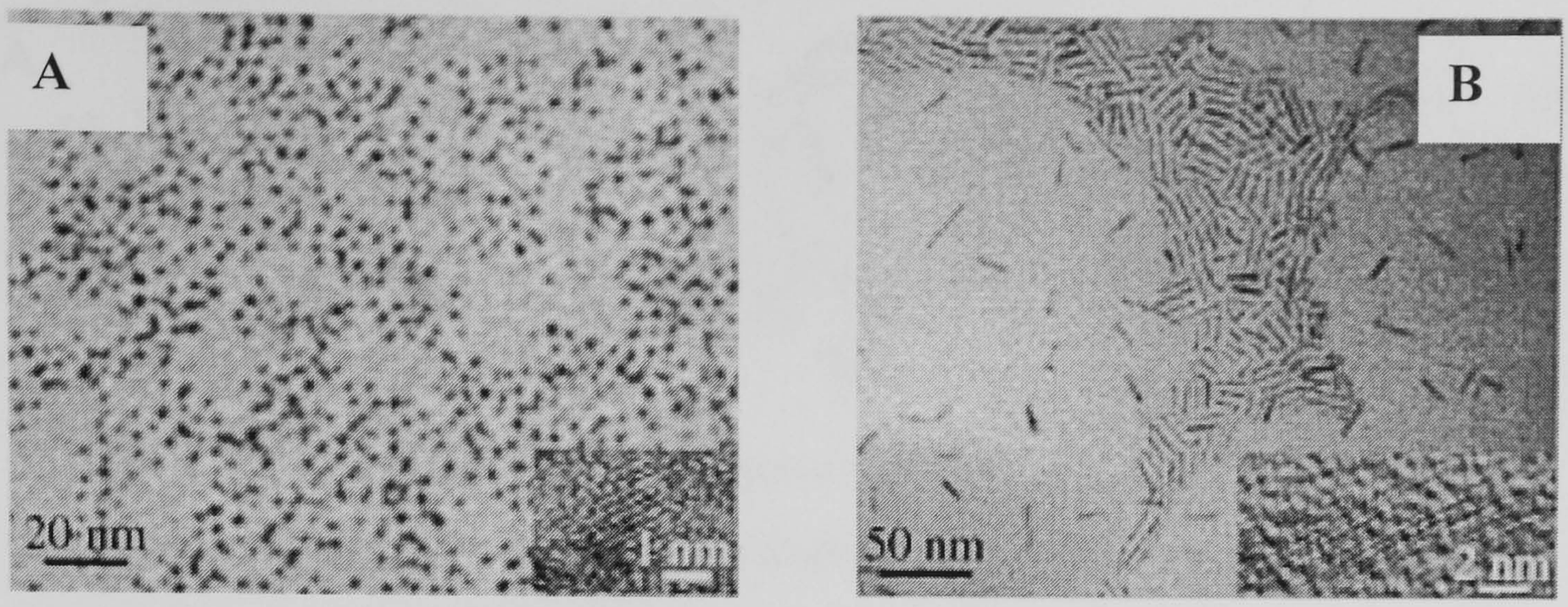


Figure 7 – TEM images of anatase TiO_2 (a) nanodots and (b) nanorods formed by nonhydrolytic aminolysis of $Ti(OPr)_4$, from Zhang et al.[7]

2.2.2 Synthesis of TiO_2 nanostructures in reverse micelles

Micelles are formed by surfactants in aqueous solutions beyond a certain surfactant concentration and are characterised by orientation of hydrophobic surfactant chains toward the interior of the micelle, while the hydrophilic groups are oriented away from the micelle, toward the surrounding aqueous medium. Reverse (or inverse) micelles form in the non-aqueous solutions and have the opposite surfactant orientation, hydrophilic ends toward the interior, hydrophobic chains towards the surrounding medium. Micelles are often globular, but other shapes are also possible, depending on the nature and concentration of the surfactant, temperature, etc. Synthesis of nanocrystalline titania using reverse micelles has been reported[82,83]. Normally, the titanium alkoxide precursor is added to the microemulsion containing reverse micelles. The hydrolysis of the alkoxide takes place within the micelles resulting in formation of TiO_2 networks. The micelles play a dual role, primarily acting as a nanoscopic reactor and also as a physical barrier, preventing uncontrolled growth, which can ultimately lead to undesirable agglomeration between the particles. The particle shape is typically equiaxed, stemming from the globular shape of the micelles, but anisotropic 'shuttle' (Figure 8A) and 'petal' (Figure 8B-C) structures have also been realised[83]. The advantage of the reverse micelle route is that by altering the amount of surfactant, micelle size, and therefore nanoparticle size, can be adjusted. The underlying hydrolytic synthesis implies the problems mentioned earlier, potentially the formation of amorphous products[82], which require calcination.

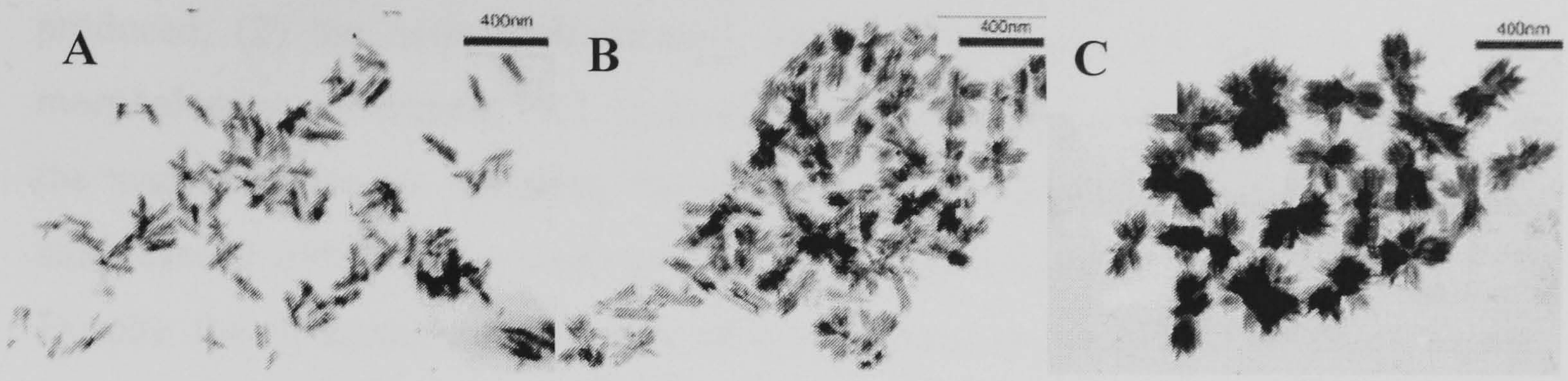


Figure 8 – TEM images of TiO_2 nanoshuttles and nanopetals formed by hydrolysis of $Ti(OBu)_4$ in reverse micelles, after: (a) 5 days (b) 10 days and (c) 20 days of synthesis; from Zhang et al.[83]

2.2.3 Hydrothermal and solvothermal routes for the synthesis of TiO_2 nanostructures

Hydrothermal processing has been extensively used for the synthesis of TiO_2 nanostructures[5,8,84-97]. The procedure is carried out in sealed pressure vessels (autoclaves), which can be Teflon-lined. Hydrothermal reactions are carried out in aqueous solutions, at elevated temperatures and pressures. High pressure operation enables temperatures significantly above the 'normal' boiling point of water. The precursors used for the synthesis of TiO_2 can be amorphous or crystalline TiO_2-based sols obtained by hydrolysis of $TiCl_4$ or $Ti(OR)_4$ as well as commercially available crystalline TiO_2 nanoparticles. In a typical process, the TiO_2 precursor is added to an alkaline, usually NaOH, solution. The vessel is sealed and heated for up to a day at elevated temperatures, usually 100-250°C. The resultant product is recovered by washing and centrifugation; washing can be either with deionised water or an acid solution (e.g. HCl or HNO_3). Kasuga et al.[5,84] were the first to claim that the hydrothermal method can be used to produce single-crystal anatase nanotubes (Figure 9A). Typical nanotube dimensions observed were 8 nm in diameter, with a wall thickness of 3-5 nm and lengths of ~100 nm. However, this method has been subject to some controversy in terms of the product composition, particle morphology and the formation mechanism. The original reports by Kasuga et al. suggest that the nanotubes formed are anatase, which are formed by rolling of the planar titania sheets during the second stage, acid treatment. These observations have been contested at first by the Peng group[87,88], claiming, based on HRTEM, X-ray diffraction and Raman spectra of the resulting powders, that: (1) titanate ($H_2Ti_3O_7$) rather than TiO_2 is

produced, (2) the main hydrothermal step in NaOH solution leads to nanotube morphologies; subsequent HCl treatment only causes surface defects and finally (3) the nanotubes are not seamless, but more scroll-like. Several research groups have since agreed with the latter findings[92,94-96], whilst others maintain the original view[86,89]. Despite the disagreement in terms of crystal structure and the conditions in the solution which lead to the formation of the nanotubes, a broad formation mechanism can be proposed: 2D lamellar sheets of titania / titanate form first by digestion of the raw 3D precursor, which then undergo a rolling process (depicted in Figure 10A) to ultimately form more scroll-like (Figure 9B-C) 1D structures rather than seamless tubes. The sheets have a high surface free energy and readily undergo a rolling process to attain a more stable energy state.

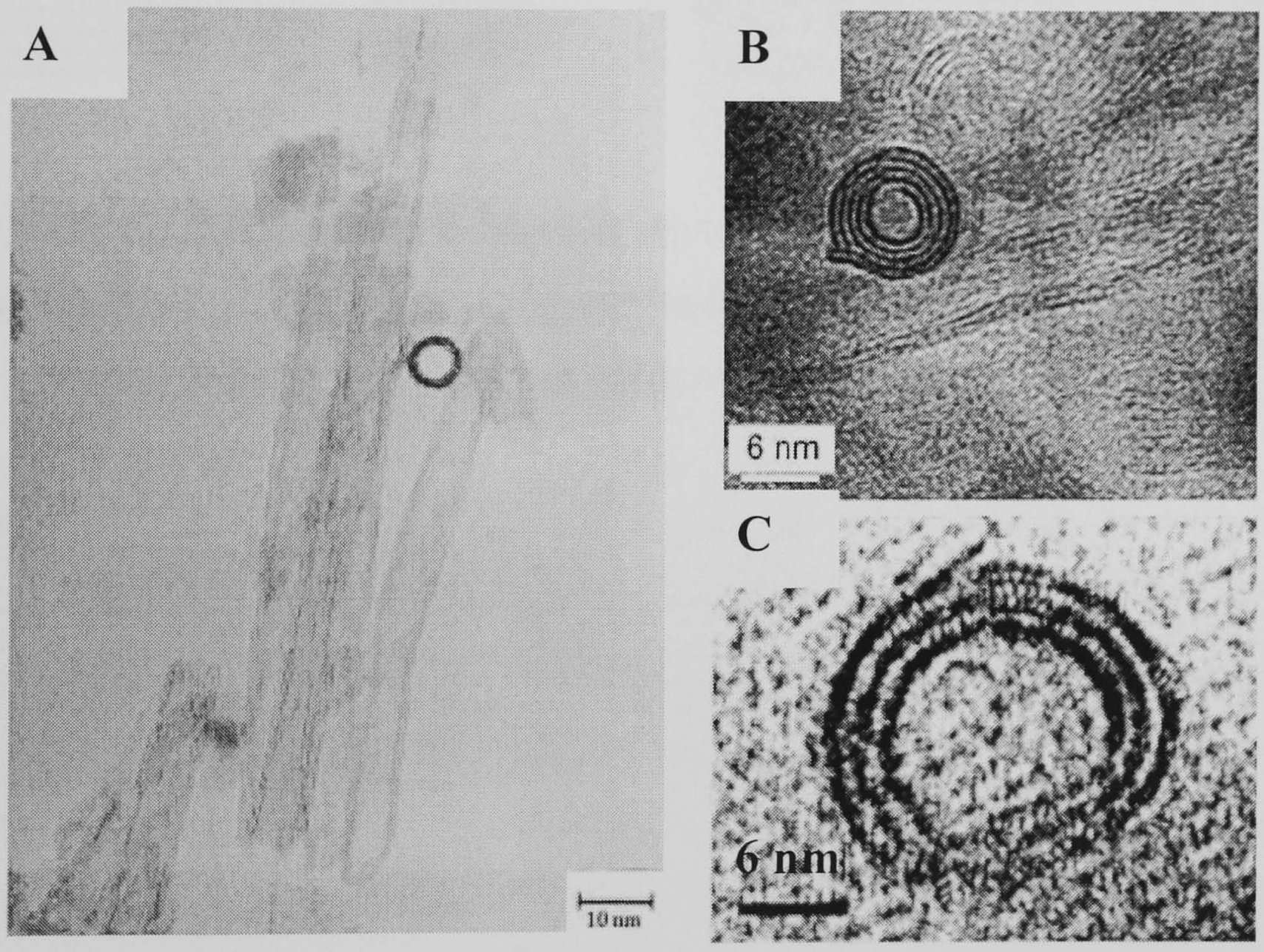


Figure 9 – TEM images of TiO_2 nanotubes grown by hydrothermal treatment of titania precursors or powders by (a) Kasuga et al.[84]; (b) Wang et al.[89] and (c) Chen et al.[88]

Although not as versatile as the sol-gel routes, hydrothermal processing can be used to produce morphologically different TiO_2 structures. In addition to nanotubes, controlled formation of nanofibres[96], nanorods and nanospheres (Figure 10B-C)[93] have been reported. Andersson et al.[91] have combined sol-gel hydrolysis of $Ti(OBu)_4$ in reverse micelles with hydrothermal treatment to produce nanoparticles for photocatalytic applications.

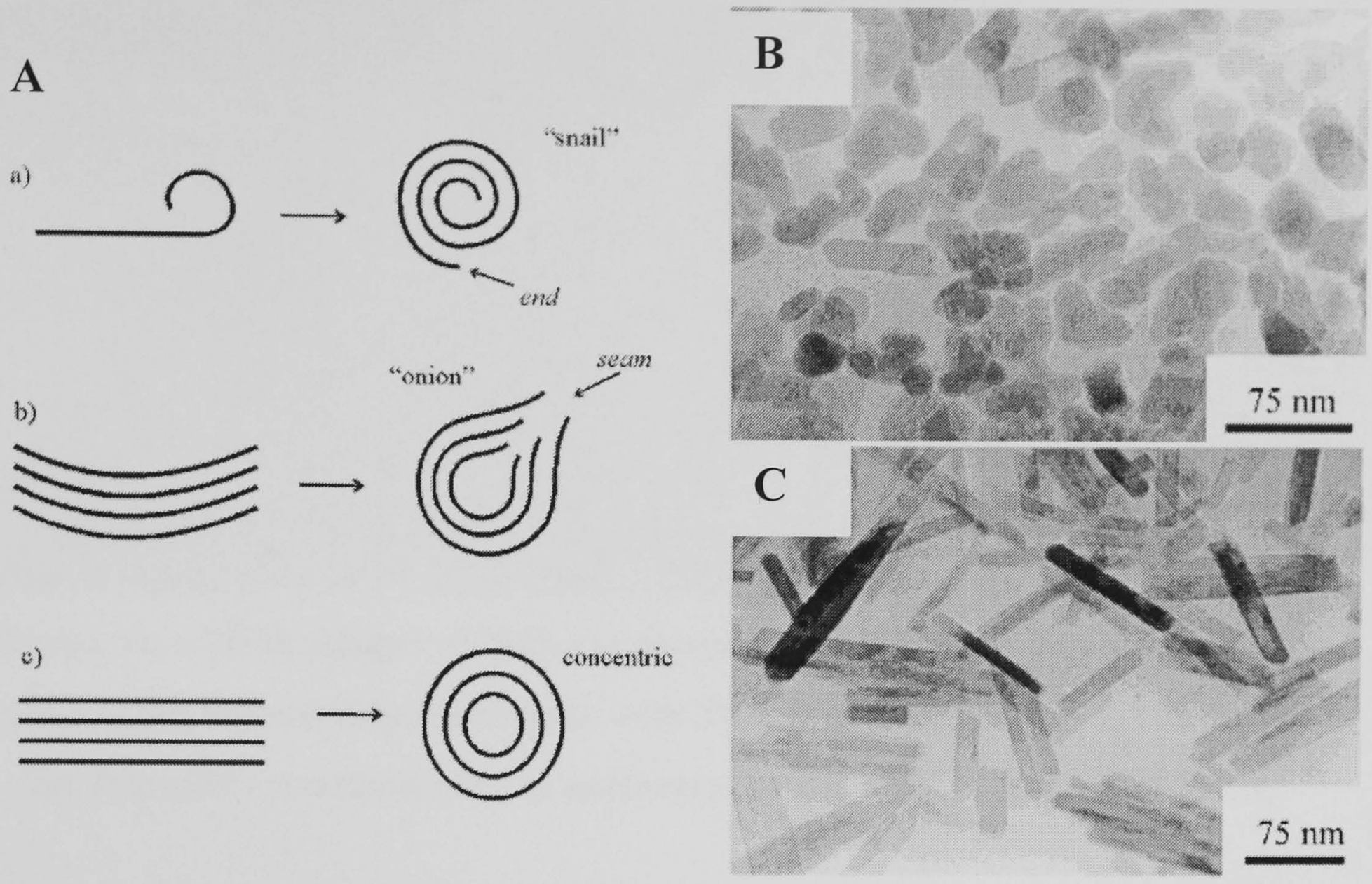


Figure 10 – (a) Nanotube formation routes according to Bavykin et al.[95]; (b, c) variation of hydrothermal conditions to produce (b) short rods and (c) nanowires, from hydrolyzed $TiCl_4$ sols, from Zhang and Gao[93]

Solvothermal processing is nearly identical to the hydrothermal route, with the exception that it is carried in a nonaqueous medium. In a sense, there is an analogy with hydrolytic vs. nonhydrolytic sol-gel methods. By selecting organic solvents with a high boiling point, reactions can be carried out over an even greater temperature range than with conventional hydrothermal route, which, in turn, allows better control of the size, shape and crystallinity of the TiO_2 product. Nanocrystalline anatase nanoparticles (Figure 11A) and nanorods (Figure 11B) have been grown using the solvothermal route with or without structure directing ligands[98-100].

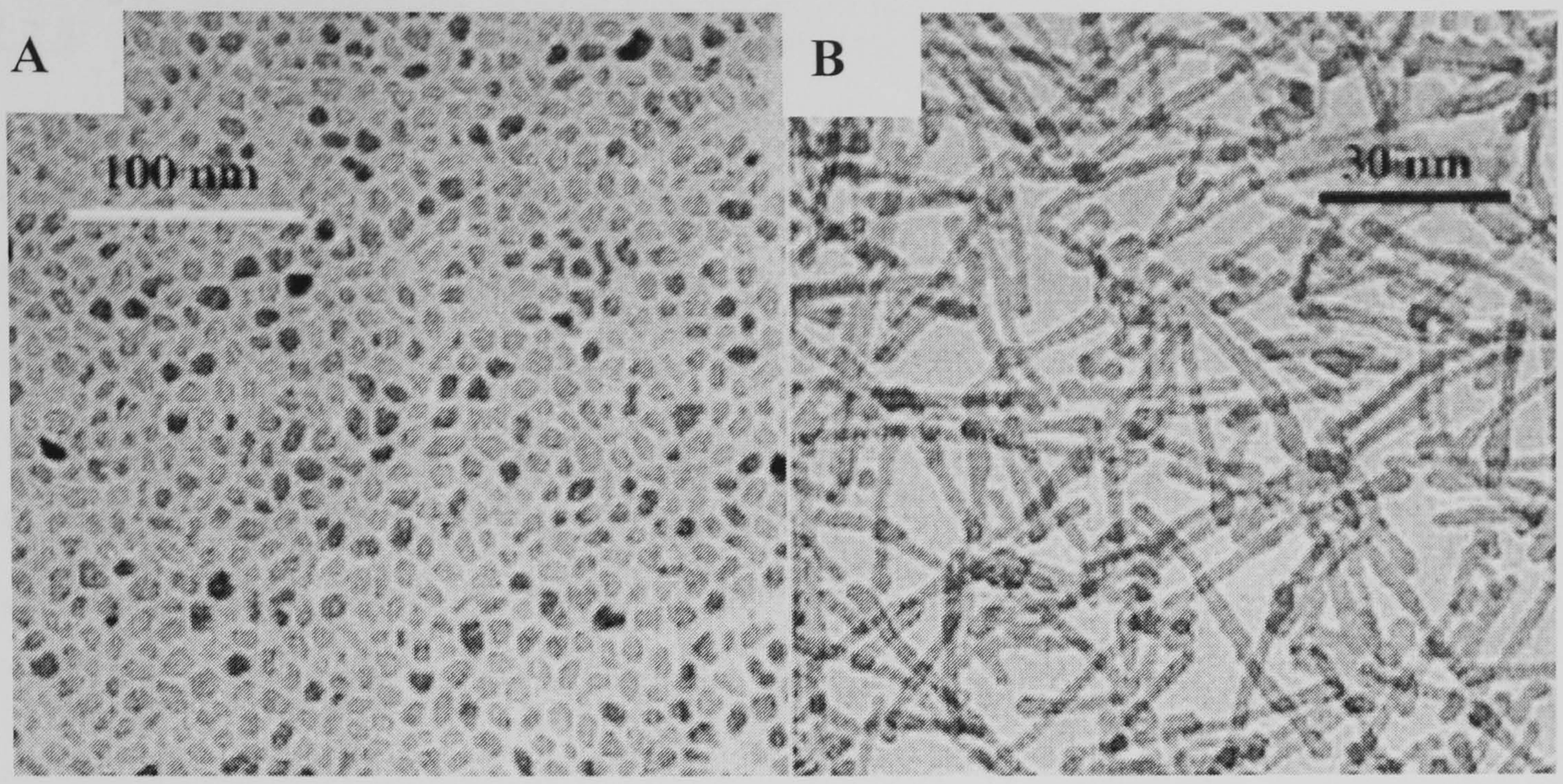


Figure 11 – TEM images of TiO_2 (a) equiaxed nanoparticles and (b) nanorods, grown using the solvothermal route with $Ti(OBu)_4$ as precursor and NH_4HCO_3 / linoleic acid / triethylamine as surfactants in cyclohexane, from Li et al.[100]

2.2.4 Synthesis of TiO_2 nanostructures using direct oxidation methods

By subjecting pure titanium sheets to anodizing current and / or oxidising environment, well-aligned polycrystalline TiO_2 nanotubes and nanorods have been obtained[101-105]. The procedure usually involves anodization in aqueous solution of an oxidiser (HF[101] or NH_4F[105]), with an optional thermal post-treatment to induce crystallinity in case of an amorphous product[102]. Direct oxidation without anodization has been reported for synthesis of TiO_2 nanorods using a H_2O_2 solution[103] or acetone[104]. The product, although well-aligned and of exceptional morphology displays very large particle diameters (~ 100 nm, Figure 12).

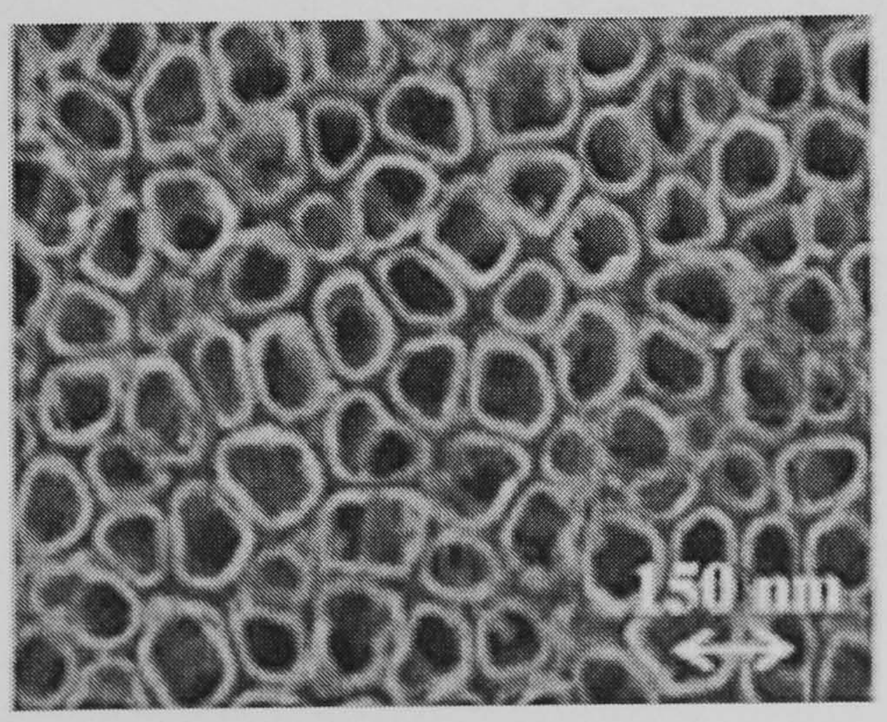


Figure 12 – Cross-sectional SEM image of porous TiO_2 nanotube array grown by anodization of titanium in NH_4F solution, from Macak et al.[105]

2.2.5 Chemical and physical vapour deposition (CVD/PVD) of TiO_2 nanostructures

Vapour deposition refers to any process in which materials in a vapour state condense to form a solid material. It is usually carried out at elevated temperatures in a furnace, under vacuum and is very common, e.g. for the catalytic synthesis of CNTs. Two types of vapour deposition can be distinguished – chemical and physical deposition. In the former case, a chemical reaction takes place during the deposition, while in the latter the pre-formed material is physically deposited onto a substrate. Both routes have been used to synthesise TiO_2 nanorods.

In a typical CVD procedure[106] the titania precursor (in this case titanium acetyl acetonate) is vaporised and preheated before being fed into the high-temperature zone (500°C-700°C) of the furnace. Chemical deposition of the TiO_2 precursor takes place, producing polycrystalline TiO_2 nanorods (Figure 13A) and nanowalls, depending on the reaction conditions. In PVD, Ti powder is oxidised in a high-temperature zone of the furnace, while TiO_2 nanowires (Figure 13B) deposit onto an alumina substrate in the low-temperature zone[107].

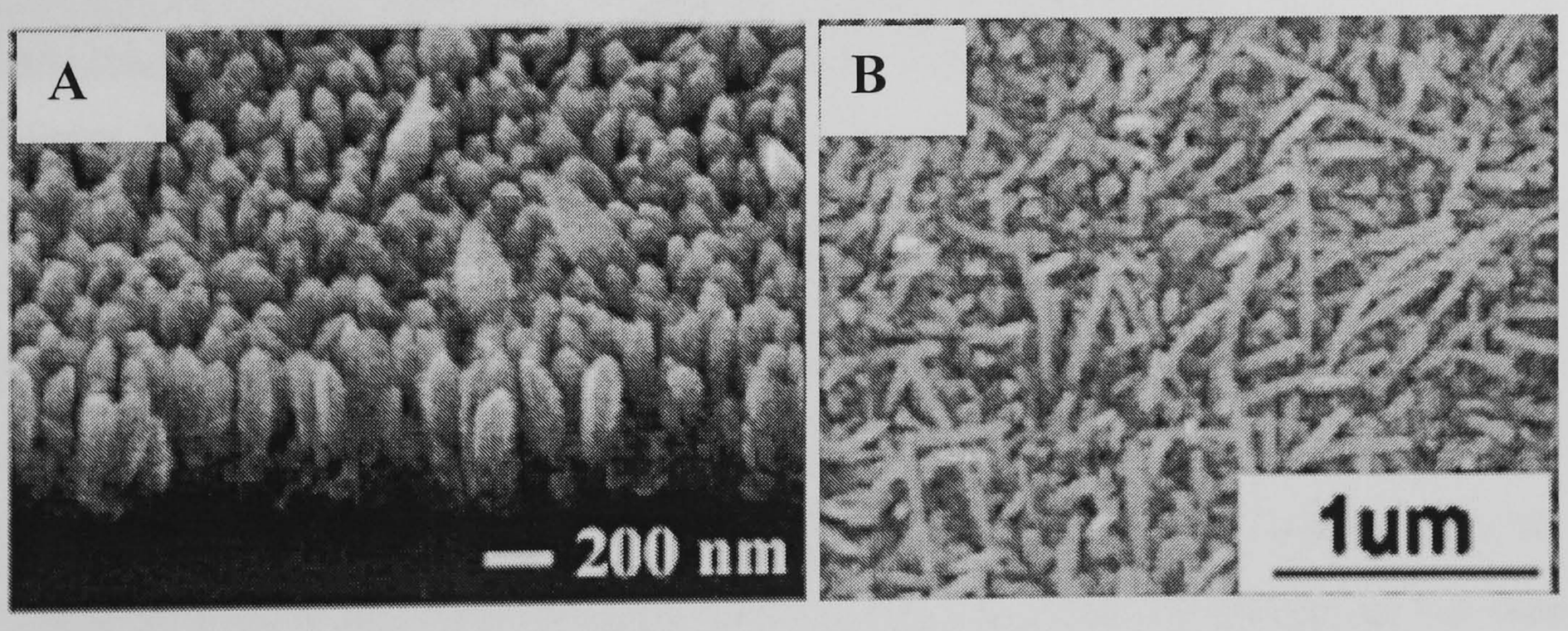


Figure 13 – TEM images of TiO_2 (a) nanorod and (b) nanowire arrays, grown by CVD (from Wu and Yu[106]) and PVD (from Wu et al.[107]), respectively

2.2.6 *Electrodeposition of TiO_2 nanostructures*

The electrodeposition method was used for the first reported synthesis of titania nanotubes in 1996 by Hoyer[4]. $TiCl_3$ was dissolved in aqueous HCl and this solution was added to a dissolved polymer template solution. The polymer template, which was gold-coated, acted as a cathode in the electrodeposition process onto which amorphous TiO_2 is deposited by hydrolysis of $TiCl_3$. Subsequent template dissolution and washing of the product, followed by thermal annealing at 450°C resulted in anatase TiO_2 nanotubes. As can be seen from the SEM images, although the as-deposited nanotubes (Figure 14A) have well-defined morphology, on annealing (Figure 14B) the nanotubes sinter and partially lose their morphology. A similar process was carried out recently using AAM to produce pure anatase TiO_2 nanowires[9].

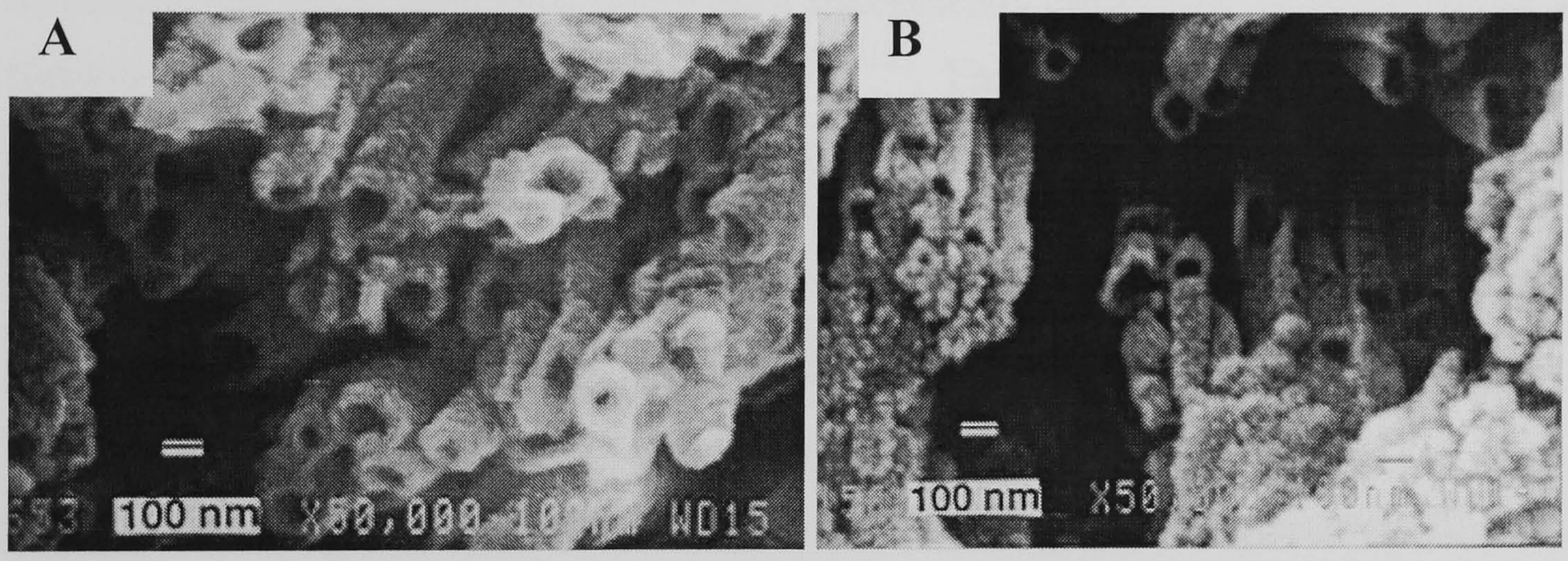


Figure 14 – SEM images of the (a) as-prepared and (b) annealed TiO_2 nanotube arrays prepared by $TiCl_3$ electrodeposition onto a polymer template, from Hoyer[4]

2.2.7 *Synthesis of TiO_2 nanostructures using sonochemical methods*

Ultrasonic treatment is used very commonly for improving the dispersion of nanoparticles in dispersions and breakage of agglomerates. However, in the case of synthesis of nanoparticles, the fascinating sonochemical effects do not come from direct interaction of ultrasound with molecular species, but due to formation, growth and implosive collapse of bubbles in a liquid, generated by ultrasonic irradiation. The latter effect produces enormous local heating (~5,000 K), high pressures (~ 1,000 bar) and dramatic heating and cooling rates (> 10^9 K/s). These conditions promote intimate mixing between reaction constituents at the nanoscale. Sonochemical synthesis has been used for producing both equiaxed[108,109] and anisotropic (Figure 15)[110] TiO_2 nanostructures.

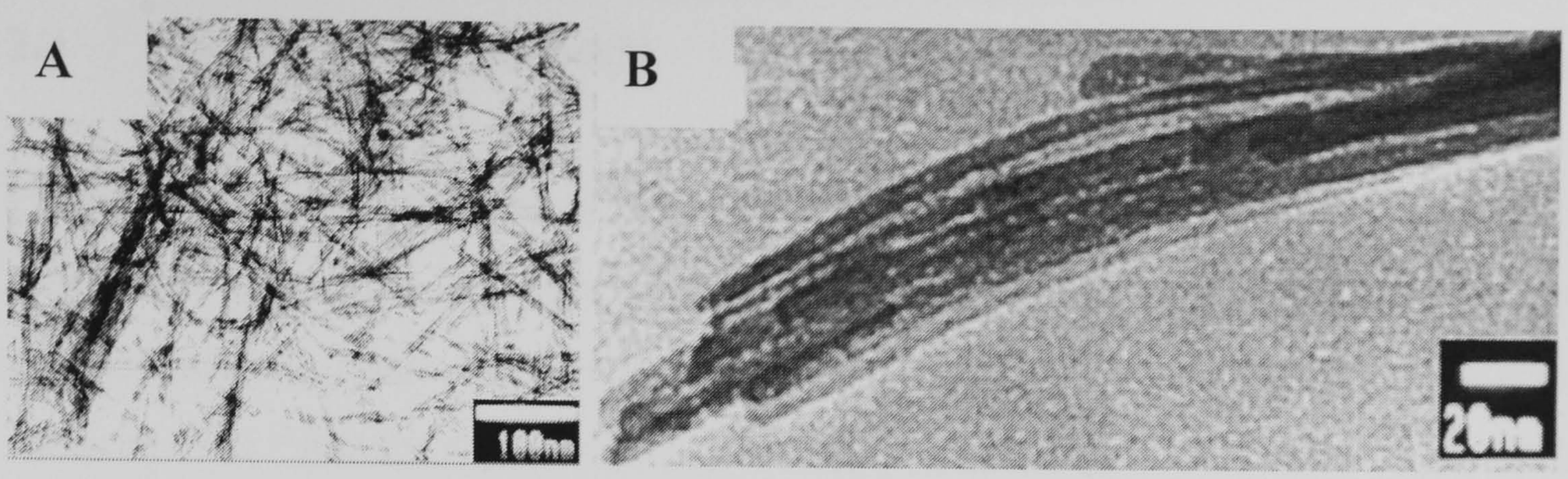


Figure 15 – TEM images of TiO_2 (a) nanotubes and (b) nanowires; by sonochemical route from TiO_2 powder treated with NaOH / HNO_3, from Zhu et al.[110]

2.2.8 Synthesis of TiO_2 nanostructures using microwave method

Microwave radiation is an efficient way of achieving rapid heat transfer and selective heating of chemical reactions. It has been successfully employed for synthesis of TiO_2 nanostructures by several research groups[111-113]. This method partly builds on sol-gel and hydrothermal processing, with the exception that pulsed microwave radiation is used to provide heating and facilitate nanoscale growth of TiO_2 crystals.

2.3 Summary of the TiO_2 synthesis state-of-the-art

TiO_2 nanostructures have been synthesised using numerous methods, which have been briefly reviewed. TiO_2 nanorods, as the main subject of the present thesis, can be grown using a variety of routes and conditions. However, sol-gel processing stands out as the most promising candidate for the synthesis of TiO_2 nanorods using the nonhydrolytic pathways, in particular. The advantages of this method over others are multiple – the reactions are carried out using standard precursors and equipment, without the need for an elaborate experimental setup (cf. pressurised vessels for hydrothermal synthesis or furnaces for CVD/PVD). Further, the quality of the products is superior to that obtained by other methods, which are often amorphous (hydrolytic sol-gel, electrodeposition, etc.), polycrystalline, with poor morphology or too large particle size (cf. hydrothermal, direct oxidation, template growth). Sonochemical and microwave routes, although promising, are unpredictable and control over particle morphology is generally difficult. On a general note, for all synthesis routes, several factors remain unstudied – reaction yields, product purity (for SDA-assisted sol-gel routes) and ultimately the costs associated with the synthesis. This data, if published, would provide a further basis for comparison of different synthesis routes.

2.4 Nanocomposite materials

Composites are materials made from at least two elements, with resulting properties different to that of the individual constituents on their own. Commonly, the two main components of a composite material are the bulk matrix material and the reinforcing material. The function of the matrix is to surround and support the filler, maintaining its relative positions. Matrices are usually classified into polymers, ceramics or metals, although polymers are by far the most widely used. The mechanical, physical and chemical properties of the filler material and the matrix are combined and, ideally, enhanced in the composite material. Overall, the composite properties are determined by the:

- Properties of the matrix
- Properties of the filler
- Ratio of the filler to matrix in the composite
- Filler orientation within the composite
- Matrix-filler interfacial properties (i.e. adhesion)

Composite materials can be natural (e.g. wood, bones, teeth) or synthetic (e.g. concrete, plywood, fibreglass). Nanocomposites are a subgroup of composite materials, where at least one constituent has a characteristic dimension below 100 nm.

At the moment, some of the strongest materials in the world are carbon fibre composites, but interest in nanocomposites is experiencing a surge, owing to unique properties of the nanoscale filler materials. Before considering synthetic nanocomposites, it is important to appreciate that most naturally occurring composites, e.g. mollusc shells, bone and teeth tissue in vertebrates, cellular organisms, etc. have a nanoscale structure, which is sometimes exploited in the design of novel materials. Historically, the first nanocomposites, subject to extensive research for the past two decades, were clay (layered silicate) - polymer nanocomposites[114,115]. In layered silicate clays (most commonly, montmorillonite, hectonite, saponite), 1 nm sheets of silicates are stacked closely and the interlayer (gallery) space is occupied by inorganic cations. High aspect ratio (10-1000) and large surface area of silicate nanolayers (760 m^2 g^{-1}) are ideal nanocomposite components, but are not easily dispersed as they

prefer to stack. Replacement of inorganic cations with organic ions (surfactants) enhances the layer separation process (exfoliation). The exfoliation process enables fabrication of true nanocomposites, where individual sheets are well-dispersed within the polymer. Figure 16 is a schematic illustration of differences between conventional, intercalated and exfoliated clay-based nanocomposites.

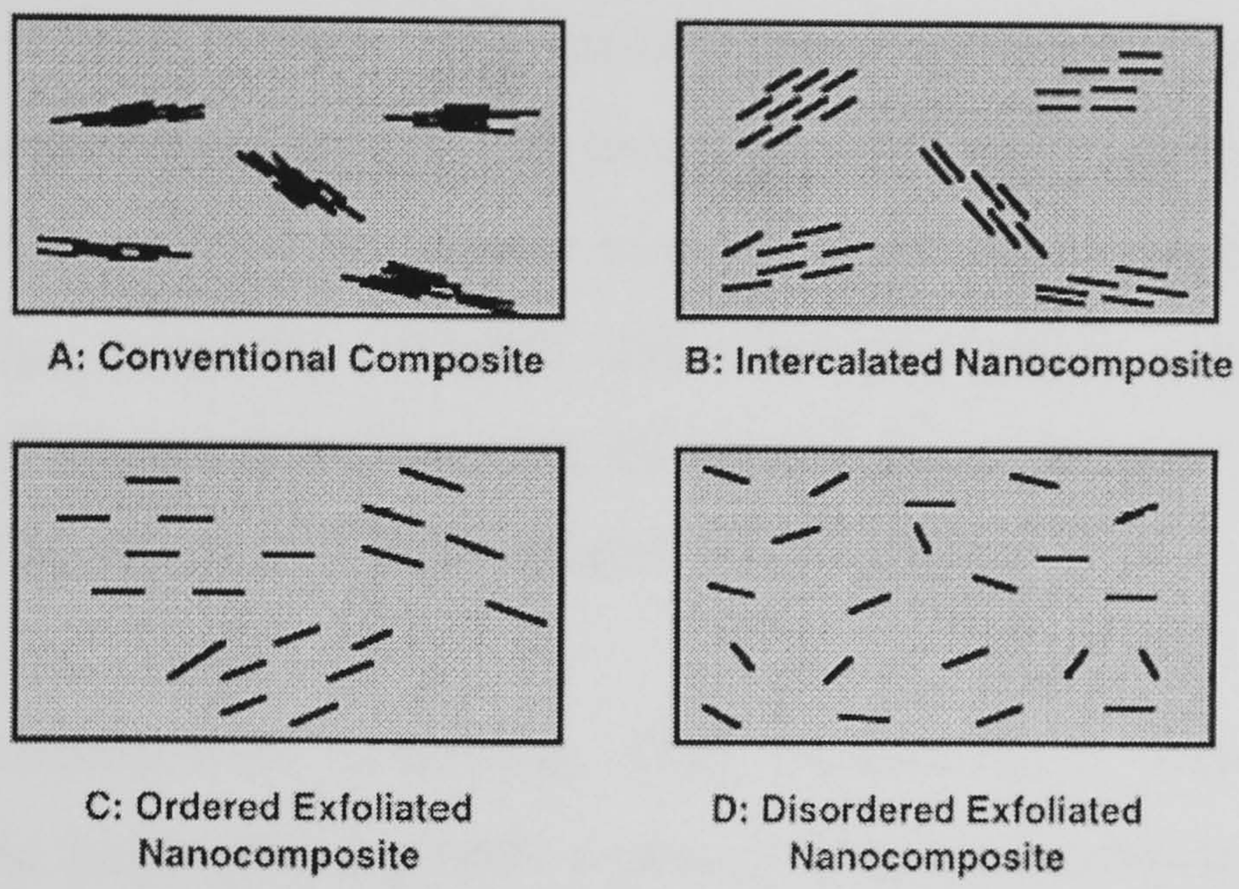


Figure 16 – Different types of polymer-clay composites, from LeBaron et al.[114]

Layered silicate reinforcements have been widely used in engineering polymers to give some significant property enhancements – improved modulus, strength, higher heat distortion temperature and flame retardancy[116-118]. Two findings in particular stimulated interest in this field:

1. The studies on Nylon-6-montmorillonite by Toyota group[119-121], showing that only small amounts of filler are needed for pronounced improvement in mechanical and thermal properties
2. The observation by Vaia et al.[122] that it is possible to process clay-polymer nanocomposites by melt-mixing without the use of organic solvents.

Overall, dispersion and fine tuning of surface chemistry of silicate layers is the key to attaining improvement in material properties. The recognition of C_{60} (fullerenes) and carbon nanotubes (CNTs) in 1985[16] and 1991[17], respectively, also triggered a surge in the field of nanocomposites. Perfect CNTs, especially, have remarkable properties, although different synthesis routes result in products of variable qualities (i.e. lattice perfection, diameter, graphitic orientation, etc.). For these reasons, CNTs are perceived as excellent candidates for use in nanocomposites[123].

2.5 TiO_2 nanocomposite materials

A critical review of the most significant advances in this area of research will be presented in this section. In the current project, the aim was to introduce TiO_2 nanorods into a polymer matrix, for the purpose of fabricating composites with enhanced optical and mechanical properties. There are many reports in the literature where both equiaxed and anisotropic titania nanoparticles have been combined with precious metal particles to obtain novel composite materials with interesting semiconducting, magnetic, catalytic and photoconductive properties[124-136]. Such applications, albeit novel and exciting, go beyond the main scope of this project, and hence will not be scrutinised in great detail in this review.

Polymer nanocomposites containing TiO_2 nanostructures have been frequently reported in the past, covering both equiaxed and, to a substantially lower extent, anisotropic TiO_2. For the latter, the most exciting findings have been reported in the fields of photocatalysis, photovoltaics and similar electronic devices, utilising various conducting polymers as matrix. TiO_2-polymer nanocomposites for optical, structural and biomedical applications almost exclusively explore equiaxed particles, either commercial nanopowders, frequently aggregated, or particles grown by in-situ hydrolysis of titania precursors, which have questionable crystallinity.

TiO_2 nanocomposites can be generally classified according to potential application for which they are intended:

1. Photocatalytic, electronic and electrochemical devices (solar cells, photocatalysts, polymer electrolytes in batteries / fuel cells, sensors etc.)
2. Optical applications (UV shielding, transparency, tuneable refractive index)
3. Structural composites (materials with enhanced mechanical/thermal properties)
4. Biomedical applications (scaffolds for tissue engineering, etc.)

Each of these groups will be discussed in this order in the following sections. It is worth noting that the electronic and electrolyte applications are rather specific and not classical examples of bulk nanocomposite materials. However, there are useful lessons to be learnt about processing and blending of titania and polymers.

2.5.1 TiO_2-polymer composites for photocatalytic and electronic applications

2.5.1.1 Background of TiO_2 photocatalysis

The new generation of TiO_2 nanoparticles are undoubtedly mostly used in polymer nanocomposites that make use of the photocatalytic activity of TiO_2. Interest in TiO_2 photocatalysis, in general, began with Fujishima and Honda[137] in 1972, with their study into electrochemical-photolytic water decomposition on TiO_2 electrodes. Several comprehensive reviews investigate the photocatalytic behaviour of TiO_2 presenting some older findings from the 1990s (see e.g. Fox and Dulay[138], Mills et al.[139], Hoffmann et al.[140], Linsebigler et al.[141], Mills and Le Hunte[142], Peral et al.[143]) as well as recent research (e.g. Agrios and Pichat[144], Fujishima and Zhang[145]) involving nano-particulate TiO_2. At the time of writing (05/2008), research on TiO_2 photocatalysis encompasses around 10,000 publications, showing a steady growth. So what makes TiO_2 photocatalysis so attractive to researchers? Before presenting the theoretical aspects of semiconductor photocatalysis, it is relevant to note that in addition to TiO_2, other semiconductors (ZnO, Fe_2O_3, CdS and ZnS) also display similar phenomena, but TiO_2 is by far the photocatalyst of choice in many applications, since it is biologically and chemically inert, stable with respect to chemical and photo-corrosion, and inexpensive.

Semiconductors, unlike metals, do not have a continuum of electronic states, but instead posses a forbidden energy region, which extends from the top of the filled valence band to the bottom of the vacant conduction band. This void energy region is usually referred to as the band gap. TiO_2 is a wide band-gap semiconductor with band-gap energies of 3.0 and 3.2 eV for the anatase and rutile phases, respectively. Promotion of an electron from the valence band to the conduction band can be induced by photo-excitation. The band-gap energy is equivalent to energy of a photon with a wavelength in the UV region (more specifically UV-A or 'near'-UV range – 315 nm to 400 nm) – typically around 385 nm and 410 nm for anatase and rutile, respectively. Promotion of an electron from the valence band to the conduction band, simultaneously leaves behind a "hole" (i.e. an electron vacancy) in the valence band. Photo-excited electrons and holes can undergo different processes; they can: (1)

recombine and dissipate the excitation energy as heat, (2) get trapped within the titania surface traps or (3) react with electron donors and electron acceptors at the titania surface, thus initiating a photochemical reaction.

A general, simplified mechanism for heterogeneous photocatalysis on TiO_2 surfaces can be described by the following:

Excitation / recombination $$TiO_2 \xleftrightarrow{h\nu > 3.0-3.2\,eV} h^+ + e^- \quad (5)$$

Redox charge transfer $$h^+ + Red \rightarrow Red^{\bullet +} \quad (6)$$

$$e^- + Ox \rightarrow Ox^{\bullet -} \quad (7)$$

where, Red and Ox refer to electron donor (reductant) and electron acceptor (oxidant), commonly surface adsorbed hydroxyl (-OH) and oxygen species. Hoffmann et al.[140] have investigated the kinetics of the above reactions by laser flash photolysis measurements and observed that the excitation, trapping and recombination reactions occur at very fast rates (~10^{-15}–10^{-8} s), while the redox reactions between the excitons and the surface adsorbed species occur relatively slowly (~10^{-7}-10^{-3} s). Being able to influence the relative balance between recombination and redox reactions is crucial in adjusting TiO_2 photoactivity for technological applications.

Surface generated species - hydroxyl radicals ($OH^{\bullet}$) and superoxide radical anions ($O_2^{\bullet -}$), are very reactive towards other adsorbed species. In case of adsorbed chlorinated hydrocarbons, further reactions lead to their complete degradation to CO_2, HCl and H_2O according to:

$$C_xH_yCl_z + \left(x + \frac{y-z}{4}\right)O_2 \xrightarrow{h\nu, TiO_2} x\,CO_2 + z\,HCl + \left(\frac{y-z}{2}\right)H_2O \quad (8)$$

As an illustration, the strong oxidation potential of hydroxyl radicals is compared with some common oxidants in Table 1.

Oxidants	Oxidation potential vs. SHE (V)
$OH^{\bullet}$	2.80
O_3	2.07
H_2O_2	1.77
ClO_2	1.49
Cl	1.36

Table 1 – Oxidative potentials of various oxidants, values obtained from Threebond publication[146]

The photocatalytic effect of TiO_2 has been utilised in many applications, which will be presented in subsequent sections. However, irrespective of the final application, several aspects need to be taken into account:

1. TiO_2 photoactivity varies strongly according to particle properties (crystallinity, particle size, crystalline phase, etc.)
2. Pure TiO_2 is photo-activated only by UV irradiation, which precludes efficient use of visible light (comprising the remaining ~90-95% of the solar spectrum)
3. Recombination of excitons is clearly undesirable if improved photocatalytic activity is advantageous

These issues have been subjected to extensive research in the past, both in the field of bulk-TiO_2 and nano-TiO_2 photocatalysis; the following sections discuss some key findings of this work briefly.

2.5.1.2 Improving / suppressing the photocatalytic activity of TiO_2

The photocatalytic activity of TiO_2 can be improved by different methods:

- *Various synthesis procedures*: Small, anisotropic single-crystal nanoparticles, with good crystallinity have better photocatalytic activity than amorphous, polycrystalline or equiaxed powders and nanoparticles due to larger particle surface area[147]. High aspect ratio particles also permit orientation and formation of percolation networks that would improve photocatalytic activity by having a more accessible particle surface area.

BARL LONDON UNIV

- *Deposition of TiO_2 onto a substrate*: The photocatalytic degradation of dilute pollutants (e.g. phenols, aldehydes, etc.) can be enhanced by the addition of high-surface area adsorbent materials, in particular activated carbon[148-151] and zeolites[150,152]. Ideally, such systems would offer material-specific advantages (enhanced adsorption of pollutants and simultaneous photocatalytic degradation), with the two components acting synergistically.

- *Complementary semiconductor*: Loss of photocatalytic activity can often be associated with large exciton recombination rates. This problem was tackled some years ago by means of transferring conduction-band electrons from TiO_2 to another semiconductor. Indeed, transport of holes and electrons was found to be possible using this strategy, as evidenced by photoelectrochemical measurements. On this basis, TiO_2 has been combined into a composite with a variety of semiconductor oxides including ZrO_2[153-156]; SnO_2[157]; MoO_3, WO_3[158], In_2O_3[159], and Nb_2O_5[160]. Sulphides or even other chalcogenides have also been used to decrease recombination rates, but in general, they are not as stable and/or cost effective as oxides.

Driven by the need to use solar light more completely, many investigations have been performed to make TiO_2 photocatalytically active beyond its absorption threshold of 400 nm. Doping of the titania lattice by metals[161-166] and non-metals[109,167-174] as well as surface modification by inorganic (metals[175,176] and semiconductors[177-179]) and organic dye sensitizers[180-182] have all been used. The principal approach is to 'introduce' new energy levels within the band gap or to achieve a suitable shift of the conduction band and / or the valence band, so that lower energy photons can be absorbed.

A very systematic study of doping 2-4 nm TiO_2 anatase colloids with metal ions and evaluation of the photo-reactivity of the doped materials has been carried out by Choi et al.[165]. Through photocatalysed degradation of chloroform, it was shown that doping the titania with as little as 0.1-0.5% of Fe^{3+}, Mo^{5+}, Ru^{3+}, Os^{3+}, Re^{5+}, V^{4+} or Rh^{3+} significantly increased the degradation rates. On the other hand, doping with Co^{3+} and Al^{3+} reduces the photoactivity because the ions act as recombination sites in the TiO_2 lattice.

Non-metal doping primarily causes a red-shift in the absorption spectrum of titania, i.e. the particles become visible light sensitized (Figure 17).

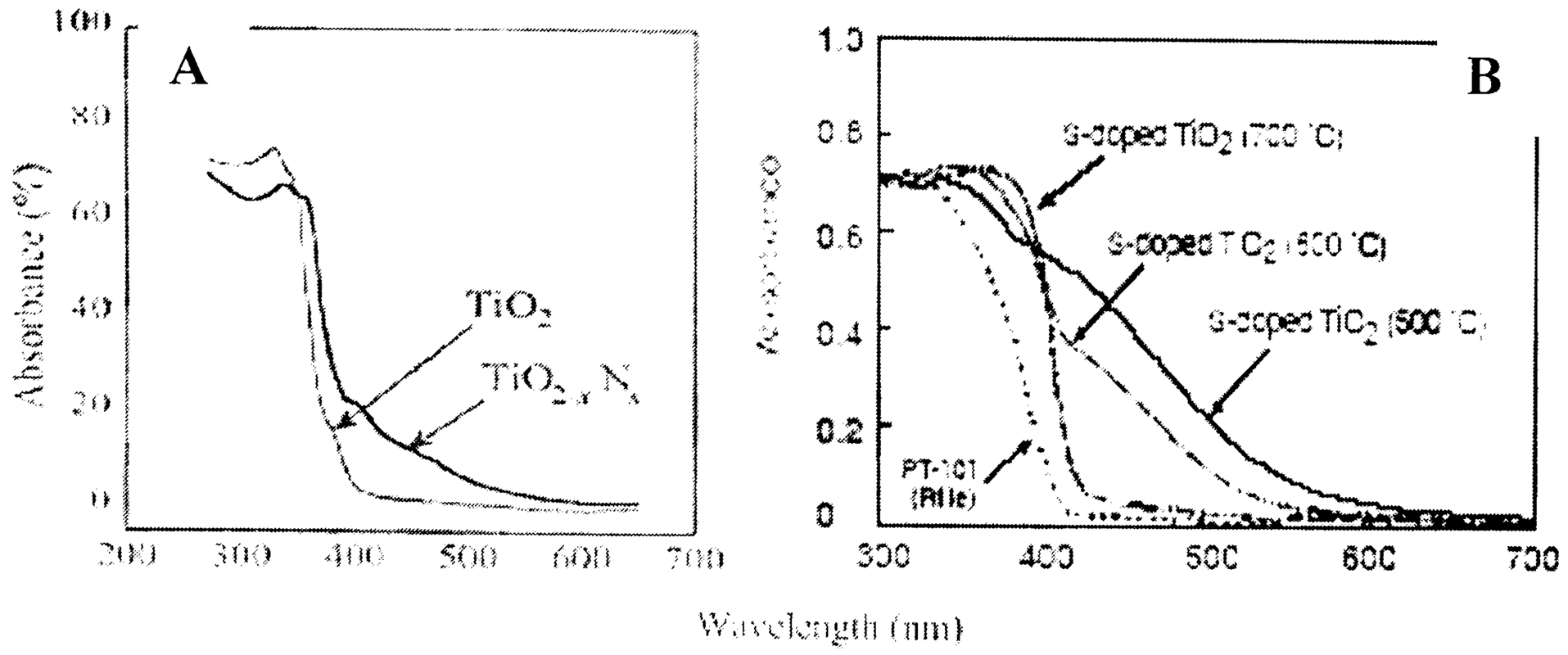


Figure 17 – UV-Vis spectra of (a) N-doped[167] and (b) S-doped TiO_2[173], showing a red-shift in absorbance with respect to pristine TiO_2

Sensitization of TiO_2 by organic dyes is probably the most advanced and widely reported method for improving TiO_2 photocatalytic response[50], heavily researched in relation to dye-sensitized nanocrystalline solar cells (DSSCs). Briefly, a monolayer of the sensitizer dye is grafted to the TiO_2 nanoparticle surface, which allows charge transfer at the dye-TiO_2 interface. The dye is excited by a photon, which then releases an electron that is transferred into the conduction band of titania, promoting further charge separation and transfer to respective electrodes. The key aspects that dictate the dye selection are:

1. The dye should absorb completely in the visible range (< 900 nm)
2. The excited state of the dye should be sufficiently long to permit injection of electrons into the semiconductor with a quantum yield close to unity
3. The energy level of the excited state of the dye should be well matched to the conduction band of the titania in order to maximise the efficiency of the electron transfer reaction
4. The dye should be stable enough to sustain ~20 years (desirable solar cell service life) of exposure to natural light

On the other hand, TiO_2 photocatalysis can be undesirable, particularly in relation to the topic of this project where mechanical improvement is desirable, as it can lead to

matrix degradation and loss of structural integrity of the composite. Reduction of photoactivity can be achieved in different ways, two of which will be discussed: (1) formation of a dense semiconductor oxide layer on the titania surface and (2) doping with transitional metal ions. Coatings based on SiO_2[183-188], Al_2O_3 [183-186,189-192] and ZrO_2[183-185] have been reported. Although some of the cited work pertains to applications of commercial nanopowders in paints and inorganic sunscreens rather than polymer composites, the mechanism for suppression of photocatalytic activity is application-independent and can be extended to nanocomposites. Dense silica layers provide a physical barrier such that the surface generated radicals cannot come into contact with organic materials and cause degradation. The main requirement, and indeed the major difficulty for effective radical quenching, is a continuous silica shell around the particle (Figure 18). Silica coatings can be quite effective in lowering the photoactivity; for example a recent study[188] showed that commercial TiO_2 nanopowder coated with ~15 wt% silica (Figure 18B) exhibited three-fold slower degradation rates of phenol compared with an uncoated titania sample. Alumina-type coatings utilise the same physical barrier principle to reduce the photoactivity and another recent publication[192] reported that titania with 7 wt% alumina and 10 wt% aluminium stearate coating resulted in almost complete suppression of the photocatalytic degradation of isopropanol. Nevertheless, it is very important to note that all these oxide coatings can also have an opposite effect, due to their stabilising effect on titania dispersions. It has been demonstrated that partial/incomplete coating can promote photodegradation of organics compared with untreated titania[187,193,194].

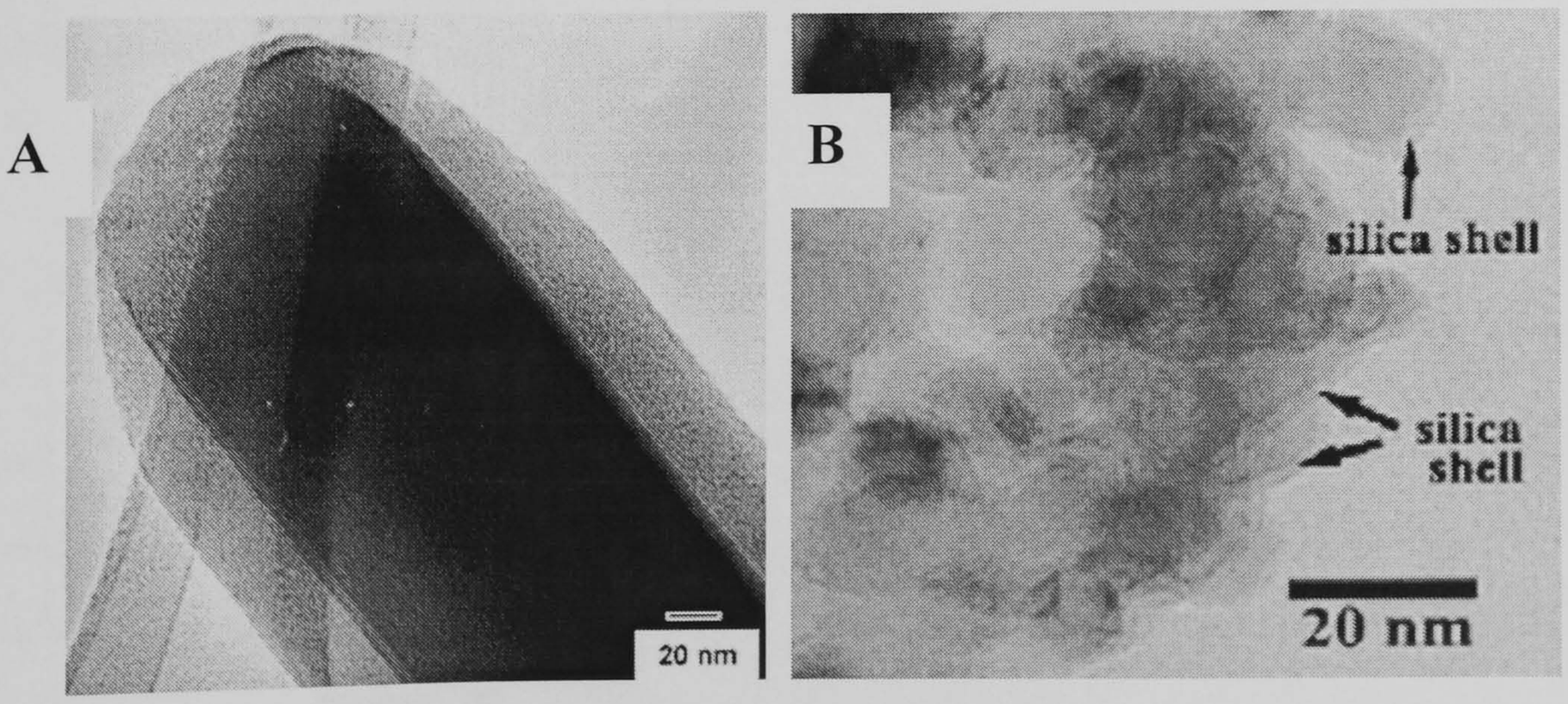


Figure 18 – TEM images showing silica coated (a) TiO_2 nanorod grown by nonhydrolytic route, from Yang and Chen[193] and (b) commercial TiO_2 equiaxed nanoparticles, from El-Toni and Sato[188]

Metal dopants have been discussed for improvement of the titania photoactivity, but depending upon the selection of the dopant, it is possible to reduce the photoactivity. Groups from Oxford[195-197] and Warwick[198-200] have found that Mn^{2+} doping into equiaxed titania nanoparticles leads to a significant reduction in degradation rates of sunscreen formulations and polymer composites, respectively. The former group has since created a spin-off company, Oxonica Ltd. and patented this technology, which is currently used in formulation of Soltan® sunscreen range. It is generally little known that inorganic sunscreens, which incorporate ultrafine titania nanoparticles, although unquestionably excellent at filtering UV-B (<320 nm) radiation and largely UV-A as well (depending on the pigment quality) also give rise to active oxygen species, which can cause DNA damage in the underlying tissue. In one article, Wakefield et al.[196] actually point to the findings of the World Health Organisation International Agency for Research on Cancer, which concludes that there is 'inadequate evidence in humans for a cancer preventative effect of topical use of sunscreen formulations against cutaneous malignant melanoma and basal-cell carcinoma' and only 'limited evidence in humans for a cancer preventative effect of topical use of sunscreen formulations against squamous-cell carcinoma'[201]. This makes total suppression of TiO_2 photocatalysis all the more important, because it would prevent indirect skin damage. As an illustration, Figure 19A shows that Mn-doped TiO_2 exhibits more complete absorbance in the UV-A range compared to other commercial titania, which are silica or silica-alumina surface treated. Further, Mn-doped titania samples result in an order of magnitude lower free radical generation rate compared with other titania samples (Figure 19B).

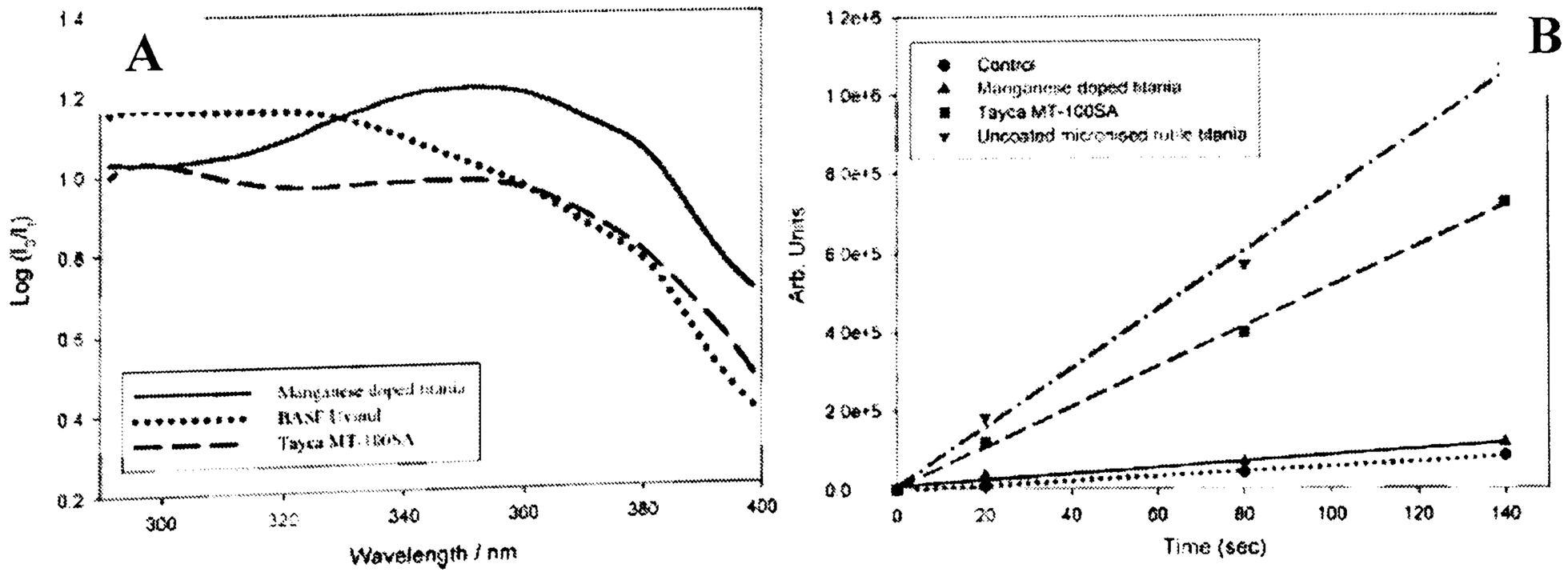


Figure 19 – (a) Absorption spectra and (b) free radical generation rates of Mn-doped titania compared with appropriate surface-treated commercial powders, from Wakefield et al.[195]

2.5.1.3 Nano-TiO_2 photocatalysis for environmental, self-cleaning and medical applications

TiO_2 is regarded as the most efficient and environmentally benign photocatalyst and has been used to address a number of issues, including, but not limited to: self-cleaning materials, degradation of mass-produced plastics, water-air purification, antibacterial and cancer treatment. This section will summarise relevant research findings in these fields.

Titania photocatalysis has found great use for self-cleaning glass, with the Fujishima group being one of the leading researcher groups in this area. In a 1997 Nature publication[202], Fujishima and co-workers report on glass onto which an anatase polycrystalline film was deposited to provide anti-fogging and self-cleaning features. Upon exposing to UV, the surfaces undergo a hydrophobic-hydrophilic transition (Figure 20) and incident sunlight was found to be sufficient in outdoor applications to render the surfaces self-cleaning (e.g. commercially available Pilkington Activ® glass).

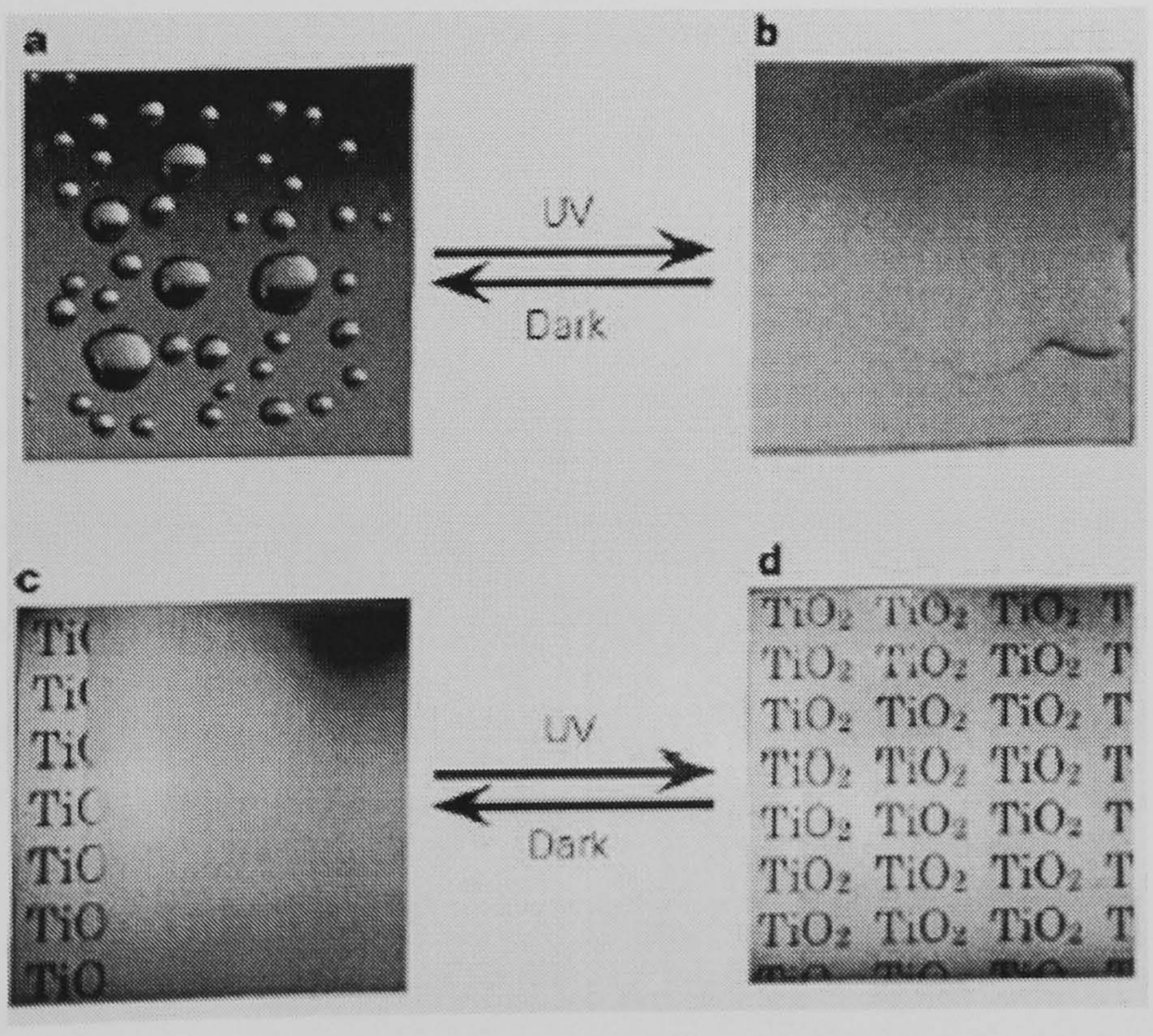


Figure 20 – (a) Hydrophobic glass surface covered by water droplets transforming into a hydrophilic film, (b) upon UV exposure; (c) fogging of glass under normal conditions and (d) anti-fogging surface upon UV exposure, from Fujishima et al.[202]

Since then, this group has published several exciting papers on this topic, both on self-cleaning glass and development of micro-patterning techniques for superhydrophobic-superhydrophilic surfaces[203-206]. Although photocatalytic degradation rates have been observed to be quite low, they have been calculated to be: "sufficient to be used, for instance, for self-cleaning glass which can degrade human daily bio-effluents given reasonable assumptions for window surface area and solar irradiation"[207] or "to remove oily finger prints very rapidly"[144,208]. Another excellent recent publication[209] reported on the fabrication of TiO_2 nanorod films deposited on glass with switchable superhydrophobicity, which can be tuned reversibly. Under normal conditions, atmospheric oxygen is trapped on the titania surface with nanoscale roughness, so that it makes the entire surface superhydrophobic. However, upon UV irradiation, the bound oxygen is displaced with –OH groups, making the surface superhydrophilic. Simply leaving the sample in the dark recovers the surface to its original state.

The degradation of mass-produced plastics by TiO_2 photocatalysis has been identified as a viable way to curb an ever-growing environmental concern of more and more plastic waste ending up in landfills ("white pollution"). Thus far, several non-biodegradable polymers have been used to fabricate degradable composites, and include poly (vinyl chloride) (PVC)[210], polystyrene (PS)[211] and polyethylene (PE)[212]. All these polymers are produced on the order of tens of millions of tons each year, with a large proportion ending up as waste in landfills, with very slow degradation rates.

The TiO_2-PS study[211] has shown that introducing titania greatly helps degrade such polymers through photogenerated radical scavenging of the polymer backbone. Experiments were done by either dispersing the commercial P25 Aeroxide® TiO_2 within the PVC [210] and PE [212] or by grafting PS onto the titania nanoparticle (70-100 nm) surface [211]. P25 TiO_2 is widely recognised as a benchmark titania nanopowder (~20 nm principal particle size, anatase-rutile mixture) in the field of photocatalysis and also for other titania nanocomposite applications. UV-light illumination for 300 h showed that the composites exhibited a 27 wt% and 29 wt% weight loss for PVC and PS case, respectively. Under the same irradiation conditions, the pure polymers degrade by up to 10 wt% at most, so introducing titania improved the degradation rate significantly. The molecular weight of PVC and PS decreased to 33% and 25% of the

original, respectively. More complete degradation was achieved with TiO_2-PE composites, although for somewhat longer exposure times (400 h) and under harsher UV-B conditions – 68 wt% weight loss and 95% reduction in M_W. Under normal sunlight conditions degradation rates for PE approach those of PVC and PS.

The following key points were made: (1) dispersion of TiO_2 within the matrix is the primary factor controlling the overall efficiency of degradation; (2) degradation leads to formation of cavities (i.e. whitening phenomenon), which scatter light and hinder further degradation by decreasing the light penetration depth and (3) the presence of oxygen through good aeration is crucial for effective photocatalysis. An interesting estimate made in the PVC study suggests that if a 5 nm nanoparticle can etch a 50 nm radius cavity, only 0.02 wt% TiO_2 would be sufficient for complete degradation of the entire polymer matrix. Unfortunately, this efficiency cannot be achieved at the present, possibly due to agglomeration of particles, progressive sample whitening and the overall low effectiveness of the photocatalytic process. Potentially, the partially decomposed materials could be used as a feedstock to another process, resulting in an environmentally and economically sound hybrid technology.

On the other hand, neither of the studies mentioned above identified or quantified the decomposition products, thus leaving some scope for interpretation regarding the overall environmental benefit offered by such process. Performing a Life Cycle Analysis for each component is essential to studies examining new environmentally-friendly technologies. In fact, TiO_2 photocatalysis leads to complete oxidation of the organics to CO_2 and water, which, one could argue, could pose an even greater environmental concern.

Another study was aimed at introducing TiO_2 nanoparticles onto surface-modified (plasma treated) cotton textiles, in order to obtain textiles with self-cleaning capabilities.[213] Results suggest that such textiles show much more rapid degradation of various organics and foodstuffs compared to the uncoated textiles. The authors, however, do not consider whether the organic cotton fibres degrade as well as a result of TiO_2 photocatalysis. Another study reports successful use of gold-capped titania nanoparticles for anti-microbial coatings[214].

Decontamination and purification of air and water by titania photocatalysis has been the subject of extensive research in the past. Several good reviews provide overviews of the current achievements in this field[139,143,144]. The suitability of photocatalysis for water treatment is obviously determined by the initial water quality and flow rate. Currently available state-of-the art systems, however, are limited to niche-applications (Figure 21) since the photocatalytic rates of pollutant degradation are low.

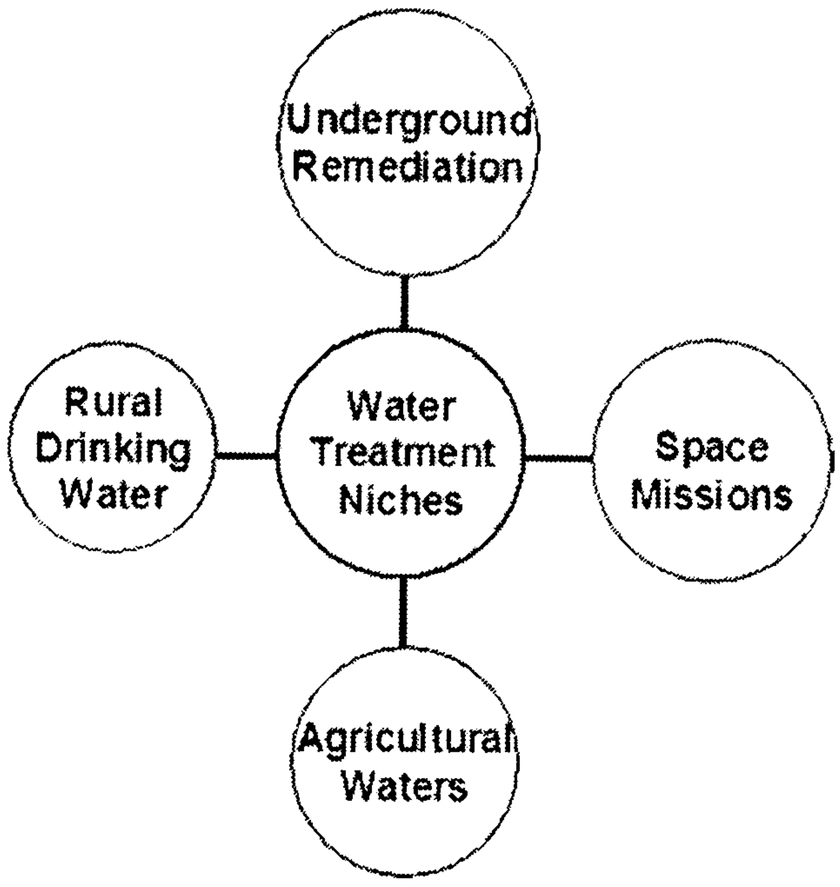


Figure 21 – Niche applications of photocatalytic water treatment, from[144]

A Canadian firm[215] has demonstrated that photocatalysis can be used successfully for the remediation of underground water containing diverse pollutants at abandoned industrial sites, with even possible use of mobile water treatment units. Additionally, photocatalytic water treatment has been found to be more economical than adsorption on activated carbon, at least in certain cases. TiO_2 photocatalysis has been identified to have significant potential for treatment of effluents of textile industry. It has been estimated that 1-20% of the total world production of dyes is lost through water effluents during the dyeing process[216]. This loss causes considerable non aesthetic pollution and eutrophication of watercourses and can form other environmentally dangerous by-products through chemical reactions.

Use of nano-TiO_2 as inorganic filler for polymer membranes has been reported frequently; membrane reactors that incorporate TiO_2-polymer systems have been recently developed to replace secondary clarification and solids separation in activated sludge systems[217-221]. Conventional, pure polymer membranes are susceptible to microbial fouling, which can cause significant pore blockage and cake

formation at the membrane surface. This build-up leads to high pressure drops and diminished membrane performance. Composite membranes containing TiO_2 nanoparticles have better performance, since TiO_2, upon UV irradiation, provides a self-cleaning feature to the membrane, preventing excessive build-up of fouling. A series of studies by the Molinari group[220-222] investigated various reactor configurations, which combine TiO_2 photocatalysis and membrane technology for remediation of pollutant-rich streams; their results give evidence of substantially lower pressure drops across the composite membranes over a longer period of time, compared with pure polymers. The studies, however, fall short of addressing the important issue of the durability of TiO_2 membrane nanocomposites. Inevitably, exposure of nanocomposite membranes to UV also leads to the degradation of the membranes themselves, and even though the degradation may take place at a relatively insignificant rate, it is however, important to have a quantitative appreciation in order to be able to compare the novel technology with existing ones.

On a slight sideline, Bae and Tak[223,224], give evidence for the significant reduction of membrane fouling solely through use of hydrophilic surface nature of TiO_2, rather than the 'usual' photocatalytic effect. Nano-TiO_2 (4-7 nm) was introduced onto the surface of polyethersulfone membranes, similar to those studied for fuel cell applications[225]. Addition of titania actually causes a slight (almost negligible) decrease in membrane permeability, but on the other hand resistances due to formation of filter cake and fouling were reduced by approximately 90% and 65%, respectively, as compared to neat membranes. A reduction in trans-membrane pressure drop would decrease the pumping power requirement for the feed stream, which in turn implies that operation of membrane reactors can be rendered more efficient and cost-effective.

Lastly, turning towards the medical applications, degradation of organic matter by TiO_2 photocatalysis might be used to treat cancer[226-228]. Research in this field is currently at an early stage, faced with many challenges and uncertainties. For instance, human bladder cancer cells deposited onto TiO_2-coated glass have been shown to be killed under UV-A irradiation; the retarding effect of photo-excited TiO_2 particles upon the growth of cancer cells developed on the backs of mice has been

demonstrated; and TiO_2 was found to reduce the formation of pyrimidine dimmers (believed to cause skin cancer) upon UV irradiation of human cells in vitro and mouse skin in vivo[229]. Although promising results to start with, some valid questions immediately arise – How does the normal tissue react to the radicals generated by TiO_2 photocatalysis? How to effectively introduce the TiO_2 implants? How to expose the TiO_2 surface to UV once implanted and what will the side-effects of UV irradiation be? Each of these problems and many more need to be addressed by researchers before any clinical trials can take place. One of the more recent promising and realistic medical applications of TiO_2 photocatalysis is a silicone catheter internally and externally coated with TiO_2; sufficient light can penetrate to render the catheter self-sterilizing and self-cleaning throughout[230]. After use, the catheter is sterilized in a small box containing a UV lamp.

2.5.1.4 Electronic and electrochemical devices with nano-TiO_2

Although electronic devices are not the primary objective of this project, an overview that reflects a significant interest in this area will be presented. Processing of TiO_2-polymer nanocomposites for electronic devices is very similar and relevant to methods used in the present work. Devices such as hybrid polymer-TiO_2 solar cells, light emitting diodes (LEDs), polymer electrolytes for fuel cells and batteries have been investigated extensively in the past, with some remarkable progress reported. Polymers offer many advantages over conventional matrix materials for electronic device, such as metals, ceramics or semiconductors (e.g. silicon), in that they have comparable or in certain instances better mechanical, electrical and optical properties, as well as benefiting from ease of manufacture and processability. For some applications, like solar cells, conductive polymers offer novel device and processing options compared with conventional silicon-based systems, which could lead to a better cost-performance balance. One may argue that using nanoscale titania for conductivity enhancement is not the best solution, given the fact that, for example, certain structural modifications of carbon nanotubes exhibit much higher electrical conductivity. However, present CNT fabrication methods are not yet developed sufficiently for selective synthesis of specific types of CNTs, so for the time being at least, conductivity enhancement in electronic devices using TiO_2 nanoparticles appears more realistic. The last five years have seen a large increase of interest in the

area of polymer-based electronic devices, with most studied matrices being those of, poly (p-phenylenevinylene) (PPV)[13,231-237], polythiophene (PTh)[238-240] and PTh derivatives (poly (3-hexyl)thiophene (P3HT)[241-245], poly(3-octyl)thiophene (P3OT)[246]), polyaniline (PANI)[247-255] and polypyrrole (PPy)[256-258].

The first observations of efficient photocurrent generation using dye-sensitized nanostructured TiO_2 solar cells date to the late 1980s[259,260]. Although very interesting both from academic and industrial stance, DSSCs will not be discussed further, since their structure does not involve TiO_2 – polymer composites. On the other hand, blends of nanocrystalline titania and conjugated polymers became of interest for photovoltaic applications in the late 1990s[261-263] and will be touched upon. Polymers which exhibit a delocalization of π molecular orbitals along the polymer chain can be classified as conjugated; improved electrical conductivity and semiconducting characteristics stem from this particular polymer feature. Relative to DSSCs, TiO_2-polymer solar cells have the added advantage of same photocurrents at much smaller device thickness, because the entire polymer-filled pore volume is available for exciton generation, rather than only a dye monolayer at the titania surface[264].

PPV and MEH-PPV (poly [2-methoxy-5-(2'-ethylhexyloxy)-*p*-phenylenevinylene]), as typical conjugated polymers, have been considered for applications as light emitting diodes and photovoltaics since 1990[265]. The motivation for fabrication of TiO_2–PPV blends (most commonly in thin film form) was to improve the photovoltaic efficiency of the pristine polymer devices. Most studies[13,231-233,235] investigate UV–Vis and photoluminescent (PL) spectra of the films as a function of various parameters (e.g. titania content and composite preparation conditions). PL spectra show that PPV emits yellow-green light at 540 nm, while PPV–TiO_2 blends were shown to strongly absorb below 510 nm, with absorbance increasing with titania content. The mechanism for improving electrical conductivity in PPV with TiO_2 is still not clear. Some researchers[231] suggest that the improvement is due to a decrease in conjugation length of the polymer chain and others[236] propose that titania forms percolation networks of nanoparticles, thus enhancing the charge transfer rates.

The two most common parameters useful for assessing the solar cell performance are the external quantum efficiency (EQE, percentage of photons converted to current) and the power conversion efficiency (η). The latter is defined as the percentage of incident power carried by light converted to current and is usually measured according to AM 1.5 standard, i.e. solar radiation with intensity of 1000 W m^{-2}, after it has travelled the length equivalent to 1.5 times the shortest height of the Earth's atmosphere. The maximum power conversion efficiency can also be measured for devices irradiated with light of discrete wavelengths.

A study by Petrella et al.[13], compares oleic acid-capped TiO_2 nanoparticles (Cozzoli-type[6]) of different morphologies (rod-like to spherical particles) for use as fillers in MEH-PPV. Irrespective of particle shape, charge separation and transfer processes were observed at the titania – polymer interface, through analysis of PL spectra. In both cases the blends showed higher photo-activity than the separate constituents. The presence of a large number of interfaces available for charge transfer is believed to play a fundamental role in enhancing the photoelectrochemical performance of the dispersed heterojunctions. However, the use of spherical nanostructures produced higher photoelectrochemical responses than the nanorod ones, most likely due to presence of bulky oleic acid molecules at the surface, which slightly inhibit charge transfer[13]. TiO_2 nanorods, synthesised by the same procedure have been used in similar MEH-PPV solar cell devices by another group recently[266], reporting maximum EQE of 24% under illumination at 430 nm and η of 2.2% and 0.49% under 565 nm and AM 1.5 illumination, respectively. These values, although not as high as reported for DSSCs (η >10%[267]), remain promising and stimulate further work.

Polythiophene (PTh) has been extensively studied for solar cell applications; it is a polymer which can be manipulated so that it behaves as a metal-like conductor or as a semiconductor, depending on the desired application. Processing of the TiO_2-PTh nanocomposites usually involves coating TiO_2 nanoparticles with PTh using electrophoretic deposition, to form nano-sized encapsulations[239,240]. Figure 22 shows a high resolution TEM of such structure, with a few nanometre-thick polymer coating clearly visible.

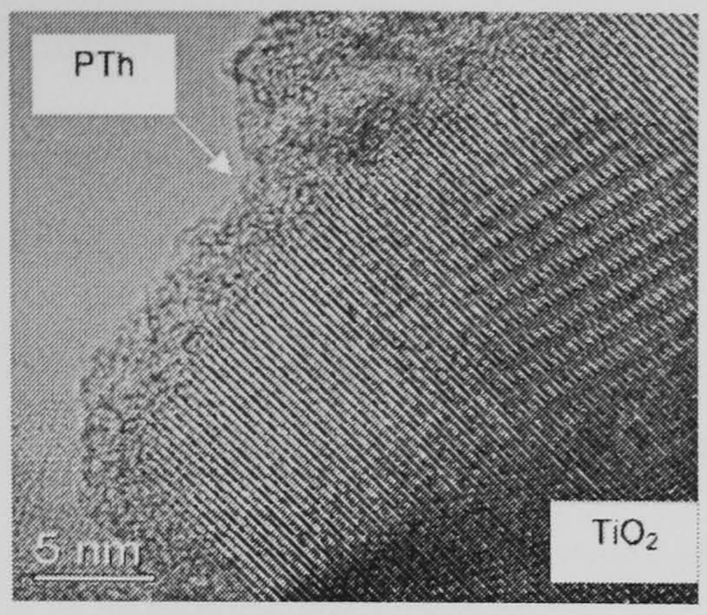


Figure 22 – HRTEM micrograph of a TiO_2-PTh nanocomposite particle, from Vu et al.[239]

A derivative of PTh, poly(3-hexylthiophene) (P3HT) has been used recently in solar cell research[241-245]. Kwong et al.[241] fabricated TiO_2-P3HT nanocomposite blends and studied the optical properties of the nanocomposites. The blends were then used to construct solar cells and evaluate the device performance. The structure of the solar cell - aluminium-P3HT/TiO_2-poly(ethylenedioxythiophene) blended with polystyrene sulfonic acid-Indium-Tin-Oxide - used in this case is depicted in Figure 23.

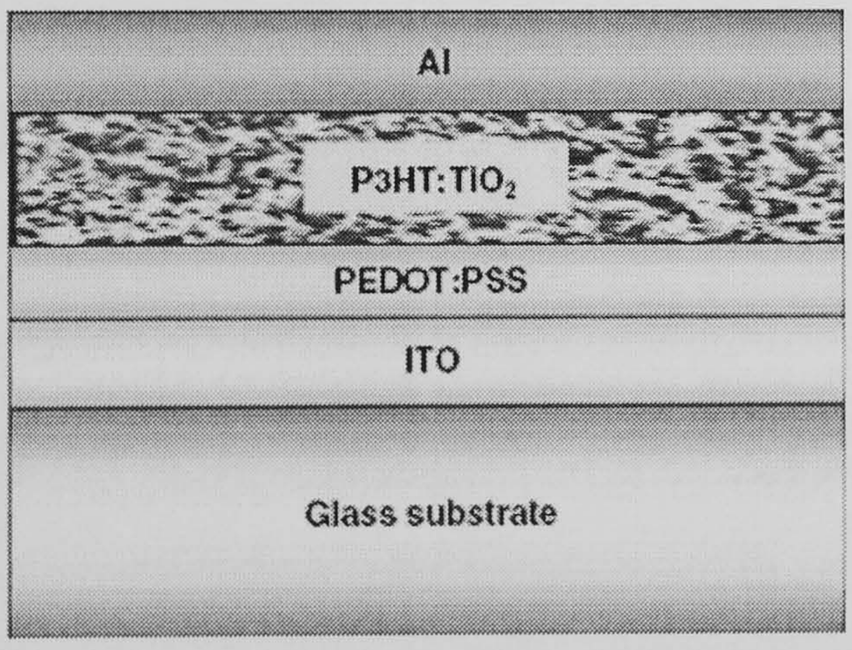


Figure 23 – Structure of P3HT-TiO_2 based solar cell, from Kwong et al.[241]

For TiO_2 loadings of 40 wt% and higher, significant improvements in efficiency became apparent, with AM 1.5 η of 0.42%, at 60 wt% TiO_2 loading, compared with 0.06% for pure P3HT. TiO_2 nanorods have also been used to fabricate solar cells with P3HT[243-245] with the most promising results published by Lin et al.[243]. TiO_2 nanorods used in their study are grown using the Cozzoli sol-gel route in the presence of oleic acid[6], which remains bound to the nanorod surface. Oleic acid was found to act as an insulator at the nanorod-polymer interface leading to poor charge separation efficiency and overall poor device efficiency (AM 1.5 η = 0.38%). The fact that interfacial properties greatly affect the cell performance was shown by performing a ligand exchange on the nanorods; when a more conductive anthracene-9-carboxylic

acid was used instead of oleic acid, the AM 1.5 power conversion efficiency increased significantly to 1.7%.

Although the use of TiO_2 polymer nanocomposites for photovoltaic applications is extensively researched, there are other applications of TiO_2 polymer nanocomposites in electronic devices. The first attempts to use conventional TiO_2 in polyaniline (PANI) date to more than a decade ago, but the use of nanocrystalline TiO_2 is fairly recent[268]. In most cases, preparation of PANI nanocomposite involves grafting a polymer precursor onto the surface of titania nanoparticles, either directly, or by using some sort of coupling agent, followed by a polymerisation step. In this way, TiO_2 can be encapsulated inside a PANI shell[247-253]; such nanocomposites show improved electrical conductivity. Infra-red (IR) spectroscopy results give evidence of strong interactions between the titania core and polymer shell. The effect of ultrasonic treatment was found to improve the TiO_2 nanoparticle dispersion[248]. Latest results[255] demonstrate that a composite of PANI with equiaxed 40 nm anatase nanoparticles has exceptional NH_3 sensing capability. The response and the recovery time are very fast (several seconds), reproducible and, unlike many other sensors, optimal performance is at room temperature. On the downside, increased ambient humidity significantly diminishes the sensing capacity and also, separate analysis of the sensitivity to CO gas shows poor sensor performance. The same research group reported in another publication[257] successful fabrication of TiO_2-polypyrrole (PPy) nanocomposites for NH_3 and CO gas sensing. Similar results were observed, i.e. the sensors are much more effective for NH_3 sensing than CO and also, humidity reduces the sensing capacity. In light of the observed effect of the humidity on the performance of NH_3/CO sensors, it is perhaps unsurprising that it has been separately reported that TiO_2-PPy nanocomposites act as efficient humidity sensors[258].

Inorganic composite polymer electrolytes were demonstrated to be effective in enhancing the ionic conductivity, modifying the mechanical stability and improving the interfacial contact with electrodes in secondary batteries (e.g. rechargeable lithium batteries) and other ionic devices[269,270]. Ion conduction enhancement appears stronger when the filler is nano-scaled and hence has a high specific area. Blending inorganic particles into polymer electrolytes has been utilised since the 1980s (e.g. micro-sized Al_2O_3)[271,272]. Several authors[230,269,273-275] have since pointed out the importance of Lewis acid-base interactions between the filler, the salt and the polymer and the local structure that surrounds the filler particles when describing the apparent increase in ionic conductivity. Best et al.[276] showed, by using a simple electrostatic model, that Li^+ experience the same potential at TiO_2 filler surfaces as in the polymer, which means that Li^+ can move between these sites with a low activation energy barrier. In a recent paper, the same authors[277] propose that the increase in ionic conductivity is due to the formation of percolating interface regions.

Relevant work for applications in batteries and fuel cells also includes TiO_2 nanotube (12-15 nm diameter, 80-120 nm long) – poly(vinyldene fluoride) (PVdF) / $LiPF_6$ solid membranes[278], TiO_2 nanoparticles (6 nm)-Nafion® - porphyrin composites[279], (trihydroxy)poly(ethylene oxide-*co*-propylene oxide) (3PEG)-$LiClO_4$ – P25 TiO_2 nanocomposite electrolytes[280], nano-rutile (20-30 nm) PVdF-hexafluoropropylene polymer electrolytes[281] and TiO_2-acetylene black nanocomposites for electrochemical Li insertion[282]. It is currently argued that inorganic oxide particles help electrolyte disassociation and promote physical cross-links with the polymer chain, thus improving ion conductivity[275]. Photocurrent density results[279] show that titania filled membranes give rise to 10 times higher photocurrent densities than the original systems. Prashantha and Park[225], consider doping polyethersulfone membranes for methanol fuel cell application. It is argued that the TiO_2 filler (<100 nm) increases the membrane selectivity, decreases reactant permeability coefficients, thus preventing reactant loss, increasing the stability and efficiency. The downside, however, was the measured decrease of the proton conductivity.

2.5.2 TiO_2 nanocomposites for optical applications

Optical properties are important, for example if the end product must be of exceptional transparency or have tuneable refractive index. Nanomaterials are particularly interesting for use in such applications. Having a size below 100 nm should preclude such materials from scattering visible light, which has significantly greater wavelengths. However, in common practice, agglomeration of nanoparticles can give problems in attaining perfect transparency. TiO_2 nanorods and nanotubes in particular, have exceptional potential for optical applications, due to their highly anisotropic nature, but as with the other areas of research, the optical behaviour of structures with anisotropic properties in a composite system has not yet been studied in detail. Additional advantages are offered by TiO_2 itself, i.e. its strong absorption in the UV spectrum, which is useful for UV shielding.

Nanoscale TiO_2 has been combined with a number of polymer systems to produce nanocomposites with interesting optical properties – poly (methyl methacrylate) (PMMA)[283], polyethylene (PE)[284], poly (ethylene phthalate) (PET)[285], poly (vinyl alcohol) (PVA)[11,286,287], poly (styrene maleic anhydride) (PSMA)[288], polyimide (PI)[289] and various thermosetting polymers (acrylic resin[290], polythiourethane[291], epoxy[292,293]).

In most instances, the processing of polymer nanocomposites involves either directly blending commercially available equiaxed TiO_2 nanoparticles[284,285] (e.g. by solvent casting or melt mixing) or, more commonly, the addition of Ti-alkoxide sols to dissolved polymer and subsequent in-situ hydrolysis to produce TiO_2. The latter approach appears particularly promising for composite processing as it enhances the dispersion of the nano-TiO_2. However, it seems surprising that identification of the TiO_2 and its crystalline phase within these nanocomposites is not much discussed. With the exception of two studies[288,293], which use XRD to demonstrate that the hydrolysis of TiO_2 sols produces nanocrystalline TiO_2 and whether it is rutile or anatase, other authors use only IR spectroscopy to identify the material structure. Although the IR is by all means a valid method, techniques like XRD and Raman spectroscopy would be more suitable and informative for TiO_2 identification. In addition to identification of TiO_2 phase, XRD could, for example, provide data on

crystal size. TiO_2 is more Raman-active, which makes it readily analysed by Raman spectroscopy.

With regards to the optical properties of the TiO_2 nanocomposites, all of the above studies report on nanocomposites of exceptional optical transparency as a result of excellent dispersion at the nanometre scale. Transmission spectra, obtained by UV-Vis spectroscopy, typically show the same absorbance in the visible region (400 – 900 nm) as that of the pristine polymer, while absorbing strongly in the UV region (< 400 nm) due to TiO_2[283,289,290,293]. Optical transparency of the nanocomposite films can be maintained for very high TiO_2 nanoparticle loading fraction, e.g. 35 wt% TiO_2 in PVA[11], 60 wt% in acrylic resin[290]. Optical transparency of the nanocomposites in the visible region and complete opacity in the UV are of great interest for UV filters and optical limiting devices, but one must always appreciate the aggressive side of exposing TiO_2 to UV, i.e. the photocatalytic effect, which can lead to nanocomposite degradation. Another unique feature of TiO_2 is its high refractive index (2.5-2.9, depending on the crystal phase), second to only a handful of materials. Polymers, on the other hand, have low refractive indices (typically 1.3-1.7); therefore adding TiO_2 to polymers provides a good way for fabricating high-refractive index composite materials, with the ease of processing and flexibility of polymers. Remarkable improvements in refractive index have been observed for TiO_2 nanocomposites in: PMMA (1.47 – 0 wt% TiO_2, 1.87 – 70 wt% TiO_2)[283], PI (1.57 – 0 wt% TiO_2, 1.99 – 90 wt% TiO_2)[289], polythiourethane (1.63 – 0 wt% TiO_2, 1.88 – 80 wt% TiO_2)[291] and epoxy (1.61 – 0 wt% TiO_2, 1.80 – 65 wt% TiO_2)[292].

A range of interesting potential applications of the TiO_2-PVA composites for UV sensing, sunscreen additives and photochromic clothing was reported recently[287]. Essentially, the reported photochromic mechanism makes use of the fact that TiO_2, if subjected to UV under anaerobic conditions, becomes reduced (Ti(IV) to Ti(III)); this leads to change of colour in titania, from white towards indigo-blue, reported as far back as 1921 by Renz[294]. If the nanocomposites are exposed to UV, their colour also changes to blue and the authors report that the colour of the composites is retained for several weeks. The effect can be fully reversed by immersion of the composites into water; water soluble PVA swells and oxygen diffuses into the composites making them colourless again. The likely degradation of the composites, however, was not

discussed. In addition to PVA, composites from other water-soluble polymers, poly (vinyl pyrrolidone) and poly (4-vinyl pyridine), display the same behaviour.

Using TiO_2 as a filler in laser-dye (organic dye used as a lasing medium) doped PMMA was also reported[295]. Laser-dye doped polymers are used as optical fibres for applications in medical devices. PMMA polymer fibres were considered as superior compared to conventional modified silicate materials due to higher efficiency, better beam quality and homogeneity. Although TiO_2 particles used for these experiments were quite large (up to 150 nm), the composite films loaded with nanoparticles exhibit lower absorbance than composites with micron-size titania. Photoluminescence spectra suggest that photoluminescence behaviour can be fine-tuned by using particles of different sizes and selecting excitation light with variable wavelengths. Remarkably, the composites have the best light emitting efficiency when the excitation wavelength is near the absorption peak in the UV-Vis spectra.

TiO_2 nanorods offer the added advantage of having anisotropic features, which, if nanorod alignment can be achieved, hold great potential for fabrication of nanocomposites with anisotropic properties, e.g. UV polarising filters. A very interesting recent publication by Dessombz et al.[296] investigates this topic, although it does not involve fabrication of nanocomposites, rather only self-standing titania nanorod films. The nanorods, grown by hydrolytic sol-gel route, dispersed in acidic solutions are oriented by shear flow in order to form a nematic liquid crystalline phase and subsequently spin-coated onto microscope glass slides and dried. These UV polarisers were characterised for anisotropic properties by means of photocatalytic degradation of methylene blue dye – the oriented nanorod films were immersed into a dye solution, which was then irradiated by polarised UV light (see Figure 24 for a schematic). By rotating the titania films, the maximum change in the dye concentration ranged from 10^{-5} M to 3.6×10^{-6} M and from 10^{-5} M to 7.6×10^{-6} M for two extreme angles of polarisation, thus indicating the anisotropic photocatalytic properties of oriented TiO_2 nanorod films.

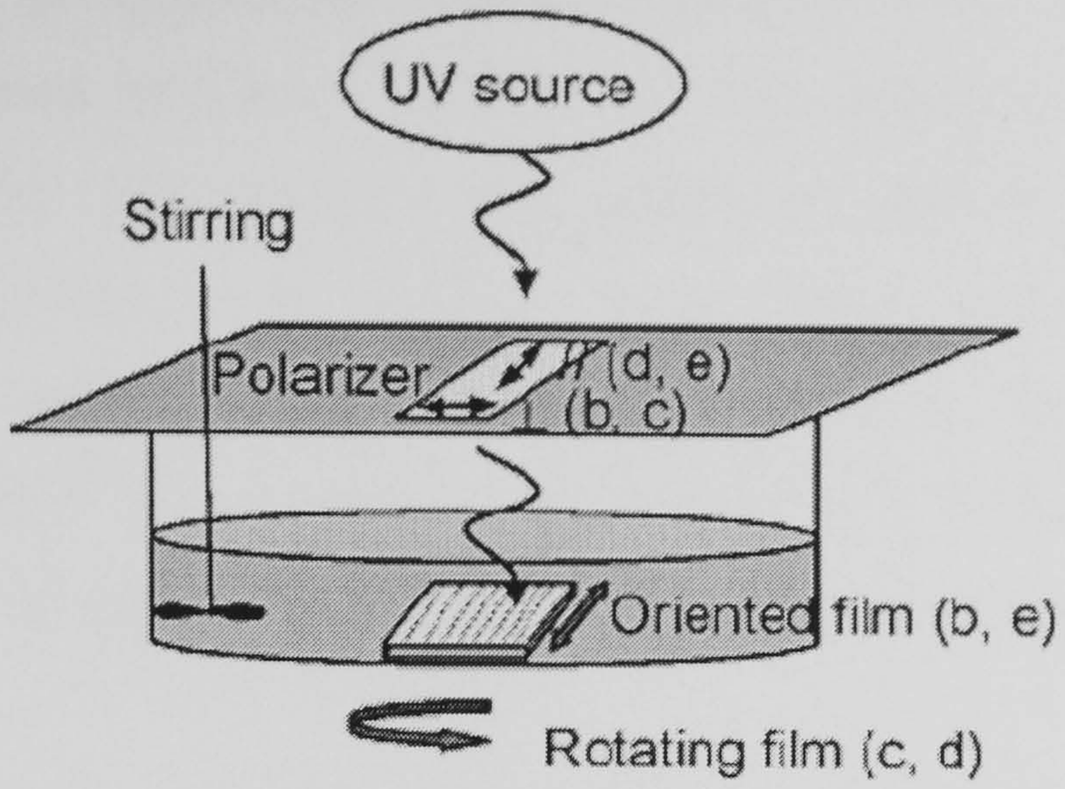


Figure 24 – Experimental setup for assessing the anisotropic photocatalytic behaviour of TiO_2 nanorods, from Dessombz et al.[296]

This work could be taken a step further if the nanorods could be introduced into a polymer matrix and aligned, either by shear or applying an electric field to yield robust, easily processed, low-cost UV polarisers. However, as will be seen in current work, alignment of titania nanorods is a major challenge.

2.5.3 TiO_2 structural composites

Despite the focus on photocatalytic properties of TiO_2, nano-TiO_2 is also a good candidate for materials which are aimed at obtaining improved mechanical and/or thermal properties. Initially, the structural nanocomposite work included polymer matrices, reinforced with titanate whiskers, with promising properties [297-300]. TiO_2 nanocomposites could be useful in everyday applications served by conventional materials, i.e. structural components, textiles, composites with enhanced flame retardancy, etc.

Several polymer systems were studied as the 'host' material for equiaxed TiO_2 nanoparticles – polyethylene (PE)[301,302], polyimide (PI)[303,304], poly (ether imide) (PEI)[305,306] polystyrene (PS)[12,307-310], poly (methyl methacrylate) (PMMA)[311-313], polyamides (PA)[314-316], polyester [317,318], poly (vinyl butyral) (PVB)[319], poly (arylene ether nitrile) (PEN)[320] and epoxy[321-324]. Nanocomposite processing was carried out using standard techniques – solution processing, melt mixing / extrusion or injection

moulding. Similar to applications discussed already, obtaining good nanoparticle dispersion and strong interfacial adhesion is very important in order to achieve optimal matrix-filler load transfer and enhanced thermal stability. The most commonly used method to achieve good filler dispersion is ultrasonic irradiation[307,312,317] and applying a coupling agent (e.g. trialkoxysilanes[307,311,314], ethylene-vinyl acetate[301,309], 6-palmitate ascorbic acid[313]) to the nanoparticle surface helps create strong interfaces between the polymer and the TiO_2 nanoparticles.

Adding up to 3 wt% of 20-60 nm equiaxed rutile to PE increases the tensile / bending strength and the Young's modulus of the composites with respect to pure PE[301]. Further increase in the loading fraction of titania in the composites led to reduction in mechanical properties compared to the optimal titania nanoparticle content. Apart from providing mechanical reinforcement, TiO_2 also provides a UV-shielding function to the nanocomposites. A three year field test was carried out, where nanocomposites were fabricated in the form of piping for micro-irrigation systems. The resistance against environmental stress cracking was increased for the nanocomposites, compared with the pure polymer.

Polyimide (PI) can be prepared from a variety of starting materials and is characterised by high thermal stability, chemical resistance and good mechanical properties. In-situ sol-gel synthesis of equiaxed 30-50 nm TiO_2 with PI has previously been reported to give rise to transparent nanocomposites, with a measured 15-20% increase of the dielectric constant and a 35% increase in storage modulus for composites with 10 wt% TiO_2[303]. However, a reduction in thermal stability and tensile strength was also observed. Another publication on TiO_2-PI nanocomposites makes similar observations, i.e. that the dielectric constant and storage modulus increase with increasing TiO_2 loading fraction, while the tensile strength decreases[304]. On the other hand, increased glass transition temperature (T_g) of the composites with increasing TiO_2 loading fraction was observed in this case, which suggests that TiO_2 enhances the thermal stability of polyimide, by immobilisation of polymer chains.

As mentioned earlier, polystyrene is often selected as a host material for TiO_2, primarily to facilitate its degradation in landfills. However, TiO_2 can also act as polymer reinforcement. High-impact PS (HIPS) is widely used for packaging, bottles,

housewares and appliances as it has good rigidity and is fairly easy to colour and process. The downside is that in spite of having a somewhat higher impact strength compared to normal PS, it has relatively poor heat deflection properties and flame retardancy. Zhang et al.[12] reported a 5-10% improvement in impact and tensile strength when 2 wt% siloxane surface-treated equiaxed 40 nm TiO_2 was added. When titania was well dispersed, additional impact energy was absorbed through plastic deformation of the composite, but adding more than 2 wt% TiO_2 leads to nanoparticle agglomeration; the agglomerates then act as stress concentrating sites. The heat deflection temperature of the nanocomposites increases with titania content and the flammability is decreased; the rheological properties of the melt remain unchanged, thus not affecting the composite processing. Wang et al.[308] report a similar degree of improvement for the impact and tensile strength of PS nanocomposites with 1 wt% 80 nm TiO_2 equiaxed nanoparticles. As opposed to the majority of publications pertaining to equiaxed nanoscale titania, nanorods have also been used for PS nanocomposites[307]. However only the processing aspects have been reported (e.g. rheological properties of the composite melts, particle dispersion) without any material characterisation.

Khaled et al.[312] have functionalised TiO_2 nanofibres (10 nm in diameter, up to several μm long) with methacrylic acid and subsequently blended them into PMMA to produce nanocomposites with enhanced (compared to pure polymer) thermal stability and Young's modulus, even for moderately high (17 wt%) TiO_2 content. PMMA nanocomposites enhanced with TiO_2 nanoparticles could be useful for applications as cements and implant biomaterials. A study by Dzunuzovic et al.[313] nicely illustrates the importance of nanoparticle-polymer adhesion. Interfacial adhesion can be improved by means of an appropriate coupling agent, e.g. methacrylic acid in the PMMA composite work by Khaled et al.[312] However, the study by Dzunuzovic et al.[313] provides evidence to the contrary, i.e. that the coupling agent can also hinder interfacial adhesion. It was observed[313] that the T_g of the PMMA nanocomposites containing equiaxed 4.5 nm TiO_2 nanoparticles, surface treated with 6-palmitate ascorbic acid does not change as a function of TiO_2 content. However, adding 1 wt% 6-palmitate ascorbic acid to PMMA, without TiO_2 nanoparticles leads to a drop in T_g from 120°C to 100°C, suggesting that the coupling agent acts as a plasticizer, reducing thermal stability.

Nano-TiO_2 (synthesised in-situ) – poly (arylene ether nitrile) (PEN) composites were fabricated with the aim of creating a material with the good mechanical properties of PEN while providing the dielectric properties of TiO_2[320]. The dielectric constant of composites containing 20 wt% TiO_2 increased by 85%, but on the downside the tensile strength decreased by 50%, most likely due to agglomeration. Overall, these materials have been identified as having good prospects for use as high energy capacitors. TiO_2-poly (vinyl butyral) (PVB) composites were analysed by Nakane et al.[319], who show that the nanocomposite films have higher Young's modulus and yield strength and lower elongation at break when up to 15 wt% TiO_2 is grown in-situ into the pristine PVB matrix. Similarly to TiO_2-PS systems[12], these nanocomposites possess higher thermal resistance than pure PVB. They also exhibit higher abrasion resistance.

Clearly, there is significant interest to consider the possibility of using high aspect titania nanorods as a reinforcing filler for polymer matrices. Nanorods possess anisotropic mechanical features, which can be passed onto the nanocomposite material by adjusting the nanorod orientation within the matrix. The possibility for nanorods to form networks of particles should be considered and also the impact this would have on the material mechanical properties, i.e. whether novel toughening mechanisms could be observed.

2.5.4 TiO_2 nanocomposites for biomedical applications

Another unique feature of TiO_2 is its bioactivity, or in other words ability to interact with biological entities and participate in biochemical pathways. Before discussing these applications in greater detail, it is important to note that there is a growing concern over the toxicity of nanomaterials. For instance, carbon nanotubes have just recently been officially classified by the UK government as a hazardous material, potentially with long-term health risks similar to those of asbestos[325]. Disruption of human epithelial lung cell functions was observed for nanoscale TiO_2[326], but it is important to note that the relative dose at which the changes were observed was ~75,000 times greater than that for carbon nanotubes (1500 μg ml^{-1} nano-TiO_2 cf. 0.02 μg ml^{-1} CNTs). Further, the study continues to conclude that the cytotoxicity of nanoscale TiO_2 is increased when the nanoparticles are exposed to UV. Given that the

most likely route for the intake of TiO_2 nanoparticles is by inhalation, it is very improbable that a person affected will ever have their lungs exposed to UV. Risk from the UV-induced DNA damage on the skin due to free radicals generated by the TiO_2 photocatalysis, however, is a valid and much more plausible concern, as mentioned previously[196].

Turning back towards TiO_2 nanocomposites for biomedical applications, the principal objectives of recent research have been to produce nanocomposites for use in tissue engineering, or more particularly to design novel, biodegradable tissue scaffolds for use in bone repair. Body implants, in general, bring about a plethora of issues – how to avoid immune response, how to design an implant with such properties that they most closely mimic those of the original tissue, and lastly how to reduce the implant cost.

Several polymers are currently under investigation for use as scaffold materials, such as – polylactic acid (in its various chiral forms) (PLA), polycaprolactone (PCL), polyglycolic acid (PGA), polylactic-co-glycolic acid (PLGA), polyhydroxybutyrate (PHB), etc. The common feature of these polymers is their biodegradability. This feature ensures that tissue scaffolds fabricated from such materials would degrade in a controlled manner, so that the new tissue can be successfully grown into surrounding tissue. These polymers already have the approval of US Food and Drug Administration (FDA) for use in certain clinical applications.

The most notable work in this area was done by Webster and various co-workers[327-331], who primarily investigated nano-TiO_2 – PLGA systems. PLGA is a copolymer of PLA and PGA, all of which belong to a group of aliphatic polyesters. PGA is a fast-degrading polymer in aqueous solutions, which loses its mechanical integrity between two and four weeks. PLA on the other hand degrades more slowly (order of months, or even years), due to presence of an extra methyl group in its chain, hence rendering it more hydrophobic than PGA. Due to this fairly large difference in degradation rates, it follows that the degradation rate of copolymer of PLA and PGA, PLGA can be designed to suit a particular application. Early work by Webster et al.[327] was directed towards investigating the cytocompatibility of novel TiO_2-PLGA composites that mimic the nanometre surface roughness of organic and inorganic phases of bone.

Specific to this work is that the polymer surface was treated with NaOH to make it rough on the nano-scale. Results show that for pure PLGA and pure TiO_2 films, osteoblast (bone-forming cell) density increases on moving from glass (reference) through conventional sub-micron to nanophase PLGA or titania. For PLGA samples, chondrocyte (cartilage-synthesising cell) density was stagnant, while for pure titania, it initially increases (compared to glass reference) and then remains constant. Composites which involve one of the conventional materials, non-treated PLGA or sintered sub-micron TiO_2, show higher cell densities, but the largest increase is evident for composites of nano-PLGA and nano-TiO_2. The main argument for observing such huge increase in cell densities was that nanometre rough surfaces have a much greater area on which cells can attach and proliferate.

In subsequent reports[328], this work is expanded upon by looking at the long-term functions and intracellular responses of chondrocytes relevant to bone growth. Relevant properties that were studied as a function of time were: cell density (1, 4 and 7 days), total intracellular protein synthesis (14 and 21 days), alkaline phosphatase activity (21 days), and chondrocyte expressed protein-68 (CEP-68) synthesis (21 days). Cell density remained stagnant throughout the study period (1-7 days) on the nanocomposite samples. This stagnation was explained by the fact that the cartilage forming cells go from highly proliferative phase, when new cells are formed, to a state of maturation, whereby cells actively participate in formation of matrix that eventually mineralises and is finally remodelled by osteoclasts (bone-resorbing cells) and osteoblasts to produce woven bone. Total intracellular protein synthesis was most markedly increased for nano-TiO_2/nano-PLGA composites, both with respect to time and with respect to other samples. Similarly, alkaline phosphatase activity was increased by about 30% on the nanocomposite samples compared with substrates involving at least one conventional material. Alkaline phosphatase participates in the mineralisation process and therefore represents a useful marker of cellular response. CEP-68 synthesis was measured with gel electrophoresis and its intensity band was most significantly increased for nano-TiO_2/nano-PLGA composites.

A very similar study was published in 2005[330], looking at the same type of nanocomposites with the aim of improving cell adhesion and inducing a cellular response. Results from this study provided the first evidence that osteoblast functions

(specifically, adhesion, synthesis of alkaline phosphatase, and deposition of calcium-containing mineral) increased on PLGA scaffolds containing nanophase compared to conventional grain size titania. Further, osteoblast functions improved with increasing nanophase TiO_2 loading in the composites. Because the chemistry, material phase, porosity and pore size of the composites were similar, this study implies that the surface features created by adding nanophase rather than conventional titania were a key parameter that enhanced functions of osteoblasts.

As with the majority of studies investigating titania nanocomposites, the dispersion of TiO_2 was perceived as an important factor that dictates the performance of the outcome material. Webster et al.[331] analysed the effect of power used for ultrasonic treatment during composite preparation on osteoblast adhesion and long-term cellular functions. SEM showed improvement in dispersion as sonication power was increased. Surface roughness and surface area seem to be optimal for samples sonicated at intermediate powers. Cell adhesion followed the same trend, although the control samples (pure titania and glass) show highest cell adhesion. The same result as for cell adhesion was observed for total cellular protein synthesis, although with even smaller differences between composites and control samples. Collagen content was highest on samples sonicated at higher power even when compared with the control samples; results are also very time dependent. Alkaline phosphatase activity and calcium deposition are more or less independent from the sonication power, but are strongly time dependent, with a significant increase for samples analysed after 21 days, compared to those studied after 7 or 14 days. Although the pure ceramics exhibit best results for some of the properties, they cannot be used on their own, due to their brittleness and poor processability.

One of the more recent studies looks at potential use of titania in orthopaedic/dental implants made out of titanium coated with hydrothermally treated hydroxyapatite-nanoscale titania-PLGA[329]. It was shown that sol-gel processing of composite implants can reduce the crack formation between titanium and hydroxyapatite (material with similar composition and structure to mineral phase of bone). Although the surface is crack free, it still possesses micron size surface roughness that is key to good adhesion of cells to the implant material.

Other researchers have also made attempts to fabricate TiO_2 – polymer nanocomposites for use in biomedical applications. Poly (D,L- lactic acid) (PDLLA) and P25 TiO_2 have been combined to fabricate nanocomposite films[332]. Such nanocomposites were characterised by immersion of films into simulated body fluid to observe hydroxyapatite formation (related to basic cellular response) on composite surface. Increase in titania content results in films with greater surface roughness (observed by SEM), but however, no hydroxyapatite formation was observed on nanocomposite surface. The same research group also investigated in a similar manner the use of P25 titania as a filler for polyester (PET)[333] in order to create nanocomposites for biomedical use that offer the processability of thermoplastics combined with good elasticity of rubber. A relatively low concentration of TiO_2 (<<1%) was found to improve the fracture strength by 100% and elongation at break by 300%. However, the nanocomposites were found to be biologically inert, since no hydroxyapatite formation was observed even after 3 weeks of immersion in simulated body fluid.

Polycaprolactone (PCL) is another thermoplastic polymer commonly used in biomedical engineering. It is flexible, but has low melting point, poor stability and tendency to crack. Introducing titania into such polymer was shown to have beneficial effect on overall composite performance, by improving the tensile strength and increasing the T_g[334]. Goto et al.[335] have fabricated bioactive bone cements based on polymethyl methacrylate (PMMA) and equiaxed TiO_2 nanoparticle composites. The results have shown that nano-TiO_2, if properly surface-modified with a silane agent, has improved binding to the bone than pure PMMA. The mechanical properties such as tensile and compressive strength are comparable or better than for the pure polymer.

As in previous sections, nanorods may offer advantages over equiaxed particles in biomedical applications:

- Surface roughness – similarly to work outlined above, titania nanorods possess nanoscale surface features that in some cases resemble that of the original tissue. This factor is important when designing materials that need to have a high degree of compatibility with the surrounding and original tissue.

- As the primary particle dimension (diameter) is reduced, the surface-to-volume ratio increases, meaning that the same quantity of nanorods provides greater surface area than micron-sized particles and conversely, this could provide extra surface sites for cells to attach and interact with the nanocomposite tissue implant.

- Formation of networks and lattices is expected to be beneficial, as a mechanical reinforcement due to improved stress transfer and also may provide interesting surface features.

2.6 Concluding remarks

The extensive commercial use of bulk TiO_2 powders, combined with an interest in nanomaterials in general, have stimulated the research into next-generation, nanoscale TiO_2 materials. This research can be broadly divided into two categories - development of synthetic methods for the fabrication of TiO_2 nanostructures and application-oriented research. The present state-of-the-art synthetic procedures have received some well-earned attention and undoubtedly hold great potential for the fabrication of single-crystal, single-phase, morphologically diverse and well-defined TiO_2 nanoparticles with a small size distribution. On the other hand, these new synthetic procedures have been developed on a small scale, with typical product yields reported at or below gram-scale. Ensuring that the material properties remain unaffected after scale-up remains an obstacle to wide-spread use of TiO_2 nanoparticles in various applications. Indeed, the vast majority of the numerous publications reporting novel nanocomposite materials containing nano-TiO_2, exploits commercially available nanoparticles. These materials are often present as large agglomerates, thus losing the main advantages associated with the nanoscale.

Perhaps surprisingly, very few research groups have produced TiO_2 nanocomposites, with high-quality, individually-dispersed TiO_2 nanoparticles and even in those rare cases, the focus is almost exclusively on equiaxed nanostructures. In essence, this represents the truly novel aspect of the present work, i.e. to fabricate TiO_2 nanocomposites using anisotropic TiO_2 nanostructures, specifically nanorods and

investigate the resulting material properties. Anisotropic titania nanorods that have been used in functional polymer nanocomposites have been entirely used for applications in electronic devices.

The specific objectives of the research presented in this thesis were to:

1. Use or modify the existing sol-gel procedures to synthesise high-quality TiO_2 nanorods. The high-quality specification pertains, amongst other factors to crystallinity, morphology, particle size distribution and dispersibility in different solvents.

2. Modify the titania nanorod surface chemistry by removing the structure directing ligand capping from the nanorod surface and subsequently treat chemically in order to enhance the nanorod-polymer interface in the eventual composites and to control the TiO_2 photocatalytic capacity to degrade the matrix.

3. Fabricate TiO_2 nanorod – polymer nanocomposites, together with suitable controls, by a solvent casting technique. The composite properties – optical, mechanical and thermal, were characterised using different analytical techniques in order to identify areas of potential interest, where further development should be pursued.

3. Materials and Methods

3.1 Materials

The chemicals used for the experimental work are listed in Table 2, together with basic information, structure, purity, supplier, etc. These materials were used as received, unless specified otherwise. Additionaly, the following thermoplastic polymers were used for the fabrication of composites:

1. Poly (D,L- lactic acid), $[-CH(CH_3)COO-]_n$, PDLLA, inherent viscosity 1.87 dl g^{-1}, obtained from Purac Biochem, Gorinchem, The Netherlands
2. Poly (methylmethacrylate), $[-CH_2C(CH_3)(COOCH_3)-]_n$, PMMA, M_w = 120,000 g mol^{-1}), Sigma-Aldrich, Gillingham, Dorset, UK
3. Poly(vinyl alcohol), $[-CH_2CHOH-]_n$, PVA, M_w = 70,000 – 100,000 g mol^{-1}, Sigma-Aldrich, Gillingham, Dorset, UK

Chemical Name	Acronym	Formula	Mw (g mol^{-1})	Min. purity (wt %)	Supplier
3-aminopropyl trimethoxysilane	APTS	$H_2N(CH_2)_3Si(OCH_3)_3$	179.3	98	Sigma-Aldrich, Gillingham, Dorset, UK
Brilliant Blue R		$C_{45}H_{44}N_3NaO_7S_2$	826	90	Sigma-Aldrich, Gillingham, Dorset, UK
Chloroform		$CHCl_3$	119.4	HPLC grade	VWR, Lutterworth, Leicestershire, UK
N-dodecylamine		$C_{12}H_{25}NH_2$	185.4	98	Sigma-Aldrich, Gillingham, Dorset, UK
Ethanol		C_2H_5OH	46	99.5	VWR, Lutterworth, Leicestershire, UK
Ethylene glycol		$HOCH_2CH_2OH$	62.1	99	Sigma-Aldrich, Gillingham, Dorset, UK
Glycidoxypropyl trimethoxysilane	GlOPS	$(CH_3O)_3Si(CH_2)_3OCH_2(CHOCH_2)$	236.3	99	Dow Corning, Seneffe, Belgium
Heptadecane		$C_{17}H_{36}$	240.5	99	Acros, Geel, Belgium
Hydrochloric acid		HCl	36.5	37	VWR, Lutterworth, Leicestershire, UK
Isopropanol	IPA	C_3H_7OH	60.1	HPLC grade	VWR, Lutterworth, Leicestershire, UK
Oleic acid	OA	$CH_3(CH_2)_7CH=CH(CH_2)_7COOH$	282.5	90	Sigma-Aldrich, Gillingham, Dorset, UK
Phosphorous pentoxide		P_2O_5	141.9	98	Acros, Geel, Belgium
Potassium chloride		KCl	74.6	99.5	VWR, Lutterworth, Leicestershire, UK
Potassium hydroxide		KOH	56.1	85	VWR, Lutterworth, Leicestershire, UK
Sodium silicate		$Na_2Si_3O_7$	242.23	20-50 (aq)	Sigma-Aldrich, Gillingham, Dorset, UK
Tetrabutylammonium hydroxide	TBAH	$(C_4H_9)_4N^+OH^-$	259.5	25 (aq)	Sigma-Aldrich, Gillingham, Dorset, UK
Tetrahexylammonium hydroxide	THAH	$(C_6H_{13})_4N^+OH^-$	371.7	40 (aq)	Sigma-Aldrich, Gillingham, Dorset, UK
Tetramethylammonium hydroxide	TMAH	$(CH_3)_4N^+OH^-$	91.2	40 (aq)	Sigma-Aldrich, Gillingham, Dorset, UK
Tetramethylammonium chloride	TMACl	$(CH_3)_4N^+Cl^-$	109.6	98	Sigma-Aldrich, Gillingham, Dorset, UK
Titanium (IV) chloride		$TiCl_4$	189.7	98	Sigma-Aldrich, Gillingham, Dorset, UK
Titanium dioxide (5nm anatase)		TiO_2	79.9	99	Nanostruct. & Amorph. Mat., Houston, TX, USA
Titanium dioxide (P25 Aeroxide)	P25	TiO_2	79.9	99.5	Evonik (Degussa), Frankfurt a.M., Germany
Titanium tetraisopropoxide	TTIP	$Ti(OC_3H_7)_4$	284.2	98	Acros, Geel, Belgium
Tri-n-butylphosphine oxide	TBPO	$(C_4H_9)_3P=O$	218.3	95	Sigma-Aldrich, Gillingham, Dorset, UK

Table 2 – Chemicals used in experimental work

3.2 Preparation of TiO_2 nanorods (TNR)

3.2.1 General synthesis setup and equipment

The synthesis of TNR was carried out inside a 2-neck Pyrex flask (typically 100 ml) connected to a water-cooled condenser and a Schlenk line (N_2 / vacuum). Although an annular Liebig-type condenser provided sufficient contact area for adequate cooling of hydrolytic reactions, it could not provide satisfactory cooling duty for the high temperature nonhydrolytic syntheses, which resulted in breakthrough of the gaseous phase into the Schlenk line. For the latter synthesis, a Graham condenser was used, with an internal coil, which has a much larger surface area and therefore greater cooling duty. This design, although more difficult to clean and susceptible to fouling, was found to greatly reduce the volatilisation of reaction contents and provides a more robust solution when the reaction was scaled-up. The reaction flask was immersed into a paraffin oil or molten metal bath, heated on IKA Yellowline MSC Basic (Staufen, Germany) 500 W electrical hotplate with a ceramic surface (Figure 25). The hotplate also provides magnetic stirring of the reactor contents. Where high temperatures were required (e.g. 300°C), several minor problems were addressed. Normal magnetic stirring bars are covered by PTFE in order to provide inertness and ease of cleaning, but at 300°C, the PTFE sleeves were found to crack severely, exposing the iron to the reaction medium, which in turn causes contamination of the latter. Glass-covered bars, despite being more fragile, were successfully used instead. Secondly, having a good seal at the flask–condenser and the flask neck–septum connections was important in order to avoid any material loss. An acceptable seal was initially difficult to achieve with ordinary silicon grease and standard polyacetal clips, which degrade, melt and contaminate the reaction at 300°C. Metal clips and silicone-free Glisseal grease (stable up to 320°C; VWR, Lutterworth, Leicestershire, UK) were used to provide adequate sealing. New rubber septa were used for each run, since they degrade significantly during the reaction.

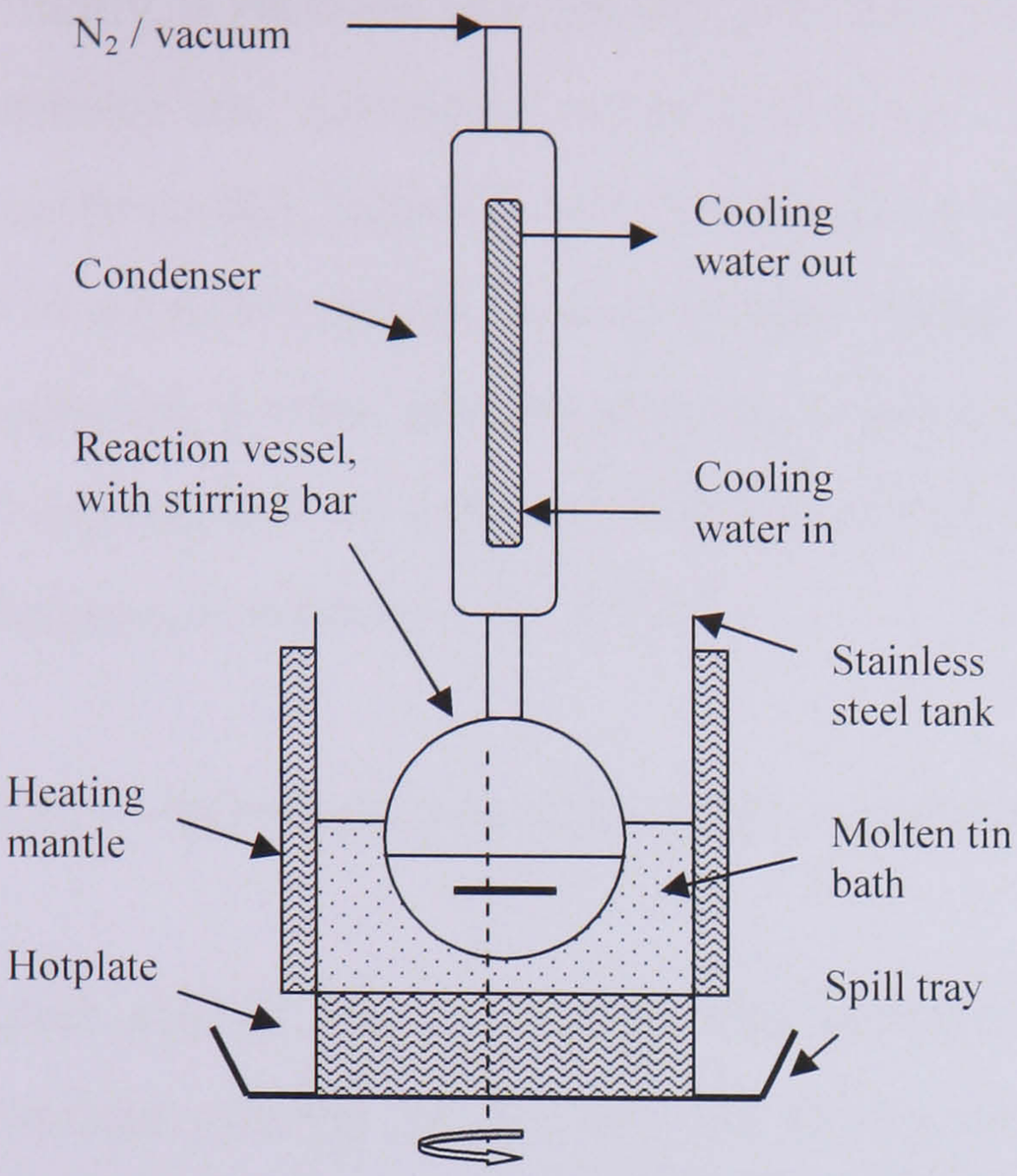




Figure 25 – Schematic and a photograph of the experimental setup for the nonhydrolytic synthesis of TNR

The molten metal bath originally designed by Dr. Sabina Chyła for the nonhydrolytic synthesis of TNRs utilised Wood's metal (Volume ~0.2-0.3 l), a eutectic alloy of bismuth, tin, cadmium and lead, with a melting point of ~70°C. This alloy was replaced by pure tin (V~1 l), when the reaction was scaled-up by a factor of 3, on molar basis. Tin was selected as a less-toxic (cf. Pb - neurotoxin, Cd – carcinogen) and a more cost-effective alternative, despite the higher melting point (232°C). The greater volume of tin could not be adequately heated to 300°C solely by the hotplate, so an additional heating element was introduced – a 250 W quartz heating coil was wrapped around the tin vessel and the whole vessel was heavily insulated with glass wool and aluminium foil to minimise heat losses. The power input into the coil was separately controlled using a potentiostat.

The primary method for solid-liquid separation was centrifugation. Centrifugation of reaction mixtures was carried out on two different units, both bench-top models. Initially, a Herolab UniCen unit was used (Wiesloch, Germany), with 8 x 30 ml rotor capacity and maximum centrifugal force of 18,000 g. This unit was replaced by a similar model, Sigma 2-16K (Osterode am Harz, Germany), a refrigerated unit with 6 x 30 ml rotor capacity and maximum centrifugal force of up to 21,500 g. Refrigerated operation is very advantageous as it increases the durability of the centrifuge tubes. Polypropylene-co-polymer (PPCO), 30 ml centrifuge tubes were used (Oak Ridge, Nalgene, Rochester, NY, USA).

3.2.2 Hydrolytic synthesis of TiO_2 nanorods

Oleic acid (175 g, 560 mmol) was kept for 1 h in a heated oil bath at 100°C under constant stirring in vacuum, for drying and degassing. The temperature was then brought down to 80°C and the atmosphere changed to N_2. TTIP (7.3 g, 25.5 mmol) was added to the oleic acid and mixed for 5 min. Finally, TMAH (18 g, 200 mmol) was rapidly added to initiate and maintain a fast hydrolysis reaction, which was then allowed to proceed for 6 h. The product was centrifuged to obtain a fine precipitate, which was then washed using IPA and ultrasonicated to wash away the oleic acid and any unreacted reactants. This centrifuge-wash sequence was repeated at least three times to purify the nanorods.

3.2.3 Nonhydrolytic synthesis of TiO_2 nanorods using TOPO / dodecylamine ligands (TNR_{TOPO})

This synthesis provided the majority of nanorods used in this project (overall, about 25 individual syntheses, each producing up to 1 g of TNR_{TOPO}). In a typical synthesis, a TOPO-dodecylamine mixture (12 g and 6.7 g, 30 mmol and 36 mmol, respectively) was dissolved in heptadecane (8.3 ml) inside a 100 ml Pyrex flask, connected to a condenser and a Schlenk line (Figure 26A). The dissolved surfactants were initially vacuum-dried at room temperature for 1 h to remove any residual water. The atmosphere was then changed to nitrogen and $TiCl_4$ (1.16 g, 6 mmol) and $Ti(OPr)_4$ (1.74 g, 6 mmol) were injected. Addition of $TiCl_4$ turns the mixture red (Figure 26B), and after TTIP was added it becomes light-yellow (Figure 26C), indicating the formation of a precursor complex. At this point the mixture remains clear, but after the vessel was heated to 300°C and allowing the reaction to proceed for 20 h, under reflux, the mixture becomes cloudy and white (Figure 26D). Upon cooling, the white colour of the mixture changes to grey. The product mixture was washed with IPA and centrifuged (20 min; 21,500 g) to recover the fine-particle sediment. The supernatant was dark-red and clear (Figure 26E), suggesting that the particles have been completely removed, which would otherwise give it a cloudy appearance. After 3 wash-centrifuge cycles, the wet product paste was vacuum-dried at 25°C. Additional washing resulted in incomplete separation following centrifugation, presumably due to removal of nonpolar organic functionalities and exposure of hydrophilic titania surface. The drying temperature must be kept as low as possible to minimise agglomeration and sintering. Finally, the dried material was ground into a fine white powder using marble pestle and mortar.

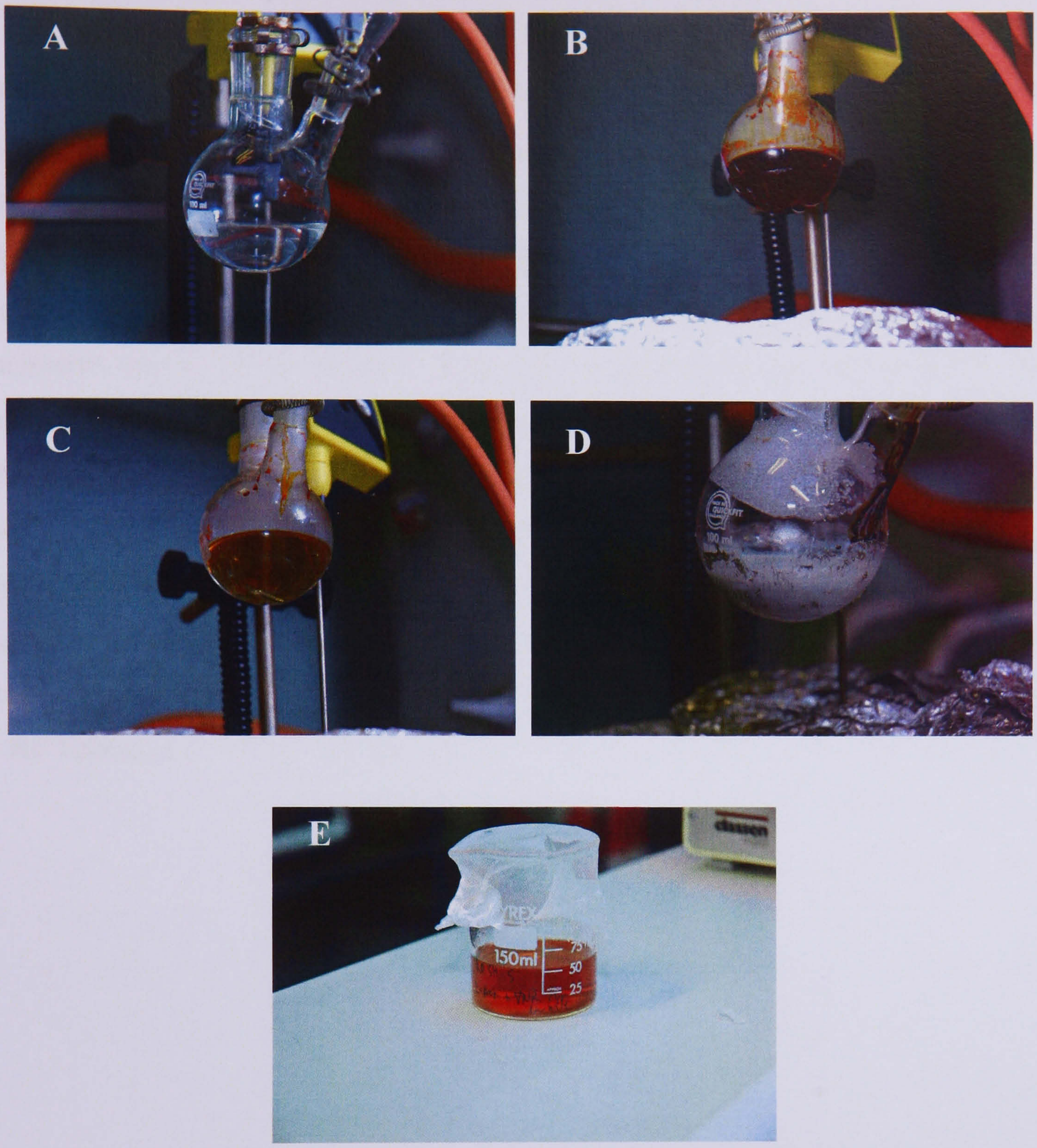


Figure 26 – Stages in the synthesis of TNR_{TOPO}: (a) TOPO + dodecylamine + heptadecane, (b) after adding $TiCl_4$, (c) after adding TTIP, (d) after 20 h at 300°C and (e) product supernatant (waste)

3.2.4 Nonhydrolytic synthesis of TiO_2 nanorods using OA ligand (TNR_{OA})

This procedure was originally developed by Dr. Sabina Chyła and Dr. Ben Cottam within our research group and used to synthesise TiO_2 nanorods of higher aspect ratio. The synthesis is again nonhydrolytic, but the surfactant is oleic acid dissolved in heptadecane. The setup and reaction conditions are otherwise identical to those for synthesis of TNR_{TOPO}, except that the reaction is split into two 4 h segments – a pre-nucleation step at 110°C, in an oil bath and a high temperature step at 300°C. The entire quantity of $TiCl_4$ and 1/3 of TTIP are added prior to the pre-nucleation step, while the remaining 2/3 of TTIP are added before heating to the high temperature stage. Splitting of the synthesis is beneficial in that it leads to a more controlled crystal growth. Care needs to be taken when transferring the flask from oil to molten metal bath to remove the excess oil from the flask, since any residual oil on the flask surface burns when exposed to 300°C. The reaction is worked-up in the same manner as for TNR_{TOPO}.

3.3 UV-assisted removal of structure directing agents ("stripping") and stabilisation of aqueous dispersions

The photocatalytic removal of adsorbed surfactants from the titania surface or simply "stripping", was performed by high intensity UV-A irradiation (UVP B-100AP 100 W flood lamp, Upland, CA, USA, λ=365 nm). This procedure is one of the unique and novel aspects of this project and was extensively used to produce hydrophilic titania nanorods without leading to any changes in morphology or crystallinity. The schematic and the actual setup are displayed in Figure 27 and Figure 28, respectively. After dispersing the dry 'as-synthesised' nanorod powder, typically 500 mg, in 20 ml $CHCl_3$, a two phase mixture was prepared by adding additional 50 ml of water. The mixture is then stirred magnetically in a partially closed vessel and irradiated with UV light, with the UV source located 15 cm from the vessel. Due to potentially harmful nature of UV radiation, the entire setup was kept inside a box-like polyester fabric enclosure to minimise exposure. In order to facilitate complete oxidation of hydrocarbon species on the nanorod surface, air was slowly bubbled through the mixture (20-30 ml min^{-1}). For the majority of experiments, air was supplied from a pressurised cylinder, which was later replaced with a simple air pump used for aeration of fish tanks. Although bottled air provided satisfactory results, it is generally difficult to provide steady aeration using the manual regulator valve without a flow metre, with typical problems involving excessive bubbling and decreasing cylinder pressure over time. Replacing the air cylinder with a small air pump provided a simple way to achieve steady air flow, with the additional benefit of improving the overall process safety. The importance of supplying air to the process was confirmed, by irradiating sealed aqueous titania dispersions and observing a grey-blue colour change, indicative of formation of Ti(III) species, a phenomenon reported almost a century ago by Renz[294] and also discussed in Chapter 2 in relation to UV sensing by TiO_2-PVA nanocomposites reported by Nussbaumer et al.[287]

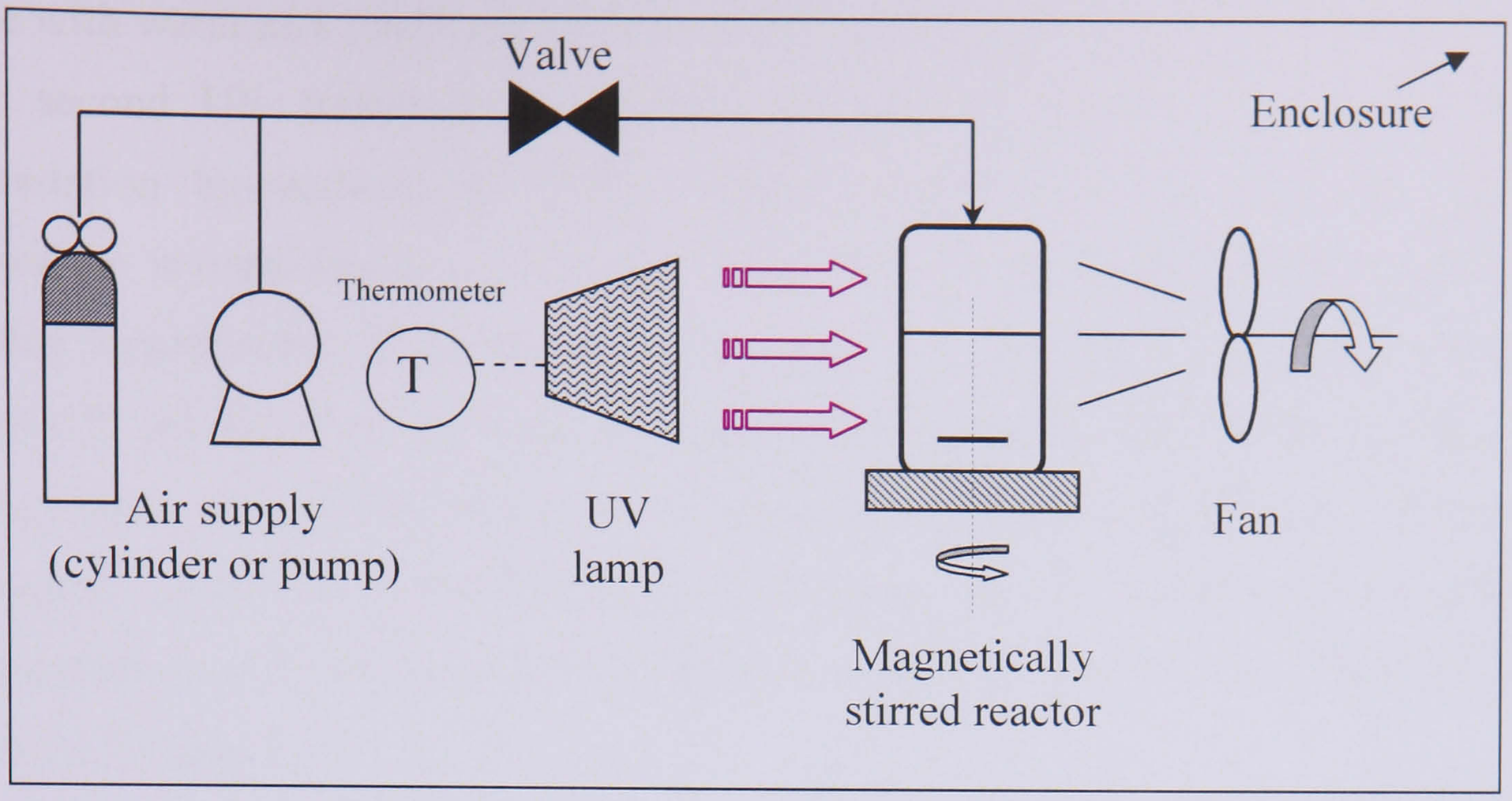


Figure 27 – Schematic for the stripping setup

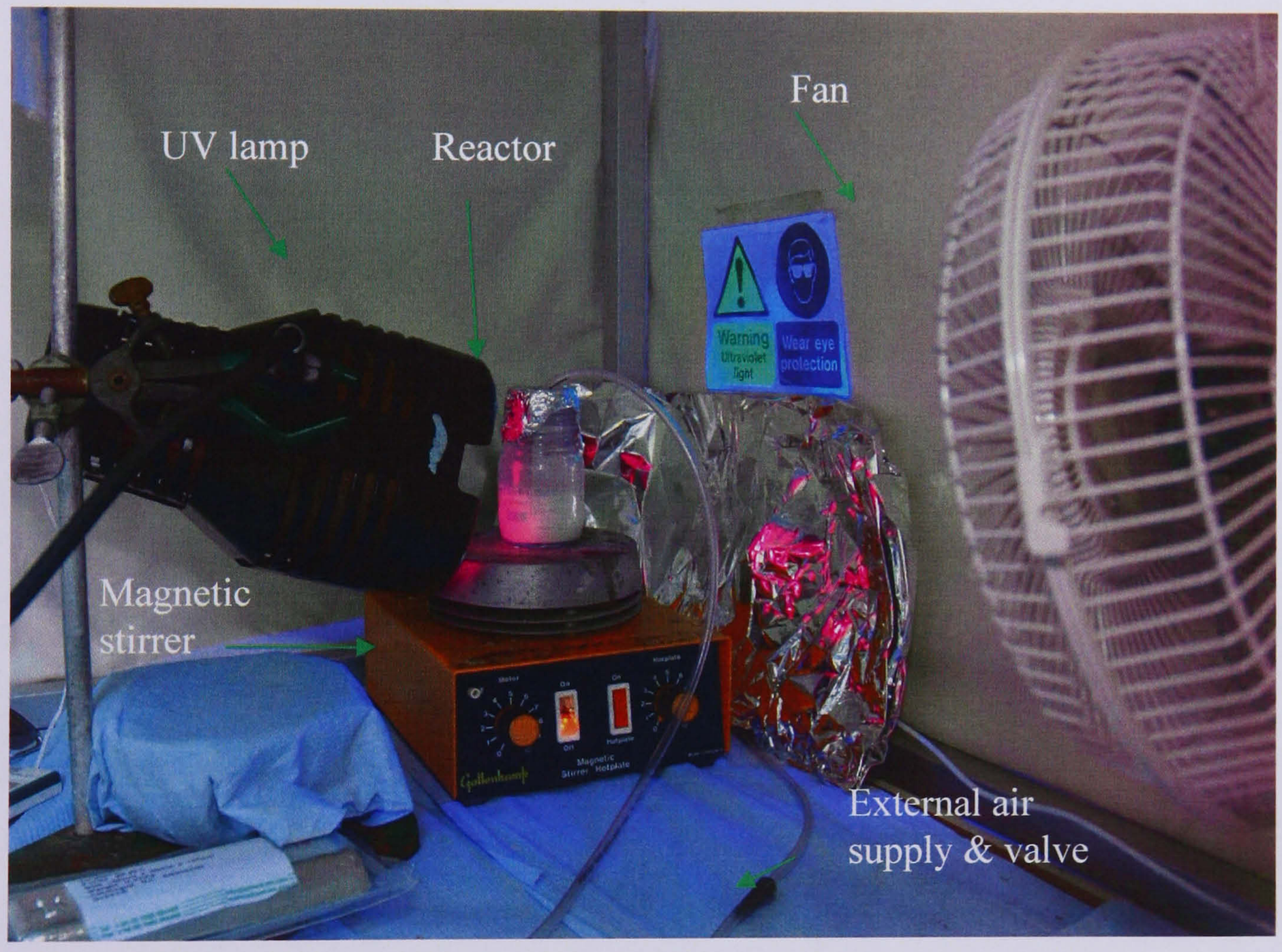


Figure 28 – Photograph of the stripping setup inside a boxed enclosure

The mixture was irradiated for 48 h, during which time most of the chloroform evaporates or degrades to CO_2, HCl and $COCl_2$, as described in a previous study on TiO_2-catalysed photodegradation of chloroform by Kormann et al.[336], leaving a cloudy, unstable nanorod dispersion in water. Despite the small amounts of HCl and $COCl_2$ evolved, it is important to conduct this experiment in a well-ventilated area, as a precaution. The nanorods were recovered by centrifugation, washed

once with water and irradiated again with UV for 24 h, under the same conditions. The second UV treatment is a further purification step, to ensure that no degradation by-products of $CHCl_3$ remain attached to the TiO_2. The final dispersion is centrifuged, washed with water, and the resulting dispersion used in further experiments. Although used primarily for TNR_{TOPO}, this procedure is generally applicable to any type of organic-capped titania nanoparticles. Indeed, experiments with TNR_{OA} were also carried out. Aqueous dispersions of these "stripped" nanorods, both TNR_{TOPO} and TNR_{OA}, can be stabilised and made transparent by addition of solution of TMAH or TBAH, which will be discussed in detail in Chapter 4.

3.4 Silanisation of "stripped" TNR_{TOPO} and effect on nanorod photocatalytic activity

Typically, TiO_2 nanorod water dispersions (100-200 mg TNR_{TOPO} in 50 ml water), well-dispersed with TMAH (100 mM TMAH), were placed in a 100 ml flask and magnetically-stirred at room temperature. APTS (300 μl) was diluted in ethanol (50/50 by volume) and added dropwise to the nanorod dispersion, using a syringe pump (Figure 29). Silane addition was carried out over 3 h, leaving the mixture to react for a further 1 h. Initially stable and clear dispersions would become increasingly unstable and cloudy as a result of silane addition, indicating a change in the titania nanorod surface character. The coated product was recovered by centrifugation and washed with water. Stabilisation of coated TNR dispersions was achieved by reducing the pH to below 2, using HCl. The procedure described was used without modification for silanisation with glycidoxypropyl trimethoxysilane and sodium silicate.

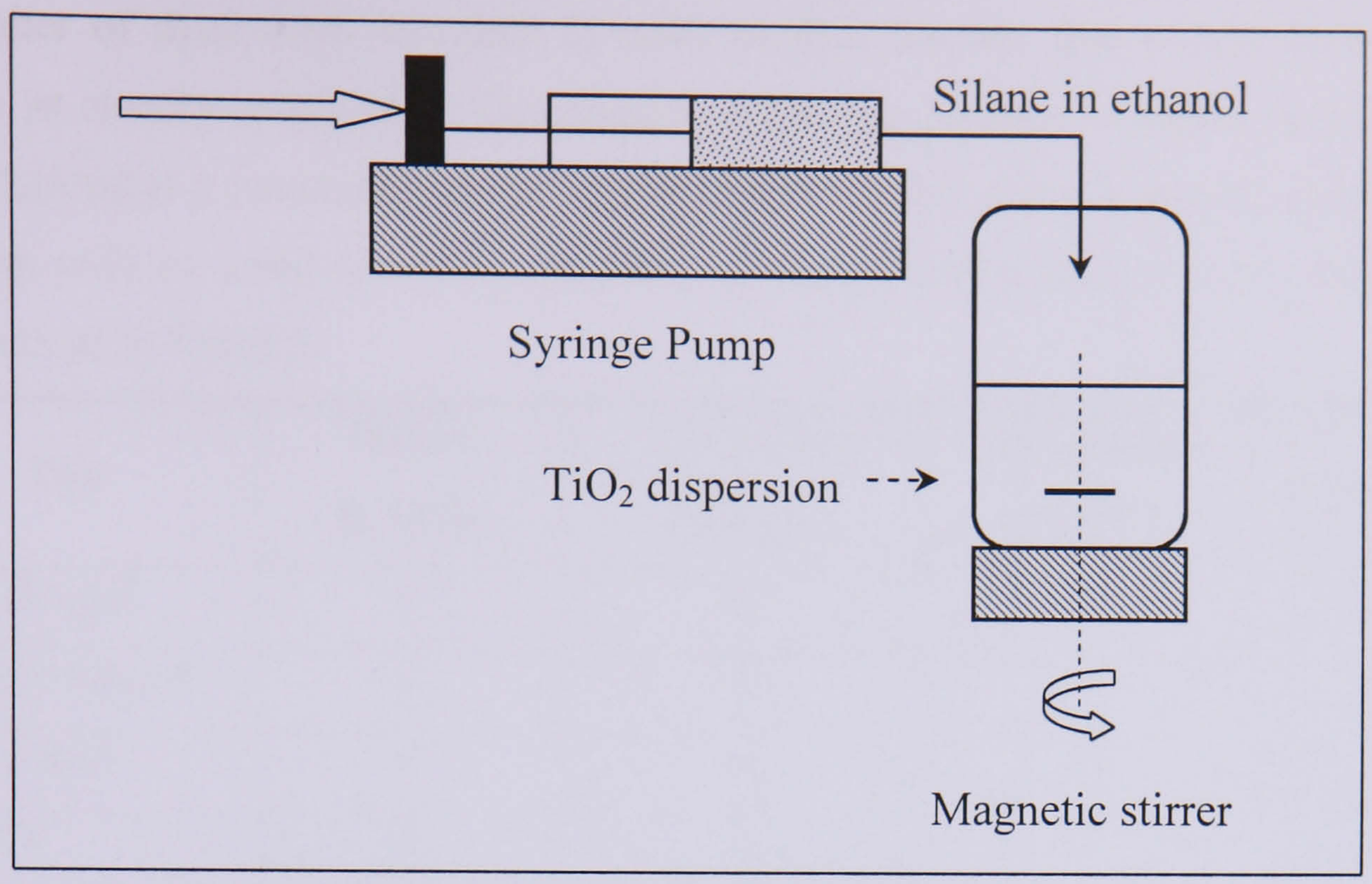


Figure 29 – Schematic for the silane addition setup

Dye-bleaching experiments on dispersions of stripped and silane-coated TNR were performed under artificial UV light in order to assess the efficiency of the silane coating in reducing the TNR photocatalytic activity. As discussed in Chapter 2, TiO_2 photocatalysis is a viable route for the degradation of textile industry waste effluents that contain toxic and / or environmentally harmful organic dyes[216]. As the dye is photocatalytically degraded, its concentration will decrease. Due to its strong light absorption in the visible range, even at very low concentrations (~ 0.01-0.1 mM), concentration and, therefore, rate of degradation can be monitored using UV-Vis spectroscopy. The choice of the dye was made according to several criteria:

1. *Photo-stability:* the dye should be as stable as possible under UV so that natural photolysis of the dye is minimised and the degradation occurs primarily due to TiO_2 photocatalysis.
2. *pH-stability:* most organic dyes are very sensitive to pH, which will vary hugely for the stripped (pH>12) and coated (pH<2) TNR dispersions. The dye must be stable across this range and, ideally, without a significant change in absorption behaviour.
3. *Solubility in water:* TNR dispersions are in water and the dye must be compatible in this aspect as well.
4. *Toxicity:* Not a primary concern, but important to minimise the risk, if possible.

A number of dyes were screened in order to find the one that would match these criteria as closely as possible. The primary screening process involved preparing the dye solutions at a concentration of ~0.1 mM and assessing the degree of solubility in water as well as stability within the pH 1-13 range. The results of this analysis are summarised in Table 3.

Dye	Water Soluble	pH stable (pH<2)	pH stable (pH>12)	Non-toxic
Rose Bengal	✓	×	✓	×
Brilliant Blue R	✓	✓	✓	✓
Congo Red	✓	×	✓	×
Eosin Y	✓	×	✓	✓
Martius Yellow	✓	×	✓	✓
Nile Blue	✓	×	✓	×
Solvent Blue	×	N/A	N/A	×
Solvent Yellow 7	×	N/A	N/A	×

Table 3 – Properties of organic dyes considered for evaluation of TiO_2 photocatalytic activity

All of the dyes considered, except Brilliant Blue R, were unstable at very low pH and some of them were not even water soluble. Hence, Brilliant Blue R, an anthraquinone dye (Figure 30) was selected. Subsequent trials with pure dye solutions revealed that although not completely UV-resistant, the rate of degradation is significantly slower than in the presence of TNR. Finally, it is non-toxic and relatively harmless.

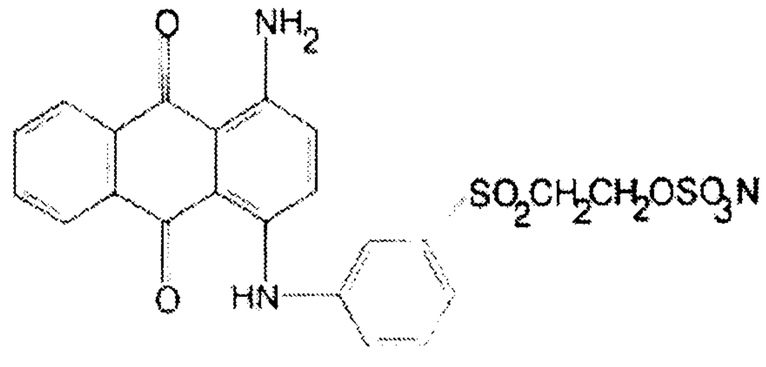


Figure 30 – Structure of Brilliant Blue R

The experimental setup for the dye bleaching experiments is identical to that used for stripping (Figure 27), with the exception that it is carried out inside a 25 ml vial instead of a 100 ml flask. Ideally, continuous sampling and spectroscopic analysis would provide the most accurate means for measuring the absorption and hence the rate of degradation. However, this would require significant time and resources to

achieve (peristaltic pump, special cuvette, modification to the UV-Vis instrument, etc.), so manual sampling at discrete intervals was used instead. The purpose of this experiment was to provide a general idea about the relative photocatalytic activity of the two TNR samples, rather than measuring the absolute values.

The governing equation for calculation of the dye concentration from the absorbance measured by UV-Vis spectroscopy, at a given time, is the Beer-Lambert law:

$$A = \log_{10} \frac{I}{I_0} = \varepsilon \cdot L \cdot C_D \qquad (9)$$

The absorbance A, defined as the log of the ratio of detected to incident intensity, is directly proportional to the light path length (cuvette size) L and the concentration of the dye C_D. The molar extinction coefficient or molar absorptivity ε is a quantity measuring the extent of light absorption by a chemical species and is its intrinsic property. In order to calculate the molar absorptivity for the present case, dye solutions with different concentrations were prepared: 10 μM, 30 μM, 50 μM, 80 μM and 100 μM. These solutions were analysed by UV-Vis spectroscopy, and using Beer-Lambert's law, the molar absorptivity was determined for a specific wavelength. Having determined the molar absorptivity, the concentration of the dye in the titania dispersions can then be calculated as a function of UV irradiation time. Attempts were then made to fit the observed concentration profiles to an expression describing the overall rate $\frac{dC_D}{dt}$ for the dye consumption. The following was proposed:

$$\frac{dC_D}{dt} = -k_1 \cdot C_D - k_2 \cdot C_T \cdot C_D \qquad (10)$$

This assumes that the decrease in dye concentration occurs via two pathways – first order photolysis ($-k_1 \cdot C_D$ term) and pseudo-first order TiO_2 photocatalysis ($-k_2 \cdot C_T \cdot C_D$ term, C_T – titania concentration). However, the observed degradation rates do not match the proposed kinetic model and were not fitted to a particular model. Instead, values for the dye concentration as a function of UV irradiation time were used to calculate the dye half-life time, which is a simple and useful parameter that illustrates the photocatalytic capacity of stripped vs. coated TNR dispersions.

3.5 Composite preparation

Solvent casting was the principal route for the fabrication of TNR composites. Three polymers were used, organic-soluble PDLLA and PMMA as well as water-soluble PVA. The first two were mostly used for composite fabrication in the early stages of the project, when the as-prepared organic-capped TNR were directly blended with the polymer. Subsequent development of the stripping procedure that led to stable TNR dispersions in water, created an opportunity for direct processing with water-soluble polymers. Several polymers were considered – poly (vinyl pyrrolidone) (PVP), poly (ethylene oxide) (PEO) and poly vinyl alcohol (PVA), with the preferred choice being PVA, due to its better film forming capability and ease of processing.

3.5.1 Processing of the PDLLA and PMMA composites

In a typical experiment (Figure 31), the polymer (2 to 4 g) was dissolved in chloroform, which was found to be a suitable solvent, both for the two polymers used and the organic-capped titania nanorods. Vigorous stirring, over 3 h, was used to ensure complete polymer dissolution. The optimal weight contents, for PDLLA and PMMA solutions were found to be 4 and 8 wt%, respectively, striking a good balance between ease of film formation and nanoparticle dispersion, which are, in turn, favoured by high and low viscosity, correspondingly. The TiO_2 nanorod dispersion or P25 powder were then added to the polymer solution, in a drop-wise / incremental fashion over 30 min.

The blend was initially stirred, then subjected to ultrasonic treatment to break-up nanoparticle agglomerates and to facilitate good dispersion within the matrix. Sonication was initially carried out in an ultrasonic bath (Grant Ultrasonic Bath MXB6, UK), for 30 – 60 min, followed by the use of an ultrasonic probe (U50, IKA Labortechnik, Staufen, Germany). Such high energy treatment is commonly used to achieve significant improvement of dispersion. The potentially undesirable side-effect is physical damage to the nanorods, such as fracture or defect formation, as well as scission of polymer chains. Ultrasound damage is known to occur with carbon nanotube dispersions[337]; although it is unlikely that the smaller titania nanoparticles undergo equivalent damage, ultrasonic probe treatment was limited to no longer than 5-10 min, as a precaution.

The solution was then cast onto a solid substrate, either onto glass microscope slides (25 mm x 75 mm) or into a PTFE mould (35 mm x 120 mm). Usually 2-3 ml of solution was used for the former and larger amounts (>20 ml) for specimens cast in mould. For a range of different filler-to-polymer ratios, the total solids content in the blends was kept constant at values already identified as optimal for the two pure polymers, i.e. 4 wt% and 8 wt% for PDLLA and PMMA, respectively. Additionally, the amount of polymer used per loading was fixed, which results in different absolute solid content per unit volume. In order to achieve uniform film thickness, the casting volume was adjusted appropriately, on a dry mass basis. As an illustration, consider the following three samples, assuming that the combined weight content of the polymer and the filler is fixed at 4 wt%:

	Sample 1	*Sample 2*	*Sample 3*
	Pure PDLLA	5 wt% composite	10 wt% composite
	2 g PDLLA	2 g polymer	2 g polymer
Filler:	0 g	0.105 g	0.222 g
Total comp.:	2 g	2.105 g	2.222 g
Total blend:	50 g	52.625 g	55.55 g
Normalised:	***1***	***1.05***	***1.11***
(wrt. PDLLA)			
Measured			
film thickness:	0.33±0.01 mm	0.29±0.01 mm	0.31±0.01 mm
(cast in moulds)			

The normalised values (1, 1.05, 1.1, etc.) were referred to as a mass adjustment factor, which was taken into account when adjusting the volume. For example if 2 ml of pure polymer sample were cast, then ~2.1 ml of 5 wt% composite sample would be cast. The assumption made is that the density of the solution does not change, so that the mass factor can be directly used as an approximation for the volume adjustment factor, which is not strictly true (TiO_2 density ~3.9 g cm^{-3}, polymer density ~1.2-1.3 g cm^{-3}), but introduces only a small error given the low absolute solids content and greatly simplifies the calculation.

During casting it was found that PMMA nanocomposite films adhere very strongly to the glass slides and were prone to cracking when peeled from such surfaces. Therefore, casting films into the PTFE mould was found to be a simple way of obtaining free-standing films. The deep PTFE moulds also allowed films with several hundred μm thickness that were more suitable for mechanical characterisation. The depth of the moulds allows casting greater volumes of the composite per unit area as opposed to casting on glass slides.

The ultrasonication, casting, and solvent evaporation stages are strongly influenced by the viscosity of the solution. Having a solution of lower viscosity is beneficial during ultrasonication, as cavitation (and hence mixing) is enhanced at low viscosities. Conversely, a higher viscosity is desirable during the casting and solvent evaporation stage, as increased viscosity stabilises the liquid surface and prevents formation of 'ripples' and uneven film surfaces. Most of the solvent is removed by natural evaporation, usually overnight. Chloroform, although an excellent solvent for the polymers used, is also a highly volatile solvent (b.p. ~62°C, vapour pressure ~26 kPa at 25°C), making it necessary to reduce its evaporation rate as much as possible. Suitable control was achieved by covering the cast films with a Petri dish, thus raising the chloroform vapour pressure over the sample surface. In order to facilitate residual solvent removal, the almost dry films were placed into an oven at 30°C for a week.

In addition to the composite films, pure polymer films and, in some cases, polymer with oleic acid (OA, 90:10 ratio by mass) films were cast as controls. The reason for adding specifically 10 wt% of oleic acid to PDLLA and PMMA was because this value was estimated as the highest content of oleic acid that could be expected in composite films with a very high TNR loading (40 wt% TNR). The PMMA and PDLLA nanocomposites were prepared exclusively using TNR with OA as a structure directing agent, hence the OA controls. The TiO_2 nanorods used for fabrication of TNR-PMMA and TNR-PDLLA nanocomposites (03/2005 - 03/2006) were prepared by Dr. Sabina Chyła using hydrolytic and nonhydrolytic sol-gel techniques. One set of TNR-PMMA composites was prepared towards the end of the project (09/2007), using particularly well-dispersed batch of nanorods synthesised by the author in accordance with the procedure described in section 3.2.4; this set will be discussed in more detail in Chapter 5.

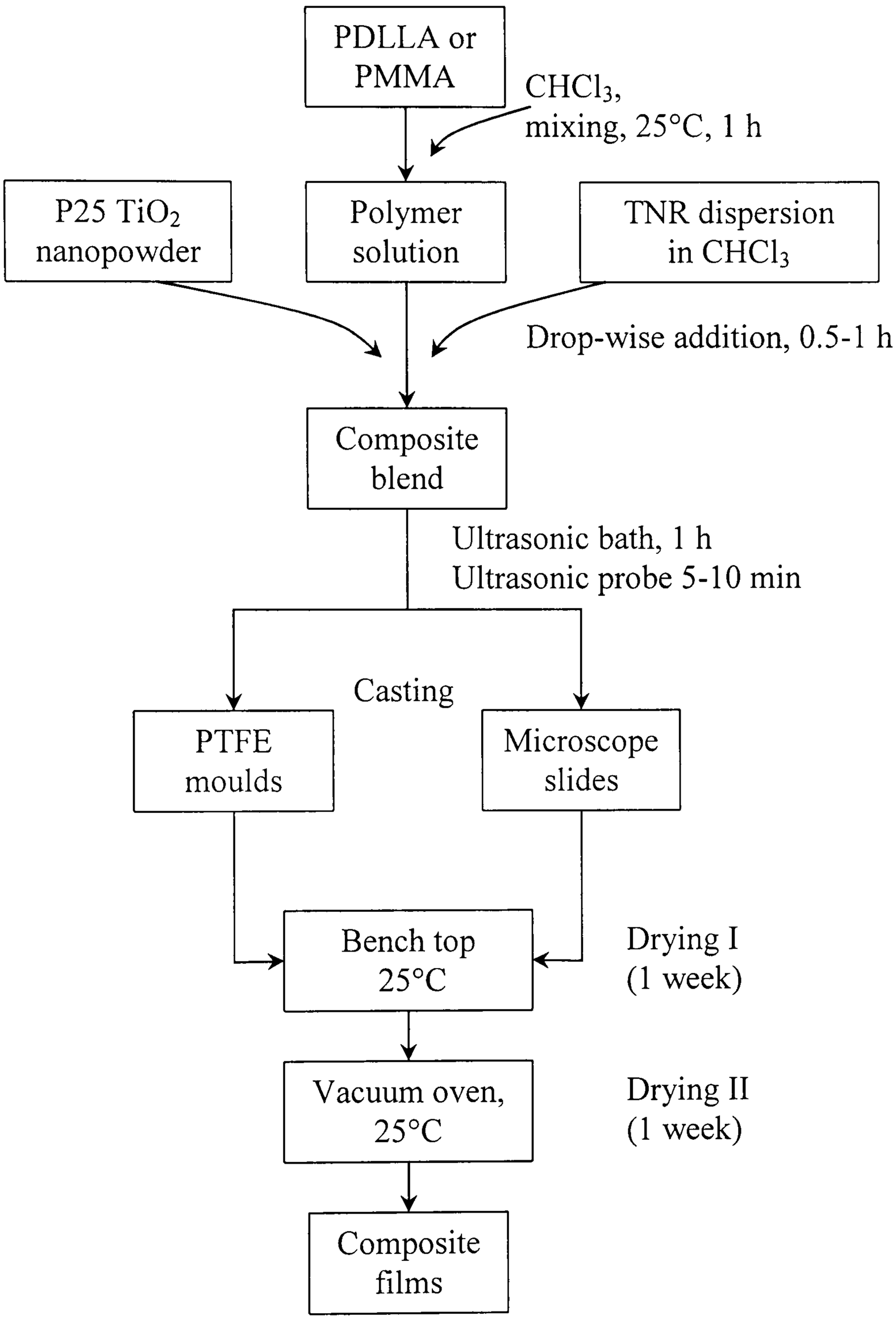


Figure 31 – Fabrication of TiO_2 – PDLLA / PMMA composites

3.5.2 Processing of the PVA composites

PVA composites were processed in a similar manner to PDLLA / PMMA composites (Figure 32). PVA (2 g) was dissolved in water at 80°C, stirred magnetically in a sealed flask for at least 1 h, before adding stabilised aqueous TiO_2 nanorod dispersions (stabilised with 70 mM and 170 mM of TMAH for TNR_{TOPO} and TNR_{OA}, respectively) drop-wise, using a syringe pump, over a 0.5-1 h period. Amounts added depended on the desired loading fraction of the nanorods in the final nanocomposite film. The total TNR-polymer solids content in the blend solution was adjusted to 5 wt%, which was found to optimise the processability. The investigated range of TiO_2 nanorod loadings was 1, 5, 10, 20 and 30 wt% for TNR_{TOPO} and 1, 5 and 10 wt% for TNR_{OA}. In all cases, the nanorod dispersions mix readily with the polymer solution without any particle precipitation. TNR nanocomposite solutions were well-mixed using a magnetic stirrer for a further 1 h at 80°C, before casting 2-3 ml on microscope glass-slides (25 x 75 mm) and about 20-30 ml in poly (tetrafluoroethylene) (PTFE) moulds (35 x 120 mm). The exact amounts cast were varied according to different TiO_2 loadings such that the cast films are of approximately the same thickness, in the same manner as described in section 3.5.1. The films on glass were covered with a Petri dish and left to dry at ambient conditions for a week, while the PTFE moulds were left in an oven filled with silica gel and dried at 40°C over several days. The silica gel was regenerated every day, by heating at 120°C for 2 h. All samples were further dried for a week in a P_2O_5-filled desiccator (0% RH) at room temperature to ensure complete water removal.

Films of pure PVA and PVA with TMAH were also cast to provide a suitable control. The amount of TMAH in the latter controls was added such that it corresponds to amounts present in the respective TNR_{TOPO} or, upon interpolation, TNR_{OA} filled samples. Films with commercial anatase 5 nm nanoparticles were also prepared, in order to investigate the dispersion and optical properties in comparison with nanorod-filled composites. Anatase powder was dispersed in a small amount of water, using ultrasonic treatment and this semi-stable dispersion was slowly added to the polymer solution, in the same way as described for TNR-PVA nanocomposites. Initial attempts to stabilise the aqueous dispersions of these particles with TMAH were not successful; these composites were prepared without TMAH. The remainder of the processing was identical, except that, in addition to stirring for 1 h at 80°C, the solutions were also sonicated for 15 min in an ultrasonic bath to improve dispersion.

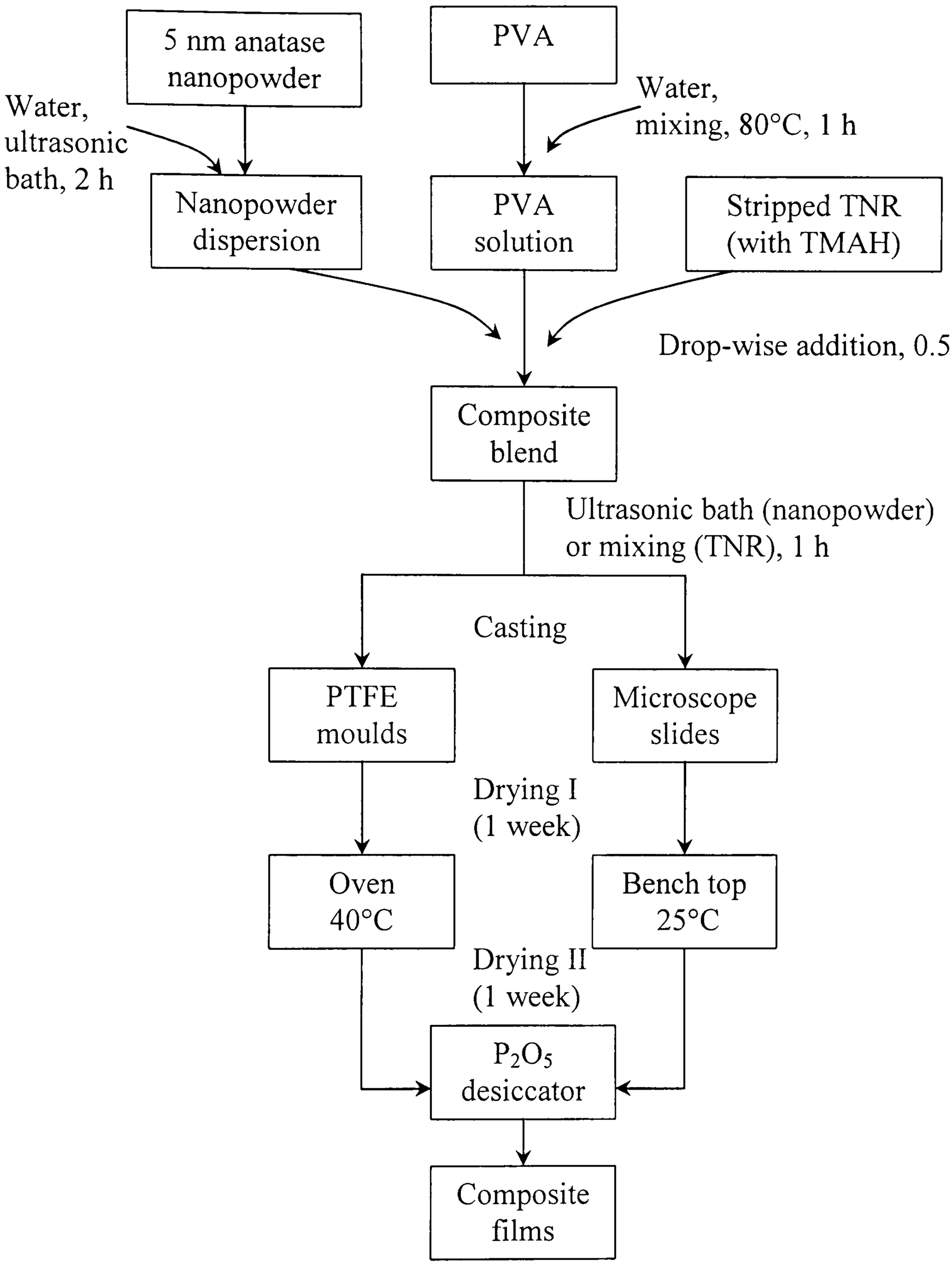


Figure 32 – Fabrication of TiO_2 – PVA composites

The nanocomposites were then characterised either as-prepared or were subjected to UV treatment to assess their stability under UV. The UV treatment was performed on PDLLA/PMMA composites under a Spectroline Q-22NF/F 40 W UV lamp (Westbury, NY, USA), emitting at 365 nm, while the PVA composites were illuminated with the 100 W UVP UV-A lamp mentioned at the beginning of section 3.3. The distance from the lamp to the samples was 15 cm in all cases.

3.6 Analytical techniques used for materials characterisation

3.6.1 Analysis of the nanomaterial morphology using Transmission Electron Microscopy (TEM)

TEM has become a vital technique in nanomaterials research, since it can reveal the specimen structure at the sub-nanometre level. Indeed, the current TEM facilities (e.g. FEI TITAN 80/300) resolve atomic features down to 0.14 nm. Please refer to Williams and Carter[338] for a comprehensive treatise on the theoretical aspects of TEM. Morphology and dimensions of the nanoparticles were studied using a JEOL 2010 instrument (JEOL, Tokyo, Japan) operating at 200 kV in bright field imaging mode. The samples were prepared by applying a dilute particle dispersion in chloroform or water onto a holey carbon / copper grid (Agar Scientific, Stansted, Essex, UK) and allowing the solvent to evaporate.

3.6.2 Analysis of the composite morphology using Scanning Electron Microscopy (SEM)

SEM was used to analyse the surface morphology of the nanocomposite films. A high-energy electron beam is focused onto the sample surface, causing interactions with the material. The electrons can backscatter or cause excitations within the material, which results in emission of electrons from the material analysed. Most importantly, secondary electrons are emitted, which are used principally for topographic contrast in the SEM, i.e. for visualization of the surface texture and roughness. A secondary electron signal can resolve surface structures down to the order of 10 nm or better[339]. Composite samples were cryofractured and chromium sputtered before being observed with a LEO Gemini FEG-Scanning Electron Microscope (LEO Elektronenmikroskopie, Oberkochen, Germany) operating at 7 kV.

3.6.3 Powder X-ray Diffraction (XRD) for structural, crystallinity and phase identification of TiO_2 nanomaterials

XRD is a crystallography technique whereby an X-ray diffraction pattern produced by the sample is analysed to reveal its crystallinity and crystal lattice[340]. The fundamentals of the XRD method can be found, for example in a textbook by Giacovazzo et al.[341] In relation to this work, XRD was used to identify which, if any, crystallographic modification of TiO_2 was present. X-ray diffraction measurements were carried out on a diffractometer type PW1710 (Philips, Amsterdam, Netherlands) using Cu-Kα radiation with $\lambda = 1.5406$ Å. Finely ground TNR powder was placed on the sample holder and a few droplets of acetone were added to distribute the powder uniformly. The XRD measurement was carried out on the sample with the double of the diffraction angle 2θ ranging between 10° and 70° in 0.02° or 0.04° increments and scanning step time of 1 s.

3.6.4 Structural and phase identification analysis of TiO_2 nanomaterials using Raman spectroscopy

In Raman spectroscopy, a monochromatic (laser) beam is passed through a sample and the radiation scattered is monitored. A fraction of the incident photons interact with the sample molecules, give up some energy, and emerge as scattered light with lower energy and frequency – Stokes radiation. Another fraction of incident photons interact with excited molecules, hence collecting energy and emerge with higher energy and frequency, called anti-Stokes radiation[342]. The very small changes in frequency between incident and scattered radiation are very specific to the chemical bonds in molecules, which makes Raman spectroscopy a useful technique to identify structure and crystal phase of the sample. As opposed to XRD, which can give relative measure of contribution of different crystal phases, Raman spectroscopy can only be used to identify which phase is present.

Raman spectroscopy was carried out using LabRam Infinity instrument (Horiba Jobin Yvon Ltd., Edison, NJ, USA) with a 633 nm He-Ne laser (red). Spectra were collected from thin powder films, about 5-10 mg on glass slides in 100-1000 cm^{-1} range and compared with reference data[343]. For each sample, three measurements, with an average of two scans each, were collected.

3.6.5 *Analysis of the particle dispersion in the nanocomposites using optical microscopy*

Optical microscopy is a useful tool for observing the structure of materials at the micrometre scale. Due to the 'large' wavelength of photons used (visible light: 400-800 nm), it has a low magnification power for studying nanometre-sized objects, but can nevertheless be utilised to quickly identify nanoparticulate agglomeration within the matrix. Small scale agglomeration cannot be observed, so a satisfactory appearance in the optical microscope is 'necessary but not sufficient' evidence of good dispersion. Agglomeration can be observed under microscopes operating in light-transmission mode, while reflectance microscopy can show composite surface morphology at the micrometre level. The overall simplicity and non-destructive nature of optical microscopy makes it a suitable analytical method for preliminary study of the nanocomposites. A light-transmitting microscope Olympus BX2 (Watford, Hertfordshire, UK) was used, equipped with a CCD camera for image capture.

3.6.6 *Analysis of optical properties of titania dispersions and composites using UV-Vis spectroscopy*

UV-Vis spectroscopy was already mentioned in some detail earlier as a technique used to assess photocatalytic activity of titania dispersions. In general, UV-Vis spectroscopy was also used to study optical properties of other samples – nanorod dispersions in nonaqueous solvents, composite films, and their photocatalytic degradation. The technique works by passing monochromatic light through a sample and comparing the intensity of incident light with that transmitted. Samples can be analysed at a single wavelength or a range of wavelengths to give either a single value for absorbance (defined below) or a full spectrum. By using Beer-Lambert law (eq. 9), it is also possible to calculate concentrations of components within a sample if they are not known, assuming that the molar absorptivity can be measured (as described in Section 3.4).

UV-Vis spectra were recorded using a Perkin-Elmer Lambda 950 spectrophotometer (Waltham, MA, USA) in absorbance mode over a scanning range from 300 nm to 800 nm at 2 nm intervals. Liquid samples were placed in a 10 mm path length cuvette (either quartz glass or PMMA) and composite films, either free-standing or on a glass substrate, were attached in front of the cuvette holder. For very poor dispersions, which lead to significant light scattering, an integrating sphere detector was used instead, since it is constructed such that it minimises the scattering effects. For both the integrating sphere and the standard detector, the procedure for the collection of the spectra is identical.

3.6.7 Measurement of composition of TiO_2 nanorod powders and composite films using Thermo-Gravimetric Analysis (TGA)

TGA is a relatively straightforward analytical technique for observing changes in sample weight against temperature, using a very accurate balance, thermal control and temperature monitoring. This method can provide information such as degradation temperatures, absorbed moisture content, relative level of individual components (through variation in decomposition temperatures for different materials), residual solvent, etc. The experiments can be carried out in an inert atmosphere or in the presence of oxygen.

Tests were carried out using a Perkin Elmer Pyris 1 TGA (Waltham, MA, USA). Characterisation of TNR samples was performed to estimate the organic content and also, the pure TiO_2 concentration in liquid dispersions. The high accuracy of the TGA balance makes this technique very useful for such concentration measurements. The general procedure involved placing several mg of TNR powder or 100-120 mg dispersion inside a platinum pan. The sample is initially heated to 110°C under N_2 atmosphere, where it is kept for 1 h to dry the sample / remove the solvent. If a powder dried under ambient conditions is used, the moisture content can be measured during this stage. The gas was then changed to air and heated at a 10°C min^{-1} rate up to 600°C or 700°C. The sample was then held at the final temperature for 20 min before allowing the furnace to cool down.

The TiO_2 content, degradation behaviour, and thermal stability of the composites were also studied using the TGA. Single layer, disc-shaped specimens of the composites (1-2 mg) were dried for 1 h at 110°C in N_2 to remove any water and then heated to 700°C at 10°C min^{-1} in air.

3.6.8 Measurement of the glass transition temperature of the composites using Differential Scanning Calorimetry (DSC)

A common, but not exclusive approach to performing DSC entails subjecting the sample and an inert reference material to heating or cooling in a controlled manner and measuring the heat-flow required to maintain a zero temperature difference between the sample and the reference. Heating and cooling can be achieved in the same chamber (heat-flux) or independently (power-compensation). DSC measures the heat flux as a function of temperature and allows one to measure the melting point, heat of melting, glass transition temperature, curing and crystallisation effects, as well as to identify phase transformations. In this thesis, the focus was on measuring the glass transition temperature of the nanocomposites and the thermal stability of the composites with respect to pure polymer. The instruments were a Perkin-Elmer Pyris Diamond DSC (Waltham, MA, USA) and a TA Instruments Q2000 DSC (New Castle, DW, USA). Aluminium pans were used to hold the disc-shaped samples (5 – 10 mg), which were dried thoroughly in a desiccator over P_2O_5 (0% RH) for several days. The temperature range scanned varied according to the polymer, but typically involved initially heating the sample from ambient temperature up to 200°C at 10°C min^{-1}, cooling it down to ambient temperature at 20°C min^{-1} and repeating this cycle two more times. The results from the first scan are usually not analysed as this scan serves to remove any thermal history from the material.

3.6.9 Measurement of the storage modulus and the glass transition temperature of the nanocomposites using the Dynamic Mechanical Thermal Analysis (DMTA)

DMTA involves applying a forced periodic stress to the composite film sample and recording the resultant strain as a function of temperature and frequency. The most common properties that can be studied with this technique are the modulus (stress divided by the strain resulting from the applied force) and glass transition temperature. This technique is particularly powerful for experiments with polymers, due to their time-variant properties, whereby the response of the material can be out-of-phase from the applied stress. Thus, the instantaneous modulus is resolved into two parts – in-phase and out-of-phase modulus. The former is the storage modulus, representing the elastic response of the material and the latter is the loss modulus, representing the viscous response. Clearly, for a completely elastic material, the storage modulus would be equal to the total modulus measured and for a completely viscous material the loss modulus would equal the total. A useful indication of the energy loss in the material is the ratio of the loss to storage modulus *tan δ*, sometimes referred to as the dampening factor. For further reading, please refer to Chapter 21 of the Handbook of Polymer Testing[344].

Finally, the choice of the testing geometry is very important in doing such measurements, so that for thin films, a tensile mode is usually preferred, while for thicker samples, the measurements are taken in bending. The measurements were performed using a Triton DMA 200 (Triton Technology, Keyworth, Nottinghamshire, UK) instrument, in 3-point bending mode, at 1 Hz and 10 Hz frequencies. Experiments were carried out across a temperature range of -30°C to 70°C for PDLLA, -50°C to 120°C for PMMA and 0°C to 120°C for PVA nanocomposites.

The samples (length: 20 mm; width: 4 ± 0.1 mm; thickness: 0.2 ± 0.05 mm) were left in a closed desiccator over $MgCl_2 \cdot 6H_2O$ at room temperature (33% RH) for a week before carrying out the tests.

3.6.10 Characterisation of the wetting behaviour of the composite films using Drop Shape Analysis (DSA)

The wetting characteristics of a material surface can be assessed by measuring the contact angle between a liquid drop and the surface of the material analysed. Specifically, the contact angle is defined as the angle where the liquid-vapour interface meets the solid surface, (illustrated in Figure 33A) and is specific for a given system. In addition to the contact angle formed between a static liquid droplet and solid surface, advancing and receding contact angles can be measured in a situation where the liquid is constantly added or removed, using a syringe. For further reading on wettability, please refer to a textbook by Berg[345].

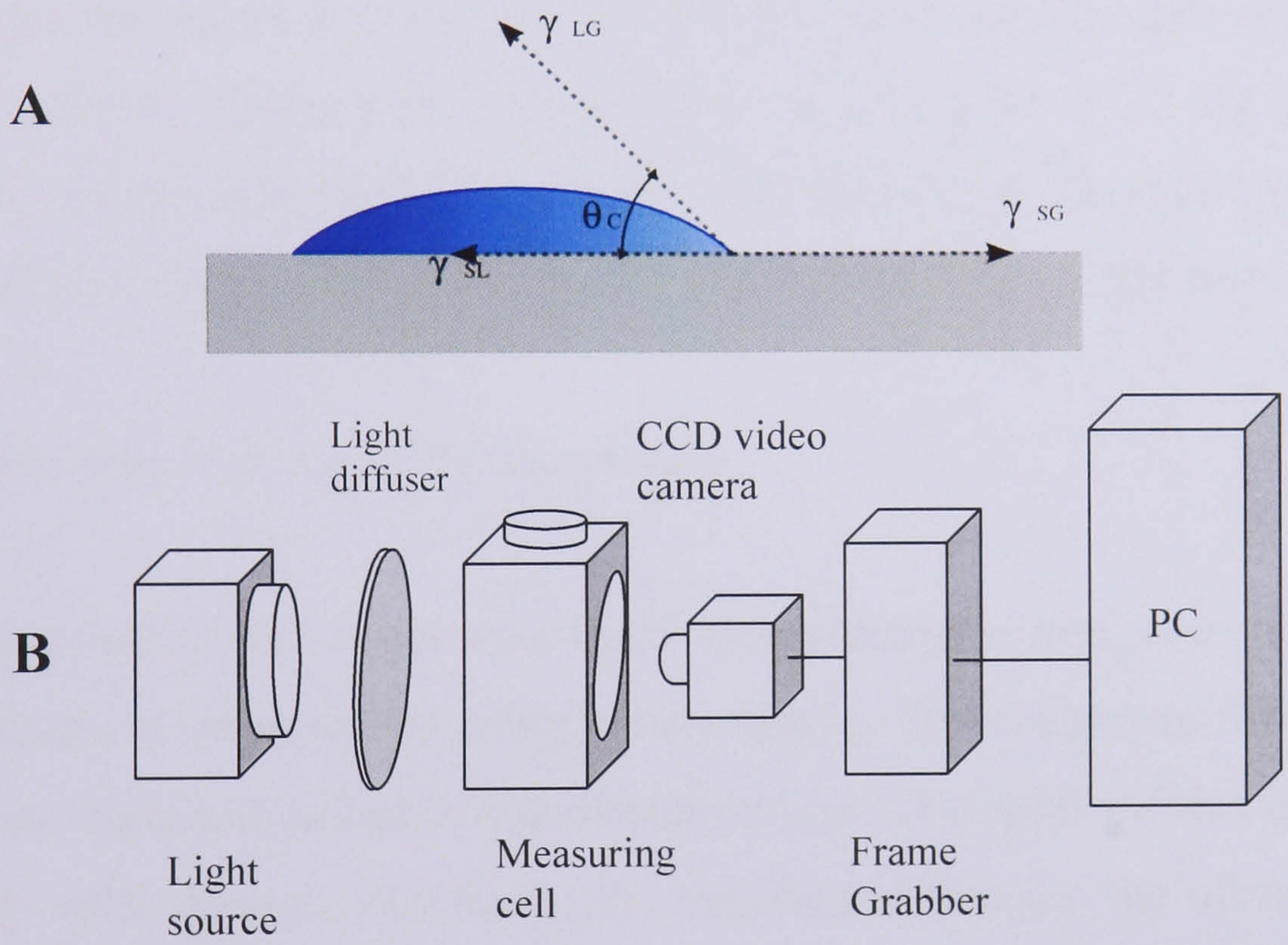


Figure 33 – (a) Contact angle diagram and (b) DSA experimental setup

The Krüss Drop Shape Analysis System DSA10 Mk2 (Hamburg, Germany) was used to measure the contact angle using the Sessile Drop method. The liquid used was water (deionised) with at least five separate measurements taken per sample. This approach involves placing a water droplet using a syringe onto the surface of the material and measuring the contact angle. A CCD camera linked to a computer captures the image of the droplet and the software determines the angle at the three-phase circumference (Figure 33B), by differentiating the slope of the drop border at the three-phase contact point. In essence, DSA is a useful tool for quantifying the hydrophilic / hydrophobic character of a material surface.

3.6.11 Surface chemistry of TNR in aqueous dispersions - ζ-potential from electrophoretic mobility measurements

Electrophoretic mobility measurements of nanorod water dispersions were carried out using a ZetaPALS instrument (Brookhaven Instruments, Holtsville, NY,USA) using the Smoluchowski approximation. Smoluchowski was the first to properly derive an equation for the calculation of the ζ-potential from the electrophoretic mobility:

$$\zeta = \frac{\mu \cdot \eta}{\varepsilon} \qquad (11)$$

where μ is the measured electrophoretic mobility, η is the viscosity and ε is the electric permitivity. Water-based dispersions of nanorods (0.25 mg ml^{-1} TiO_2) were studied, using 1 mM KCl as a background electrolyte. The pH was adjusted by titrating HCl or KOH, with six measurements taken for each pH step.

3.6.12 Mechanical properties of the composites

Mechanical properties such as the maximum tensile strength, elongation at break and Young's modulus were measured using tensile testing. The composite film sample is clamped at two ends and pulled in opposite directions. The applied force is measured as a function of elongation and these two variables determine the aforementioned mechanical properties according to:

- Tensile strength: $\sigma = \frac{F}{A}$ (12)

  where F and A are the applied force to the sample and cross-sectional area of the sample, respectively

- Strain: $\varepsilon = \frac{L - L_0}{L_0}$ (13)

  where L_0 and L are the initial sample length and the sample length after a given time of extension, respectively

- Young's modulus: $E = \frac{\sigma}{\varepsilon}$ (14)

  Young's modulus was measured in the initial, linear regime, before the material reaches the yield point.

Measurement of these properties of the composite films was carried out using a Linkam TST 350 tensile testing system (Linkam Scientific Instruments, Tadworth, UK) under ambient conditions and with a 200 N load cell. The specimens were cut and tested in accordance to ISO 527-3 and with at least five measurements per sample. The testing speed was set at 2 mm min^{-1}. The samples were dumb-bell shaped (gauge length: 21.5 ± 2.2 mm; width: 4 ± 0.1 mm; thickness: 0.2 ± 0.05 mm) and pre-conditioned as described already for DMTA measurements.

3.6.13 pH measurements of the aqueous titania dispersions

The measurement of the pH of the aqueous titania dispersions was required for a number of experiments throughout the project. The measurements were obtained using a VWR Symphony SB90M5 multi-meter, with a glass pH combination electrode. Calibration was performed prior to measurements, according to NIST standards, with five buffered calibration solutions (pH 1.68, 4.01, 7.00, 10.00 and 12.45). All samples were constantly stirred and the average of three consecutive measurements was taken.

4. Synthesis and modification of TiO_2 nanorods*

4.1 Introduction

The objective of the work covered in this chapter was to develop synthesis routes for fabrication and modification of anatase TNRs, to be used in polymer composites. A number of viable synthesis procedures have already been developed within the group. Although initial work in this thesis focused on acclaimed hydrolytic synthesis route reported previously in the literature[6], non-hydrolytic reactions were the main focus as they offer better nanorod crystallinity and greater versatility of surface chemistry. Two TNR products were obtained using non-hydrolytic synthesis, both organic functionalised.

A key outcome reported in this chapter is a novel method for 'self-cleaning' of nanorod surface, using UV to remove the organic ligands, and allowing transfer from the original dispersions in organic solvent to water. During this process the nanorod morphology and crystallinity are unaffected, providing a major advantage over conventional methods that usually rely on thermal oxidation. After UV-treatment, the TNRs are only marginally stable in aqueous dispersions, due to weak particle agglomeration; stabilisation mechanisms were therefore studied in detail. Based on the well-established use of $(CH_3)_4N^+$ cation in hydrolytic syntheses, for various purposes, the same ion was explored as a means of stabilising TNR synthesised via non-hydrolytic mechanism, for the first time.

Lastly, the photocatalytic activity of TNR, although beneficial for removal of organics post-synthesis, is expected to compromise durability and integrity of the resulting composites if they are exposed to UV (e.g. outdoor use). In order to address this potential problem, and to provide a general strategy for functionalisation, siloxanes were applied to nanorod dispersions; previous studies have shown that a dense silica layer can effectively quench any radical formation at the titania surface. Here, the goal was to explore the effectiveness of a thin silica layer whilst controlling the surface chemistry and retaining a high degree of dispersion.

---

* Section on synthesis and stripping of TNR_{TOPO} formed the basis of a paper in the *Journal of Materials Chemistry,* April 2008 (DOI: b804468f).

4.2 Results and discussion

4.2.1 Hydrolytic synthesis of TiO_2 nanorods

During initial development TNRs were synthesised using a fast hydrolysis method, using $Ti(OPr)_4$ as a precursor and oleic acid as a growth-directing ligand, previously reported by Cozzoli et al[6]. Due to OA functionalities at the surface, these nanorods can be well dispersed in chloroform and such dispersions remain stable for several hours. A typical TEM image of nanorods (Figure 34) shows clusters of high aspect ratio single-crystals, 14 ± 1.7 nm long and 2.2 ± 0.2 nm in diameter.

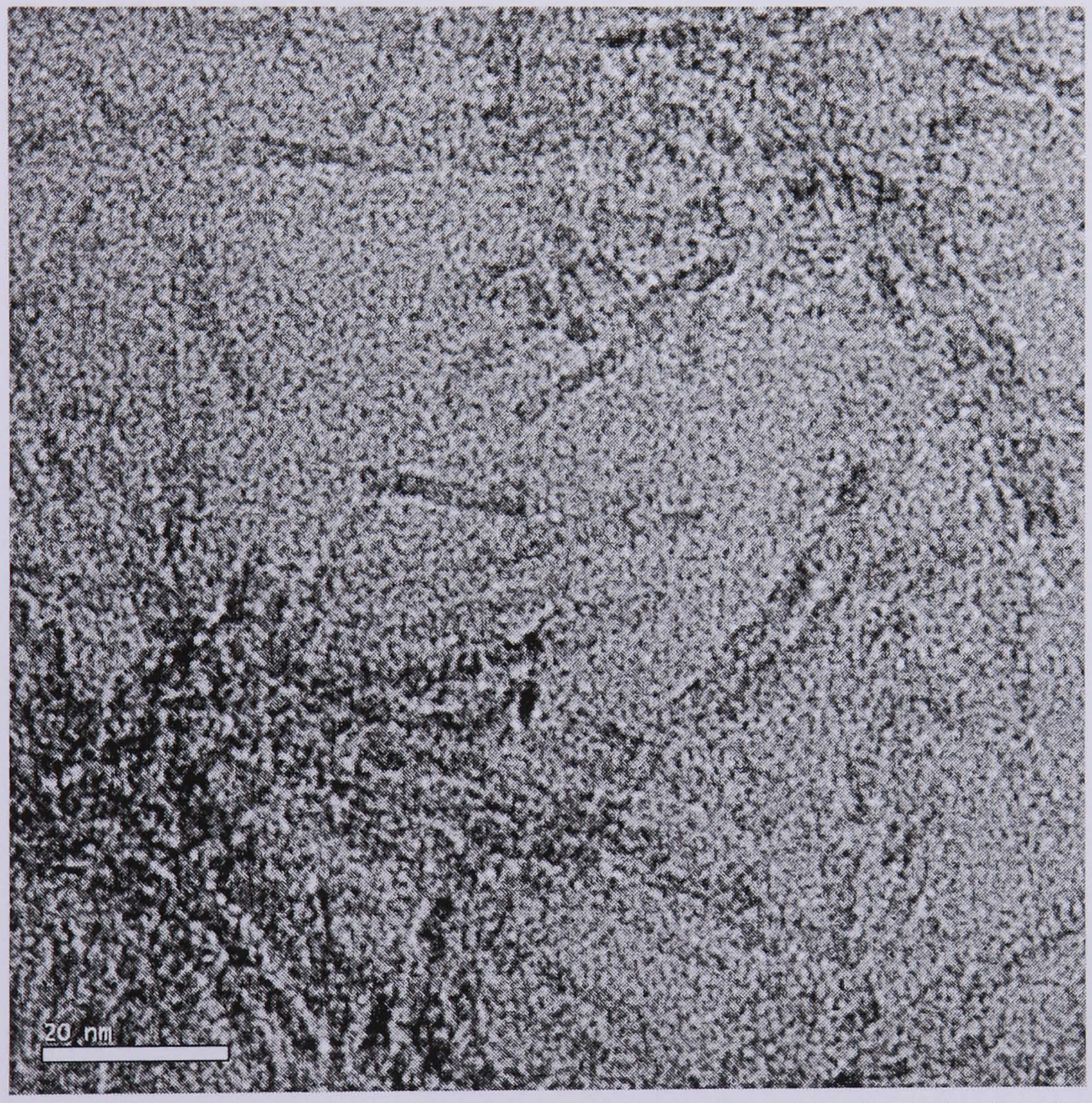


Figure 34 – TEM of TiO_2 nanorods prepared by fast hydrolysis route

The crystal phase of the nanorods was studied using X-ray diffraction and Raman spectroscopy. The XRD pattern (Figure 35) corresponds to the anatase phase and the individual planes are annotated corresponding to the standard anatase diffraction line. The strong intensity and relatively narrow width for the (004) and a comparatively lower intensity of the (200), (211) and (204) peaks imply formation of rod-like crystals that preferentially grow along the anatase c-axis. The Raman spectrum (Figure 36) reveals three peaks at 399 , 513 and 639 cm^{-1}, characteristic of the anatase phase[343]. The peaks have a high intensity, indicative of a highly crystalline material.

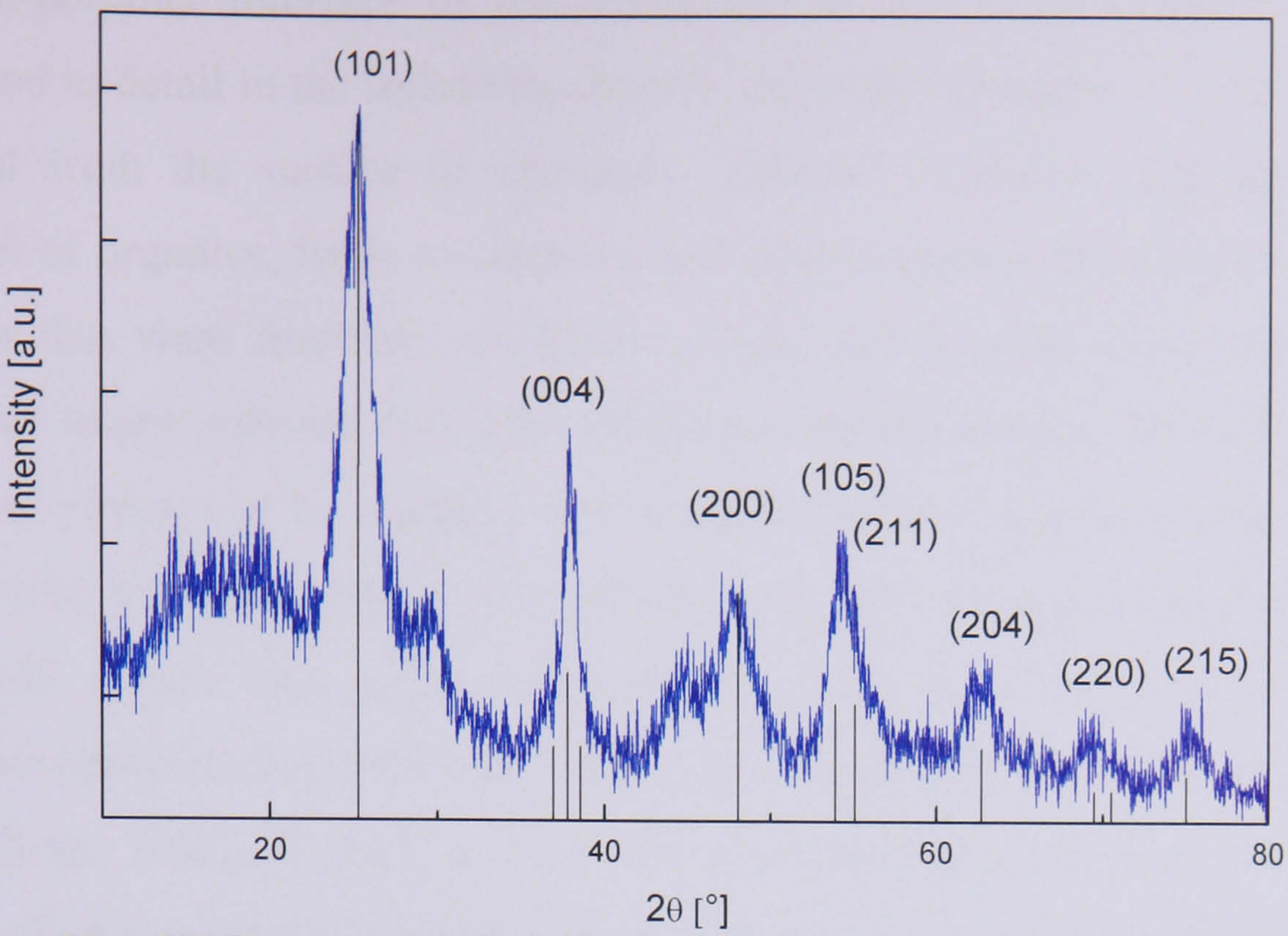


Figure 35 – XRD pattern of TiO_2 nanorods prepared by fast hydrolysis route and standard TiO_2 anatase diffraction lines

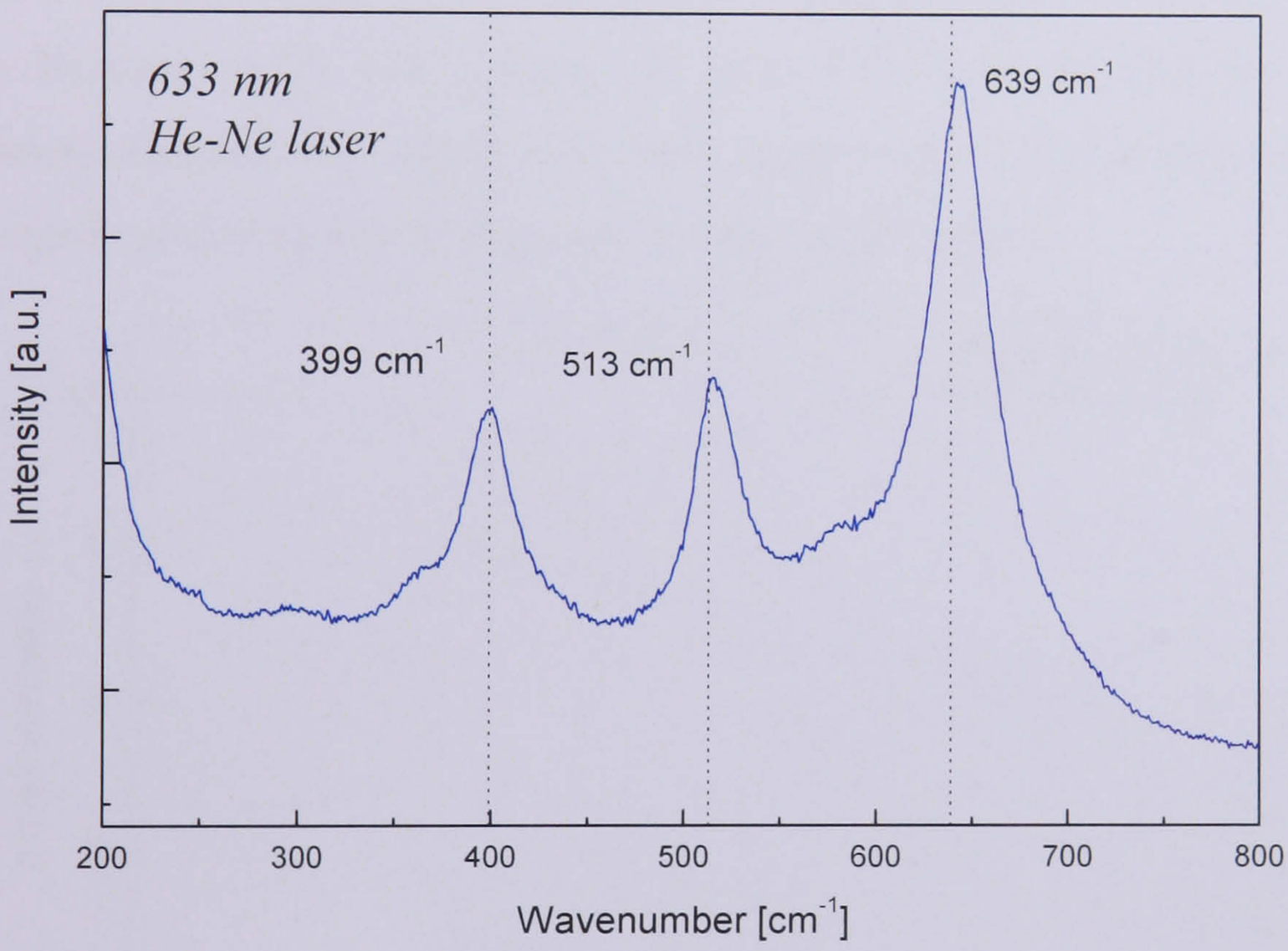


Figure 36 – Raman spectrum of TiO_2 nanorods prepared by fast hydrolysis route

The oleic acid content on the nanorod surface can be estimated using TGA and was found to be generally in the 30-40 wt% range (Figure 37). The observed weight loss is primarily due to oleic acid attached at the surface, but in addition, it is also possible that a certain fraction of reactants remain trapped within the crystal. OA-functionalised TNR from both the hydrolytic and non-hydrolytic (discussed in 4.2.3) routes, cannot be re-dispersed after drying, even at room temperature. In addition to difficulty with TNR re-dispersion from dry powders, the presence of oleic acid at the

nanorod-polymer interface in the composites is not always desirable, as will be discussed in detail in the following chapter, and early attempts were made to affect its removal from the surface of nanorods. Thermal oxidation, although effective in removal of organics, leads to sintering and agglomeration of particles. For example, samples that were thermally oxidised to pure titania using TGA, could not be re-dispersed in any solvent, even after prolonged ultrasonication. Nor was the oleic acid completely removed by washing with alcohol and centrifugation. The results for the as-prepared nanorods (Figure 37) indicate a 30 wt% organic content even after five wash-spin cycles; this result contrasts the report by Cozzoli et al[6], who claim complete removal after three such cycles. As a novel alternative, an attempt was made to purify the TNRs, by sealing a nanorod dispersion in isopropanol in a dialysis tube (Medicell International, London, UK; d=14.3 mm, M_w cut-off 12-14 kDa) and leaving it submerged in 5 l of isopropanol for several days. Isopropanol was purified by distillation every 1-2 days. TGA shows that after six days of dialysis, the organic content decreases to 20 wt% (Figure 37). Due to the slow rate and limited degree of purification, dialysis was abandoned. Self-cleaning by TiO_2 photocatalysis, became the approach of choice and is discussed further in this chapter.

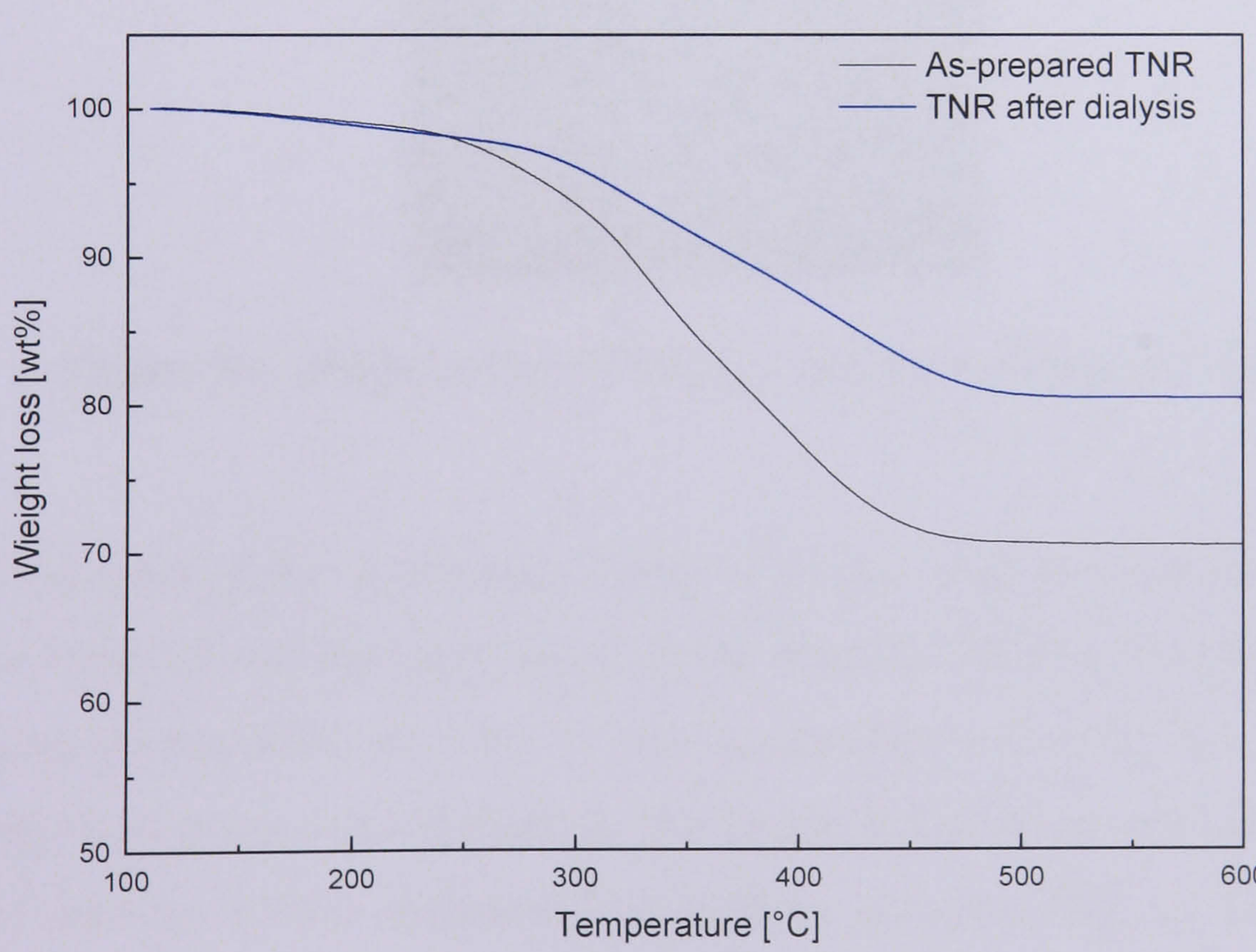


Figure 37 – TGA of the as-prepared TiO_2 nanorods and after purification by dialysis

4.2.2 Non-hydrolytic synthesis of TiO_2 nanorods – trioctylphosphine oxide and dodecylamine ligands

Although OA-functionalised TNRs cannot be re-dispersed upon drying, TNRs grown using TOPO and dodecylamine as structure directing agents can be partially re-dispersed upon drying in non-polar solvents like $CHCl_3$. The availability of a dry powder that can be stored and re-dispersed immediately prior to use is a significant advantage for composite processing. When dry, the powders were very slightly off-white and formed opaque dispersions in $CHCl_3$ (Figure 38).

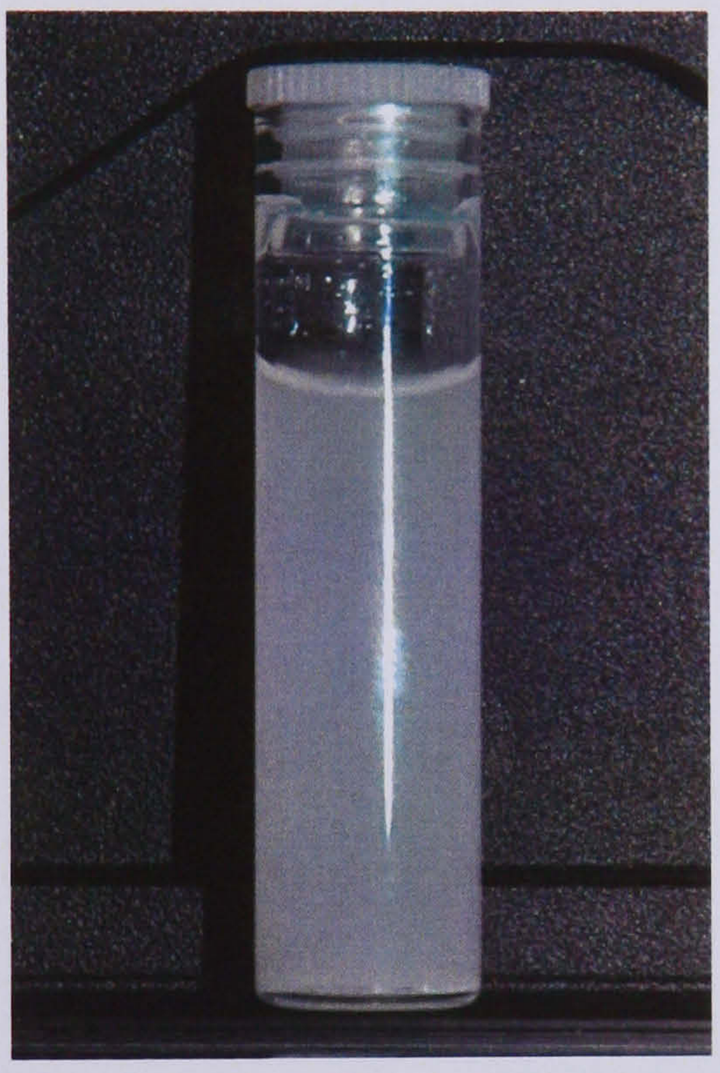


Figure 38 – Dispersion of TNR_{TOPO} in $CHCl_3$ (5 mg ml^{-1} TiO_2)

The TEM images of the as-prepared TNR_{TOPO} product synthesised at 300°C after 20 h show an irregular rod-like appearance of the particles (Figure 39). Mean measured dimensions of nanorods are 4.7 ± 1.1 nm in diameter and 14.9 ± 3.1 nm in length, giving them an aspect ratio of about 3. The crystal lattice planes are clearly visible in HRTEM and the values measured match those corresponding to the (004) in c-direction and (200) in the a-direction of the anatase lattice. Although, as will be discussed shortly, the surface of TNRs is predominantly organic SDAs, these can not be imaged using TEM.

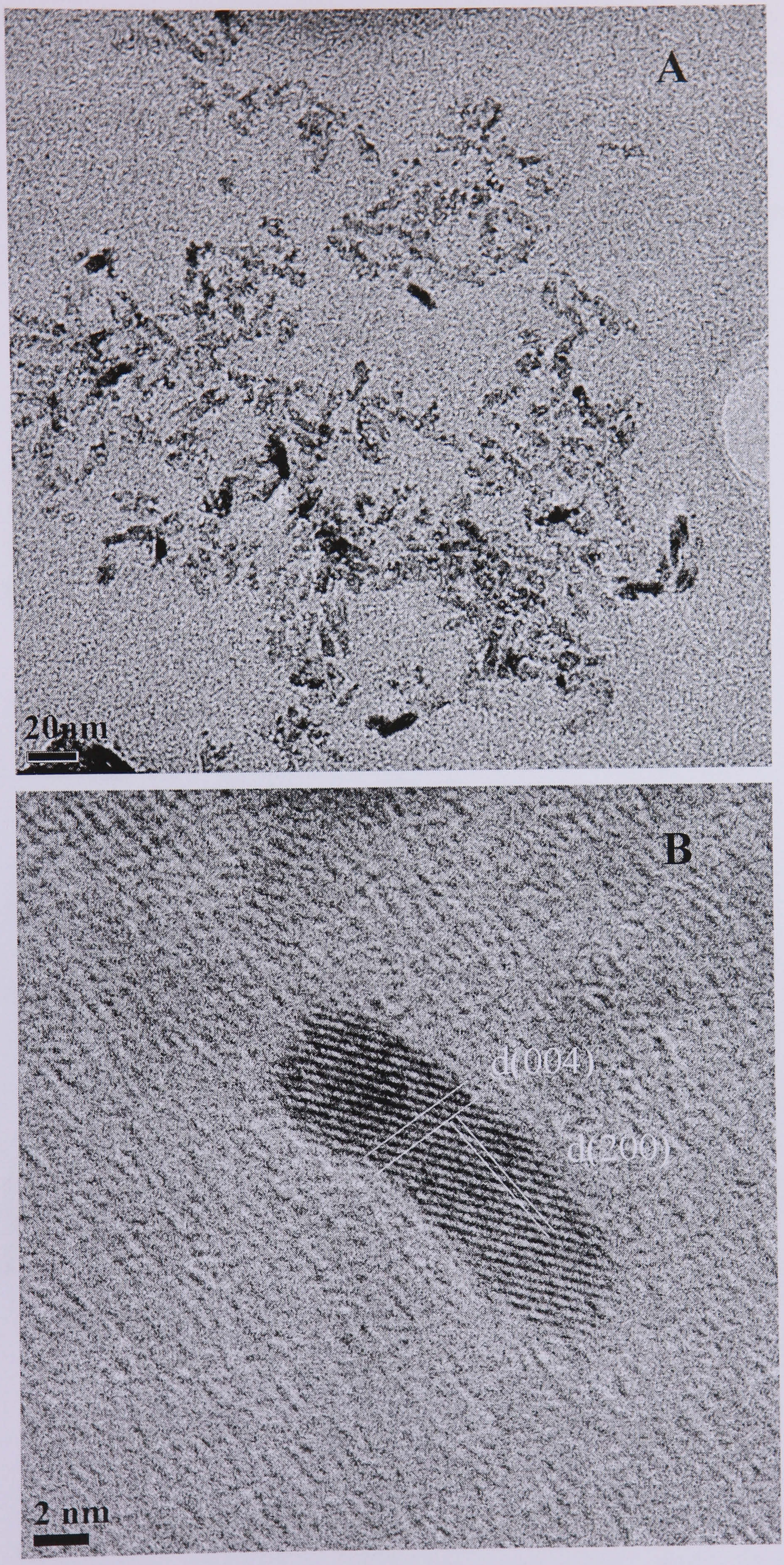


Figure 39 – TEM of TiO_2 nanorods synthesised using nonhydrolytic route with TOPO / dodecylamine ligands: (a) low resolution and (b) high resolution

The XRD data for the TNR_{TOPO} confirm that the product is exclusively anatase (Figure 40); compared to the hydrolytic product (Figure 35), the peak corresponding to the (004) plane has a higher intensity and is sharper for the hydrolytic product, which is consistent with the TEM observation that TNR_{TOPO} are shorter / have a smaller aspect ratio. Raman spectroscopy (Figure 41) also confirms anatase with peaks at 144 cm^{-1}, 197 cm^{-1}, 399 cm^{-1}, 513 cm^{-1} and 639 cm^{-1}.[343]

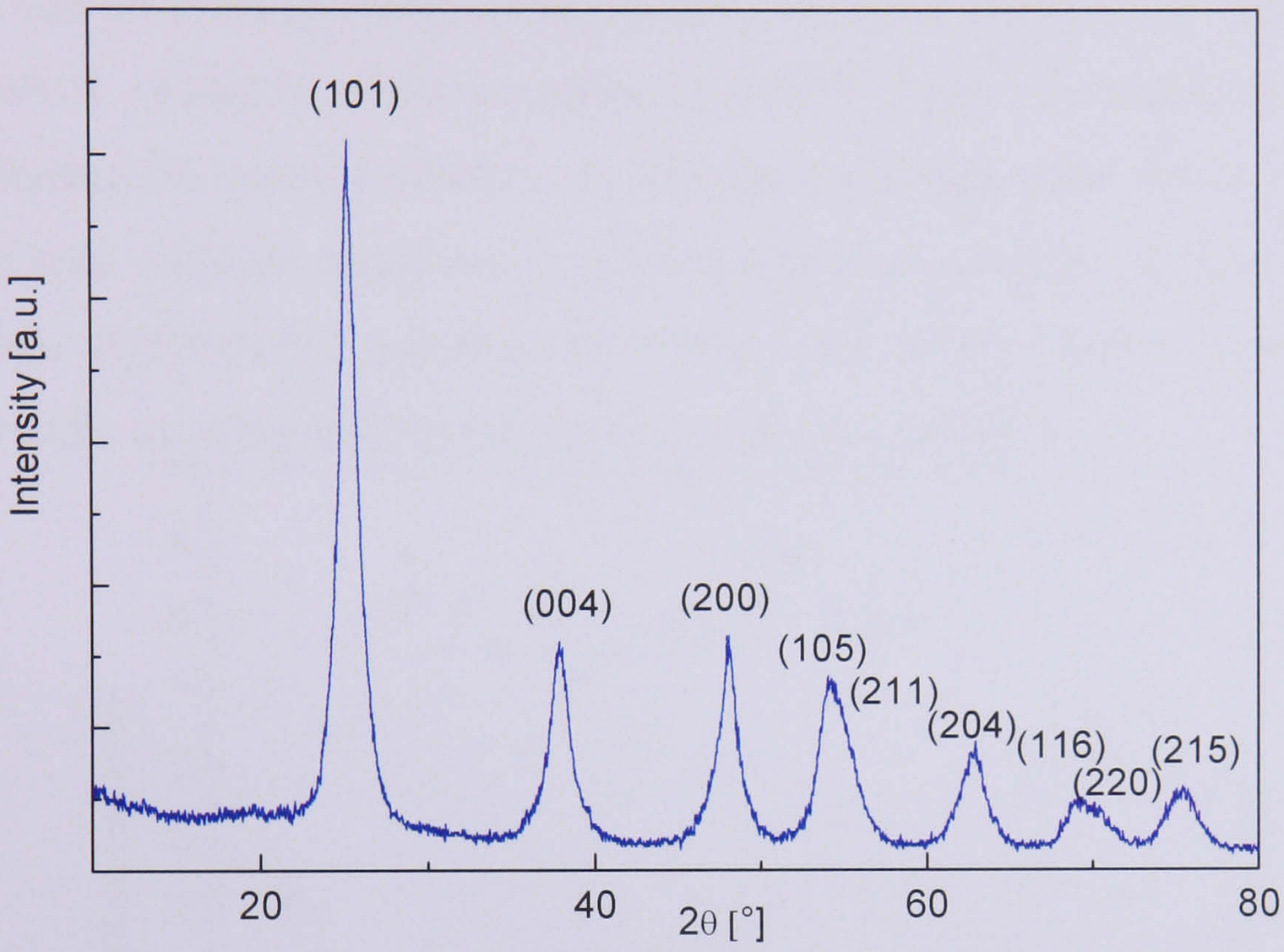


Figure 40 – XRD pattern of TNR_{TOPO}

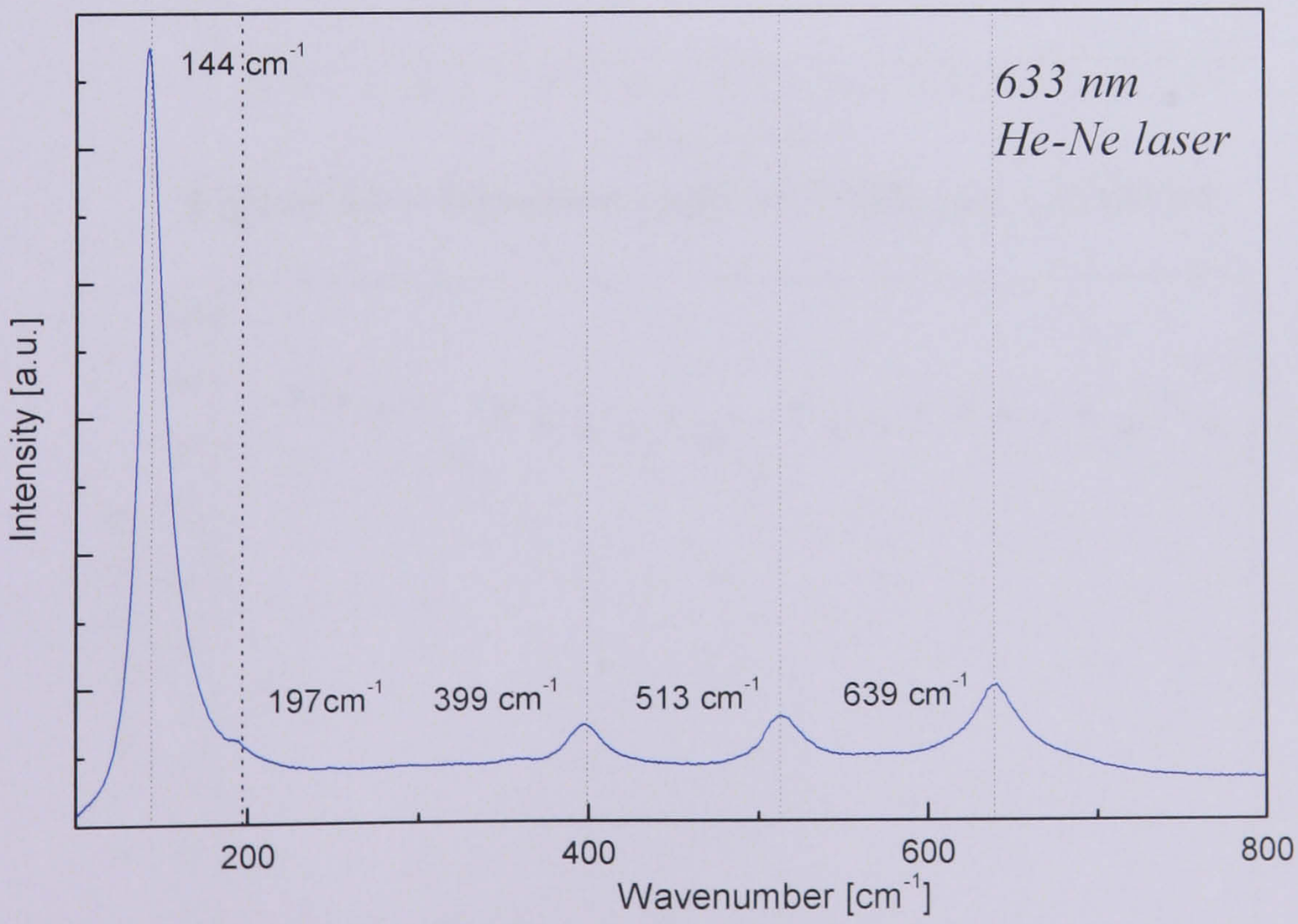


Figure 41 – Raman spectrum of TNR_{TOPO}

The TNR_{TOPO} synthesis route provided the bulk of the nanorod filler for the composite studies; a few basic details about the product consistency are therefore useful. Overall, the reaction has been repeated 25 times and the recorded yield was very high (Figure 42). On average, excluding the first two trial runs, the yield was 81.2 ± 7.8 wt%, with a positive trend. The product purity was even more consistent (Figure 43), being on average 83.5 ± 3 wt%. TGA was used to measure the organic content of the nanorod samples and the corresponding curves (Figure 44) show the onset of rapid degradation around 300°C, which is almost complete by 500°C. Typical product mass was around 1 g, including the organic content. An attempt to further scale up the synthesis by a factor of two, perhaps surprisingly did not lead to an increase in recovered product mass, thus significantly reducing the yield (~52 wt%). Further experiments with reaction scale-up were not carried out due to time constraints.

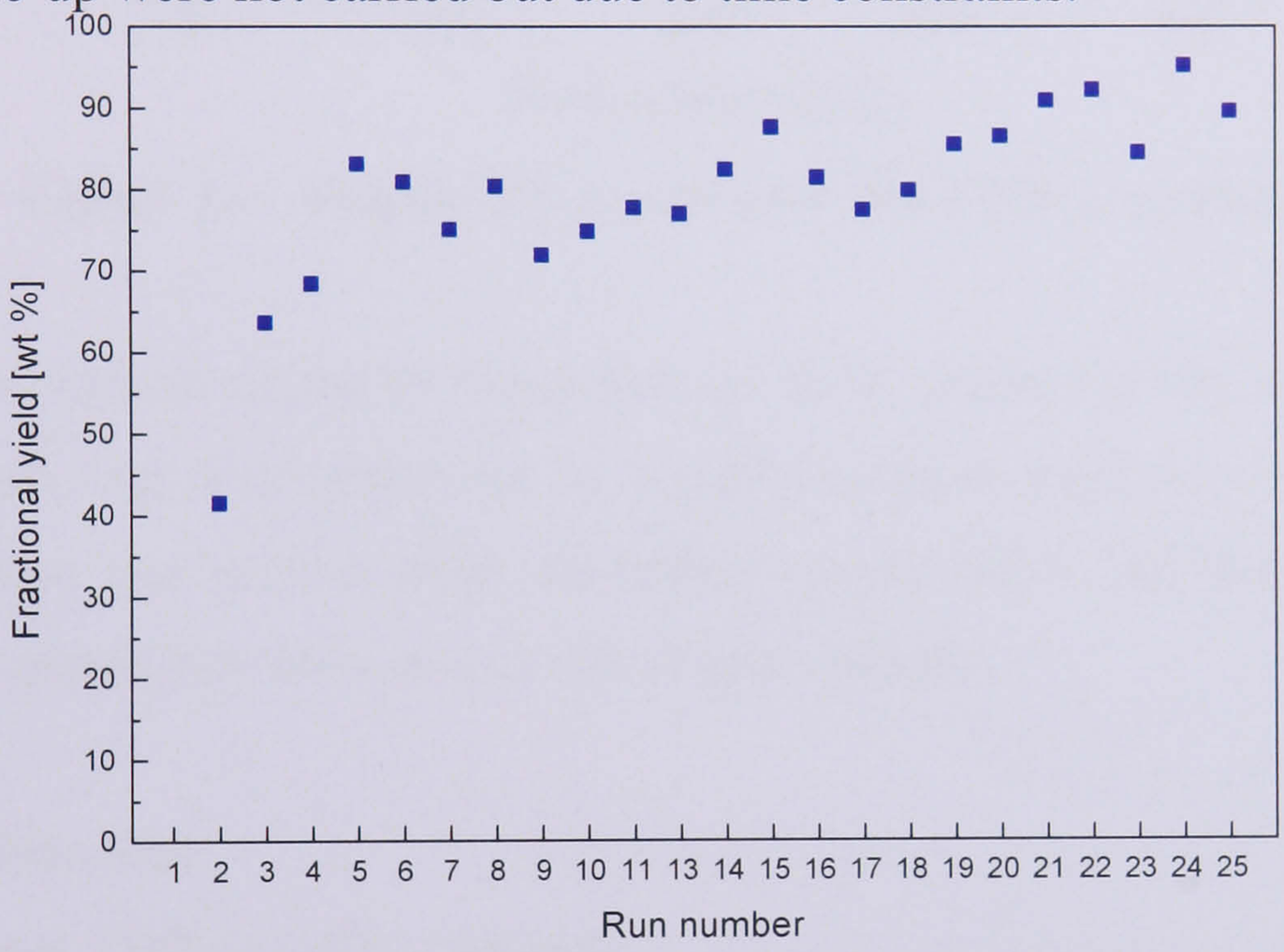


Figure 42 – Reaction yield of TNR_{TOPO} – overview

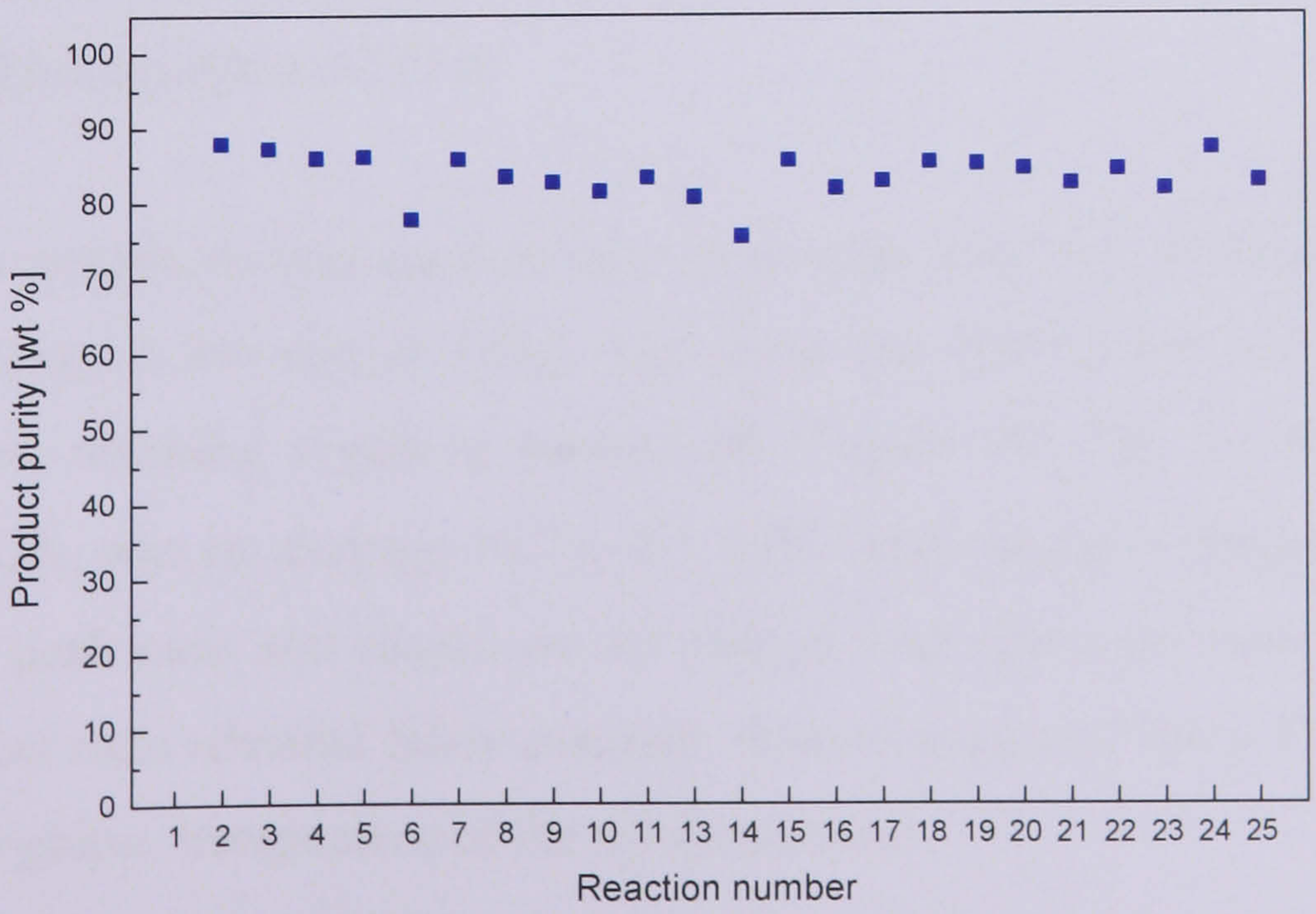


Figure 43 – Purity of TNR_{TOPO} (wt % TiO_2) – overview

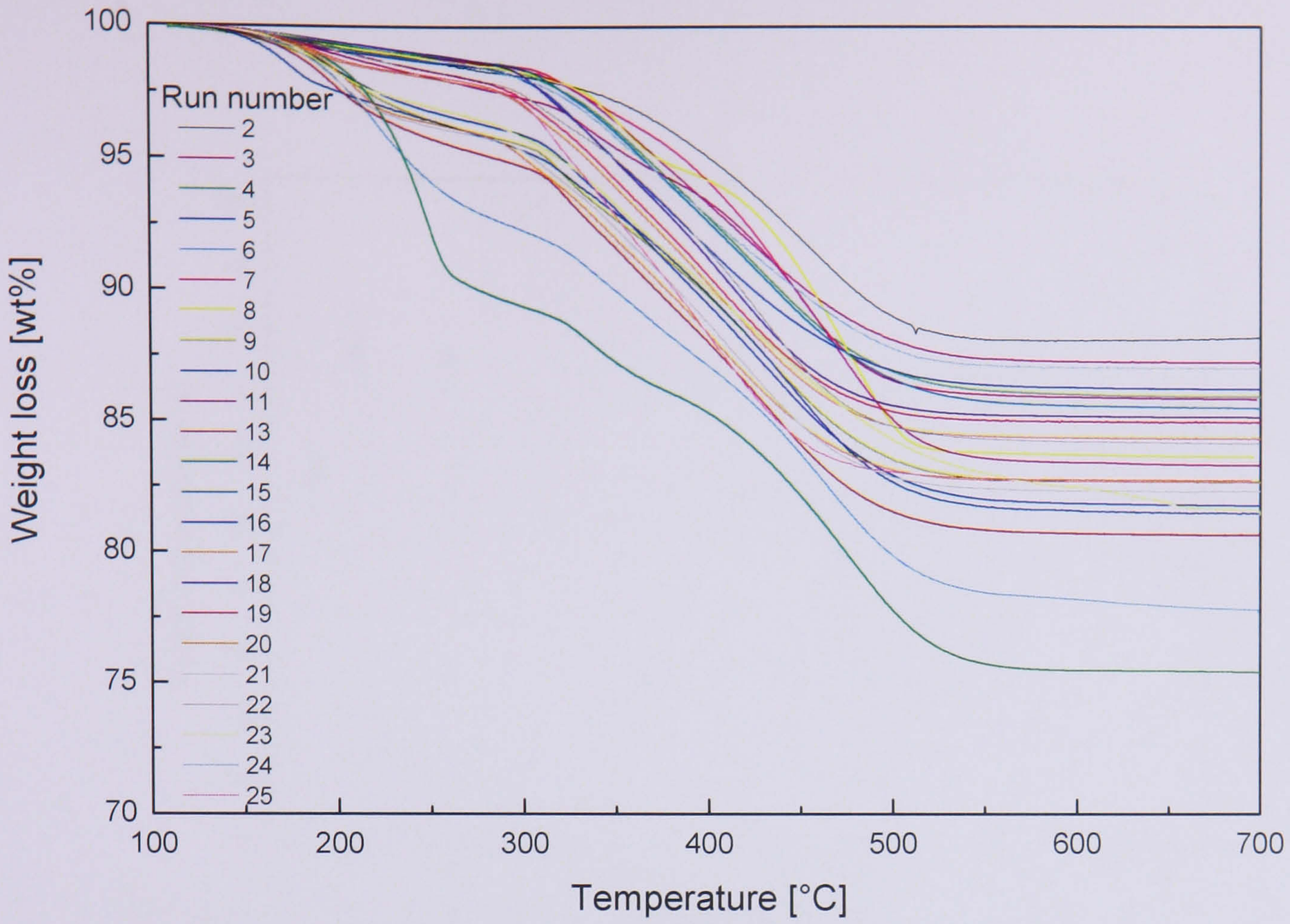


Figure 44 – Typical TGA curve for the TNR_{TOPO} sample

The effect of various synthesis parameters on yield, product purity, crystallinity and particle morphology was carried out by an undergraduate student, Jonathan James, as part of his final year project under the author's supervision. The factors investigated in this study and briefly discussed in this chapter include:

- Reaction time
- Ratio of TOPO to other reactants
- Effect of alkyl chain length in TOPO
- Addition sequence of TTIP

This set of experiments was carried out on a smaller scale (1/3 of original; theoretical yield – 320 mg cf. 960 mg of TiO_2). The yield was observed to increase for longer reaction time, reaching a plateau beyond 8h (Figure 45). The purity, measured by means of TGA, was on average 76.7 ± 8.1 wt%. XRD analysis (Figure 46) identifies anatase; the peak ratio and shapes do not change with synthesis time, suggesting that particle aspect ratio remains fairly constant. Raman spectra (Figure 47) also indicates only anatase phase, irrespective of the synthesis time.

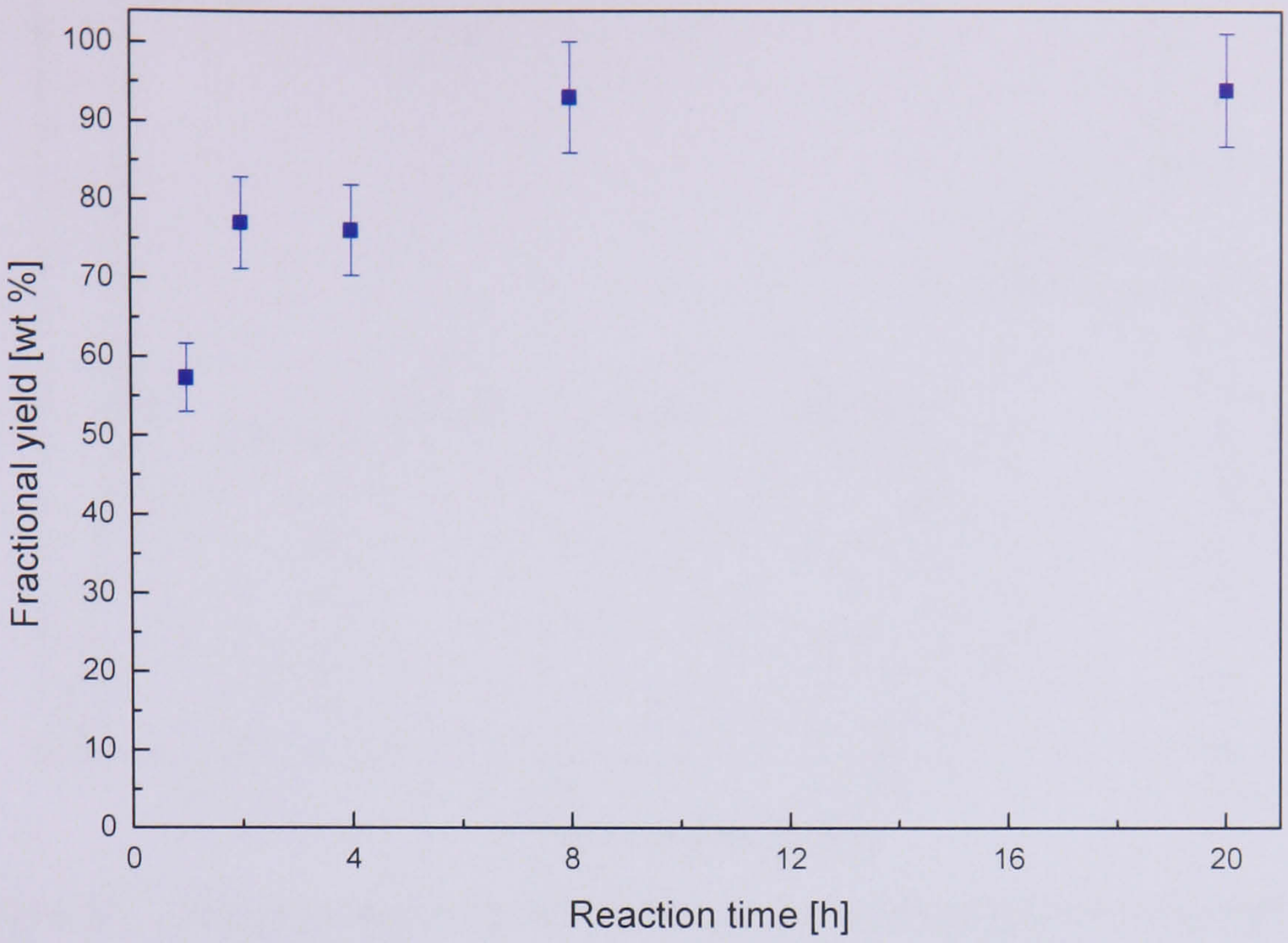


Figure 45 – Reaction yield of TNR_{TOPO} as a function of reaction time

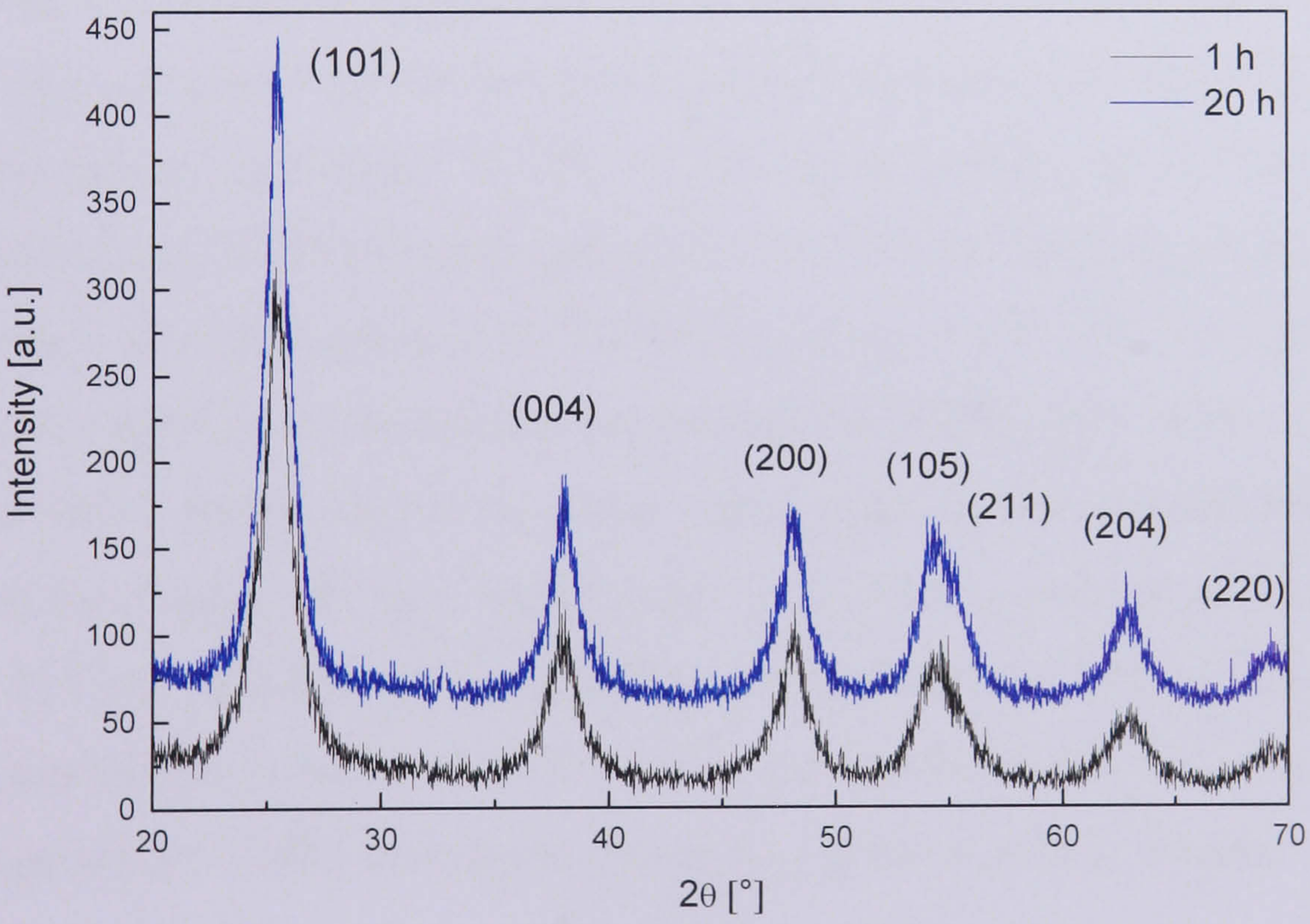


Figure 46 – XRD pattern of TNR_{TOPO} as a function of synthesis time

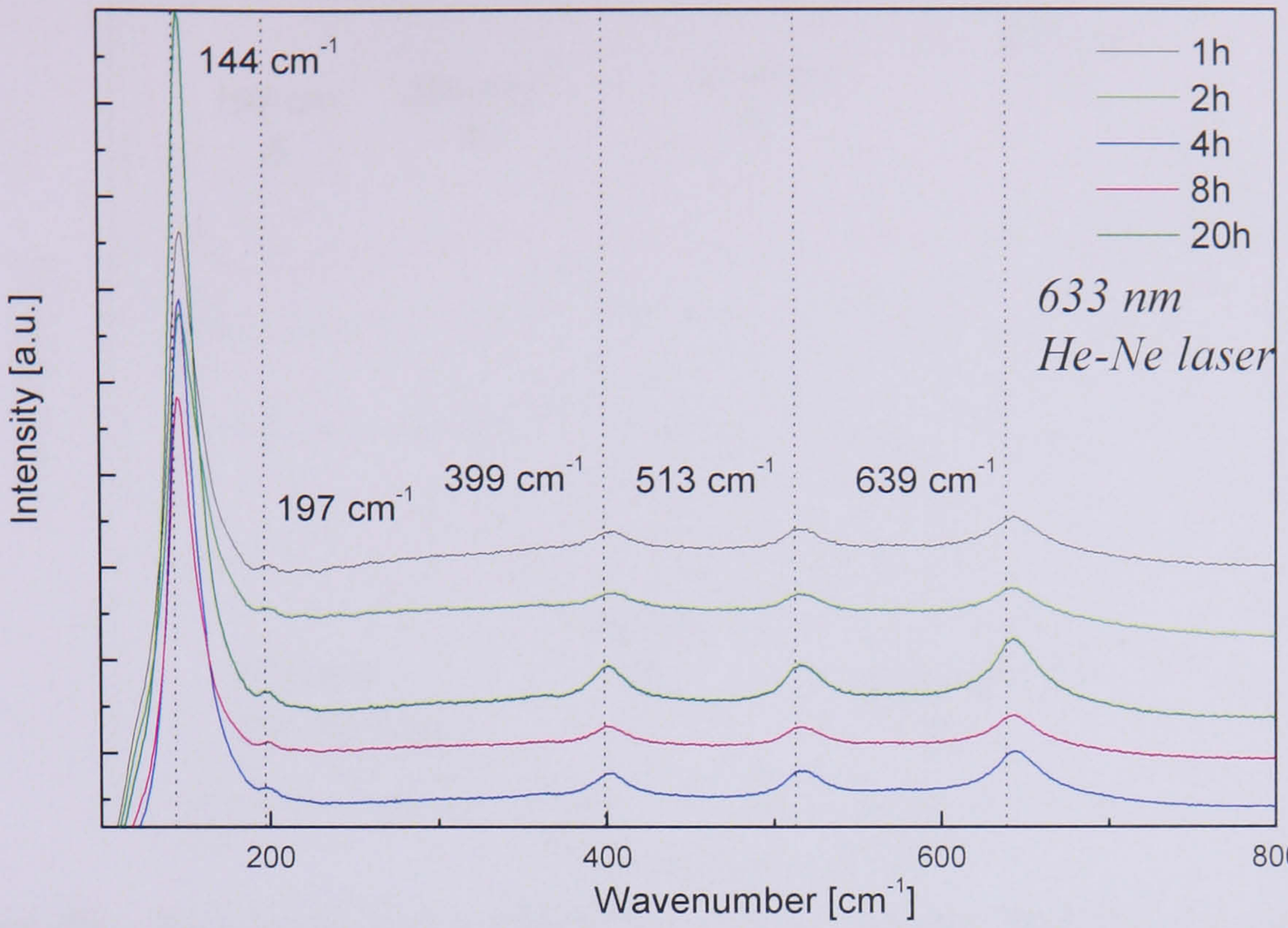


Figure 47 – Raman spectra of TNR_{TOPO} as a function of reaction time

The study of the influence of TOPO content was motivated by a desire to control morphology and to reduce costs. TOPO is both the most expensive material used and used in largest quantity by weight. To give a sense of perspective, a gram of the as-prepared TiO_2 nanorods was estimated to cost approximately £60 (including materials, utilities and labour) and about 15-20% of this figure is the cost of TOPO reactant. The original ratio of TOPO to other reactants was $TiCl_4$:$Ti(OPr)_4$:$C_{12}H_{25}NH_2$:TOPO = 1:1:6:5, which was then adjusted to TOPO for values 0, 2.5 and 10. Yield data and product purity decrease as function of increasing the TOPO ratio. However, when no TOPO was added, the product is no longer pure anatase; peaks corresponding to rutile phase were observed at 447 cm^{-1} and 612 cm^{-1} in addition to anatase peaks at 197 cm^{-1}, 399 cm^{-1}, 513 cm^{-1} and 639 cm^{-1} (Figure 48). The peak at 143-144 cm^{-1} is not helpful, as it is characteristic to both rutile (143 cm^{-1}) and anatase (144 cm^{-1}). For the lowest non-zero amount of TOPO considered, the crystal phase is purely anatase.

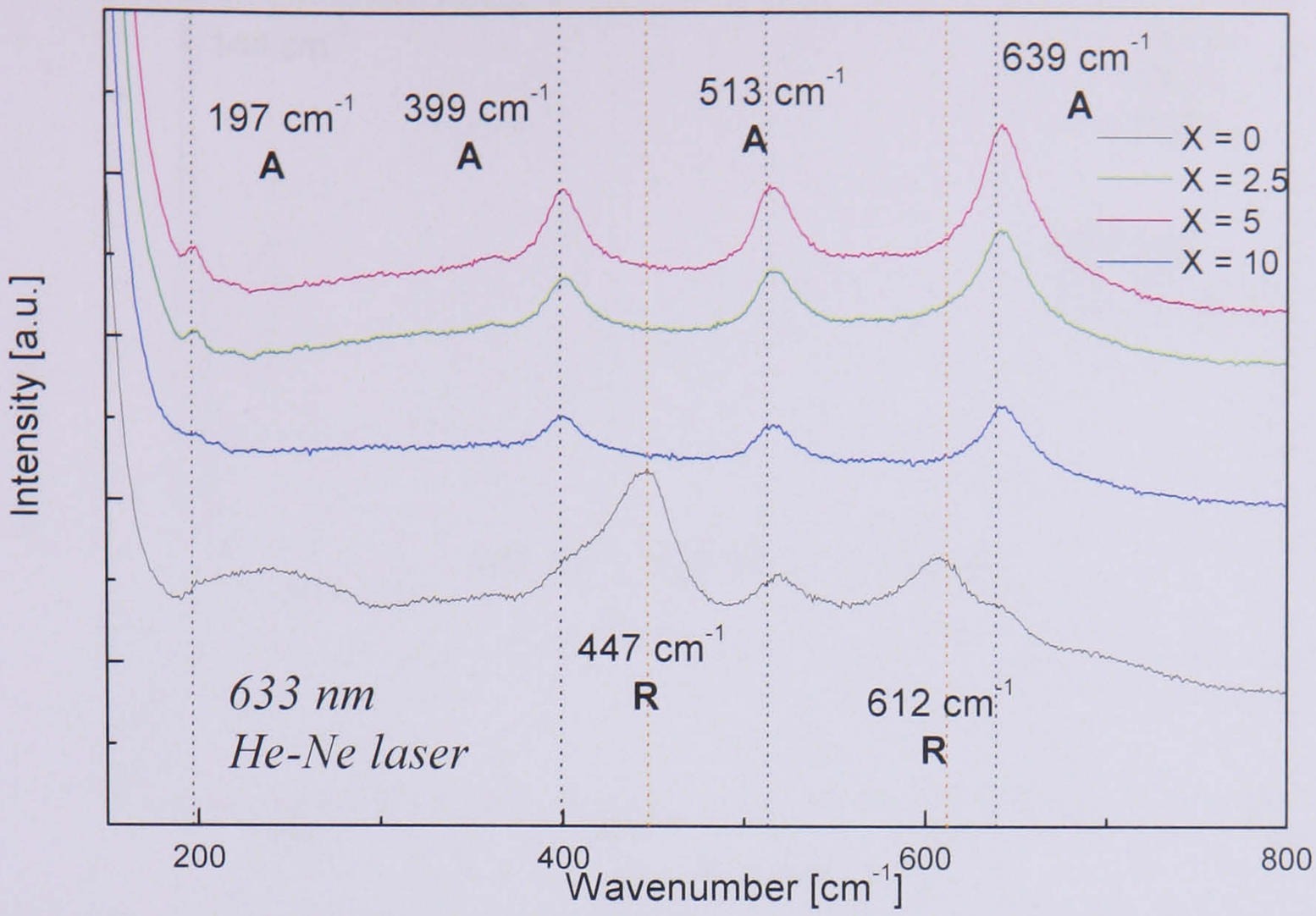


Figure 48 – Raman spectra of TNR_{TOPO} for variable TOPO content (X denotes ratio of TOPO to other reactants in the reactant composition 1:1:6:X)

The effect of the TOPO alkyl chain length was considered by replacing TOPO (C_8) with appropriate amounts of triethylphosphine oxide (TEPO, C_2) and tributylphosphine oxide (TBPO, C_4). The yield increases with decreasing chain length (77 wt%, 88 wt% and 96 wt% for TOPO, TBPO and TEPO respectively), whereas the product purity does not change significantly (73 ± 2 wt %). TEM analysis of the first sample with TEPO revealed much higher aspect ratio nanorods (10 cf. 4 for TNR_{TOPO}), but unfortunately two subsequent repeats of this procedure did not yield similar results. Raman spectroscopy shows that the product crystallinity diminishes upon shortening of the TOPO chain (Figure 49). Weaker anatase bands were observed for the TBPO case, which were almost non-existent for the TEPO sample, suggesting an amorphous product, presumably as the shorter molecules are accommodated within the growing structure.

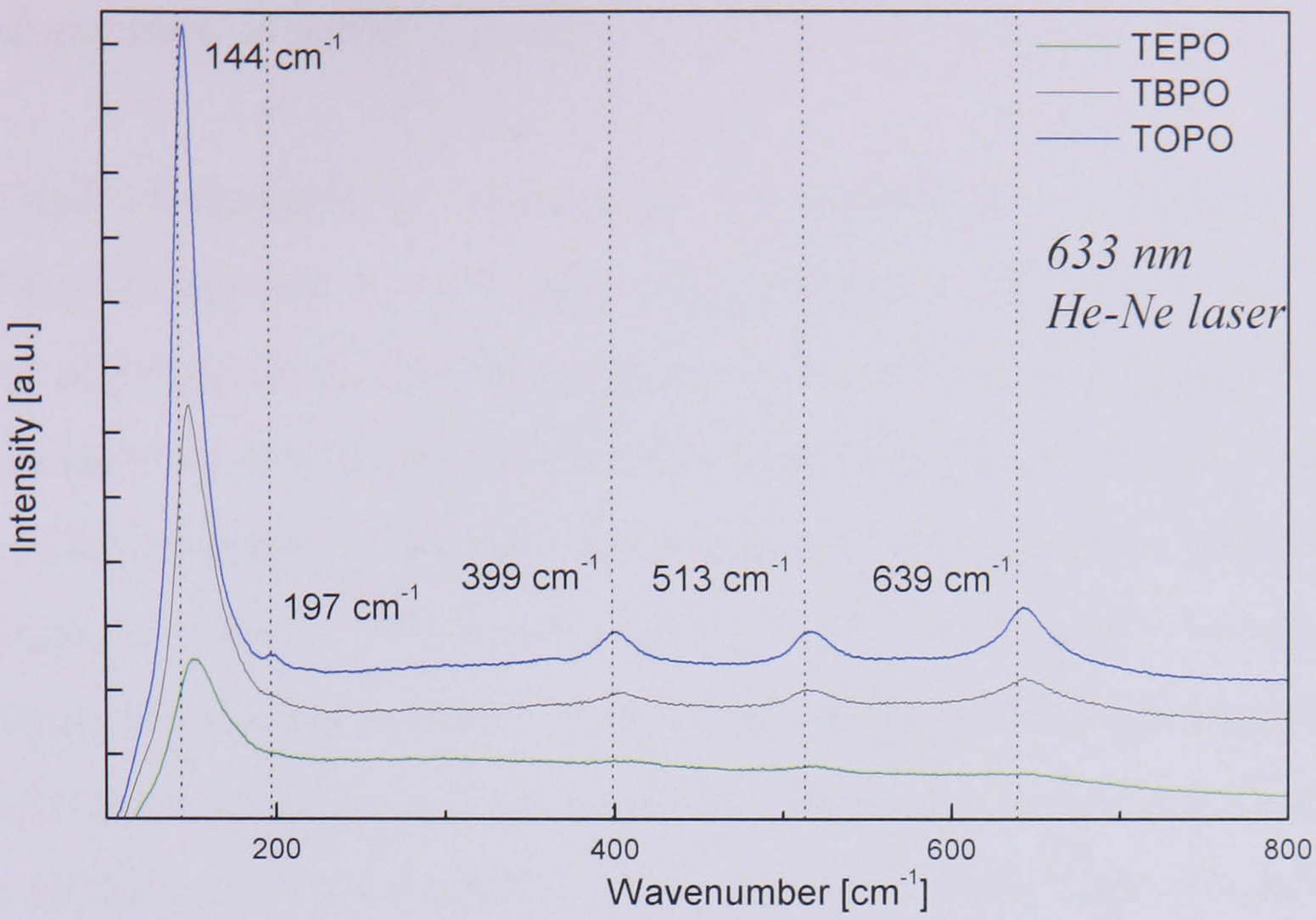


Figure 49 – Raman spectra of TNR_{TOPO} - effect of TOPO alkyl chain length

The effect of changing the temperature was not part of the current study. However, previous work within the group on similar TNR synthetic routes[346] showed that below 275°C, the reaction does not lead to formation of rod-like particles and significant amounts of amorphous material form instead.

Towards the end of this sub-study, experiments with sequential addition of TTIP were also considered. Again, it was previously noted that, for a similar synthesis route[346], adding a fraction of TTIP to the reaction mixture at a lower temperature (110°C) helps to slow down uncontrolled growth that otherwise results in polydispersed nanoparticles. Initial formation of the precursor modules was postulated to favour the formation of monodisperse 'seeds' and ultimately a more monodisperse product. For the experiments carried out for this chapter, the TEM analysis did not reveal any significant changes in the dispersity of the product, although violent boil-up of reactants was avoided at the onset of the high-temperature stage (300°C).

4.2.3 UV-assisted removal of surface organics and stabilisation of TNR_{TOPO} dispersions in water

TOPO and dodecylamine surfactants are amphiphilic molecules, having a hydrophilic end-group (–P=O and $–NH_2$, respectively) and a moderate-length saturated aliphatic chain. The hydrophilic end coordinates towards the hydrophilic titania surface while the hydrophobic surfactant chains are oriented away from the surface. The nanorod surfaces are thus relatively hydrophobic allowing for stable dispersions, as shown previously (Figure 38), in organic solvents such as chloroform. The hydrophobicity of the titania surface, although beneficial in terms of composite processing for organic soluble polymers, can also be detrimental if it hinders adhesion at the nanorod-polymer interface. This issue will be discussed in greater detail in Chapter 5; here the procedure to effect the removal of organics from the titania surface will be discussed.

Given a 2-phase mixture of chloroform and water, titania nanorods will disperse solely in the organic phase. However, upon UV-irradiation and gradual removal of the organics at the surface, titania migrates into the aqueous phase (Figure 50). As highlighted previously (Chapter 3), the degradation of the organic solvent can contaminate the titania surface, which required a subsequent washing and a second irradiation to completely remove the organics. For simplicity, the UV-assisted removal of organics and the resultant nanorod product will be refered to as ‘stripping’ and ‘stripped’ from this point, respectively.

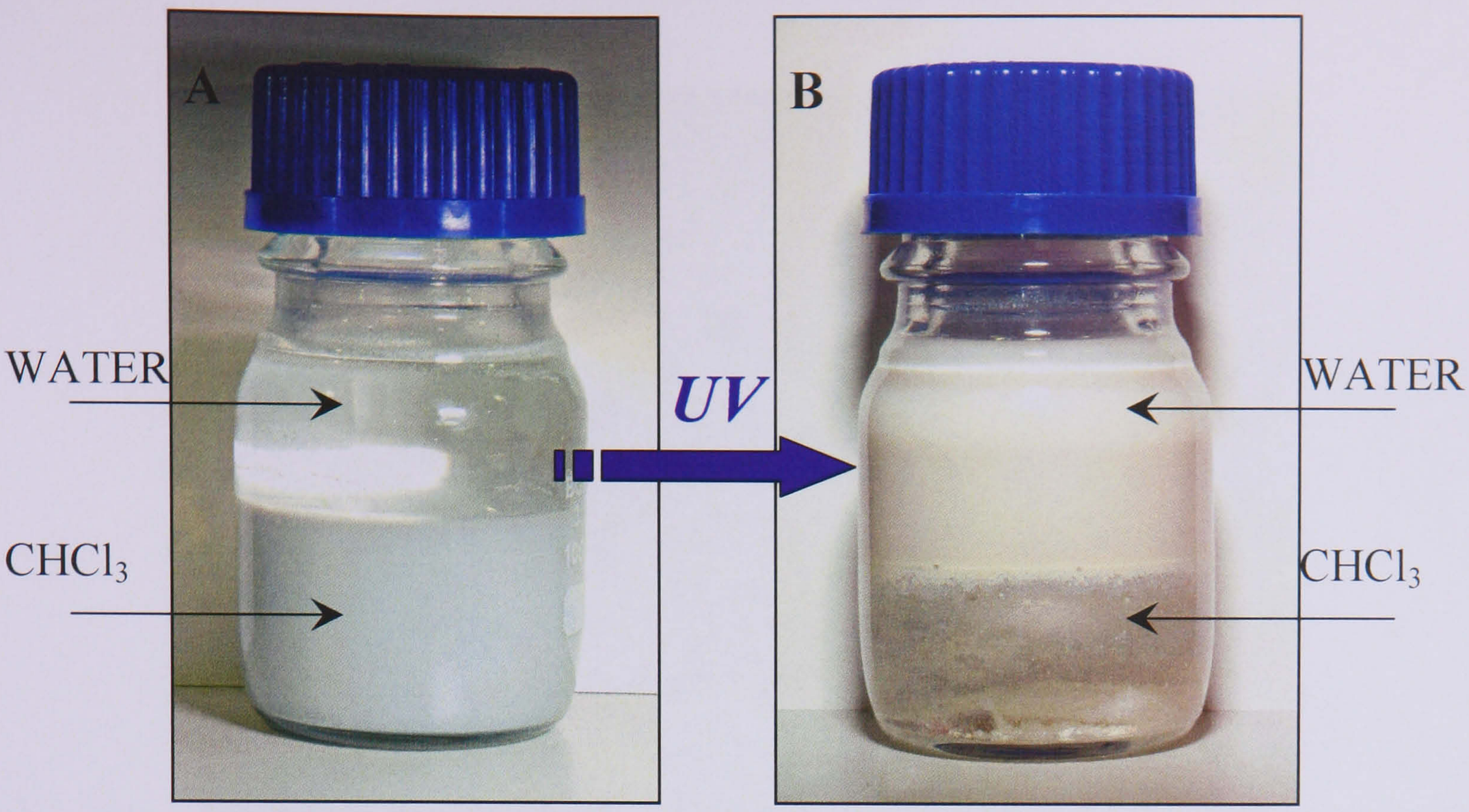


Figure 50 – Water-$CHCl_3$ mixture with TiO_2 nanorods: (a) before and (b) after 12 h of UV irradiation

From TEM, the nanorod morphology remains unchanged (Figure 51), following the stripping treatment, although the particles appear more agglomerated than the as-synthesised ones. This discovery provides a versatile new pathway for the treatment of not only titania nanostructures, but of any other inorganic oxide nanomaterial that exhibits UV-induced photocatalytic properties (e.g. ZnO, ZrO_2, mixed oxides, etc.). The stripped TNR_{TOPO} remain anatase as evidenced by XRD data (Figure 52) and Raman spectra (Figure 53). Self-cleaning of titania dispersions leads to complete oxidation of surfactants on the surface, as evidenced by the TGA data (Figure 54), which no longer shows a sharp sample weight loss associated with the presence of organic material. The gradual weight loss observed for the stripped sample throughout the temperature range can be attributed to the removal of surface-bound moisture (introduced during the stripping process) and elimination of –OH surface groups; the majority of this weight loss is reversible although sintering may lead to permanent loss of surface area. Initially, up to 250°C, weight loss curves look almost identical for the two samples, suggesting that weight loss in this region is due to removal of adsorbed water and elimination of –OH groups in both cases. IR analysis would be beneficial to investigate the surface chemistry of both the as-prepared and stripped samples; however, several attempts were not successful.

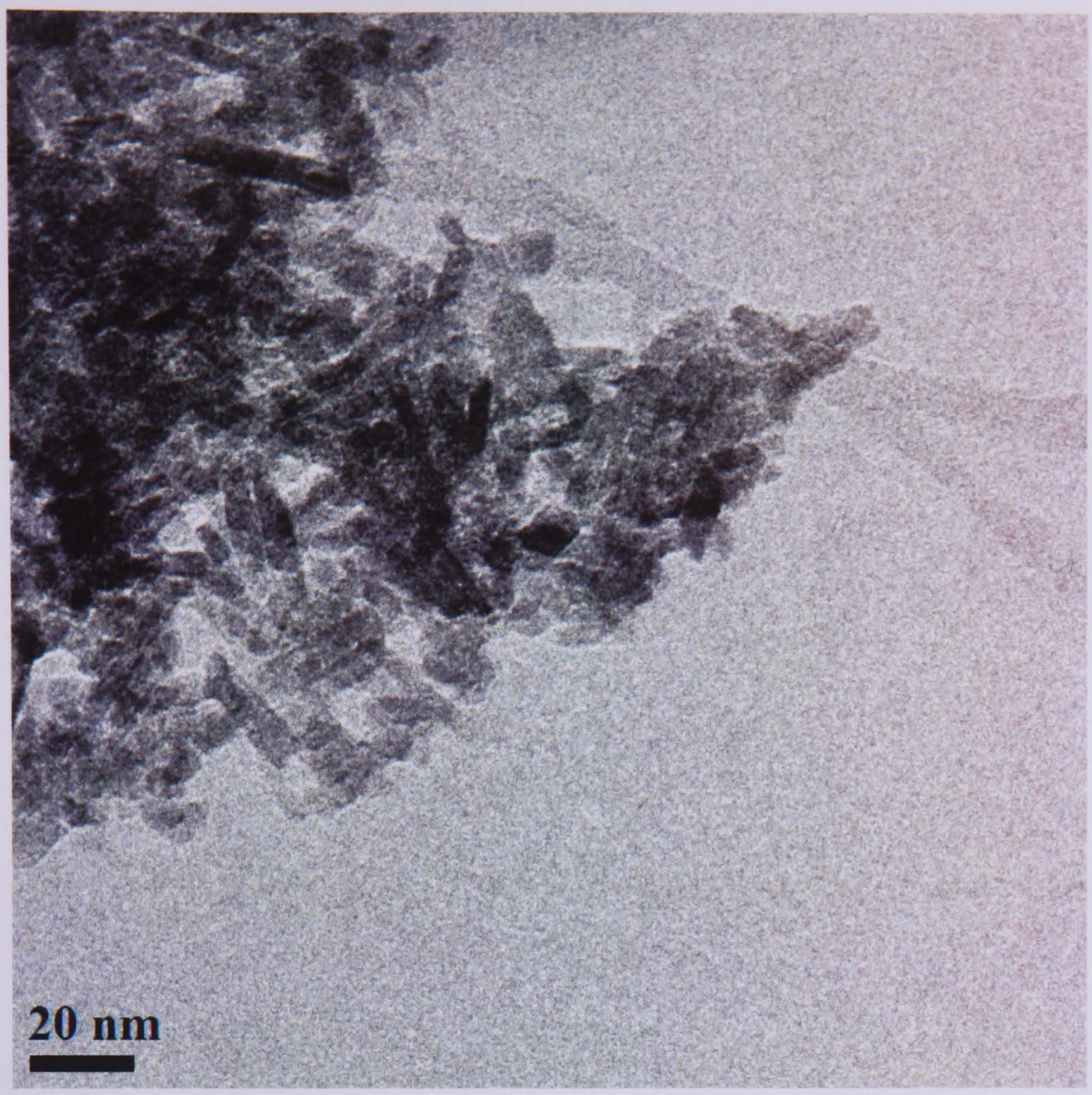


Figure 51 – TEM of stripped TNR_{TOPO}

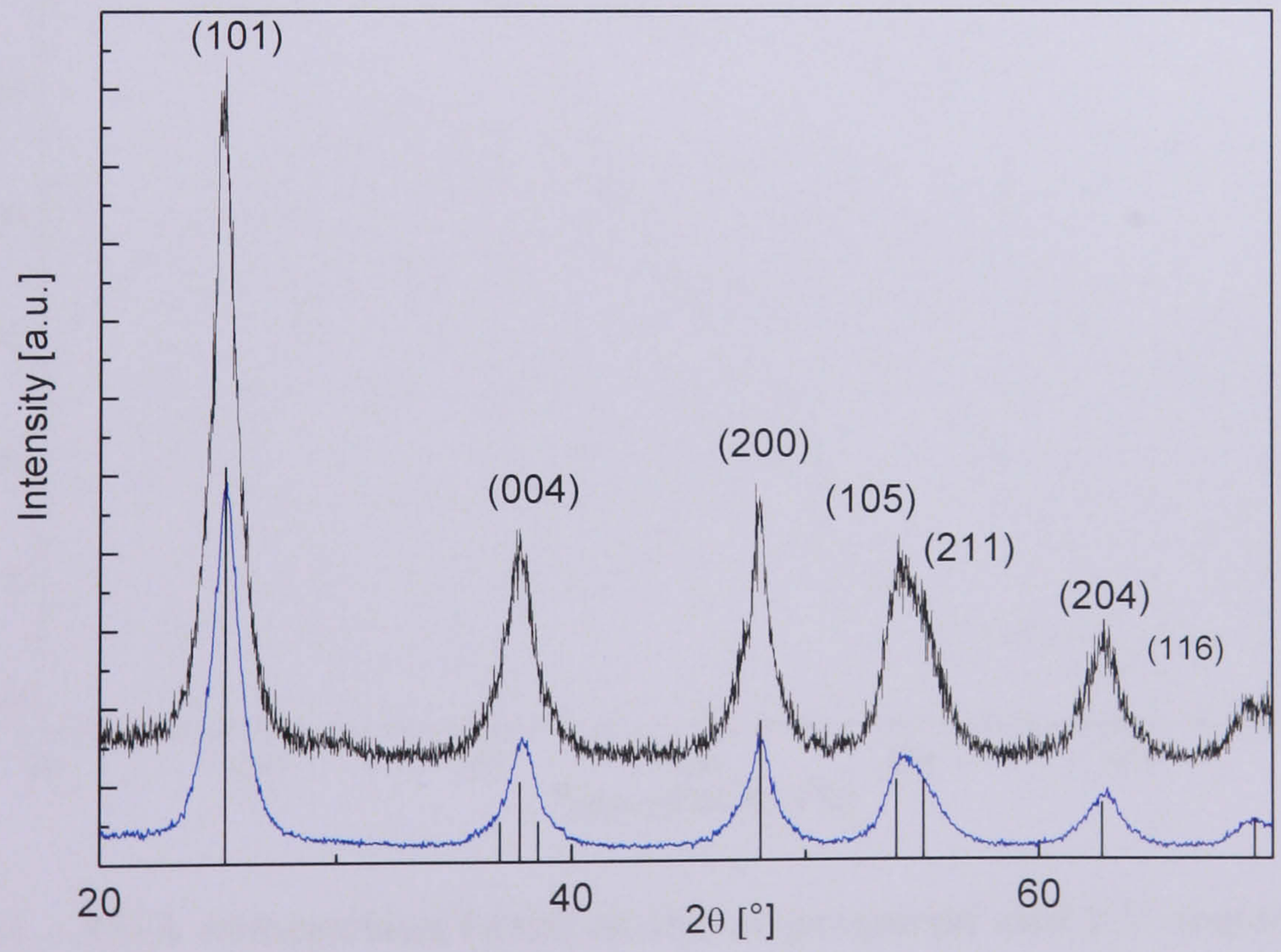


Figure 52 – Comparison of the XRD data between the as-prepared and stripped TNR_{TOPO}

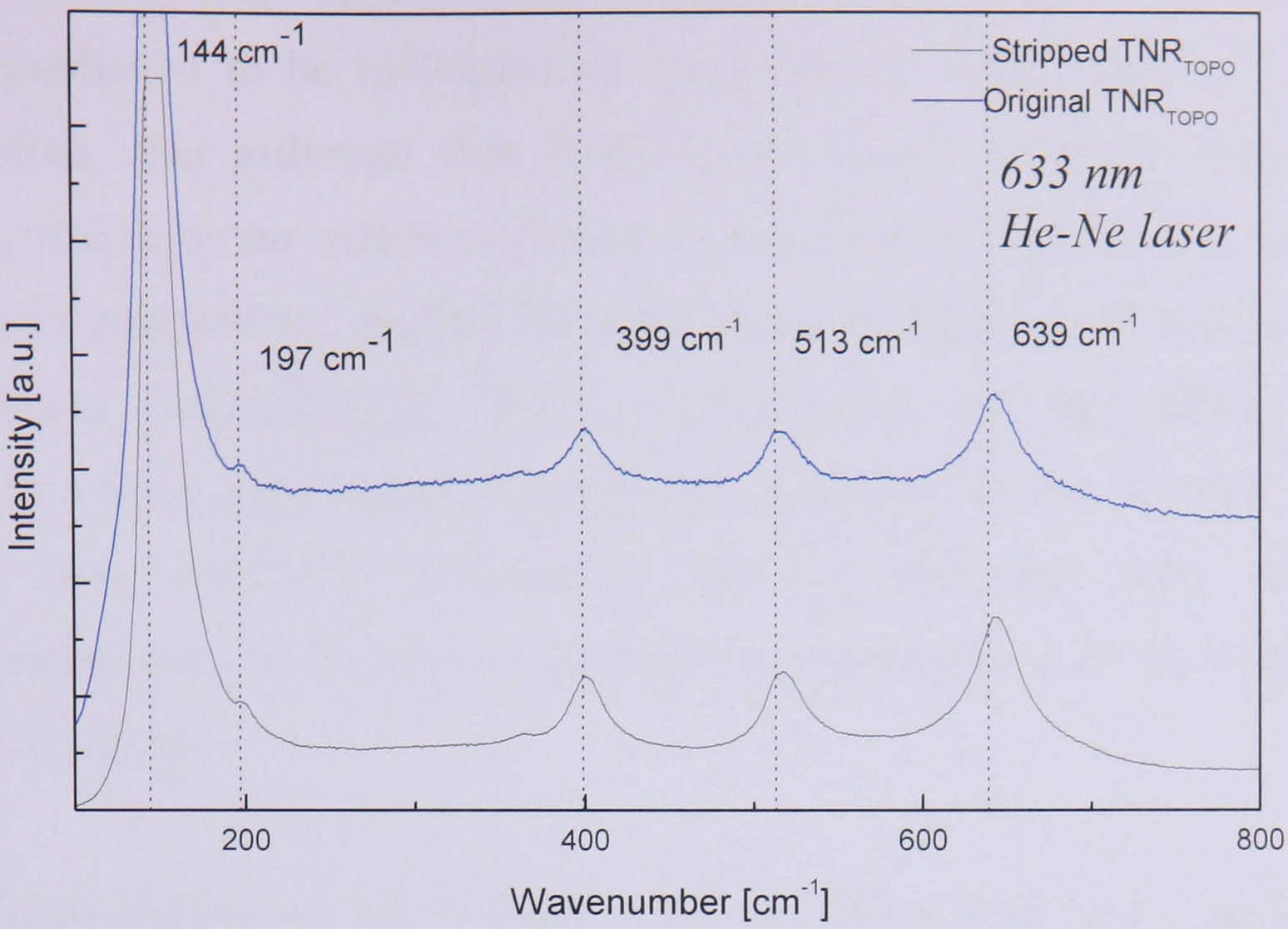


Figure 53 – Comparison of the Raman spectra between the as-prepared and stripped TNR_{TOPO}

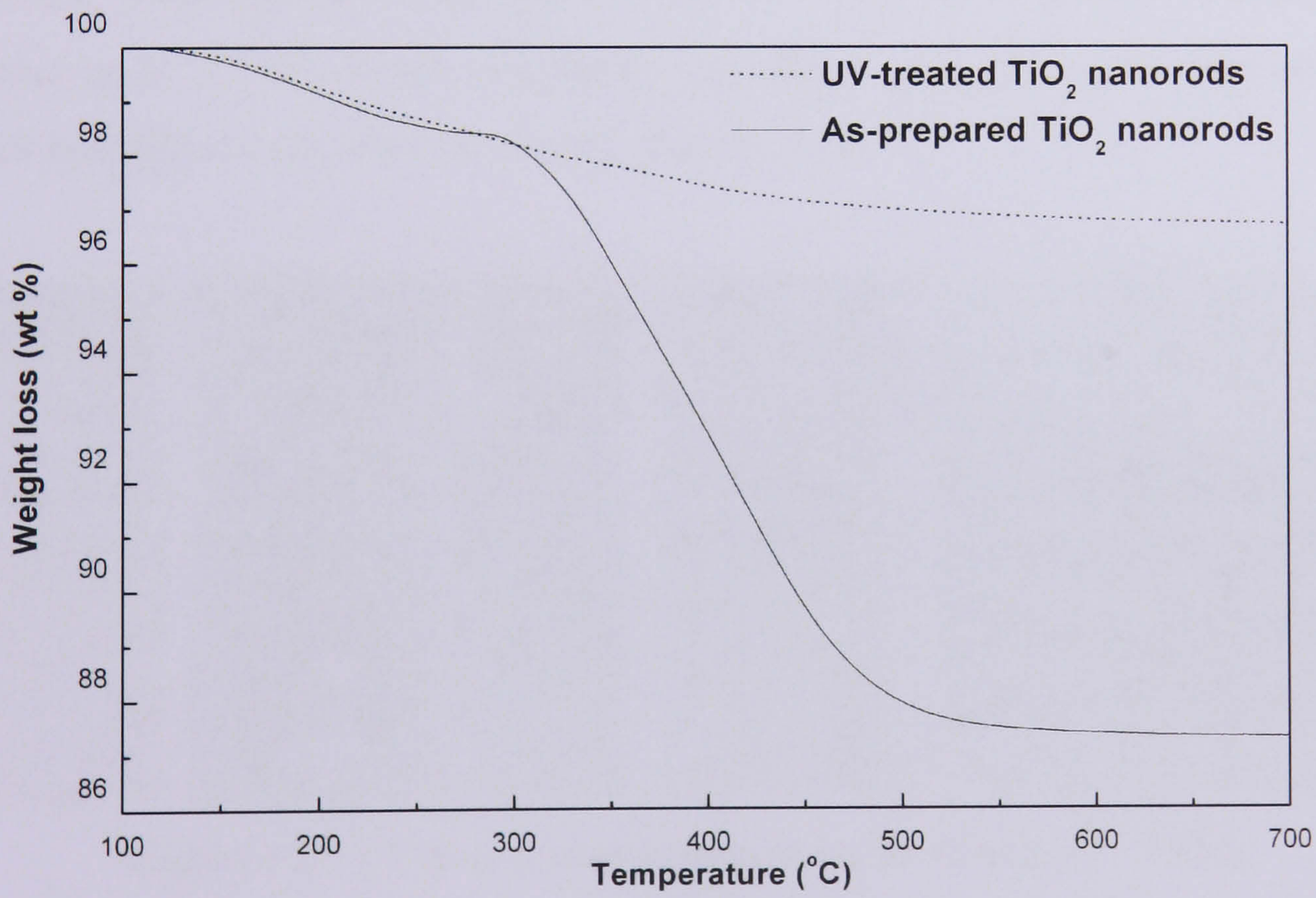


Figure 54 – TGA comparison between the as-prepared and UV-treated TNR_{TOPO}

The importance of supplying air to the process was confirmed, by irradiating sealed aqueous titania dispersions and observing a colour change to grey-blue that is well-established to be indicative of formation of Ti(III) species[294]. It is also worth noting, that although this method has been used most extensively for TNR_{TOPO}, it was by no means exclusive to this product and, as will be discussed shortly, was successfully applied for other types of titania nanorods. Initial trials also involved irradiation of TNR_{TOPO} dispersions in pure ethanol or pure chloroform and in such cases a negligible reduction in the organic content of TNR_{TOPO} was observed, presumably due to the fact that simultaneous photodegradation of the solvent overwhelmingly competes with the degradation of the surface organics.

Under normal conditions, the stripped TNR_{TOPO} form cloudy and unstable aqueous dispersions (Figure 50A, Figure 55A), that precipitate in minutes, indicating significant particle agglomeration. It was found that by adding TMAH to the dispersions, dispersion is enhanced and dispersions are stabilised (Figure 55B). Typically, preparing TiO_2 dispersions (5 mg ml^{-1}) with 50-70 mM of TMAH or more (at least up to 1.5 M), yields completely transparent and very stable dispersions that do not precipitate even after 18 months (Figure 56A).



Figure 55 – TNR_{TOPO} dispersions in water (5 mg ml^{-1} TiO_2):
(a) Original (b) Stripped + 100 mM TMAH (c) Stripped + 100 mM KOH
(d) Stripped + 100 mM TMACl and (e) Stripped + 100 mM KOH & TMACl

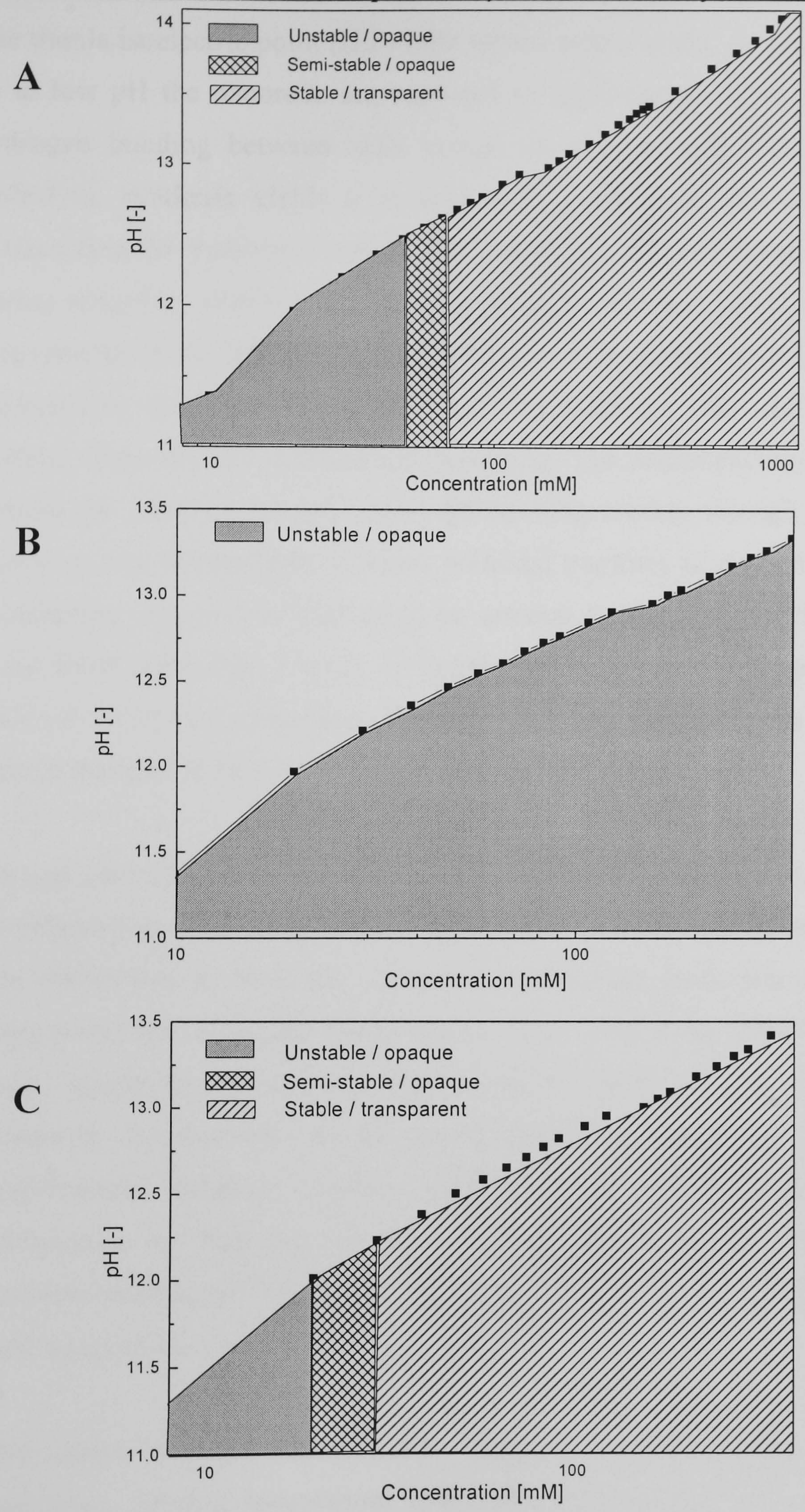


Figure 56 – Stability and optical transparency of stripped TNR_{TOPO} dispersions (5 mg ml^{-1} TiO_2) as a function of concentration of stabilising agent: (a) TMAH (b) KOH and (c) TBAH

[Note: the pH of the stripped TNR_{TOPO} dispersions is ~3.5 and was excluded from the graphs in order to present the relevant results to scale]

The titania isoelectric point (IEP) falls within mildly acidic conditions (pH 3-7)[347], so at low pH the nanorods are expected to agglomerate due to protonation and hydrogen bonding between –OH groups of adjacent nanorods. Although non-hydrolytic synthesis yields a product with a comparatively less hydroxylated surface than the hydrolytic route, –OH groups will be introduced onto the surface during stripping, which in turn facilitates agglomeration under acidic conditions. Conversely, if the pH of the dispersion is increased, the opposite process is expected to occur, i.e. deprotonation (–OH becomes $–O^-$) and stabilisation of particle dispersion by electrostatic repulsion. The electrochemical double layers around the particles prevent them approaching closely enough to agglomerate. However, the stabilisation of these colloidal particles is not solely achieved by introducing charge (i.e. high pH); an attempt to stabilise the TiO_2 dispersions using KOH rather than TMAH, by titrating the base into the dispersion (5 mg ml^{-1} TiO_2) at 10-50 mM increments, up to 500 mM was not successful; the dispersions remain unstable at all concentrations (Figure 55C, Figure 56B).

Careful selection of the counterion is, therefore, important. This effect has been investigated recently with surface functionalised gold nanoparticles[348], where it was shown that at fixed pH, quaternary ammonium hydroxides result in stable dispersions over a greater concentration range than using NaOH. In the present study, quaternary ammonium counterions are larger than K^+ ions, effectively increasing the thickness of the double layer and restricting the approach of neighbouring nanorods. Purely electrostatically-stabilised colloids tend to agglomerate at high ion concentrations as the Debye length drops[349]. The continued stability of TMAH dispersions at high concentrations again points to the importance of the cation size.

This 'steric' stabilisation was also observed by introducing an even larger counterion, tetrabutylammonium hydroxide. In this case complete stabilisation was observed from lower concentrations of 20-30 mM TBAH, suggesting that the greater size of the counterion facilitates stabilisation (Figure 56C). However, adding tetrahexylammonium hydroxide rapidly destabilises the dispersions, presumably due to greater hydrophobicity of the THA^+ counterion. Interestingly, when either TMAH or TBAH were added to a dispersion already containing KOH,

no stabilisation was observed. Conversely, if KOH was added to a TMAH-stabilised dispersion, the nanoparticles precipitate, suggesting that K^+ cations preferentially bind to the TiO_2 surface compared with $TMAH^+$. Smaller ions are expected to bind more strongly , as the unlike charges can approach more closely. The effect of TMA^+ counterion alone, in the absence of base, was studied by adding equivalent amounts of TMA^+Cl^-. However, the salt did not stabilise the dispersions, presumably due to lack of cation binding (Figure 55D). Adding a stoichiometric amount of KOH to a dispersion containing TMA^+Cl^-, increases the pH leading to electrostatic repulsion and cation binding. Such dispersions were somewhat stabilised, no particles precipitated, but were not fully optically transparent (Figure 55E). Again, preferential adsorption of K^+ presumably displaces some TMA^+ counterions at the surface.

In order to provide a more quantitative appreciation of the stability of titania nanorod dispersions upon the addition of TMAH, the dispersions were analysed using UV-Vis spectroscopy. The spectra for a 10 mg ml^{-1} TNR_{TOPO} sample show a decrease in incident light scattering, as a result of stabilisation (Figure 57). The initial spectrum of the stripped TNR_{TOPO} dispersion is very erratic throughout the entire range, due to strong light scattering, despite having been recorded with an integrating sphere detector, which should minimise this effect. Upon the first addition of TMAH (13.83 mM), the stability of dispersions was significantly improved – no apparent precipitation was observed for several hours. By further increasing [TMAH] full transparency is attained and the absorption spectra do not change upon any further increase in [TMAH] (i.e. >70 mM).

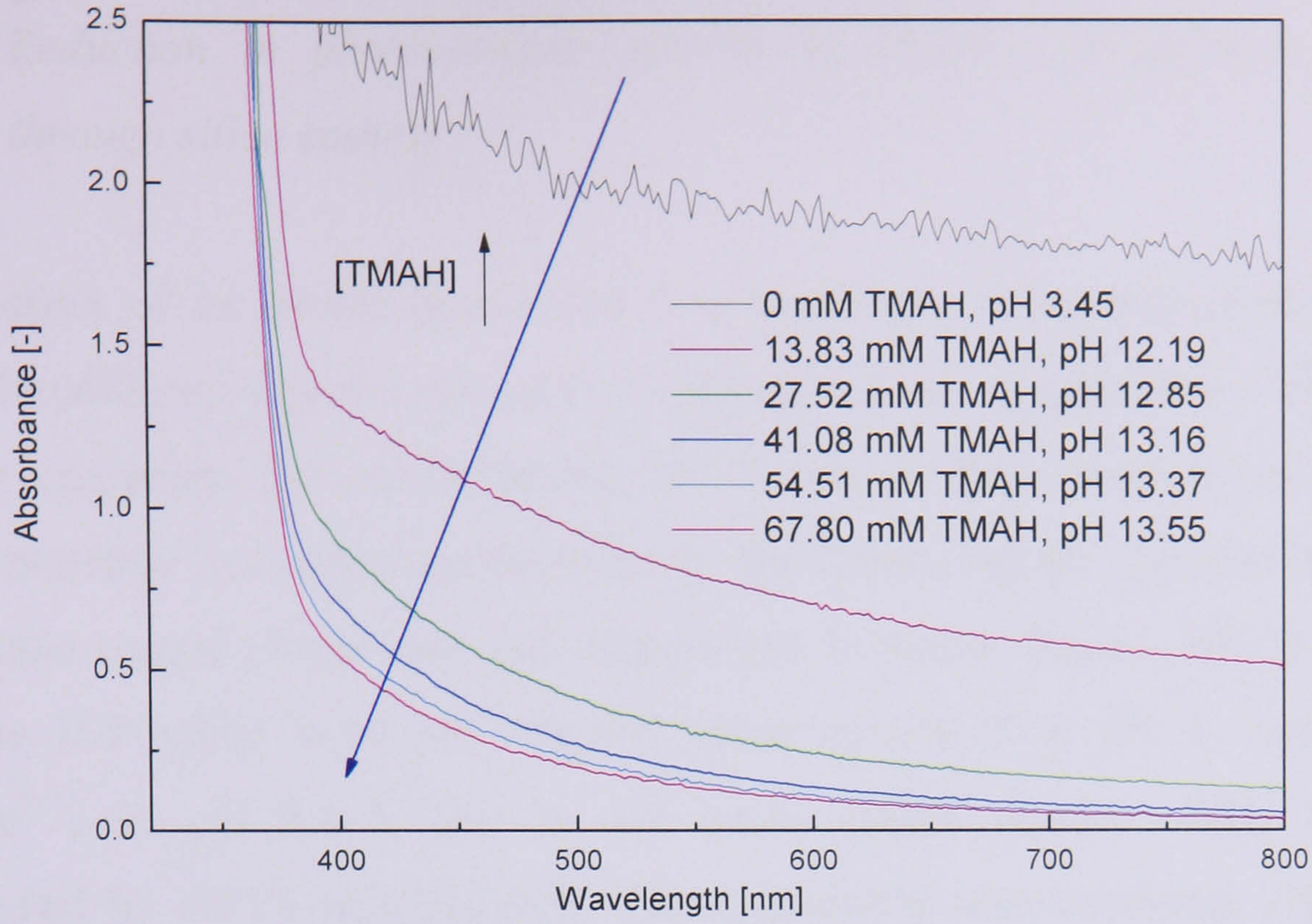


Figure 57 – UV-Vis spectra of aqueous TNR_{TOPO} dispersions (10 mg ml^{-1}) as function of TMAH concentration

The concentration of TNR in dispersion was also expected to influence the degree of stability and transparency of the dispersions. To study this effect, several dispersions with different TNR concentration were titrated with TMAH and characterised using UV-Vis spectra. For fixed TMAH concentration (41.1 mM), the UV-Vis spectra show (Figure 58), perhaps unsurprisingly, that increasing the titania concentration leads to less stable and more opaque dispersions.

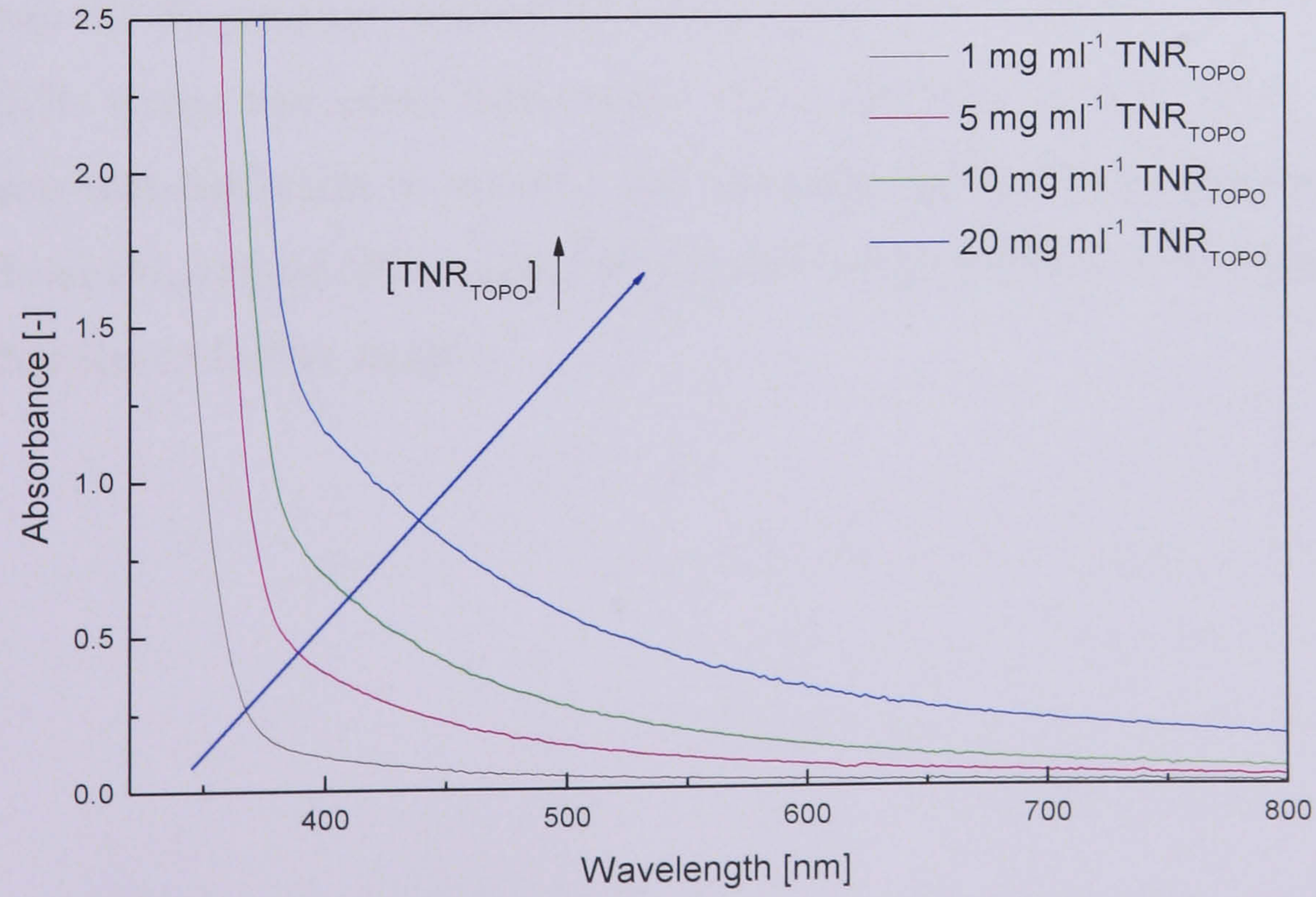


Figure 58 – UV-Vis spectra of aqueous TNR_{TOPO} dispersions as function of TNR_{TOPO} concentration for fixed TMAH concentration [41.1 mM]

4.2.4 Reduction in photocatalytic activity of TNR_{TOPO} in aqueous dispersions through silica coating

Application of an amine-terminated 3-aminopropyl trimethoxysilane (APTS) to TMAH-stabilised dispersions leads to agglomeration, suggesting a change in the surface character. For confirmation, APTS-treated dispersions were analysed by electrophoretic ζ-potential measurements. By comparing the ζ-potential of stripped and silane-coated titania nanorod dispersions in water (Figure 59), it can be seen that the IEP shifts from the original value measured at pH 3, consistent with anatase[347], to pH 6.5-7, due to the basic nature of the $-NH_2$ functionality introduced by APTS modification. The ζ-potential measurements also show that the ζ-potential becomes highly negative (>30 mV) above pH 10, indicating that the surface of the nanorods is charged, which in turn prevents agglomeration. At low pH, formation of $-OH^{\delta+}$ is expected to occur on the stripped TNR surface; however, the charge on these groups is not sufficient to achieve stabilisation of the dispersions, as evidenced by the ζ-potential measurements (~10 mV). Following a similar argument as for the stabilisation of the UV-treated TiO_2 dispersions, under basic conditions the amino groups remain neutral or partially deprotonated ($-NH^-$) and hydrogen bonding leads to agglomeration. However, at low pH, the ζ-potential increases due to protonation of the surface (formation of the $-NH_2^{\delta+}$ groups) and stabilises the dispersions. Indeed by lowering the pH to acidic conditions ($pH \leq 2$) with HCl, stable and clear dispersions were obtained. In this case, electrostatic repulsion was sufficient to achieve stabilisation, without adjusting the counterion size. However, excess HCl quickly led to particle precipitation, as expected, due to the reduction in Debye length.

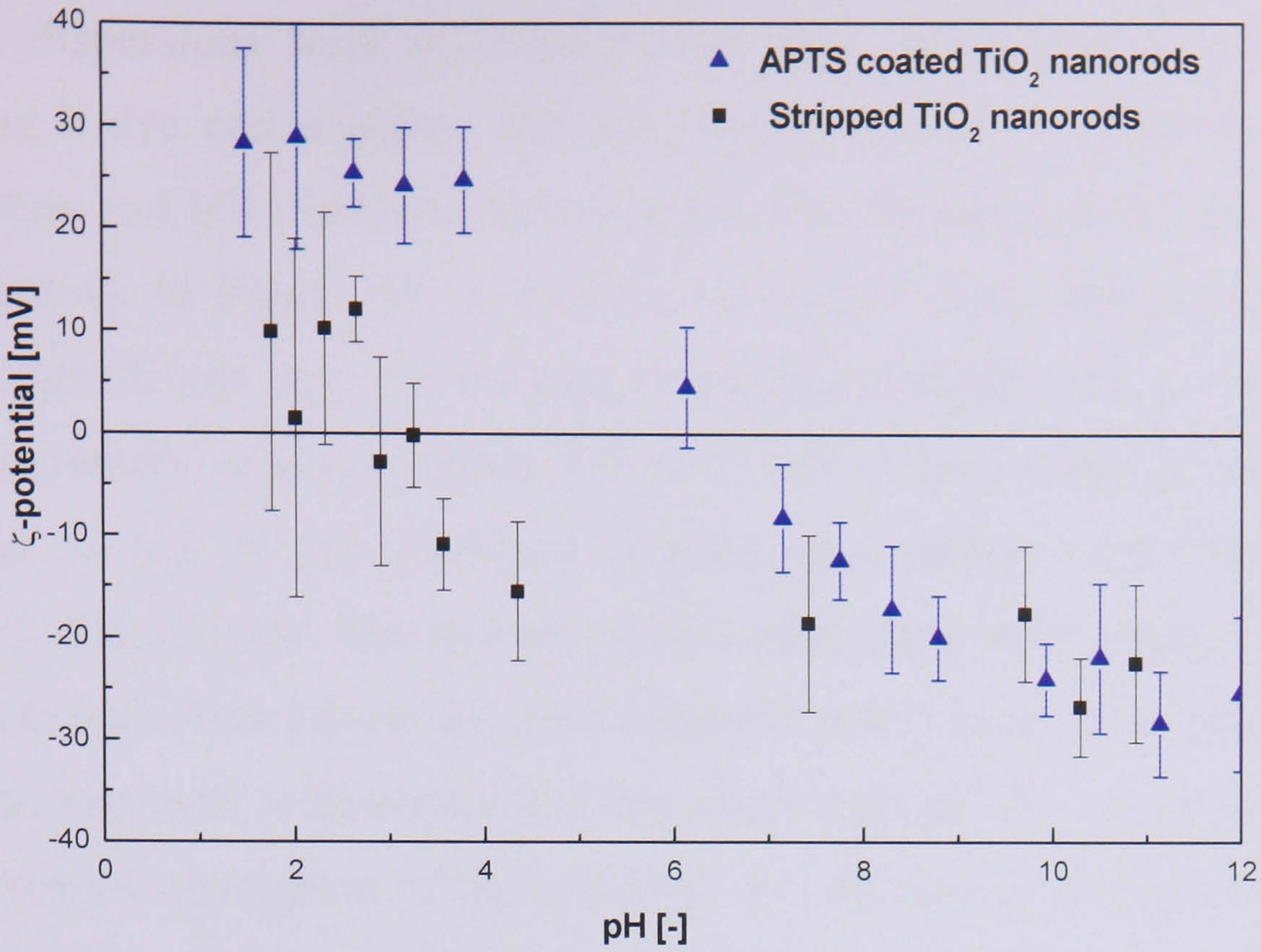


Figure 59 – ζ-potential as a function of pH for: (a) stripped and (b) APTS-coated aqueous TNR dispersions [10 mg ml^{-1} TNR_{TOPO}; 1 mM KCl background electrolyte, 20°C]

Before proceeding to the photocatalytic activity of APTS-treated TNR_{TOPO}, it is worth mentioning that APTS was not the only siloxane considered. Indeed, several other molecules were tested, including glycidoxypropyltrimethoxy silane (GlOPS) and sodium silicate (Na_2SiO_3). The former was an interesting candidate as it is water-soluble, thus permitting aqueous treatment of titania dispersions and it also contains an epoxide group, which should, theoretically, permit dispersions in organic solvents and possibly enhance adhesion with polymers such as PMMA or epoxies. However, adding 10 wt% of GlOPS with respect to titania has neither reduced the photocatalytic activity nor permitted the transfer of particles into an organic solvent. In fact, a brief qualitative experiment suggested a slightly increased activity for the silane-treated sample. Although not confirmed by further analysis, it is plausible and has, indeed, been reported previously[188] that the silica shell around the particles needs to exceed a critical thickness in order to reduce the photocatalytic activity titania. Silica is a known stabilising agent for titania dispersions[188,194], so incomplete coverage of the TNR surface by silica may be sufficient to further improve the dispersion and, overall, create a more efficient environment for the photocatalysis to occur.

Stabilised dispersions were investigated for their photocatalytic properties, by introducing a dye and studying the degradation kinetics as a function of TiO_2 concentration and UV exposure time. The baseline degradation of the pure dye in water is shown in Figure 60. A number of organic dyes were considered, but Brilliant Blue R was selected because it is water-soluble over a very wide pH range. References with pH values below 2 and ~12-13 were prepared, which correspond to pH of the stabilised original and APTS-coated TiO_2 nanorod dispersions, respectively. The dye absorbance has a maximum around 550 nm and the dye decomposition effects are most apparent at this point. The intensity at this wavelength was used to determine the dye concentration. The shape of the spectra and the absolute absorption of the solutions are affected by the pH, but the peak position and degradation trend in both cases remain unchanged.

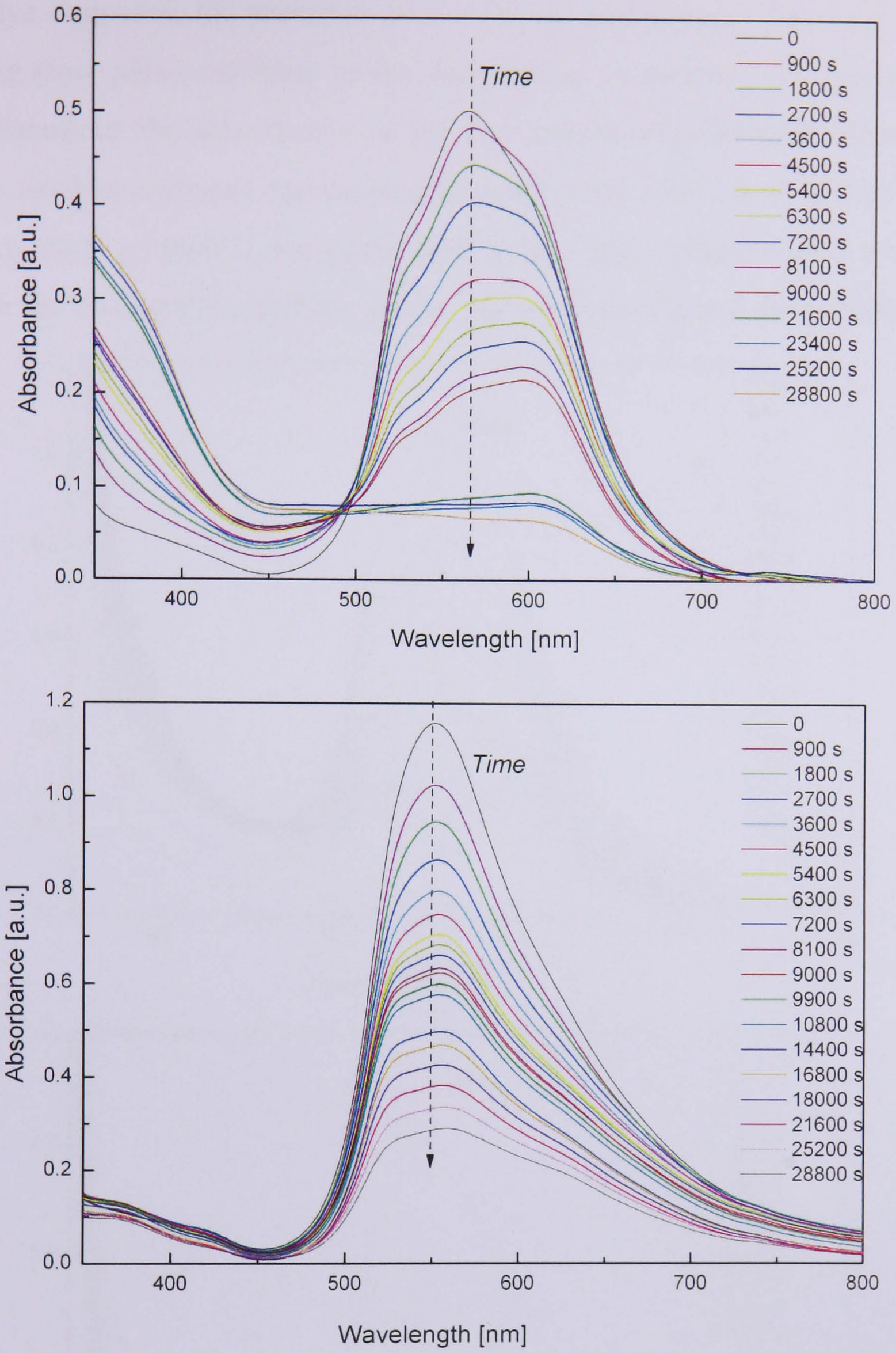


Figure 60 – UV-Vis spectra of Brilliant Blue R solutions in water at (a) basic pH 12-13 and (b) acidic pH ≤ 2, as a function of UV-exposure time

Figure 61 shows the spectra for TiO_2-catalysed dye photodegradation in uncoated and APTS-coated TNR dispersions. Again, as for the dye references, the absorption maximum at 550 nm decreases with UV exposure time. By comparing the data, it can be seen that the presence of TiO_2 catalyses the degradation, in line with strong photocatalytic activity of TiO_2. However, exposure of APTS-coated samples to UV leads to significantly slower degradation, suggesting that the silica-

type coating around the titania does indeed help reduce its photocatalytic activity. As the dye degrades, the presence of a coloured end product (high pH) or particle scattering (low pH) contribute to the data; linear corrections were made for these effects based on the absorbance at the dye minimum (460 nm). Beer-Lambert's law was used to estimate the extinction coefficient (1842.5 ± 41.9 $m^2 \cdot mol^{-1}$ and 2742.9 ± 26.5 $m^2 \cdot mol^{-1}$, for basic and acidic pH, respectively) and hence to calculate the concentration of the dye at a given point during the experiment.

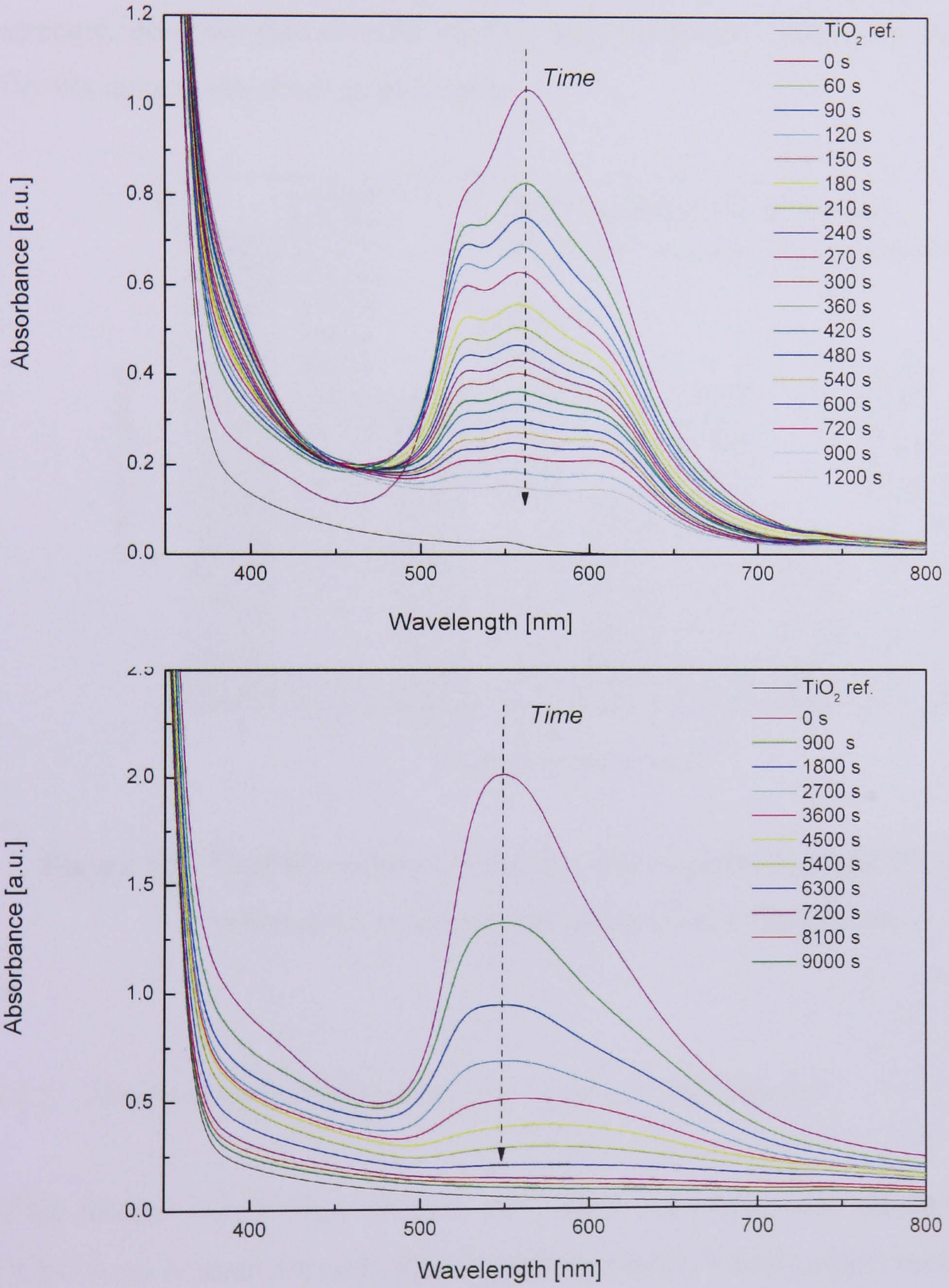


Figure 61 – UV-Vis spectra of the dye solutions containing (a) pristine, stripped TiO_2 nanorods (3 mg ml^{-1}) and (b) APTS-coated TiO_2 nanorods (3 mg ml^{-1}) as a function of irradiation time

Figure 62 shows the log-plot of the calculated dye half-life for the two sets of samples and their respective references. Overall, the coating on the titania surface increases the dye half-life approximately 3-10 times, but since the degradation rates are strongly influenced by the pH, a more accurate estimate is difficult. By reducing the concentration of the uncoated titania in the dispersion, the degradation is proportionately reduced. Half-life data for the coated samples, follows the same trend, although the value at 3 mg ml^{-1} is slightly higher than expected, possibly due to mild particle agglomeration, which can be seen in the UV-Vis data as the reaction proceeds.

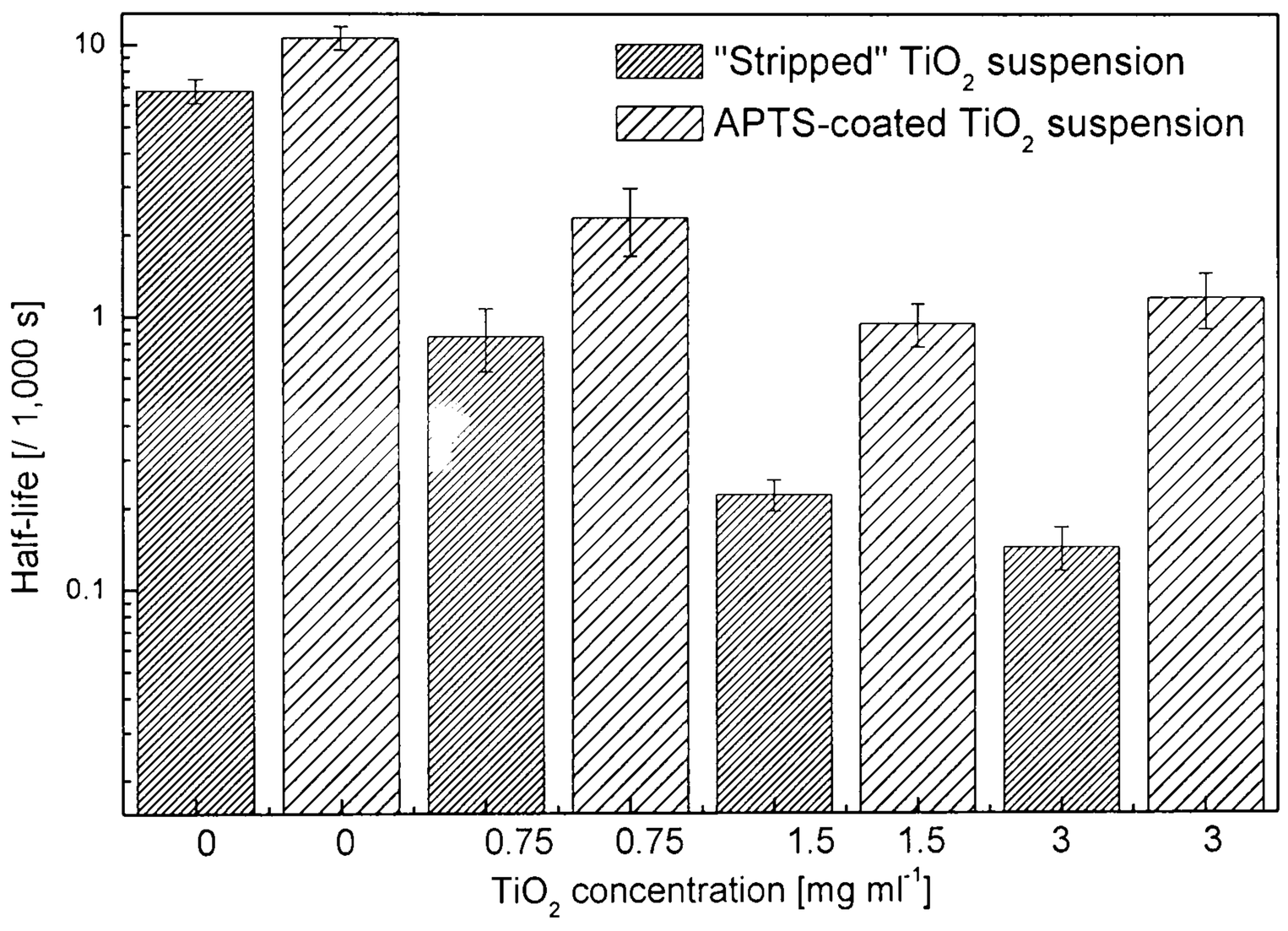


Figure 62 – Half-life values for the dye concentration in: pH 12-13 and <2 references, uncoated and coated TiO_2 dispersions

4.2.5 Non-hydrolytic synthesis of TiO_2 nanorods – OA ligand

TEM images of TNR_{OA} (Figure 63) show monodisperse single-crystal rods, 3.3 ± 0.3 nm in diameter and 40.9 ± 3.7 nm in length, with an aspect ratio of about 12. TNR_{OA} appear to be more rod-like than TNR_{TOPO} as well as more monodisperse. The lattice spacing observed in HRTEM (Figure 63B) corresponds to anatase and once again, the nanorods are elongated along the c-direction.

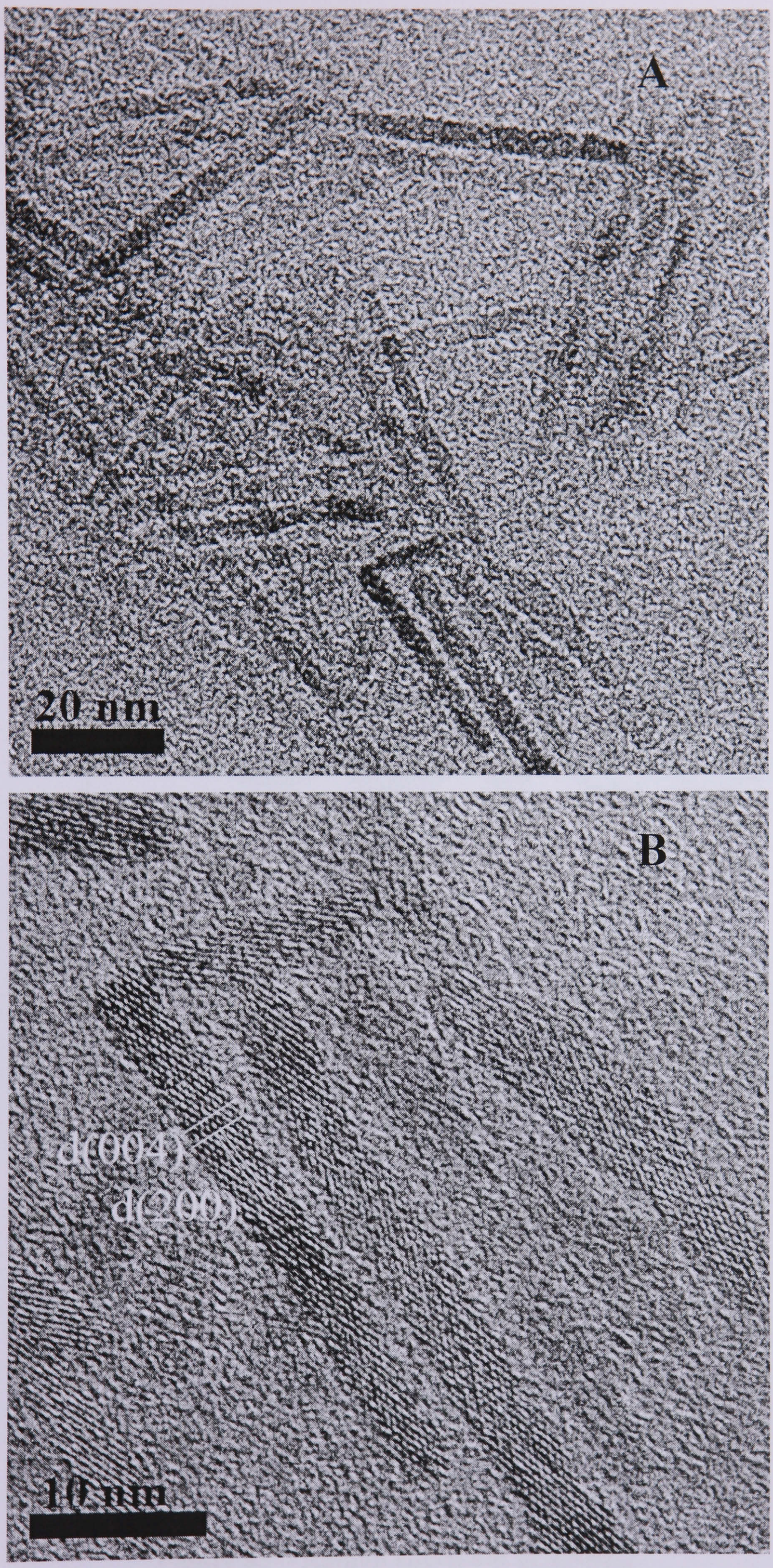


Figure 63 – TEM of TNR_{OA}:

(a) low-resolution micrograph and (b) high-resolution micrograph

The crystallinity of the TNR_{OA} product was confirmed using XRD and Raman spectroscopy. The XRD pattern (Figure 64) shows the characteristic anatase nanorod features, including a sharper (004) peak. The Raman spectrum (Figure 65) displays significant fluorescence, presumably due to considerable organic content; nevertheless, the characteristic peaks were also observed, confirming the anatase phase.

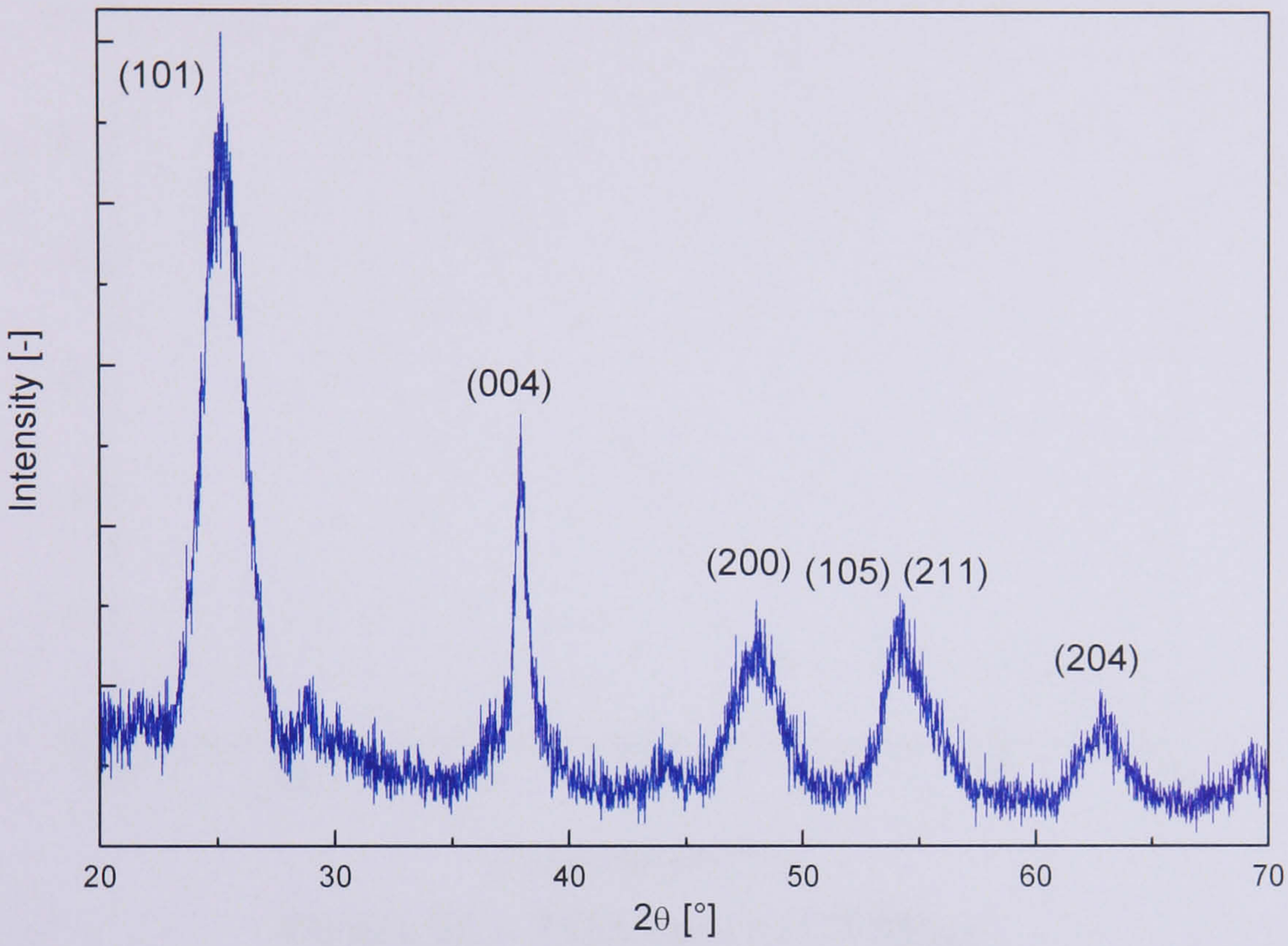


Figure 64 – XRD pattern of TNR_{OA}

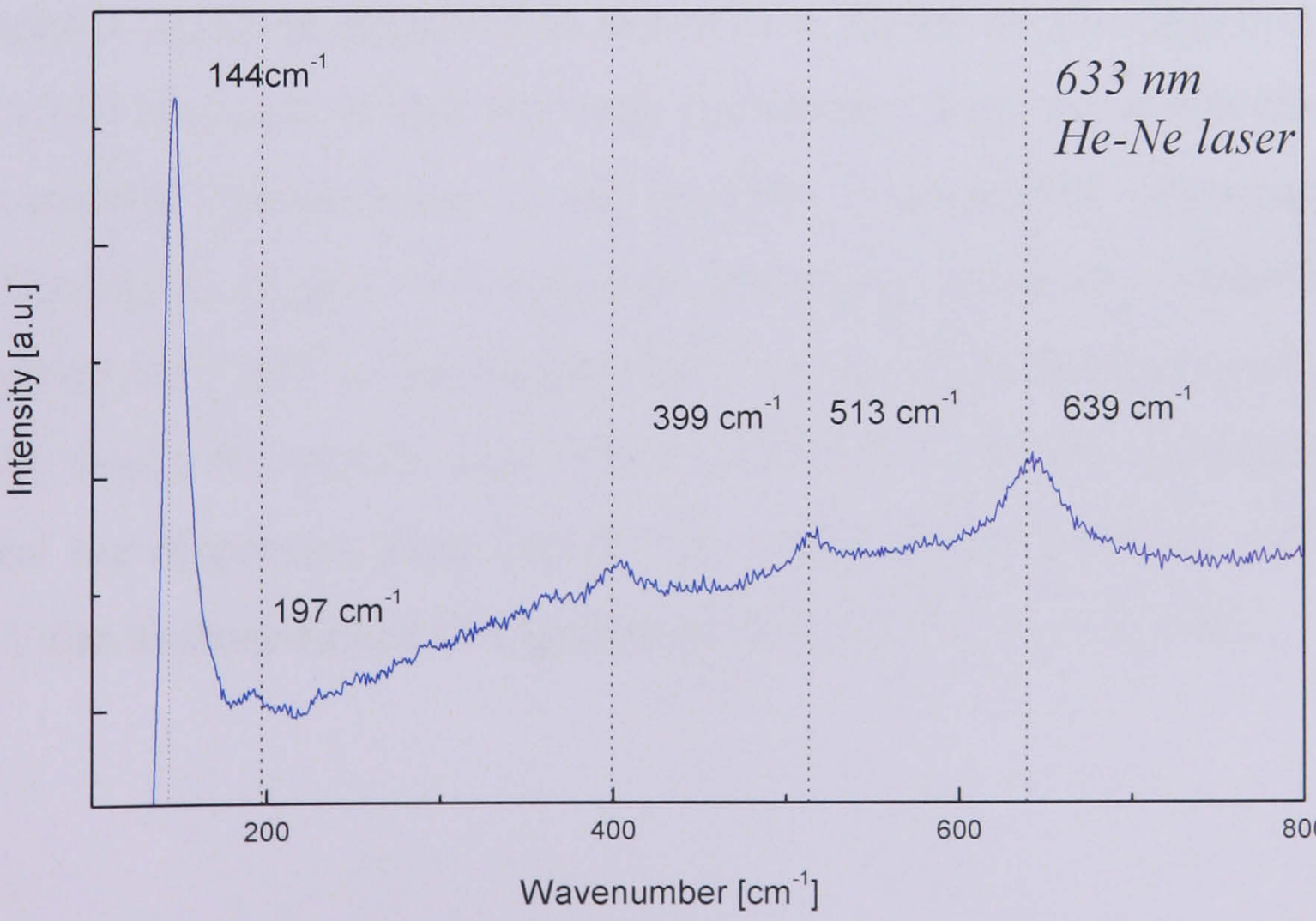


Figure 65 – Raman spectrum of TNR_{OA}

The organic content of TNR_{OA} was studied by TGA and a typical curve (Figure 66) shows that the organic content is approximately 27 wt%. This value is somewhat larger than for TNR_{TOPO}, but comparable with organic content measured for hydrolytic synthesis using OA as a ligand, as noted previously. The degradation starts at about 200 °C, reaches its maximum rate in the 300 - 450 °C range and completes by 500 °C.

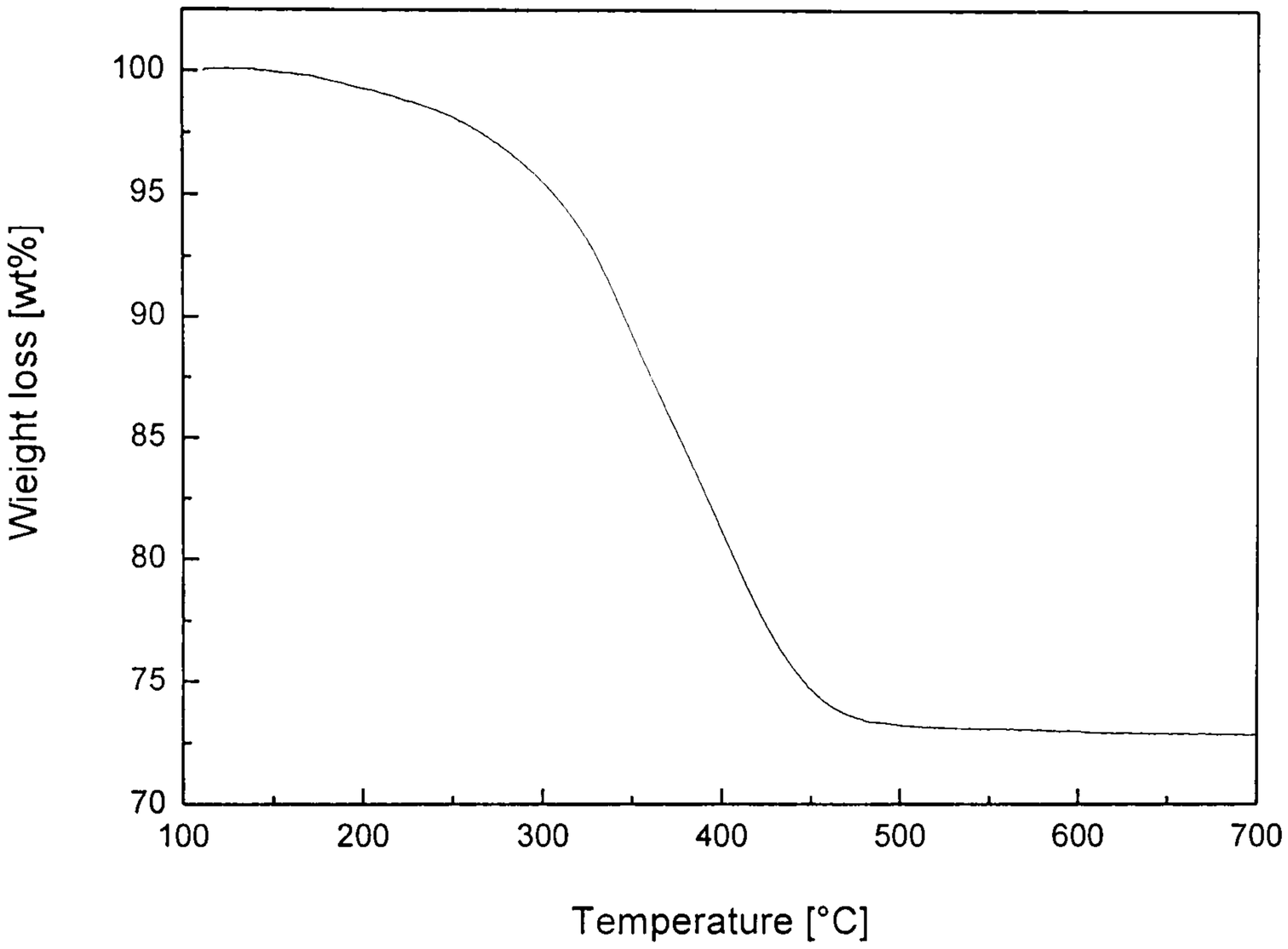


Figure 66 – TGA curve of TNR_{OA}

As in the case of $TNR_{TOPO,}$ nanorods grown using oleic acid as a ligand are produced as a paste, which can be re-dispersed in chloroform. However, re-dispersion has to be carried out while the paste is still wet with isopropanol from the purification stages; otherwise complete re-dispersion is not possible. Furthermore, obtaining a well-dispersed dispersion (Figure 67) requires prolonged ultrasonic treatment at an elevated temperature (50°C). The dispersions, with very high nanorod content (60 mg ml^{-1}), remain stable for several days after which some particle sedimentation was observed and the dispersion turns turbid. The strong dark red-brown colour of the dispersion is due to cross-linked OA functionalities at the nanorod surface.

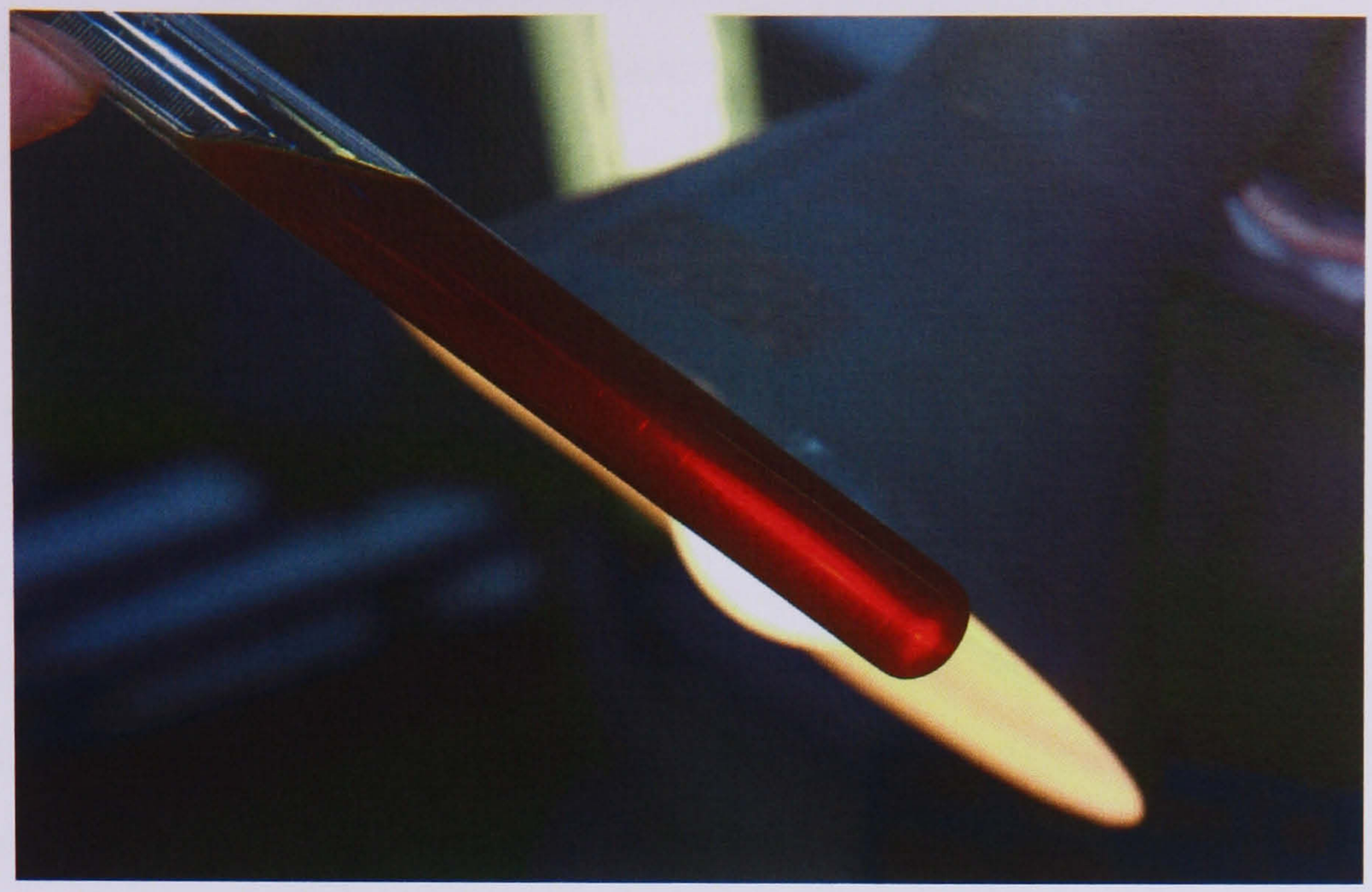


Figure 67 – TNR_{OA} nanorod dispersion in $CHCl_3$ (~ 60 mg ml^{-1})

Strong UV absorption of TNR_{OA} dispersions in $CHCl_3$ was observed using UV-Vis (Figure 68). The absorption edge shifts from ~360 nm to >500 nm throughout the range studied. The absorption increases proportionately as a function of concentration, but some light scattering occurs at long wavelengths for dispersions with high TiO_2 concentration, possibly due to agglomeration of the particles.

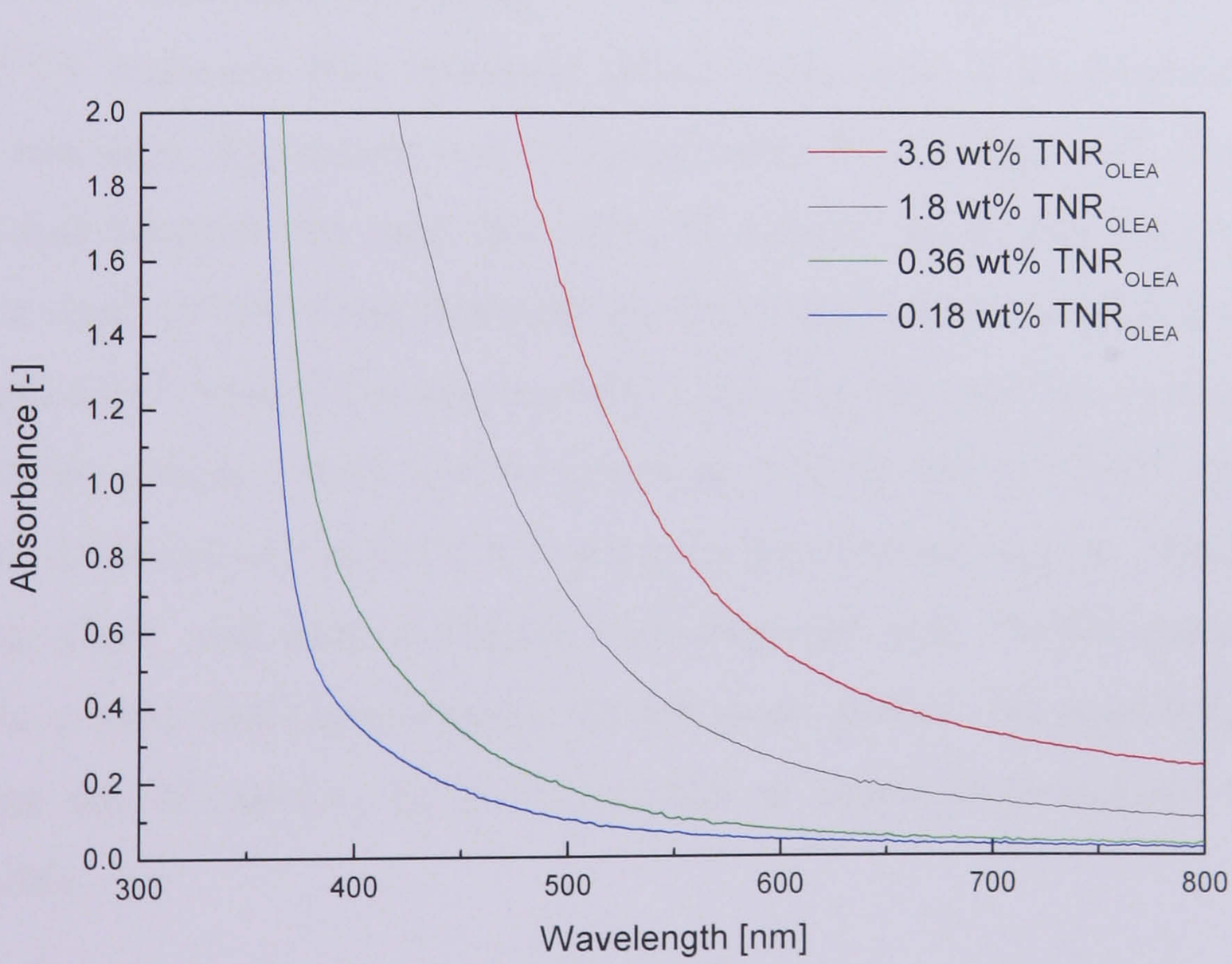


Figure 68 – UV-Vis spectra of TNR_{OA} dispersions in chloroform - function of concentration

4.2.5.1 UV-assisted removal of surface organics and stabilisation of TNR_{OA} dispersions in water

Removal of organics on the surface of TNR_{OA} can be effected in the same manner as for TNR_{TOPO}; by subjecting TNR_{OA} dispersions in chloroform-water to UV, the nanorods undergo a photocatalytic self-cleaning process oxidising the organics to CO_2 and water. The nanorods migrate from the organic phase to the water phase, as described previously (Figure 50) again yielding unstable dispersions. Stabilisation by TMAH was possible in this case as well, but the procedure is much more sensitive to TNR_{OA} concentration than for TNR_{TOPO}. In order to stabilise TNR_{OA}, higher concentrations of TMAH were required, whilst keeping the nanorod concentration low. For instance, the dispersions shown (Figure 69) contain 1 mg ml^{-1} TNR_{OA} and were stabilised with 200 mM TMAH. (cf. 5 mg ml^{-1} TNR_{TOPO} and 100 mM TMAH in Figure 55). This difference can be attributed to intrinsically higher aspect ratio of TNR_{OA}, which increases their hydrodynamic volume and the likelihood of interactions. Additionally, stripping TNR_{OA} takes longer than for TNR_{TOPO}; after two days of UV treatment, they remained almost exclusively in the organic phase. After further two days, the sample was analysed using TGA (Figure 70) and the organic content had decreased by only few wt%. The dispersion at this stage still appeared dark as a result of OA. From this point on, the dispersion was washed and centrifuged daily until day 7, when TGA was recorded again and this time the organic content was much lower, around 7 wt%. Slower stripping is likely due to higher organic content and cross-linked nature of the OA coating on the nanorod surface. These dispersions could be, albeit with some difficulty, well-dispersed with TMAH and although it is plausible to state that some organics remain at the surface, for practical purposes the procedure can be used to achieve a transfer of titania from organic into aqueous dispersions.

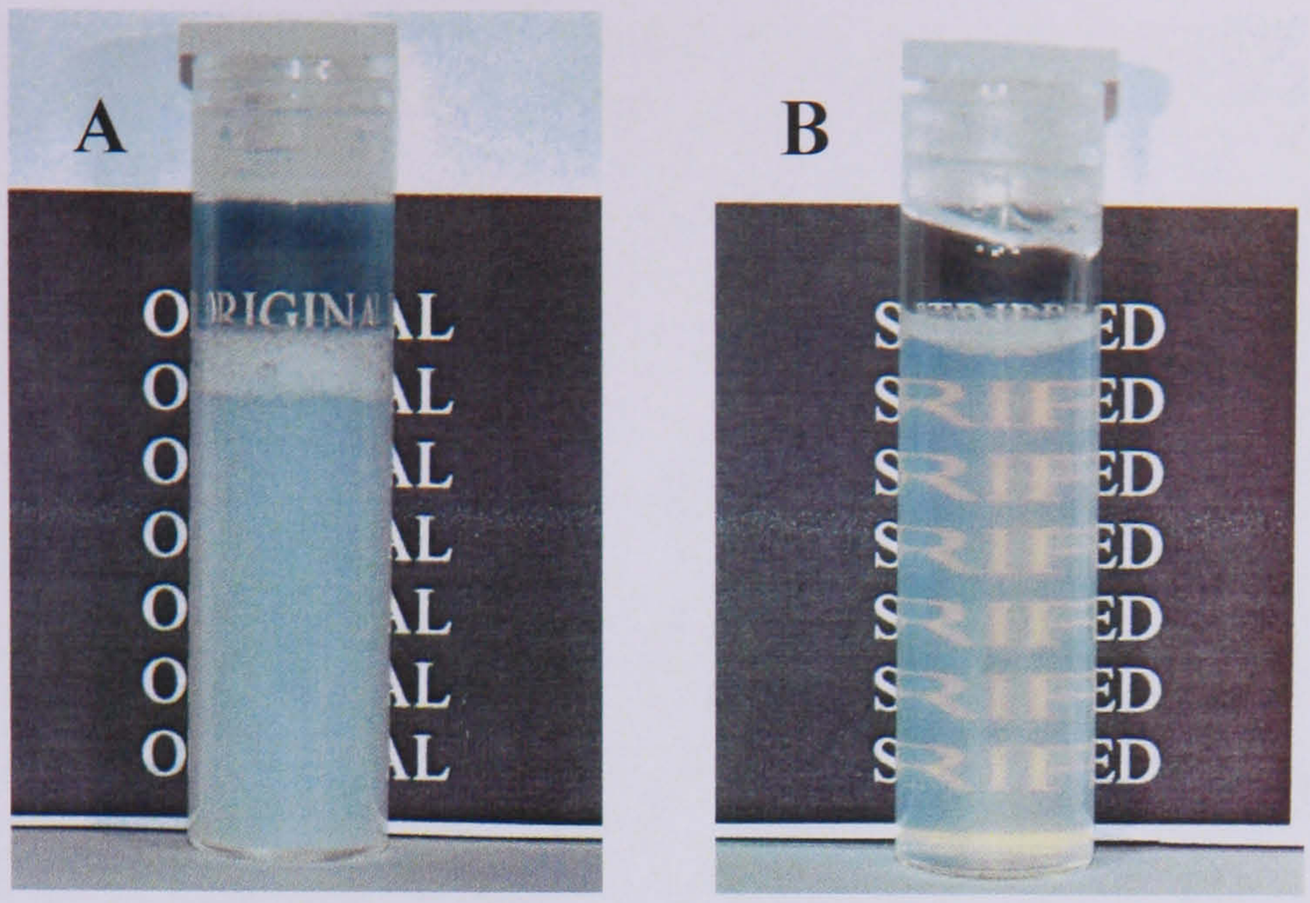


Figure 69 – TNR_{OA} dispersions in water (1 mg ml^{-1} TiO_2): (a) stripped (b) stripped with 200 mM TMAH

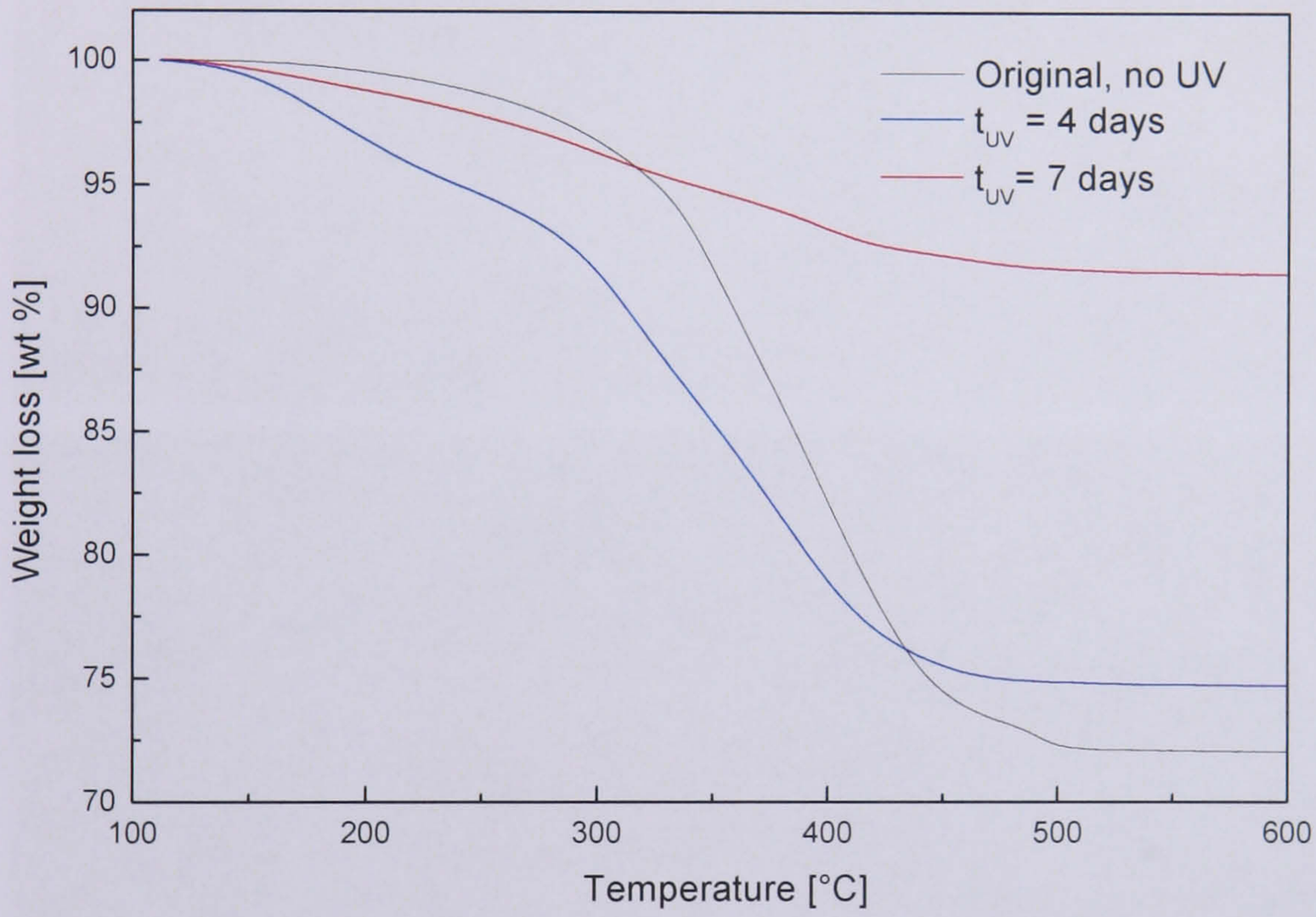


Figure 70 – TGA curves for TNR_{OA} - effect of UV irradiation time

As in the case of TNR_{TOPO}, the stripping procedure does not alter the nanorod morphology in any way, which was confirmed with TEM. The micrographs (Figure 71) reveal a more agglomerated product, but the individual crystals can still be discerned. The anatase crystal phase also remains unchanged, as confirmed by Raman spectroscopy (Figure 72). The fluorescence observed for the as-prepared TNR_{OA} (Figure 65) can still be observed, but to a much lower extent, due to the removal of organic material.

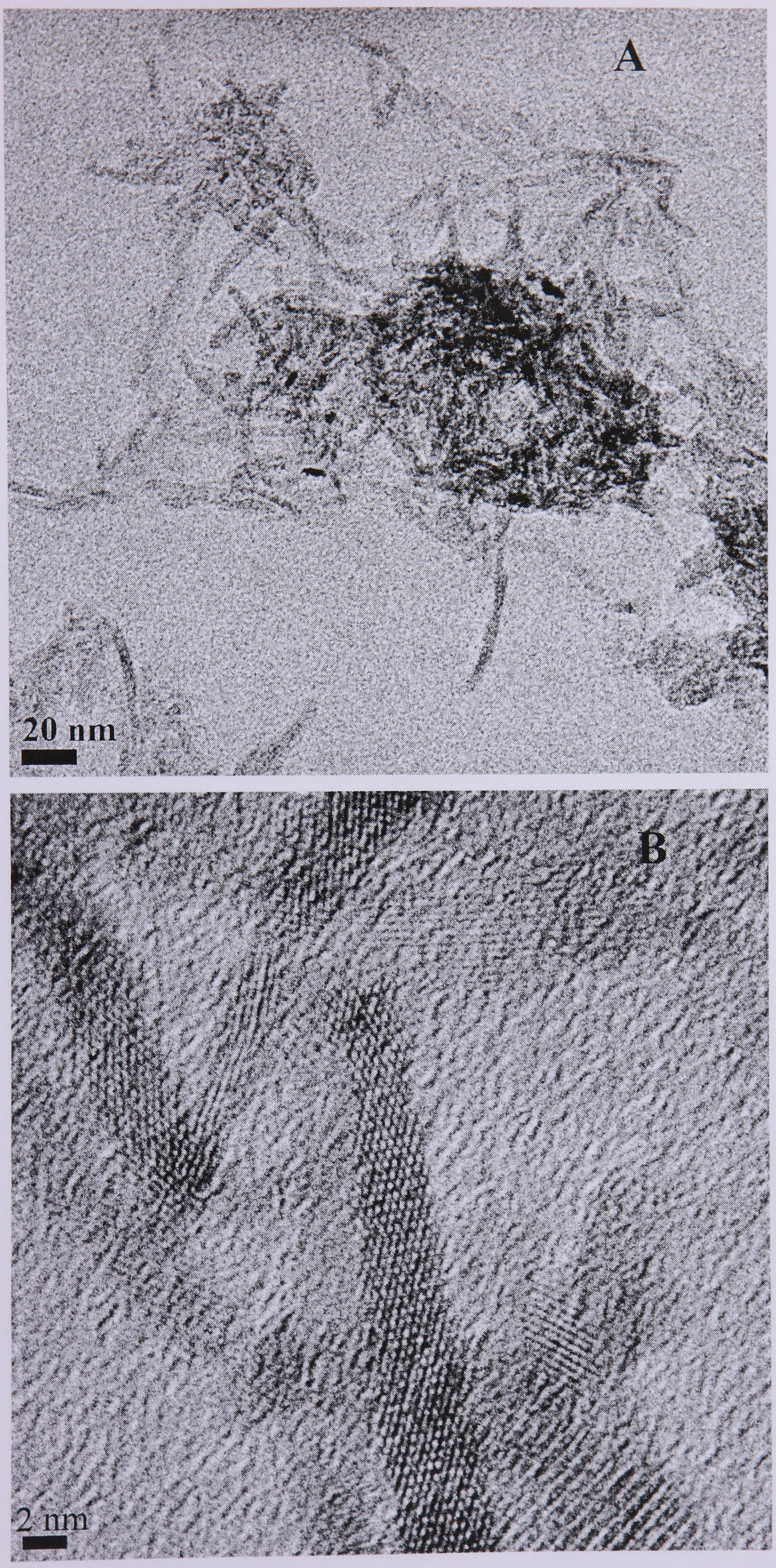


Figure 71 – TEM of stripped TNR_{OA}:

(a) low-resolution and (b) high resolution micrograph

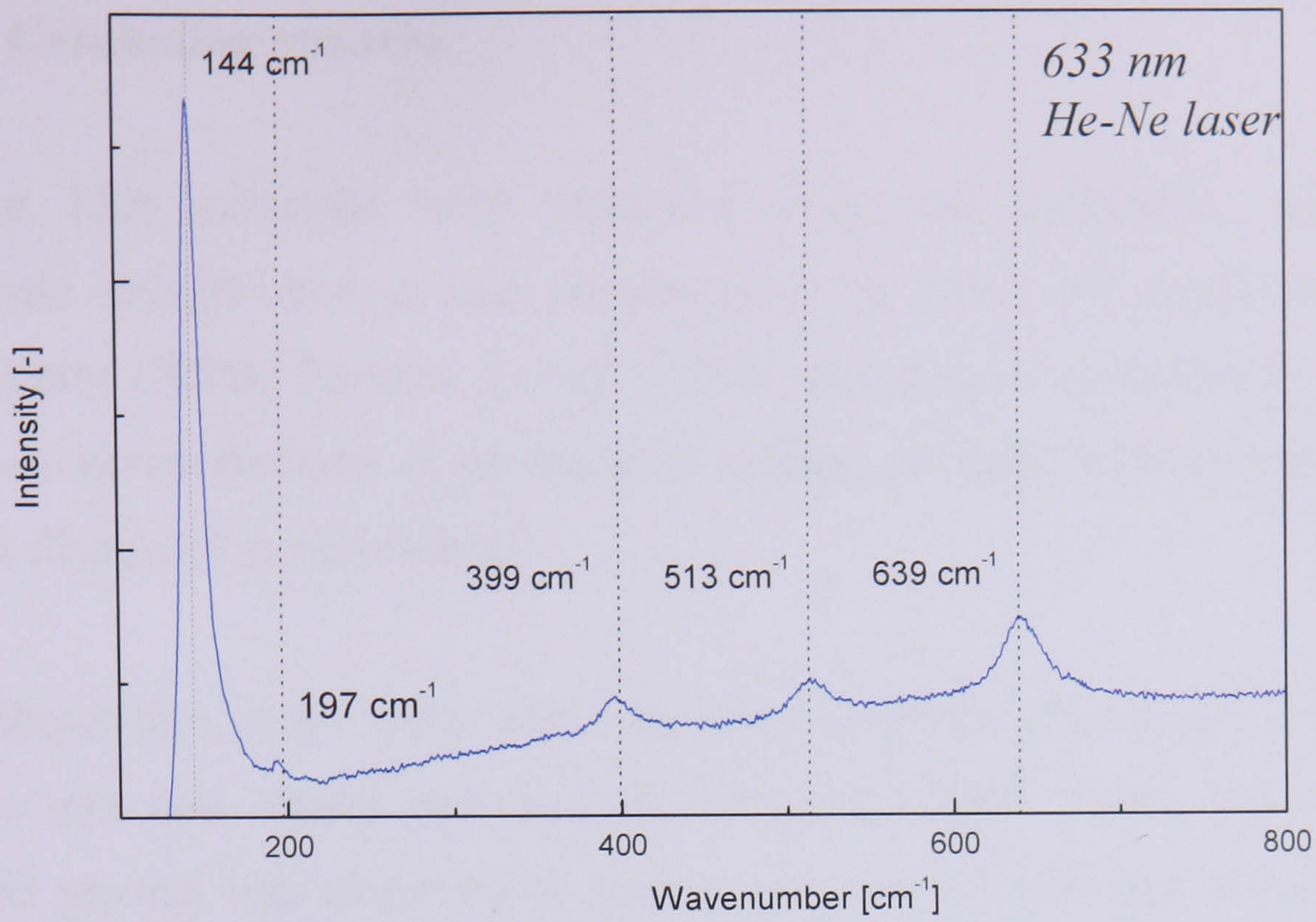


Figure 72 – Raman spectrum of stripped TNR_{OA}

4.2 Concluding remarks

Anatase TiO_2 nanorods were produced using one hydrolytic and two non-hydrolytic sol-gel routes, and characterised in terms of morphology (TEM), crystallinity (XRD, Raman), purity (TGA) and degree of dispersibility. Due to organic functionalisation at the nanorod surface, all three types of nanorods could be well dispersed in chloroform.

TEM shows that, in all cases, nanorods grow preferentially along the c-axis of the anatase unit cell, which was also confirmed by XRD. Using OA to direct the nanorod growth was observed to lead to more monodispersed as well as longer and, therefore, higher aspect ratio crystals than the combination of TOPO and dodecylamine. On the other hand, TNR_{OA} have twice as much organic material on their surface than TNR_{TOPO}, which lowers the overall purity and slows the stripping process.

The synthesis of TNR_{TOPO} was demonstrated to give a very consistent product, in terms of yield, product purity and quality. Variation of several parameters was considered briefly in order to understand the sensitivity of the process and also to optimise the product.

The major finding described in this chapter is the new procedure for removal of organics from the nanorod surface, without compromising the nanorod morphology or crystallinity. Initial attempts to 'clean' the nanorod surface using dialysis were not successful, which lead to the development of stripping method by UV light. It was shown that subjecting nanorod dispersions to UV in an aerated environment, initiates the photocatalytic mechanism of TiO_2, which leads to oxidation of surface-bound organic material. This is a powerful tool can be used to change the surface character of the nanorods and although irreversible, it is immensely useful for composite processing, whereby water-soluble polymers can be directly blended with aqueous TNR dispersions.

Following the removal of the organic ligands, the nanorods tend to agglomerate and form unstable dispersions in water. Stabilisation can be re-established using quaternary ammonium hydroxides, such as TMAH. Importantly, although the stabilising effect of TMA^+ in case of titania is known, it has been thus far exploited mainly in-situ during the hydrolytic synthesis, where the molecule is mainly used as a polycondensation reaction catalyst. In the current context TMAH is added to agglomerates of stripped TNR as a pure dispersant and is able to achieve stabilisation and transparency. Once dispersed individually, the surface can be further modified by sol-gel chemistry. In a sense, the stripping procedure brings together the advantages offered by high temperature non-hydrolytic synthesis with the well-established methods for stabilising titania surface following hydrolytic synthesis. The stripping process is versatile, as it can be used to degrade different organic ligands, such as in the case of TNR_{TOPO} and TNR_{OA}, although the treatment time varies.

In the case of TNR_{TOPO}, passivation of the photocatalytic activity was attempted by applying a silica-type coating onto the surface. Moderate reduction in photoactivity was observed by observing the kinetics of the degradation of organic dye, which was added to the TNR dispersions. The changes in photoactivity and in the ζ-potential confirm the change in surface chemistry.

5. TiO_2 nanorod – polymer composites*

5.1 Introduction

The dispersions of TiO_2 nanorods produced using the procedures described in Chapter 3 have been used for fabrication of TiO_2 nanorod – polymer composites. Control of the nanorod surface chemistry, using the photocatalytic self-cleaning technique, is critical for solution processing of the composites, as will be demonstrated in this chapter. The dispersions of pristine, organic-capped TNR in chloroform can be readily blended with organic-soluble polymers used in our work – PDLLA and PMMA, to fabricate TNR – PDLLA and TNR – PMMA composites. Conversely, the aqueous nanorod dispersions obtained by the stripping procedure are suitable for incorporation into water-soluble PVA. The basis for selecting these two organic-soluble polymers in particular was to experiment with a commonly used engineering polymer, PMMA, as well as with a more specialised matrix, PDLLA, used for biomedical applications. PVA is a niche polymer, commonly used in adhesives and packaging; the most important feature, as already mentioned, is that PVA is water-soluble, which facilitates composite processing.

Characterisation of the nanocomposite films was performed using the techniques described in Section 3.6, with the aim of analysing the optical, mechanical and thermal properties of the composites in comparison with the pure polymer films and other relevant controls. The stability of the TiO_2 nanocomposite films under UV is all too frequently ignored in research publications, unless the ultimate purpose of introducing TiO_2 into the polymer matrix is to catalyse the degradation. This chapter aims to address this issue more broadly, to compare the influence of the TNRs with that of commercial TiO_2 nanopowders on the photo-stability of the respective composites.

* Section on fabrication and characterisation of TNR-PVA nanocomposite materials formed the basis of a paper draft that is to be submitted

5.2 TNR – PDLLA and TNR – PMMA nanocomposite films

In order to qualitatively demonstrate the optical transparency of the TNR – PDLLA and TNR – PMMA nanocomposites, films on glass slides were fixed onto a sheet of paper, with appropriate sample details printed in the background (Figure 73 and Figure 74, respectively). The nanorod composites retain their transparency to a greater extent than the corresponding composites containing the commercial P25 TiO_2 as filler. For TNR-PDLLA composites (Figure 73A), optical clarity is retained up to around 5 wt% TNR, but begins to degrade for the 9.1 wt% TNR sample and higher TNR contents. The opacity is indicative of nanorod agglomeration and incomplete dispersion. In case of PMMA (Figure 74A), the composites remain transparent for even higher TNR loading fractions, up to 16.7 wt%. One possible explanation is that the PMMA blends, despite higher polymer concentrations in chloroform than PDLLA ones (8 wt% cf. 4 wt%), have a lower viscosity, which greatly facilitates ultrasonic dispersion of titania nanoparticles. Also, the differences in solubility parameters between chloroform and the two polymers might have an effect on the composite processing, and ultimately, optical clarity of the composites.

The composite samples with the P25 TiO_2 commercial filler retain their transparency only for very modest titania contents, up to 0.1 wt% TiO_2 in PDLLA (Figure 73B) and 2.5 wt% TiO_2 in PMMA (Figure 74B). Again, the higher values observed for the P25 TiO_2 – PMMA composites can be explained in an analogous way as for TNR – PMMA composites. For all samples with filler content above these threshold values, severe nanoparticle agglomeration was observed, as evidenced by complete opacity of the films. In the most severe cases (e.g. 16.7 wt% P25 – PDLLA), cracking of the film surface during drying was observed, most likely as a result of agglomerated particles, which act as defects and make the films brittle. The P25 TiO_2, unlike the TNRs, does not have a stabilising organic capping on the surface, leading to greater agglomeration; these agglomerates, in turn, scatter light more effectively, rendering the composites opaque.



Figure 73 – Scanned images of the as-prepared composite films and pure polymer controls: (a) TNR – PDLLA and (b) P25 TiO_2 – PDLLA

[Note – typical film thickness ~30 μm ± 3 μm]

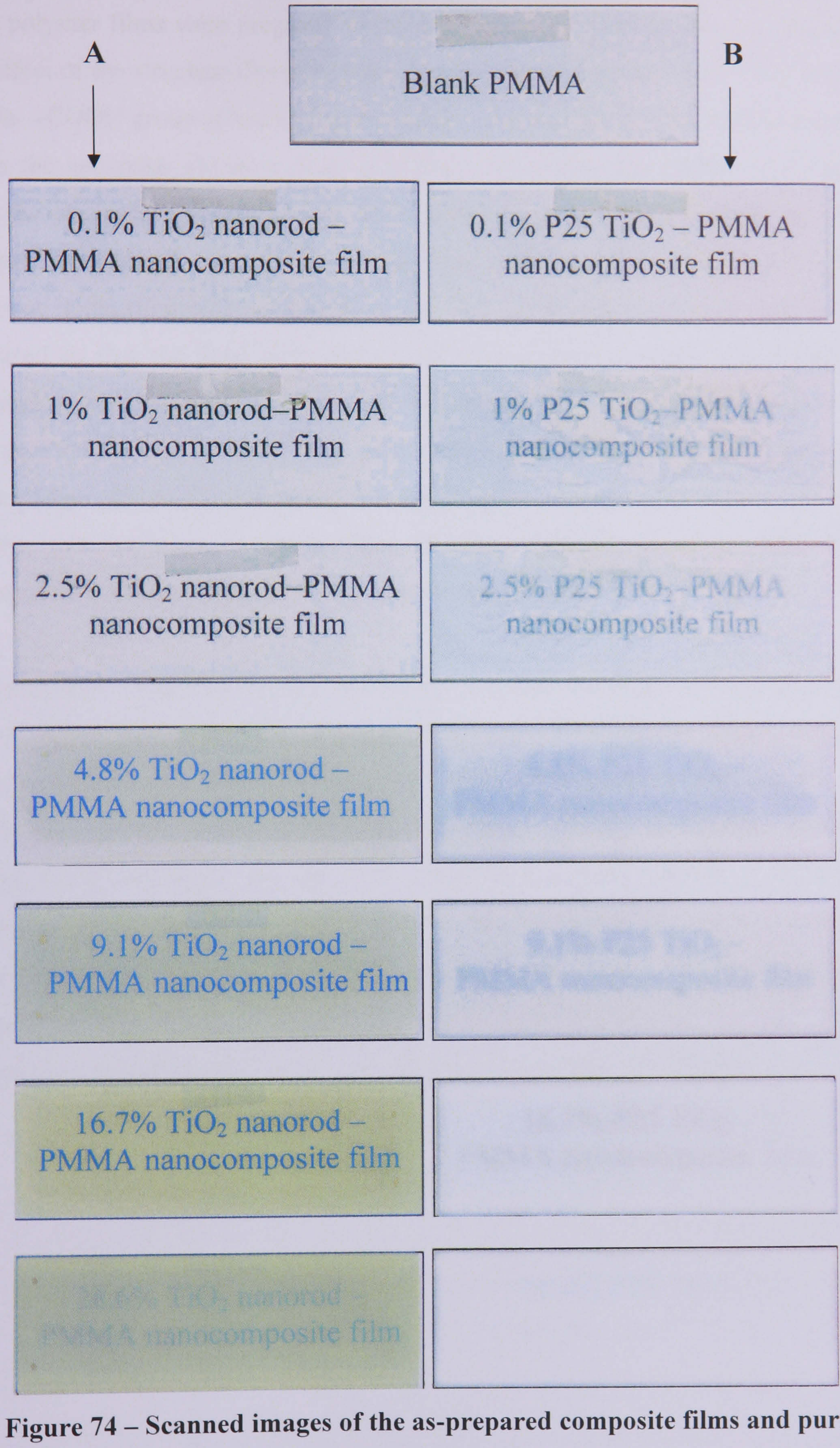


Figure 74 – Scanned images of the as-prepared composite films and pure polymer controls: (a) TNR – PMMA and (b) P25 TiO_2 – PMMA

[Note – typical film thickness ~30 μm ± 3 μm]

Pure polymer films were prepared containing only oleic acid, in order to understand the effect of the structure-directing ligand on the composite properties. Oleic acid has a polar –COOH group at one end, presumably coordinated towards the titania surface, while the non-polar aliphatic chain is oriented away from the surface and interacts with the non-polar polymer chains. This characteristic is helpful in ensuring a good dispersion, although, as will be seen later on, there are many disadvantages to its presence at the filler-polymer interface. The oleic acid-polymer control samples were prepared so that the final films have a 10 wt% content of oleic acid, which was selected as a maximum value that could be expected in a film with very high content of nanorods. In reality, some oleic acid precipitates on the film surface during the drying stage, due to phase separation, suggesting that the solubility limit of oleic acid in the two polymers is lower than 10 wt%. Optically, however, the sample transparency did not change at all upon addition of oleic acid.

Transmission optical microscopy was used to estimate the degree of aggregation and the aggregate size in the PDLLA composites at low TiO_2 content (Figure 75). Pure polymer displayed a smooth morphology; some minor features observed are most likely incompletely dissolved polymer particles or possibly air bubbles developed during the drying stage. For the TNR composites, a small number of aggregates, typically smaller than 10 μm, were observed, whereas typical size for the composites with P25 was 20-30 μm. The agglomerate density increases with increasing titania content, in both cases, however, it is much more pronounced in case of P25 composites, with the 2.5 wt% P25 TiO_2 sample being completely opaque.

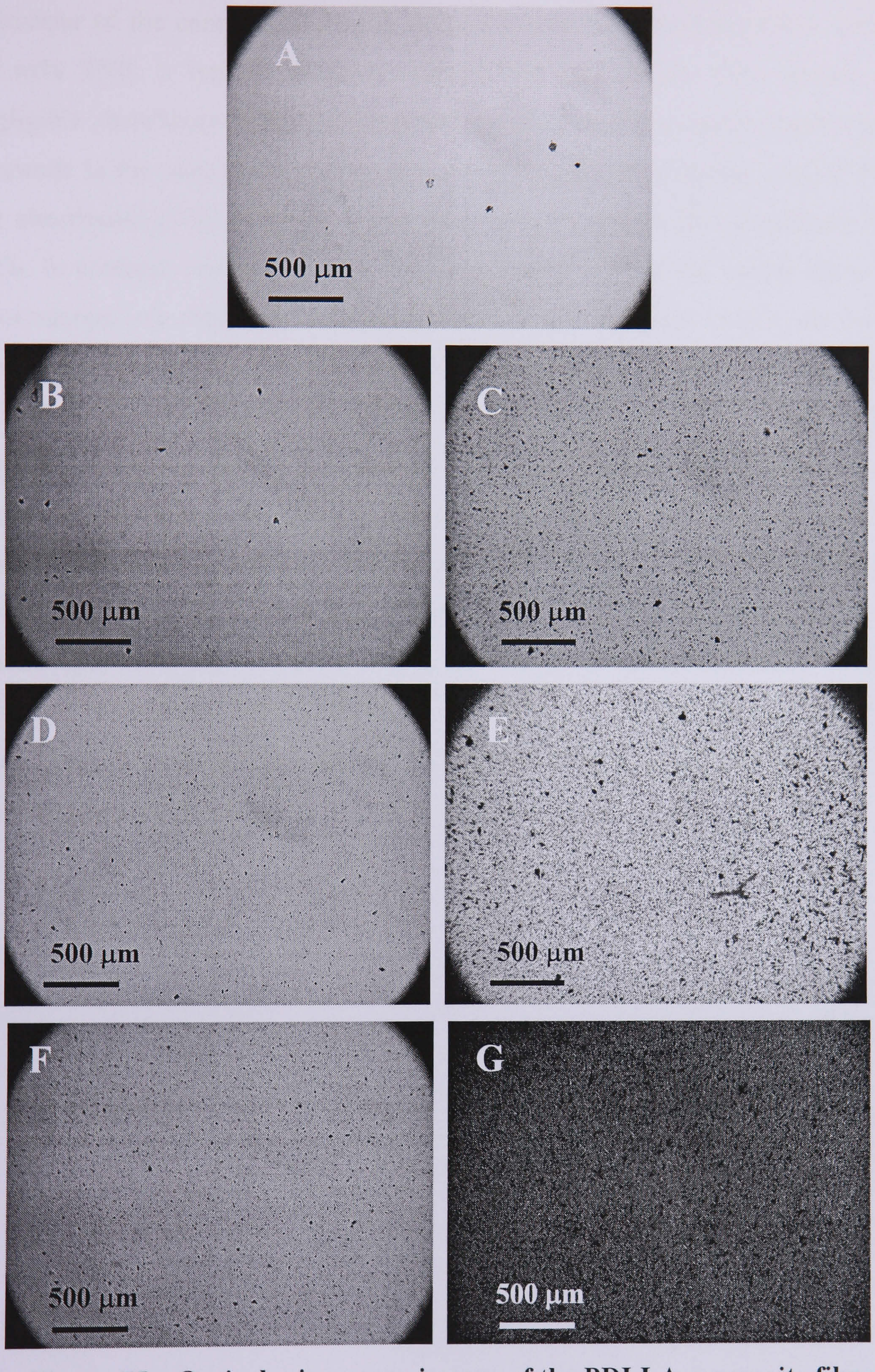
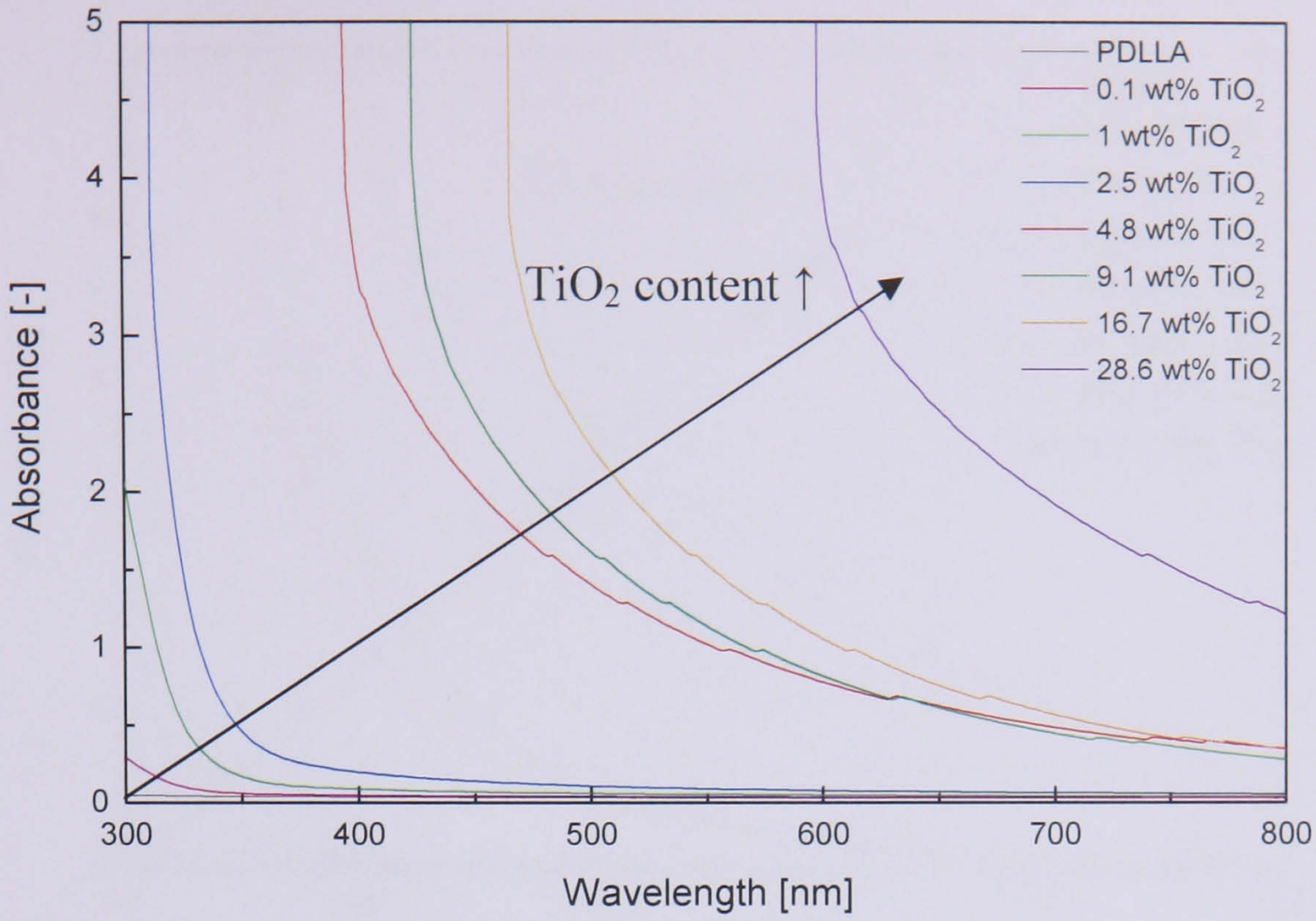


Figure 75 – Optical microscope images of the PDLLA composite films: (a) pure PDLLA; (b, d, f) 0.1 wt%, 1 wt% and 2.5 wt% TNR-PDLLA; (c, e, g) 0.1 wt%, 1 wt% and 2.5 wt% P25 TiO_2-PDLLA

UV-Vis spectroscopy was used to provide a more quantitative measure of the optical behaviour of the composites (Figure 76 and Figure 77). For composites with up to 2.5 wt% TNR, a typical spectrum (Figure 76A and Figure 77A) reveals almost negligible absorbance in the visible range; this result confirms good dispersion of the nanorods in the matrix, due to the absence of significant scattering. Below 400 nm, the absorbance of the composites increases sharply, due to UV-absorbance edge of TiO_2. In contrast, composites with P25 TiO_2 scatter light in the visible range due to poor nanoparticle dispersion. UV absorption was also observed in this case, however, the absorption edge does not rise quite as sharply as for the TNR composites. Having a well-defined absorption boundary is clearly desirable for optical limiting applications and in this particular case, UV-A filtering. In agreement with the sample images of the composites (Figure 73 and Figure 74), TNR – PDLLA and PMMA samples, with loading fractions above 4.8 wt% and 16.7 wt% TNR, respectively, display significant light scattering in the visible portion of the spectrum. For a fixed wavelength, the degree of opacity can be measured as a function of TNR loading. For a fixed TNR loading, PMMA composites scatter light substantially less than PDLLA ones, again indicating better dispersion. The absorbance scales proportionately with the increasing TNR content.

A



B

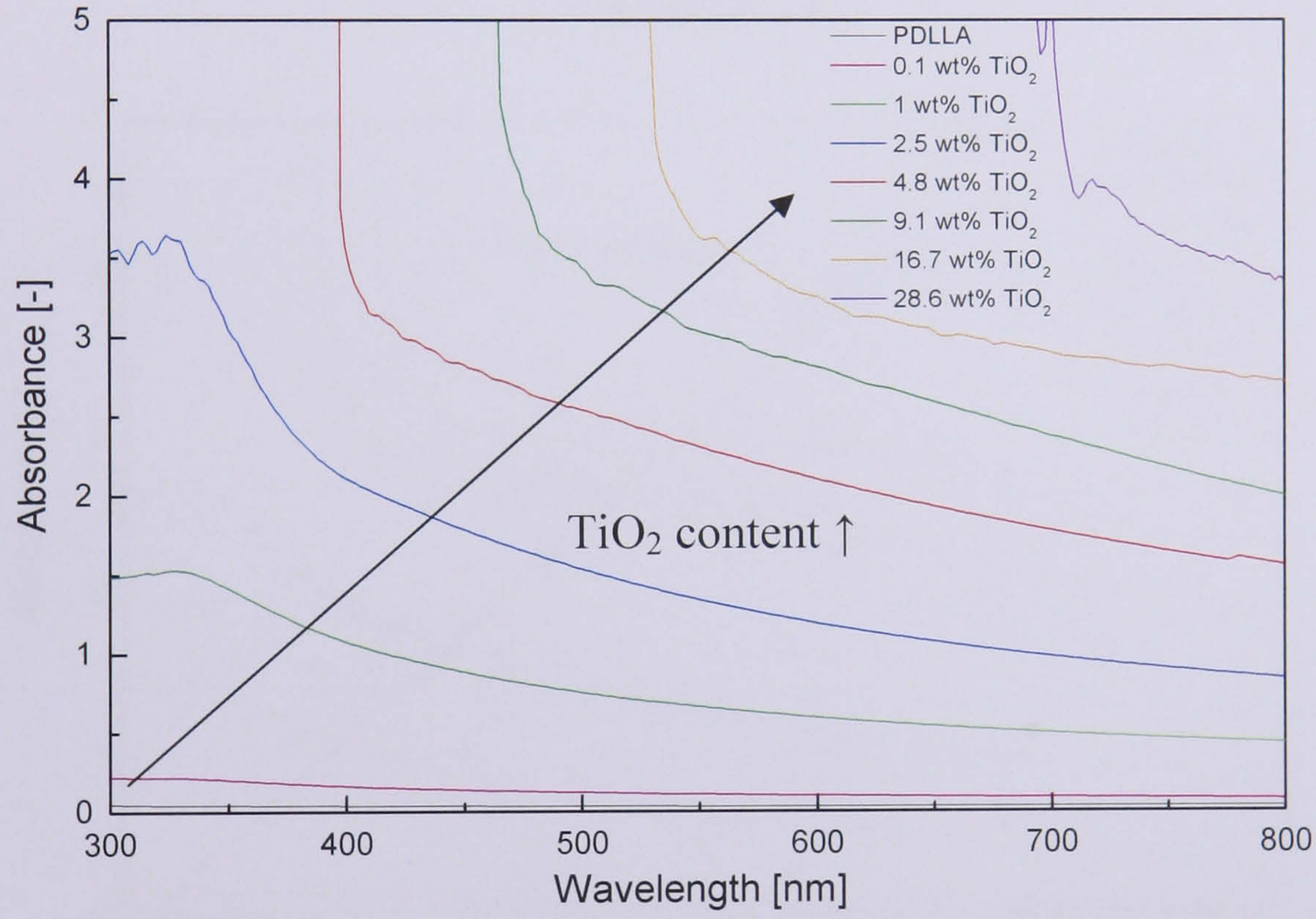


Figure 76 – UV-Vis spectra of the PDLLA composites filled with: (a) TNR and (b) P25 TiO_2

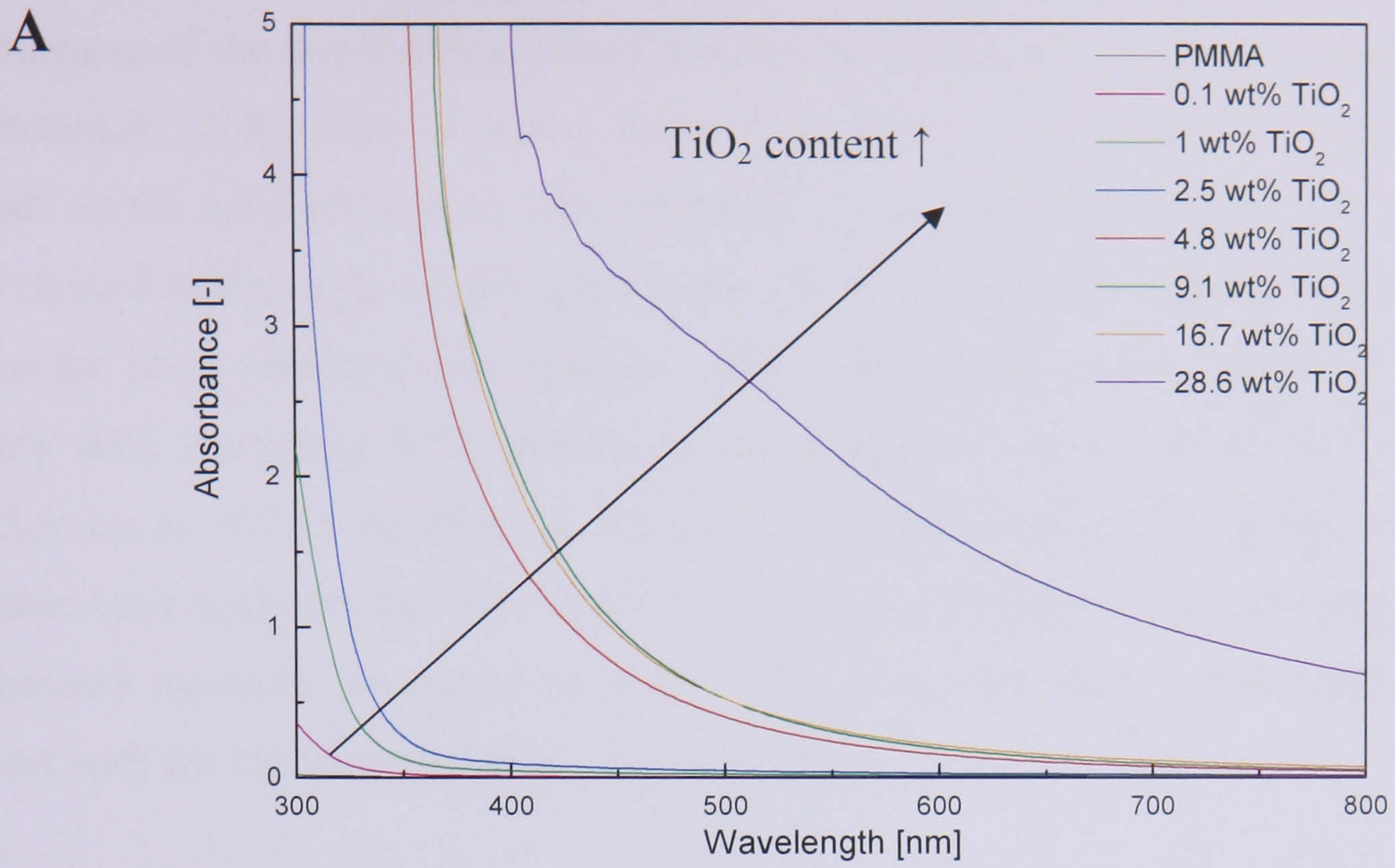


Figure 77 – UV-Vis spectra of the PMMA composites filled with: (a) TNR and (b) P25 TiO_2

The surface properties of the TNR-PDLLA composites were assessed by measuring the contact angle of water on the films, using the sessile drop method. Contact angle is a measure of the non-covalent forces between the liquid and the first monolayer of the material; in the case of strong interactions between the two, the liquid drop spreads on the solid and wets it. The wettability of the pure PDLLA by water is low, as evidenced by the high contact angle value (94.5°; Figure 78), because the polymer molecules have relatively low polarity. The water contact angle increases fairly linearly with increasing TNR loading in the composite – from 94.5° for the pure PDLLA up to 107.3° for PDLLA with 2.5 wt% TNR, indicating that the surface becomes more hydrophobic. This observation can be explained by the fact that the as-synthesised nanorods are coated by a non-polar oleic acid layer, which should not interact with the highly polar liquid used as a probe.

Conversely, a decrease in the contact angle from 94.5° to 81.7°, measured for the pure PDLLA films before and after 1 day of UV-A irradiation, respectively, was explained by the activation of the polymer surface. Oxidative processes at the polymer surface lead to formation of different types of surface groups that strongly affect the surface wettability, e.g. carbonyl, hydroxyl and hydroperoxides[350]. The contact angle decreases, again linearly, as the TNR loading fraction is increased, from 81.7° for the pure PDLLA to 53.3° for 2.5 wt% TNR. UV irradiation activates the photocatalytic mechanism of TiO_2, which catalyses the degradation of the OA capping ligands, and, subsequently, the polymer matrix. The polymer oxidation also exposes the titania at the surface, which is naturally hydrophilic, once stripped of OA, enhancing the hydrophilic nature of the composites. Similar experiments were carried out with P25 TiO_2 – PDLLA nanocomposites; however, the complete data-set could not be obtained, since in many cases the contact angle was practically zero (i.e. complete wetting / superhydrophilicity). The irradiated composite samples containing P25 exhibited greater surface roughness (observed by naked eye) and for the highest-loading sample with 2.5 wt% TiO_2, surface of the composites becomes cracked and chalking (degradation of the polymer binder, exposing the filler particles) was evident. By comparison of the wetting behaviour of the two sets of composites, it can be concluded that the commercial P25 TiO_2 nanoparticles behave as a much more aggressive photocatalyst of the composites than TiO_2 nanorods. However, one must not exclude the possibility of photocatalytic passivation of TNR surface by the SDAs.

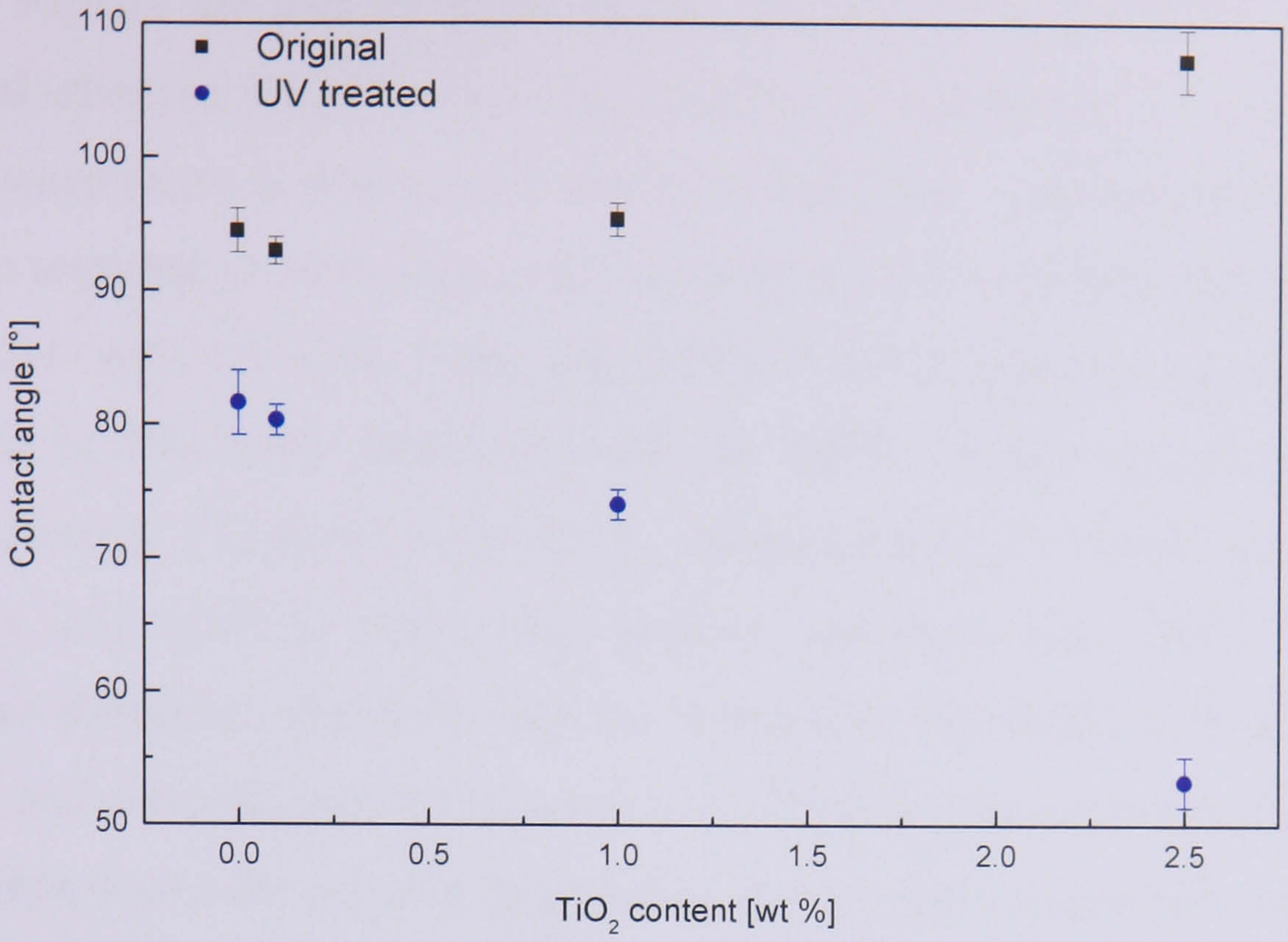


Figure 78 – Contact angles for TNR-PDLLA composite films measured by DSA

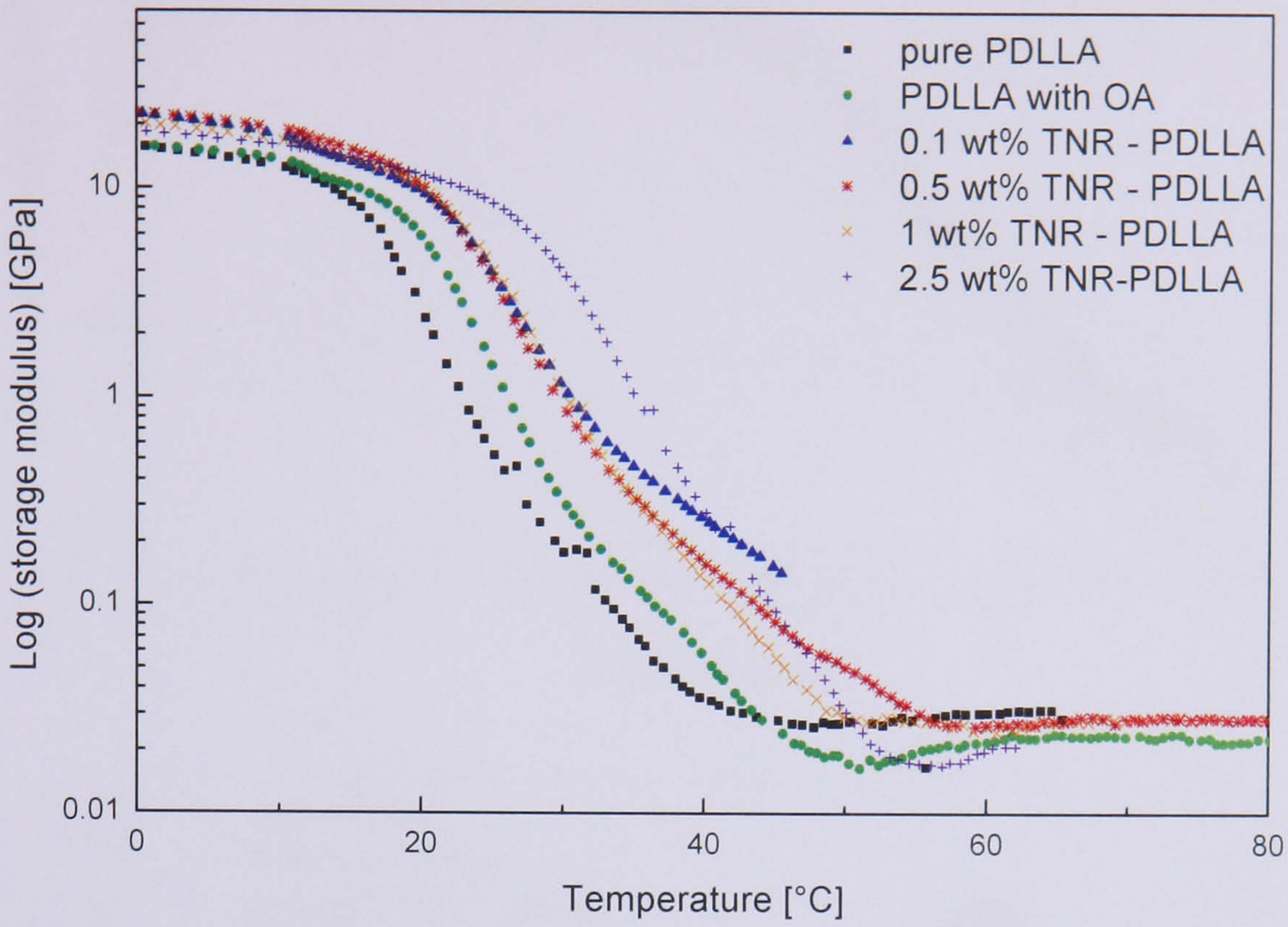
TNR – PDLLA and TNR – PMMA nanocomposite films were analysed using DMTA, to measure mechanical and thermal properties, specifically the storage modulus and the glass transition temperature. The DMTA results are presented as separate plots of the storage modulus and tan δ (the dampening factor or the ratio of loss to storage moduli), both as a function of temperature. The composites were fabricated and analysed using DMTA in two batches – composites with low (up to 2.5 wt%) and high (4.8 wt% to 28.6 wt%) TiO_2 nanorod loading fraction; the DMTA results will be presented in this order and according to the polymer system used. Although the DMTA tests were carried out by applying stress to the samples at frequencies of 1 Hz and 10 Hz, only the results for 1 Hz are included in the main body of this thesis, since the difference between the two sets is not significant (see Appendix 7.1 for the 10 Hz results).

The plots of the storage modulus against temperature for the low TNR loading PDLLA films (Figure 79A) do not vary significantly with the nanorod content. Although there is a suggestion of an increase in the modulus of the glassy phase, the differences between the curves are within the error margin of the testing equipment and indicate that adding TNR to PDLLA does not significantly affect the stiffness of

the composites. The presence of the oleic acid at the nanorod-polymer interface could possibly explain the lack of improvement. OA acts as a plasticizer and prevents interfacial adhesion. Graphs of tan δ as a function of temperature (Figure 79B) reveal that the temperature at which tan δ reaches a maximum - corresponding to the glass transition temperature of the films - increases from 24.5°C for pure PDLLA to 37.3°C for PDLLA with 2.5 wt% TNR. Pure PDLLA has a reported T_g around 57°C[351] (measured by DSC); the values measured by DMTA in this case are considerably lower. Although it is common for the T_g measurements to be lower if a mechanical technique (e.g. DMTA) rather than thermal technique (e.g. DSC) is used, the significant difference observed must be addressed. The PDLLA is a hygroscopic polymer, and although care has been taken to minimise exposure to ambient humidity, it is possible that some polymer degradation by hydrolysis might have occurred. The addition of TNRs makes the composites more hydrophobic, rendering them less susceptible towards degradation, which is in agreement with an observed increase in the T_g. However, even the highest T_g value measured (37.3°C for 2.5 wt% TNR) is lower than expected; most likely due to plasticisation of the matrix by oleic acid at the interface.

Perhaps unsurprisingly, DMTA curves for the low loading TNR-PMMA composites show a similar trend, i.e. that there is no apparent change in stiffness with the introduction of nanorods (Figure 80A). However, pure PMMA films with 10 wt% oleic acid show a marginal reduction in stiffness as compared with the pure polymer, thus supporting the argument that oleic acid acts as a plasticizer. Unlike the TNR-PDLLA composites, the values for T_g of low loading TNR-PMMA composites show no conclusive trend: 80.6°C for the pure PMMA and between 77°C and 80.8°C for PMMA with TNR. PMMA is not hygroscopic; since no significant changes were observed in the T_g for the PMMA composites, this further supports the argument that the reduction of T_g in the PDLLA case is due to hydrolysis of the matrix. Compared with the literature values for pure PMMA (~110°C, by DSC[313]), the measured values are lower, again possibly due to differences in measuring the T_g by the two techniques. The PMMA with oleic acid had a T_g of 74.8°C, suggesting again that the oleic acid is a plasticizer.

A



B

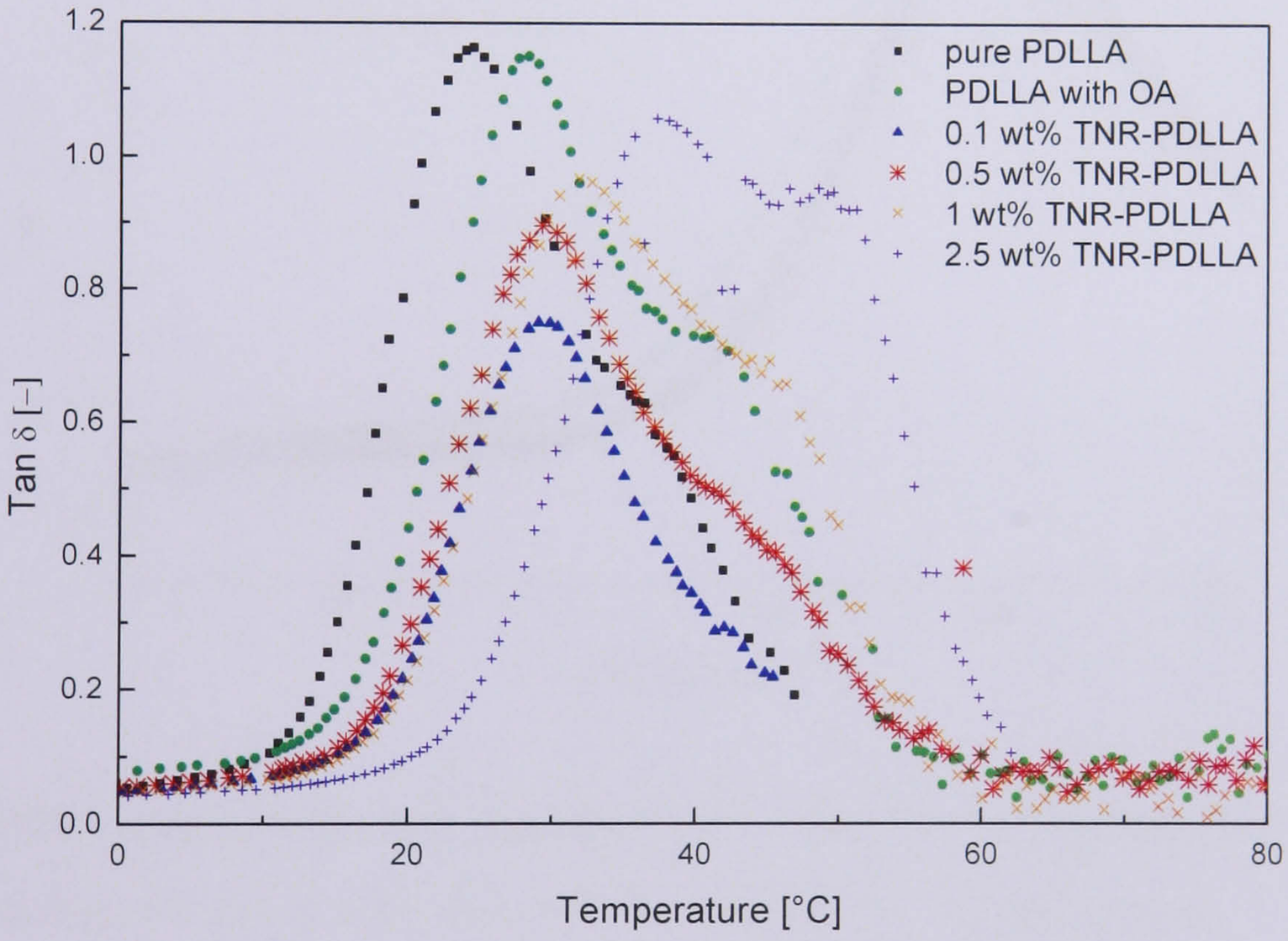
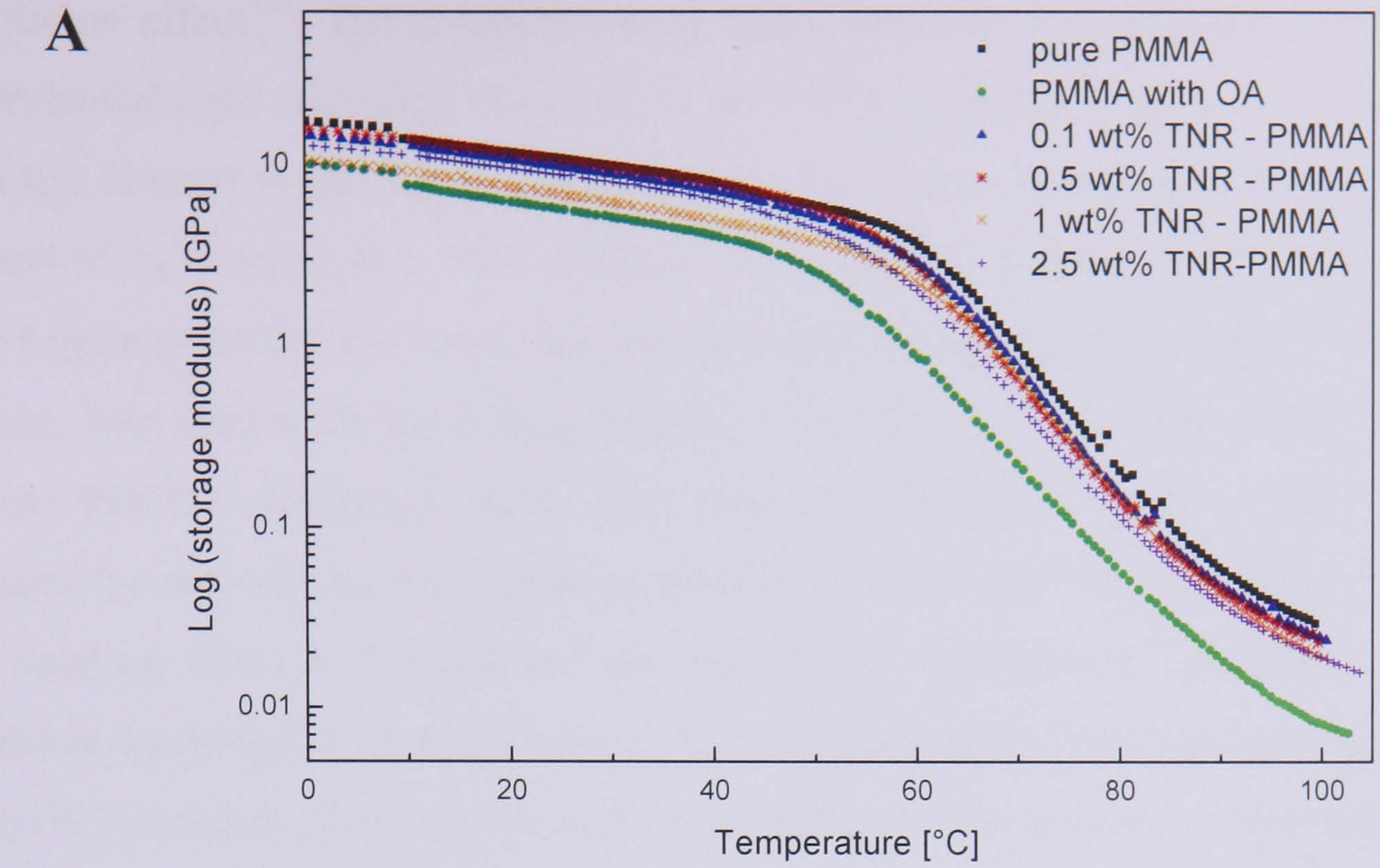


Figure 79 – DMTA results for low loading TNR – PDLLA composites at 1 Hz: (a) Storage modulus and (b) tan δ as a function of temperature



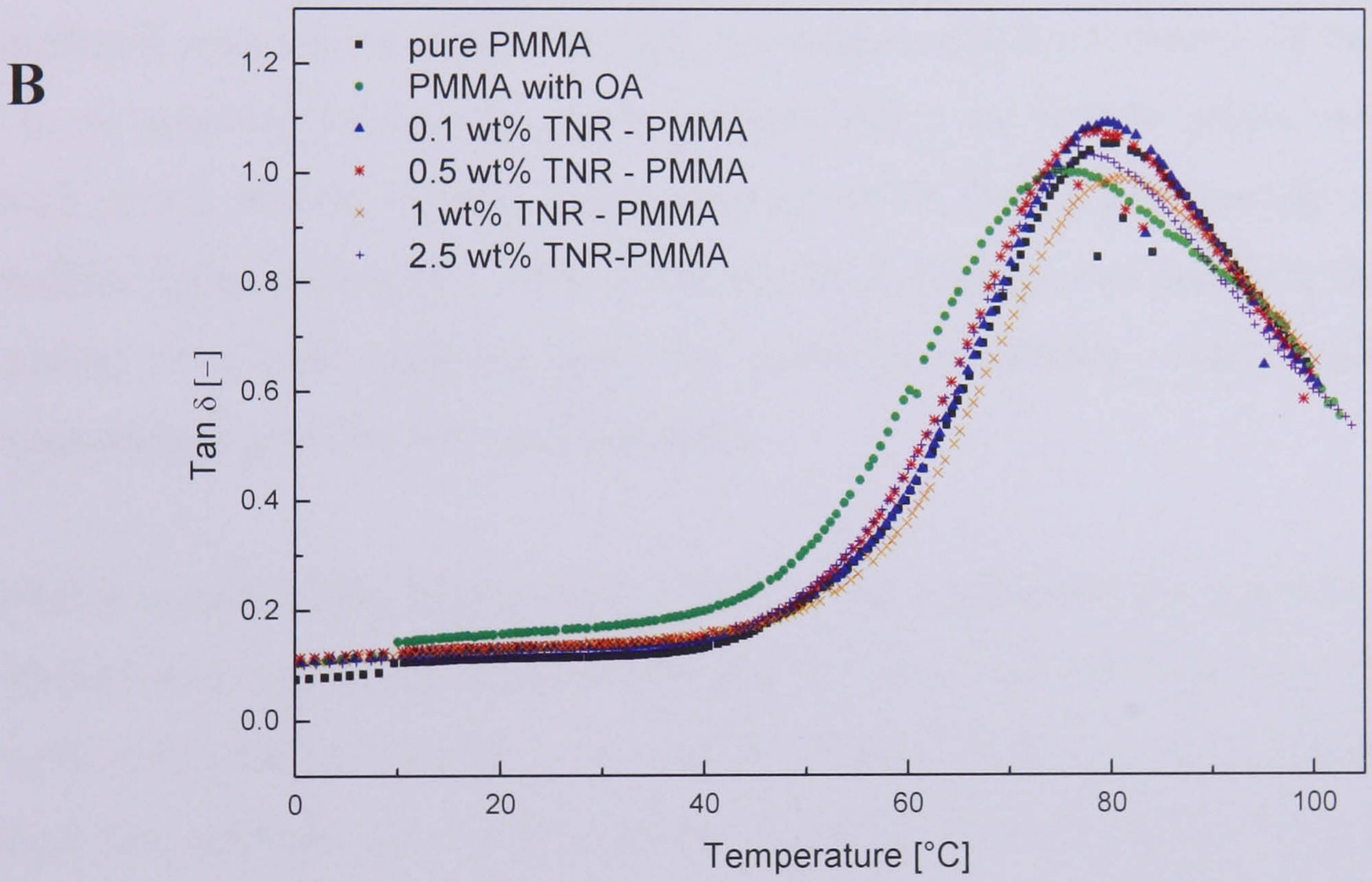


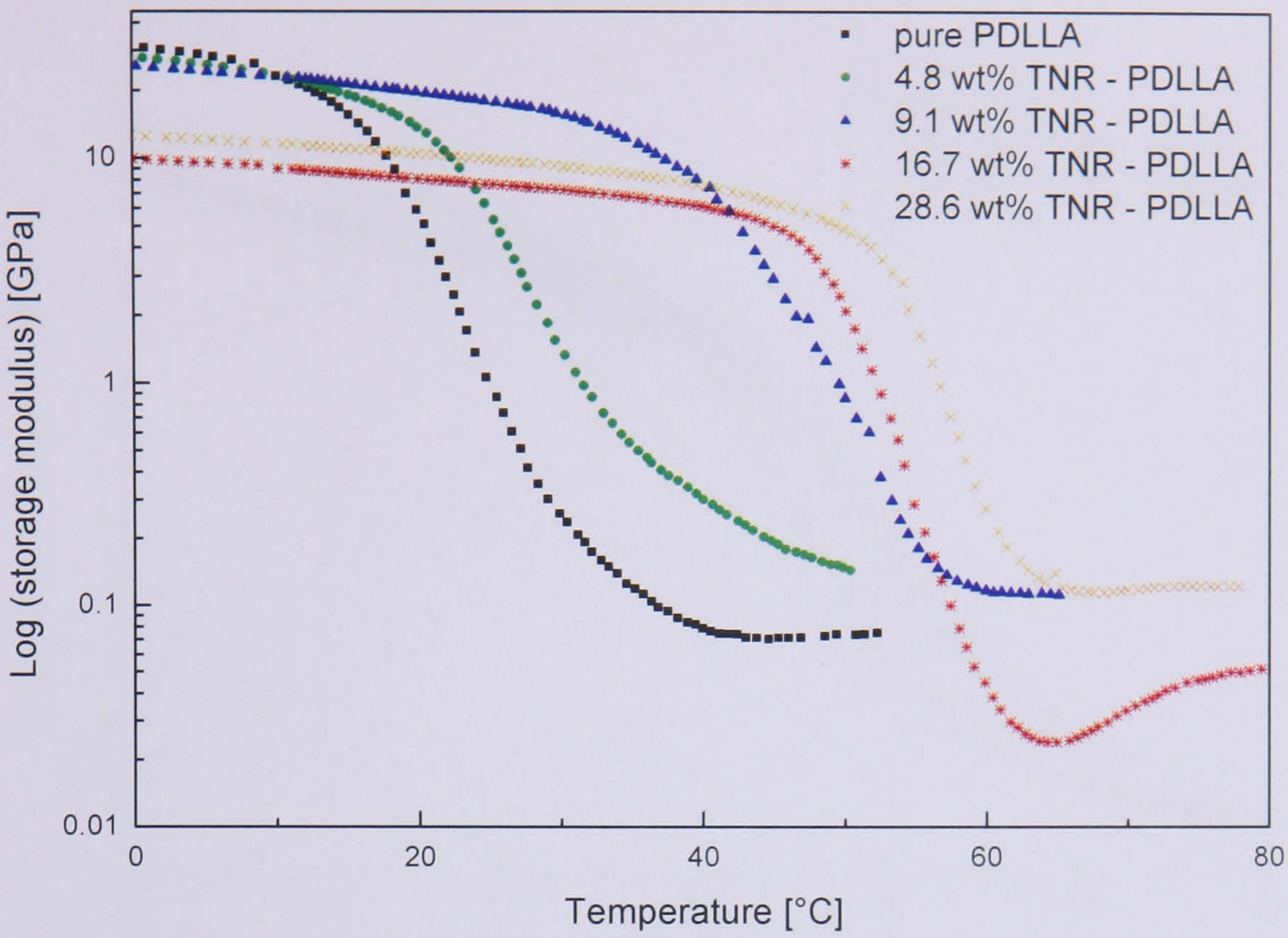
Figure 80 – DMTA results for low loading TNR – PMMA composites at 1 Hz: (a) Storage modulus and (b) tan δ as a function of temperature

Clearly, the surfactant presence at the filler-polymer interface is disadvantageous if the aim is to increase the storage modulus and the glass transition temperature of the composites. Indeed, when the results for high loading TNR-PDLLA films were considered (Figure 81A), further introduction of TNR causes the storage modulus to further decrease compared to the pure polymer. At these very high loadings, the TNR are likely to begin to form a continuous network across the entire sample, a so called

'percolation effect[352]. The combination of likely nanorod agglomeration, evidenced by substantial light scattering observed in the UV-Vis spectra (Figure 76A), and the high oleic content at the nanorod-polymer interface led to the observed decreases in stiffness of the composites. The stiffness of the highest loading sample (28.6 wt% TNR) begins to reverse the trend, but was still significantly lower than that of the pure polymer. The results for tan δ (Figure 81B) show that the T_g increases from 24.5°C for pure PDLLA through to 60°C with increasing the TNR loading. This can be explained by considering two opposing effects; on one hand, for pure PDLLA / low TNR loading PDLLA composites, the mechanical and thermal behaviour of the material is dominated by the polymer itself, i.e. the reduction from literature values in T_g (~57°C) probably arises due to hydrolytic damage of the polymer. Conversely, for composites with high TNR loading, the percolation results in formation of the oleic acid-mediated nanorod network; although the increased hydrophobicity of the films leads to an apparent increase in T_g, it is likely that even higher values would be observed in the absence of OA. Closer inspection of Figure 81B reveals that for intermediate TNR loading (9.1 wt% TNR), the tan δ displays two peaks; in this case two phases (i.e. both polymer and OA network-dominated) clearly contribute simultaneously to give the two separate peaks.

The DMTA results of the high loading TNR-PMMA composites are reported for the pure PMMA and composites with 4.8 wt% and 9.1 wt% TNR only; the 16.7 wt% and 28.6 wt% TNR-PMMA samples were very brittle and testing led to their immediate breakage. Nevertheless, the available results (Figure 82A) give evidence that initially, for 4.8 wt% TNR-PMMA sample, the storage modulus is increased compared to pure PMMA, but then decreases for 9.1 wt% TNR-PMMA films, to about the same value as for original PMMA. Extensive nanorod agglomeration (refer to Figure 77A for UV-Vis spectra of the composites) and the presence of oleic acid at the filler-matrix interface limits the reinforcement of the composites. Based on the measurements of tan δ (Figure 82B), an increase in T_g was observed with increasing titania content, from 80°C for pure PMMA to 87°C for PMMA with 9.1 wt% TNR.

A



B

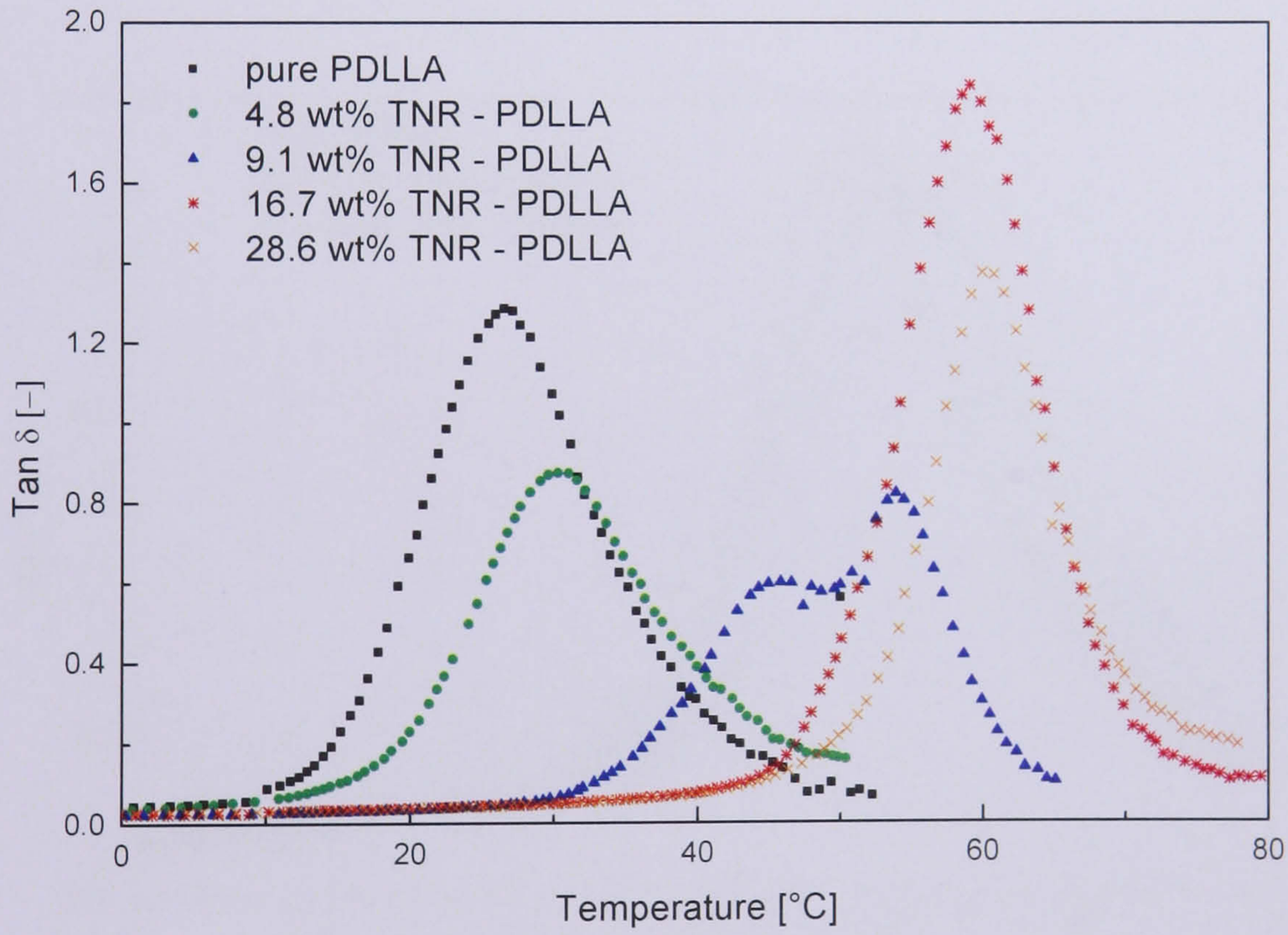
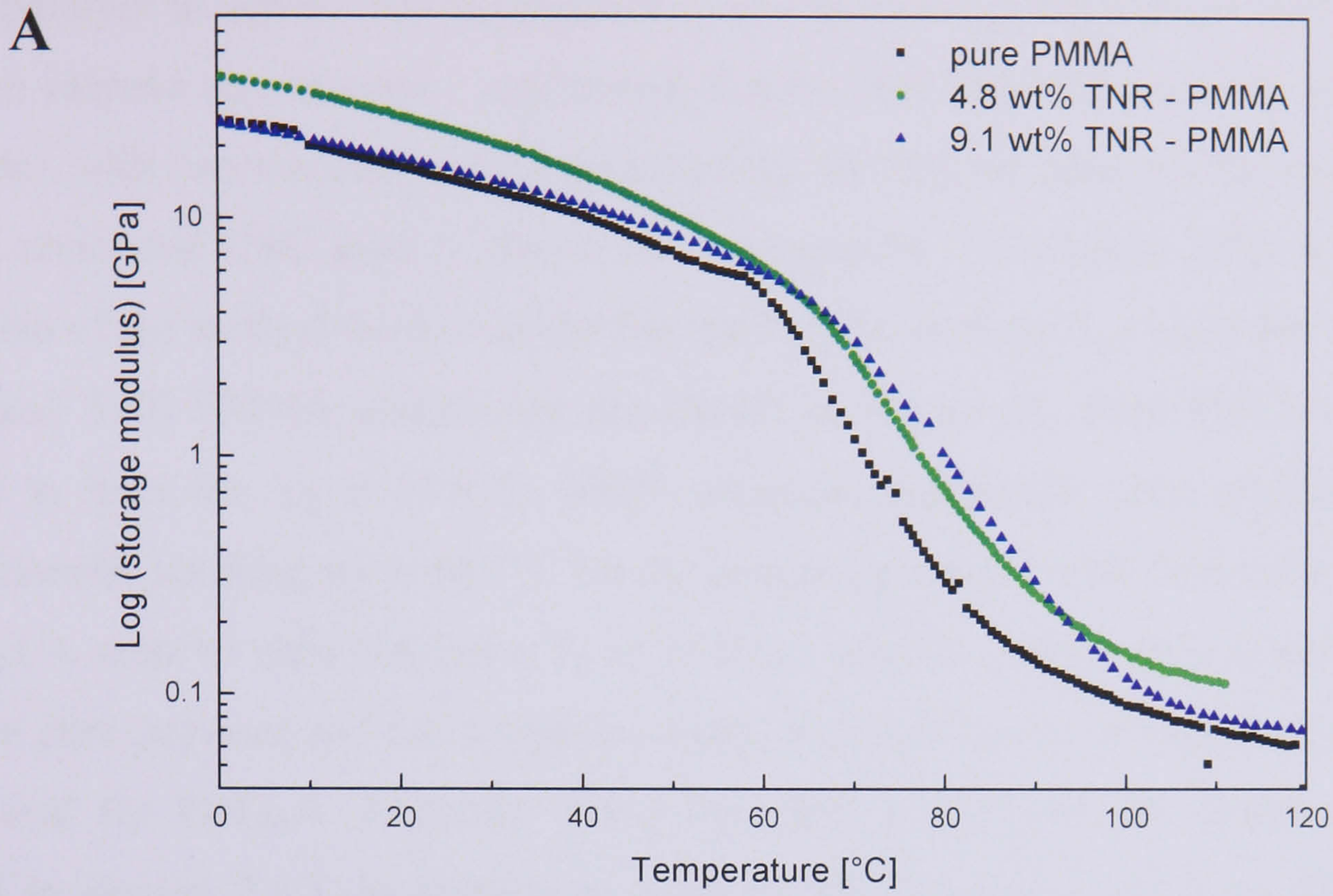


Figure 81 – DMTA results for high loading TNR – PDLLA composites at 1 Hz: (a) Storage modulus and (b) tan δ as a function of temperature



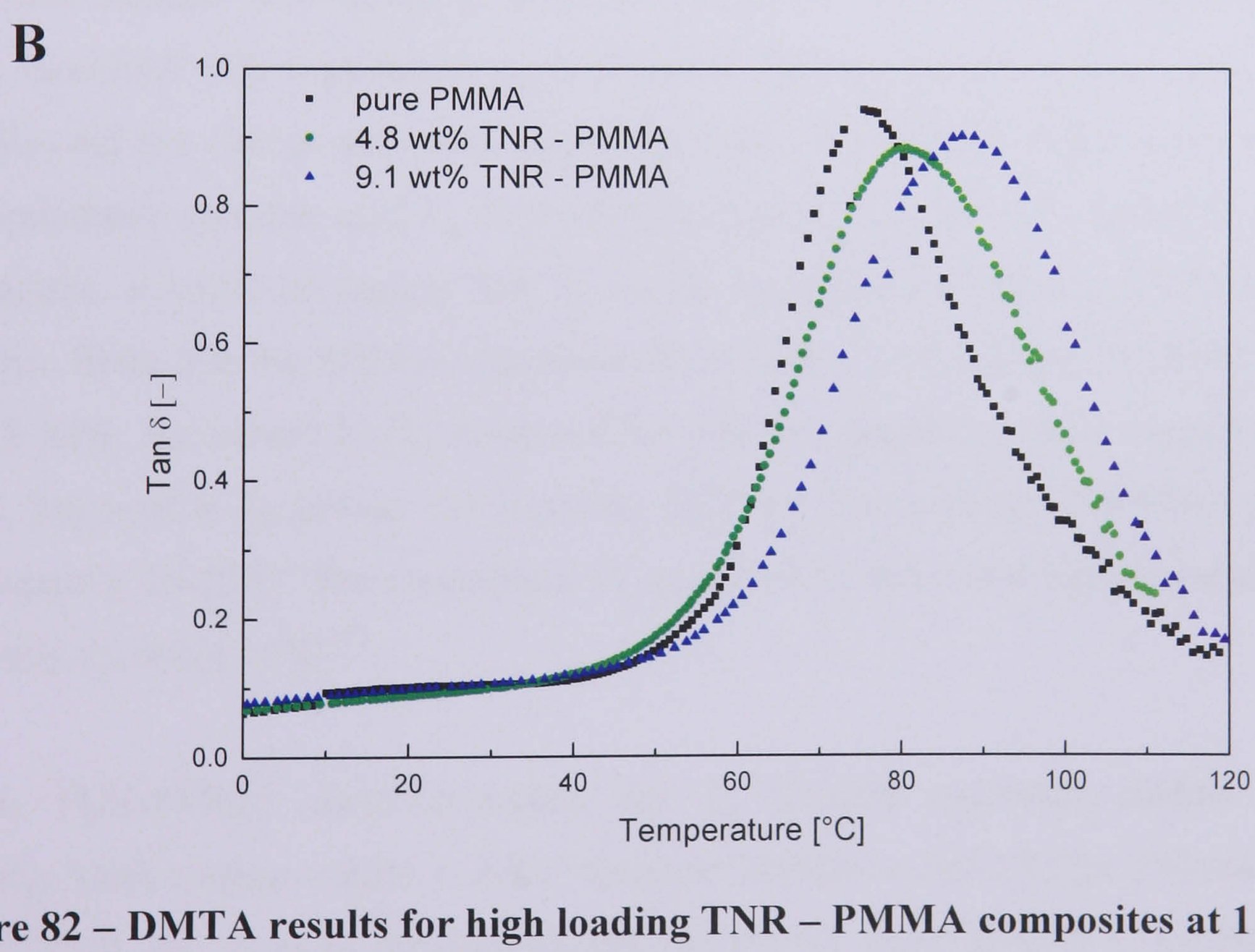


Figure 82 – DMTA results for high loading TNR – PMMA composites at 1 Hz: (a) Storage modulus and (b) tan δ as a function of temperature

DSC measurements were carried out on the polymer nanocomposites to determine the glass transition temperature as function of the nanorod loading fraction. DSC measurements for both polymer nanocomposite systems were taken in range from room temperature to 200°C. The temperature scan was repeated three times; first time in order to remove any thermal / mechanical history (residual stresses from solvent casting, etc), with two subsequent runs investigating the thermal nature of the material. A typical annotated DSC scan is shown in the Appendix 7.2 (Figure 103), to give appreciation of the method used to determine the T_g. The average T_g values for TNR-PDLLA and TNR-PMMA composites are shown in Figure 83. Pure PDLLA was measured to have the T_g at 51.6°C, which increases marginally upon addition of titania nanorods, reaching up to 54.7°C for the composite sample with 28.6 wt% TNR. Pure PDLLA with 10 wt% OA has a T_g at 39.8°C, which is significantly lower than that of the pure polymer and the composite films, highlighting the plasticizing effect of oleic acid for PDLLA. A similar effect has been reported in the literature, as discussed in section 2.5.3, in relation to work by Dzunuzovic et al.[313] on PMMA composites blended with different amounts of equiaxed 4.5 nm TiO_2 nanoparticles surface modified with 6-palmitate ascorbic acid. The T_g of the PMMA composites with TiO_2 did not change compared to pure polymer, but when PMMA was blended with 6-palmitate ascorbic acid T_g decreased significantly by 20°C[313]. Based on these observations, it could be argued that T_g would be higher in absence of OA in the composite films. For the PDLLA composite films with a TNR loading fraction higher than 4.8 wt%, the values for T_g measured by DSC are similar to those measured by DMTA, but tend to be greater measured by DSC for low loading TNR-PDLLA, by approximately 15-25°C. The variation in T_g measured by the two different techniques is typically by about 10°C[353].

For the TNR-PMMA nanocomposites, the T_g initially increases slightly with increasing TNR content – from 112.4°C for pure PMMA to 114.2°C for PMMA with 0.1 wt% TNR, but starts to decrease steadily thereafter, down to 95.7°C for PMMA with 28.6 wt% TNR. Again, plasticization by OA could be used to explain this trend, with pure polymer with 10 wt% OA having a much lower T_g, in this case down to 81.9°C, more than 30°C lower than T_g of pure PMMA.

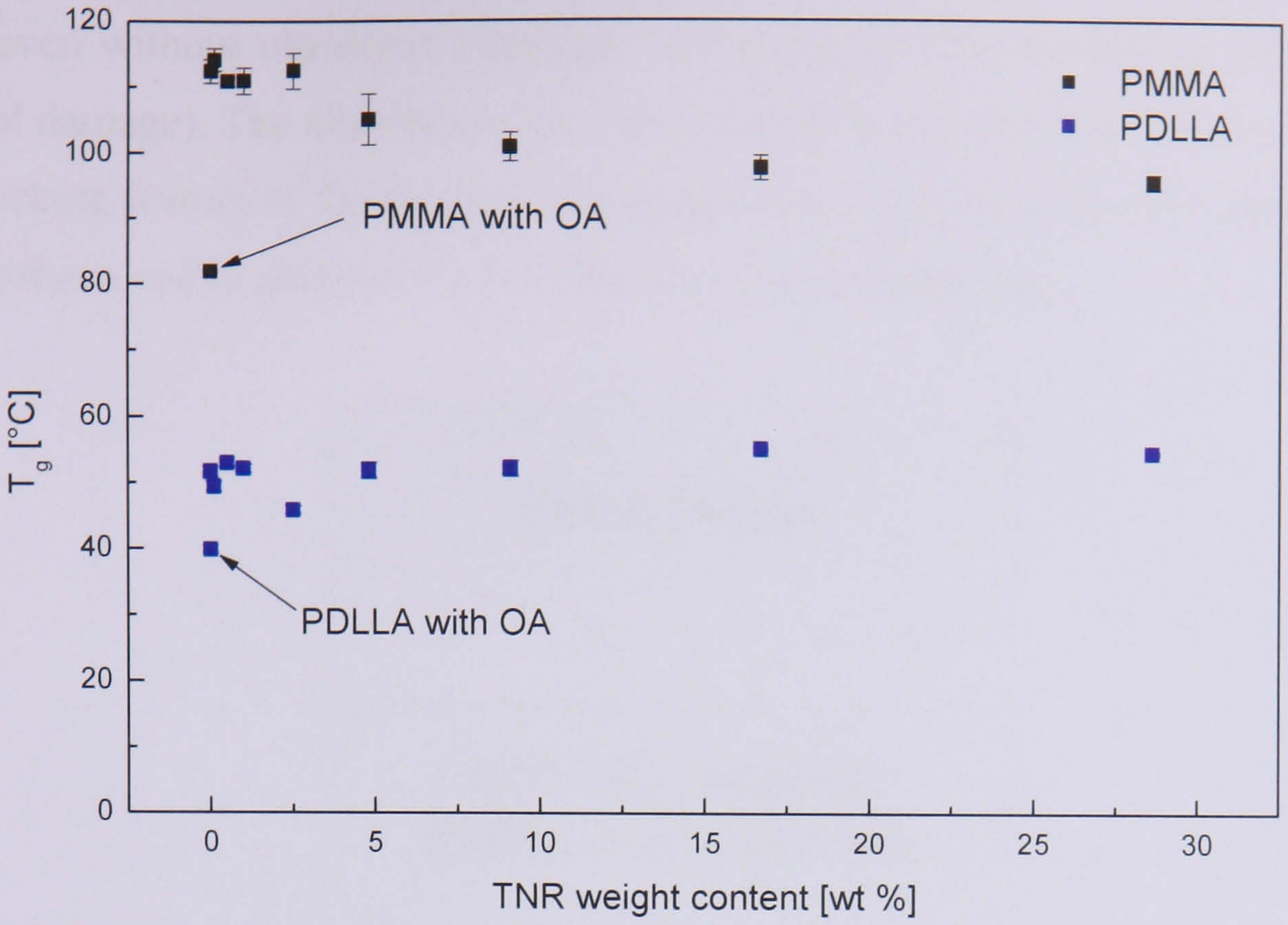


Figure 83 – Summary of T_g measured by DSC for PDDLA and PMMA composite films

5.2.1 TNR-PMMA composites made with TNR_{OA} [09/2007 batch]

This particular set of nanocomposite films is presented separately, due to remarkable nanorod dispersion achieved in the nanocomposites. The nanorods were synthesised and processed in essentially the same manner as for previously discussed TNR-PMMA composites, but after the synthesis the nanorod dispersion in chloroform was irradiated by ultrasound at temperatures above ambient (~50°C), leading to a more stable and transparent dispersion; higher temperatures appear to facilitate a more complete breakdown of agglomerates. The improvement is significant such that the subsequent blending of TNR dispersions and the dissolved polymer can be achieved using magnetic stirring, without the need for ultrasonic treatment.

Nanocomposite PMMA films containing these TNR_{OA} have exceptional optical quality (Figure 84) and remain optically clear even for very high nanorod loadings of up to 30 wt%. The light yellow colouring of the composites is due to OA capping on the surface of the nanorods, as can be seen in Figure 67. The optical behaviour of the PMMA nanocomposites was studied using UV-Vis and the results again show very low absorption in the visible range, due to excellent dispersion, which avoids light scattering (Figure 85). A quick comparison with PMMA composites discussed in the previous section indicates improved optical clarity (compared with results in Figure

77A), even without ultrasonic treatment of composite mixture (which might lead to physical damage). The absorbance increases sharply below 400 nm, demonstrating the UV blocking feature of the titania in the composites. The cut-off is very distinct, again making this a viable solution for UV filters and optical limiting.

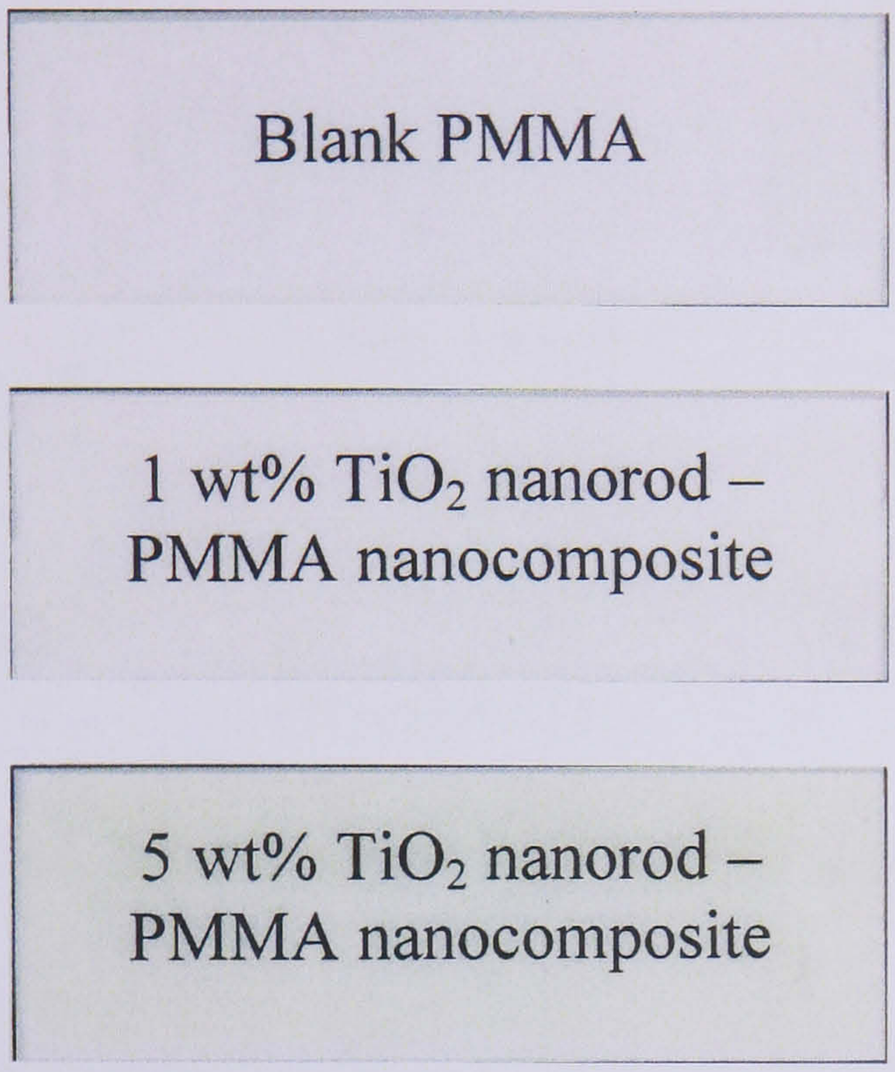


Figure 84 – Images of the as-prepared TNR – $PMMA_{09/2007}$ composites on glass slides

[Note – left portion of 30 wt% TNR sample partially peeled off from the glass slide, giving an irregular appearance; typical film thickness ~30 μm ± 3 μm]

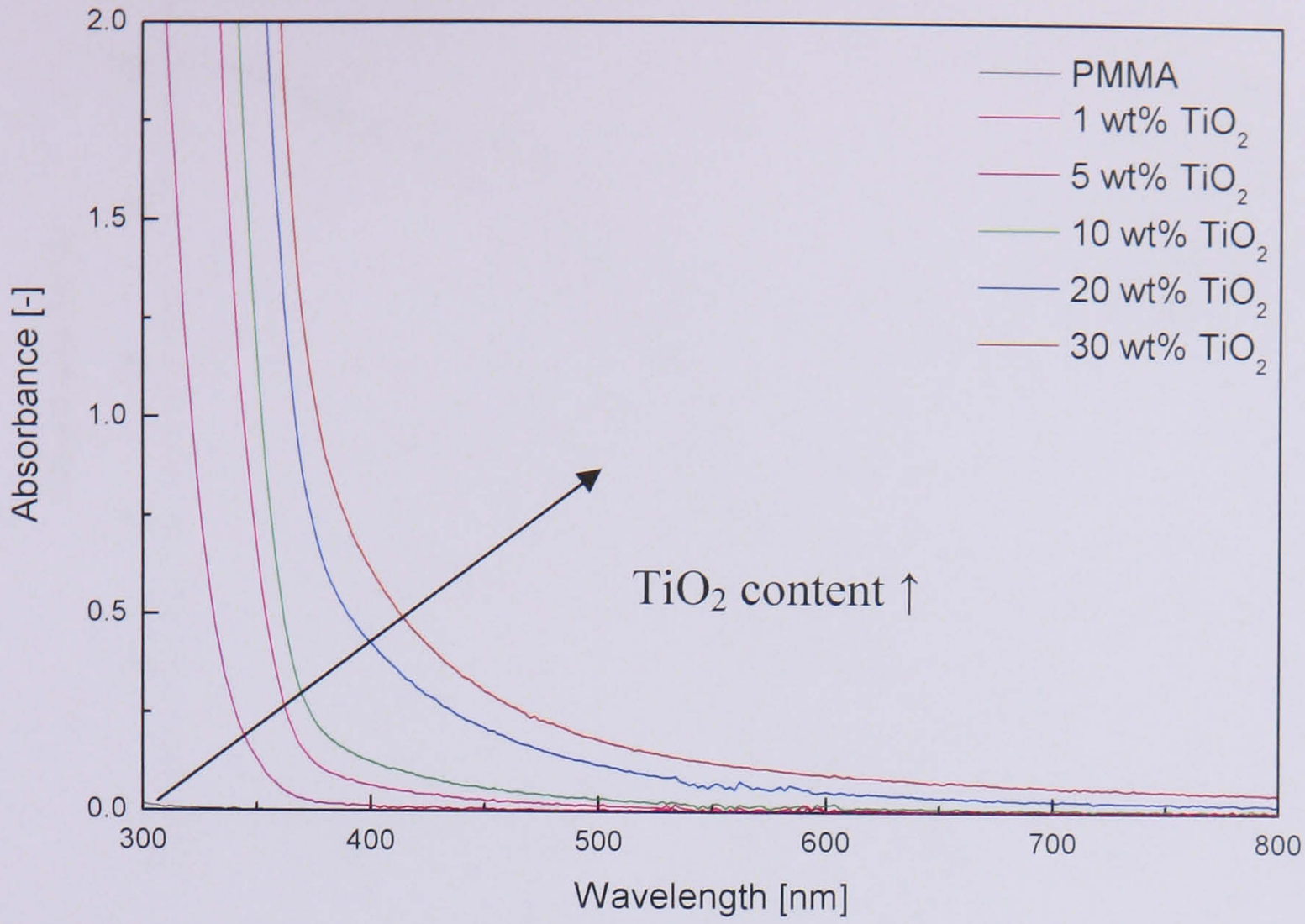


Figure 85 – UV-Vis spectra of the TNR – $PMMA_{09/2007}$ composites

The actual (rather than intended) nanorod content of the nanocomposites was confirmed by oxidising the composite samples in air, using TGA, to measure the weight of non-combustible TiO_2. The measured TiO_2 weight fractions (Figure 86) are typically less than 10% lower than intended. The match is acceptable, considering that dosing accurate amounts of titania dispersions in chloroform into the polymer solution is somewhat difficult, given the volatility of the solvent (b.p. 60°C – 62°C, vapour pressure ~26 kPa at 25°C). The degradation profile for pure PMMA shows that degradation starts above 150°C, with the greatest rate of degradation occurring between 250°C – 430°C, at which point the degradation is almost complete. Similarly for composites, the degradation onset is above 150°C, but the initial decline is followed by a plateau, and the bulk of degradation occurs within the 300°C – 400°C range. The plateau is due to the presence of a stable oxide chain in the matrix, which, as reported extensively for clay-polymer nanocomposites[354], slows the oxygen diffusion and could potentially be used for fire retardancy enhancement.

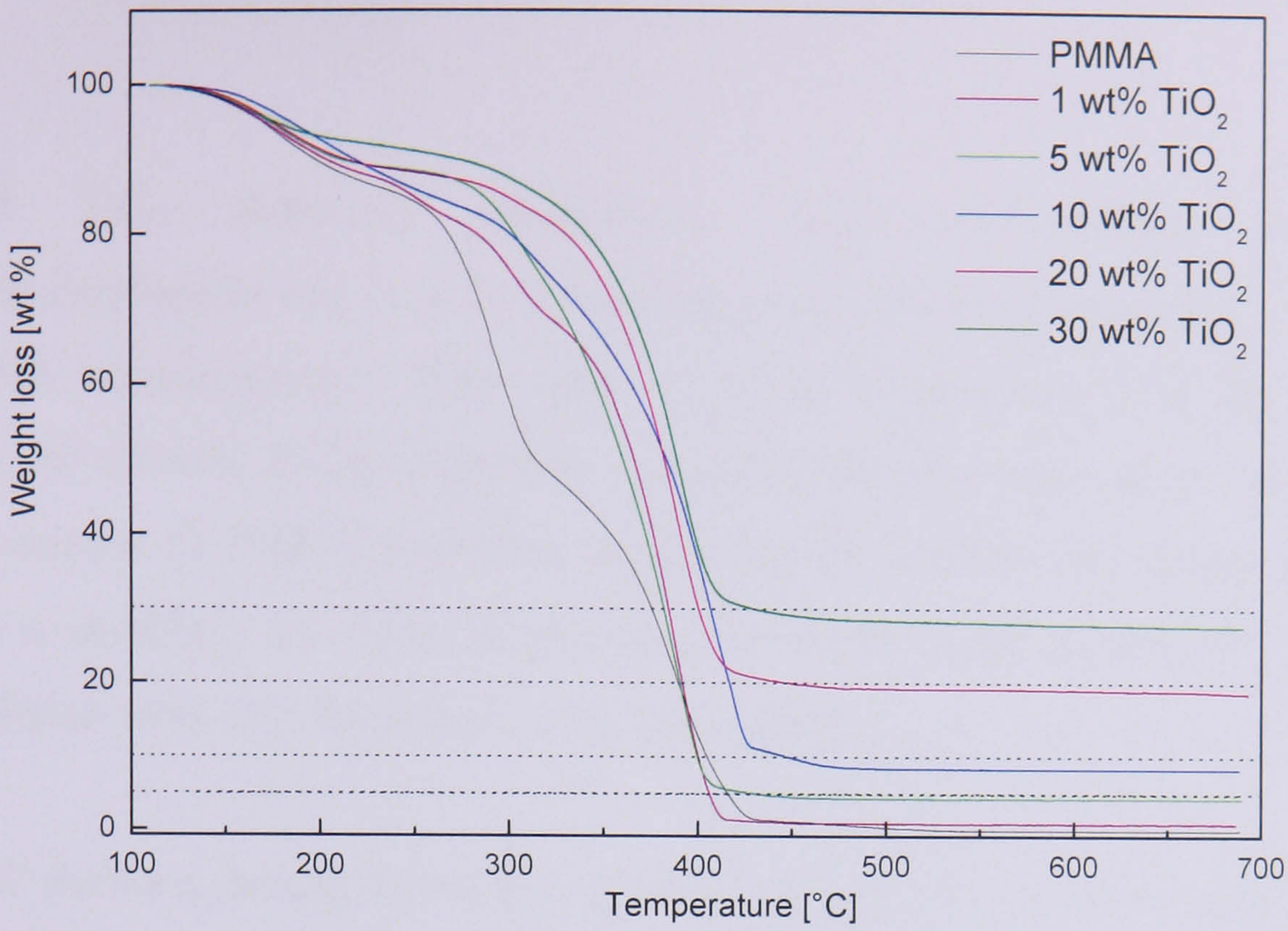


Figure 86 – Thermogravimetric analysis of PMMA and $TNR_{09/2007}$ composites

To supplement the thermal properties, the composites were analysed using DSC, in order to determine the T_g. Similar to previous batches of TNR-PMMA composites (Figure 83), values for this set of composites showed only a marginal decrease from the pure PMMA upon addition of TNR (Table 4), presumably due to the plasticization effect of oleic acid.

Sample	Tg
PMMA	111
1wt% TNR	109.5
5 wt% TNR	104
10 wt% TNR	108
20 wt% TNR	108.5

Table 4 – T_g values measured by DSC for TNR-PMMA composite films

5.3 TNR – PVA composites

Stripped TiO_2 nanorods synthesised using nonhydrolytic routes with TOPO/dodecylamine and oleic acid have been used for the preparation of two sets of TNR-PVA nanocomposite films. Sets of PVA composites, with up to 30 wt% TNR_{TOPO} or 10 wt% TNR_{OA} have been prepared, the latter only up to 10 wt%, due to limited amount of TNR_{OA} available. Additional PVA films containing only TMAH, used as a stabiliser for TNR dispersions, or commercial equiaxed 5 nm anatase nanoparticles were also fabricated as control samples.

Figure 87 shows a photograph of the actual composites fixed onto a paper background, and illustrates the transparency and the optical quality of the composite films. The high degree of transparency for all the nanorod films is indicative of excellent dispersion of nanorods in the matrix; there appears to be only a slight decrease in transparency with increasing loading fraction of TNR_{TOPO}. The films containing commercial, agglomerated particles retain some degree of transparency for low titania content, but become completely opaque at medium to high loadings (>5 wt%) due to light scattering. As mentioned in Chapter 3, the dispersant (TMAH) was not used in the fabrication of the 5 nm commercial nanopowder – PVA composites, as there was no noticeable improvement in stability of the nanopowder dispersions once TMAH was added. As opposed to TNR, which are grown as individual single-crystals, and, upon stripping, form only loose agglomerates that can be readily stabilised by TMAH, commercial nanopowders are generally present as strong agglomerates of primary particles, which cannot be broken down using high energy ultrasonic treatment or stabilising agents.

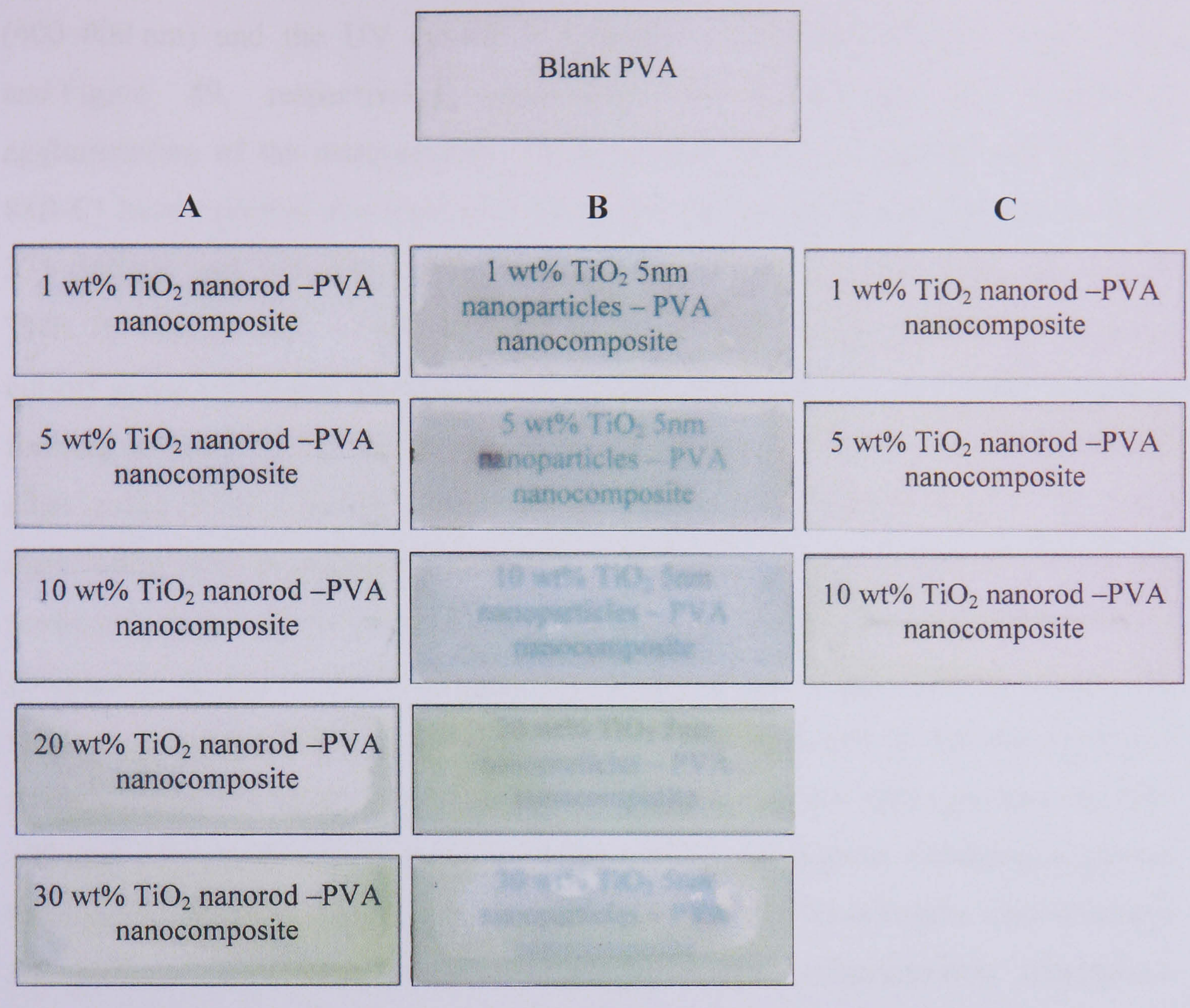


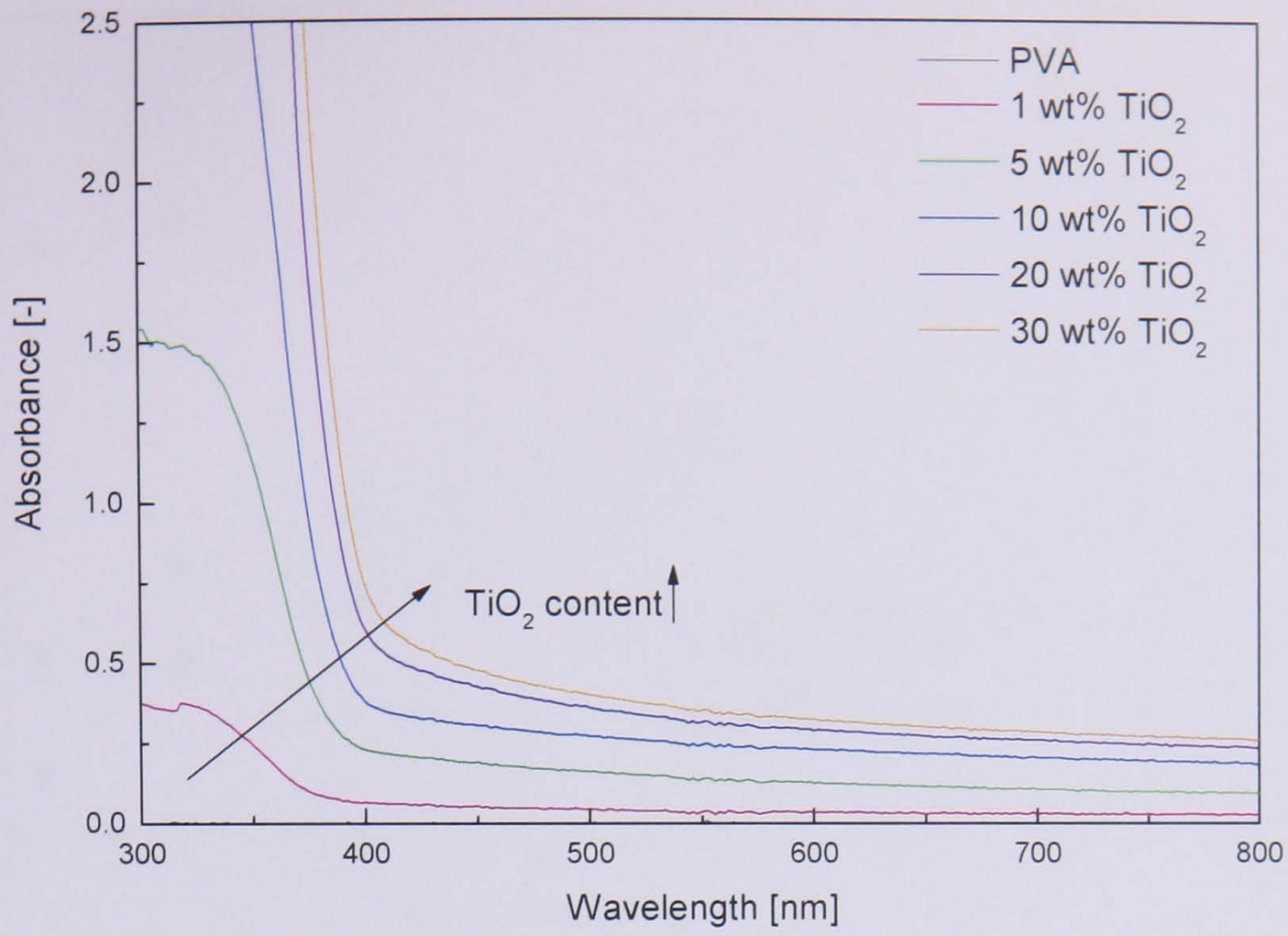
Figure 87 – Images of the as-prepared composites on glass slides: (a) TNR_{TOPO}-PVA and (b) 5 nm anatase – PVA and (c) TNR_{OA}-PVA

[Note – typical film thickness ~25 μm ± 3 μm]

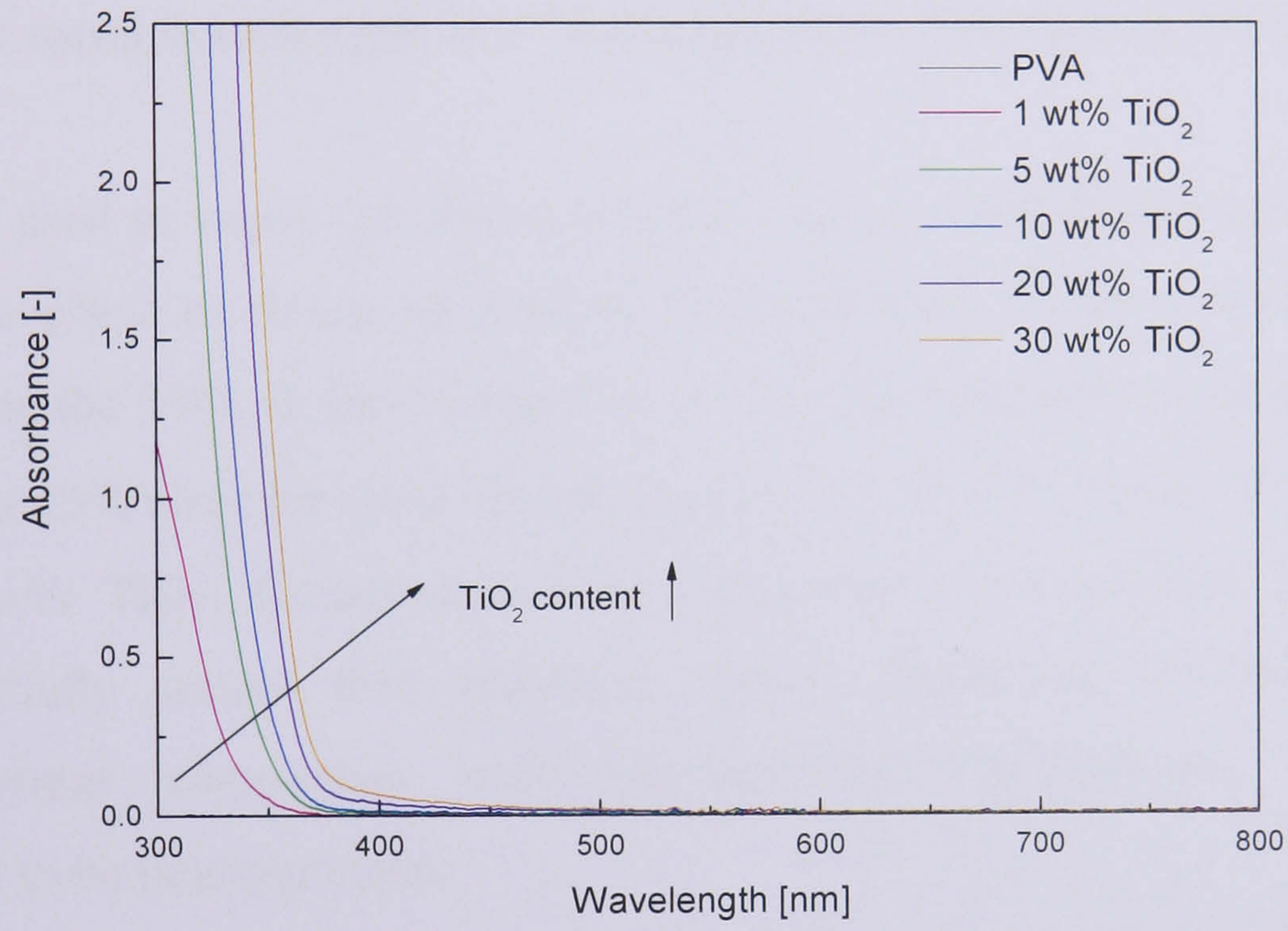
UV-Vis spectroscopy was used to compare the optical properties of nanorod-filled PVA to the 5 nm nanoparticle and pure polymer controls. The presence of TMAH in PVA did not affect the polymer absorption (spectrum not shown). The spectra measured are shown in Figure 88, together with the values for the onset of UV absorption as a function of different filler and loading content (Figure 89). The onset method was considered appropriate since UV absorption by TiO_2 is so strong that no discrete maxima could be observed. The onset point was determined as the intersection between the tangents to the visible ('horizontal') and UV ('vertical') portion of the spectra, respectively.

The 5 nm anatase nanoparticle composites scatter significantly in the visible region (400–800 nm) and the UV cut-off is typically around 380–400 nm (Figure 88A and Figure 89, respectively), suggesting poor dispersion and significant agglomeration of the nanoparticles. TNR_{TOPO} and TNR_{OA} composite films (Figure 88B-C) have minimal absorbance in the visible region and a sharp cut-off at about 335–365 nm and 325–345 nm, respectively, depending on the loading fraction of TNR. By appropriately selecting the amount of nanorods it is possible to fine-tune the cut-off in the UV region accurately, which could potentially be very useful in optical limiting devices. For a given titania loading, there is a blue shift in the UV absorption edge going from 5 nm anatase, through TNR_{TOPO} to TNR_{OA} filled PVA. This observation can be explained through well-known size quantisation effects for semiconductors[10]. Particles with a characteristic size in the order of 1-10 nm become comparable in size to the de Broglie wavelength of the charge carriers, which as a result confines the charge carriers and produces a quantisation of discrete electronic states, thus increasing the band gap energy[10]. The composites with agglomerated (50-100 nm) commercial anatase nanoparticles exhibit the highest wavelength (lowest band gap energy) UV cut-off, whereas significantly lower wavelengths were observed for TNR_{TOPO} and even lower for smaller TNR_{OA} (characteristic dimensions 4.7 ± 1.1 nm and 3.3 ± 0.3 nm, respectively).

A



B



C

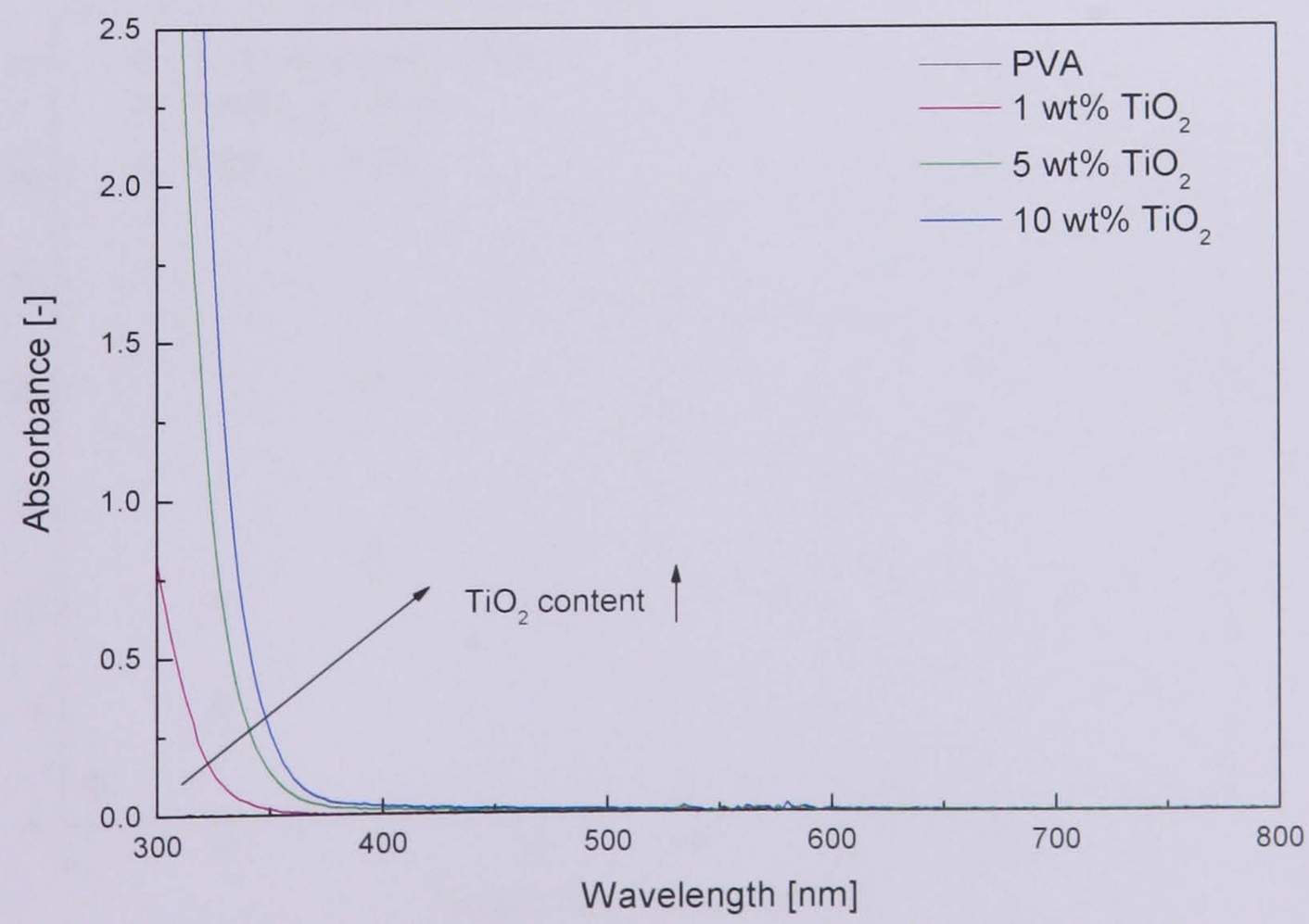


Figure 88 – UV-Vis spectra of PVA and composites

(a) 5 nm anatase – PVA (b) TNR_{TOPO} – PVA and (c) TNR_{OA} - PVA

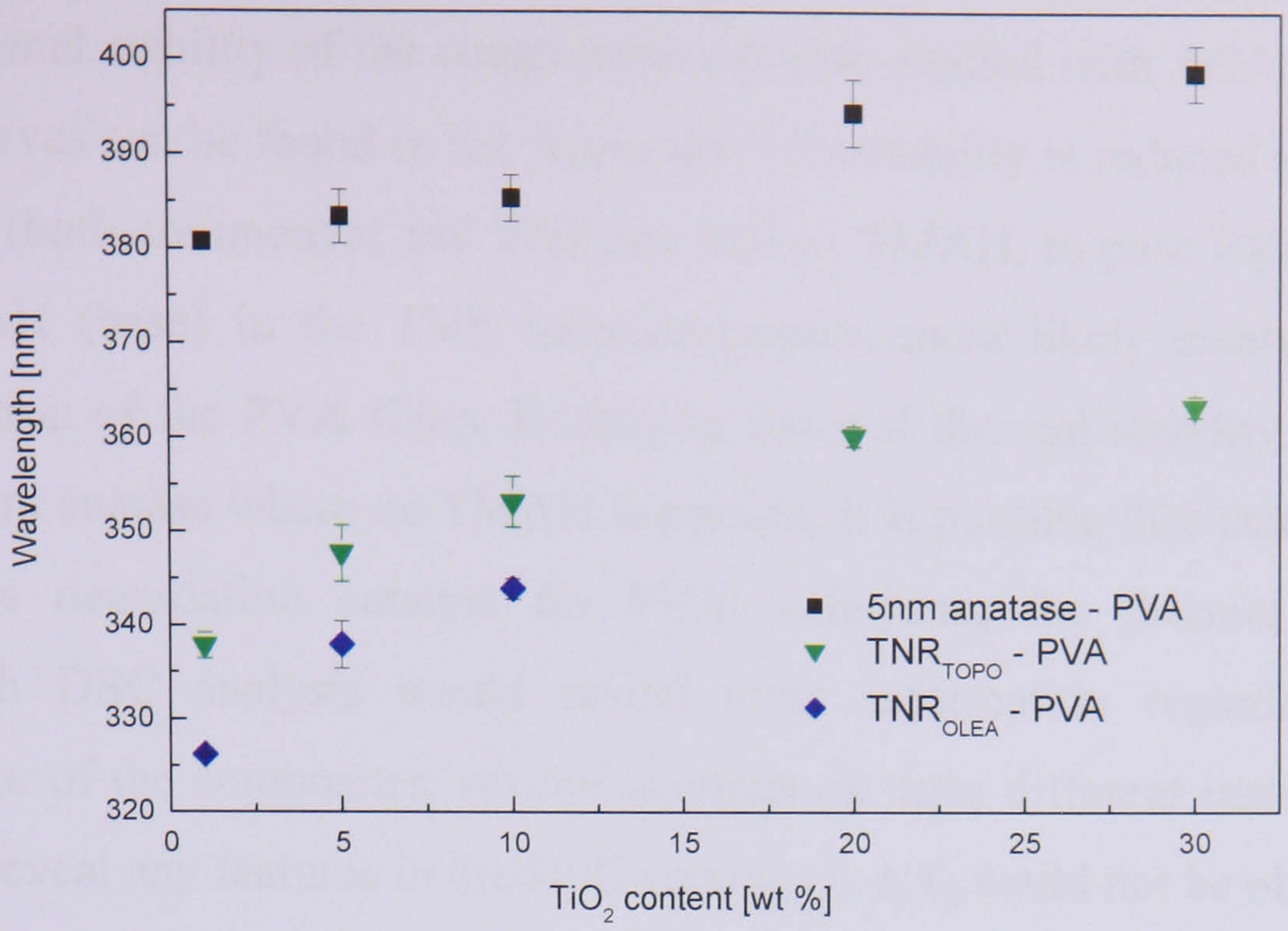


Figure 89 – UV onset wavelength of PVA composites – function of TiO_2 loading

TGA in air was used to verify the titania content in the composites (Figure 90) and also to study the effect of titania on thermal decomposition of the composites. The weight content of the TNR in the composite matches the targeted values quite well, with a maximum ±5% error for most samples, except for 10 wt% TNR_{OA}-PVA, which contains 12.6 wt% TiO_2. Composites with commercial nanoparticles have TiO_2 content substantially greater than expected, further illustrating the difficulty in processing polymer composites with agglomerated nanoparticles, since the dispersions tend to be heterogeneous.

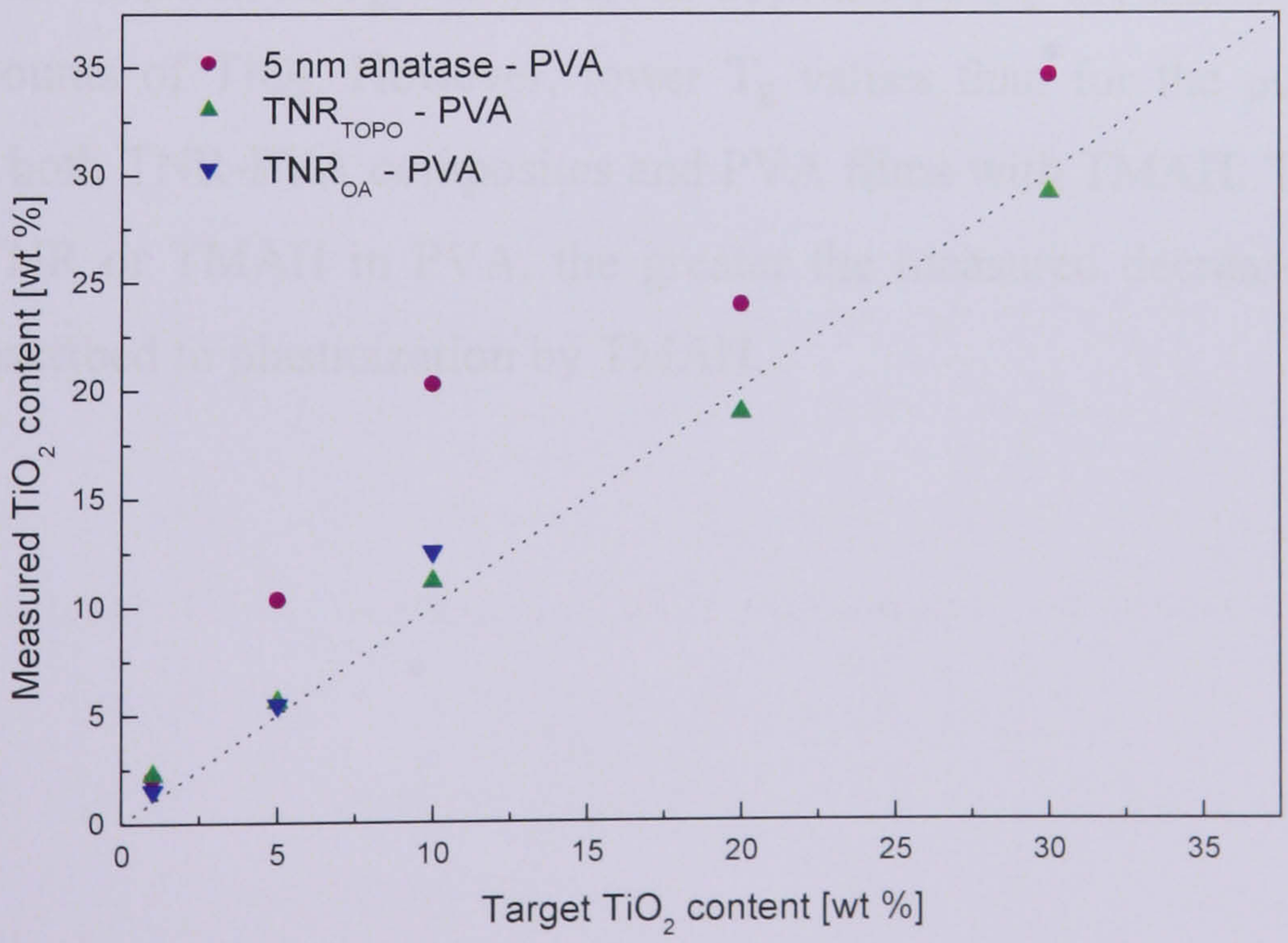


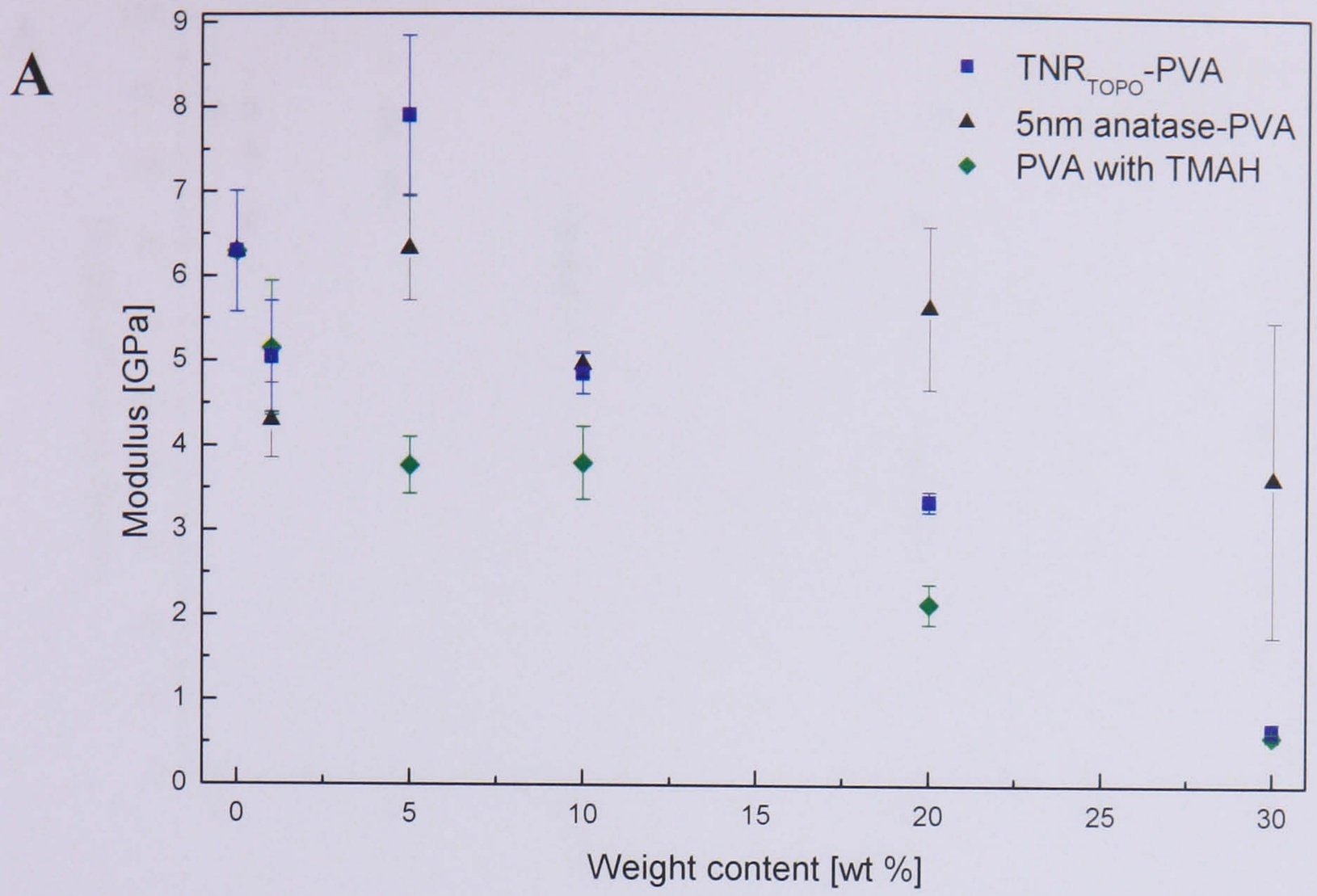
Figure 90 – Measured TiO_2 content in the composites, compared against expected values (dashed line)

The thermal stability of the composites was also studied with TGA (a full set of the TGA curves can be found in the Appendix 7.3); stability is reduced upon the addition of TiO_2 (both commercial and TNR) as well as TMAH, to pure PVA. The presence of TMAH (base) in the TNR nanocomposites, most likely catalyses the thermal degradation of the PVA films, leading to reduced thermal stability. For PVA films with 5 nm anatase where no TMAH is present, it is possible that titania agglomerates act as a degradation catalyst for PVA, catalysing the thermal decomposition. Although DSC analysis would reveal more information regarding the thermal behaviour of the composites, several attempts on three different instruments to do so did not reveal any features in the DSC curves, i.e. a T_g could not be observed.

Stiffness and the glass transition temperature of the TNR-PVA / commercial anatase-PVA composites were studied using DMTA, as a function of TiO_2 loading fraction. The data (included in the Appendix 7.4) reveal that all nanorod reinforced PVA nanocomposites have lower stiffness than pure PVA; a similar effect was observed for PVA films with TMAH, suggesting that TMAH acts as a plasticizer. Further, the variation in the stiffness of the TNR composites does not follow any conclusive trend. On the other hand, a decrease in stiffness of the PVA composites with commercial TiO_2 nanoparticles can be explained by nanoparticle agglomeration and a weak TiO_2-polymer interface. Thermal behaviour of the latter composites remains unchanged – no appreciable variation in T_g was observed between pure PVA and composites with different amounts of TiO_2. However, lower T_g values than for the pure PVA were recorded for both TNR-PVA composites and PVA films with TMAH. The greater the amount of TNR or TMAH in PVA, the greater the measured decrease in T_g of the composites ascribed to plasticization by TMAH.

The Young's modulus, measured from the tensile tests (Figure 91), decreases in proportion to the amount of TNR added. The variation in modulus for the TNR_{TOPO} composites is matched by the behaviour of the PVA loaded with an equivalent concentration of TMAH, suggesting again that the decrease in performance can be attributed to the plasticization by TMAH. An even steeper rate of decline of the Young's modulus is apparent for TNR_{OA}-PVA, due to the relatively higher TMAH loading.

The maximum tensile strength (Figure 92) and the Young's modulus (Figure 91) of PVA films loaded with TMAH drop almost linearly with increasing TMAH concentration, as a result of the plasticization effect of TMAH. The magnitude of the decrease matches that observed for both sets of TNR composites, suggesting that the nanorod-polymer interface is weakened by the TMAH. Indeed, adding 5 nm anatase without TMAH makes the films more brittle as evidenced by the decrease in the maximum tensile strength (Figure 92A), associated with increasing scatter and decreased elongation at break (Figure 93A), due to the anatase agglomerates acting as defects.



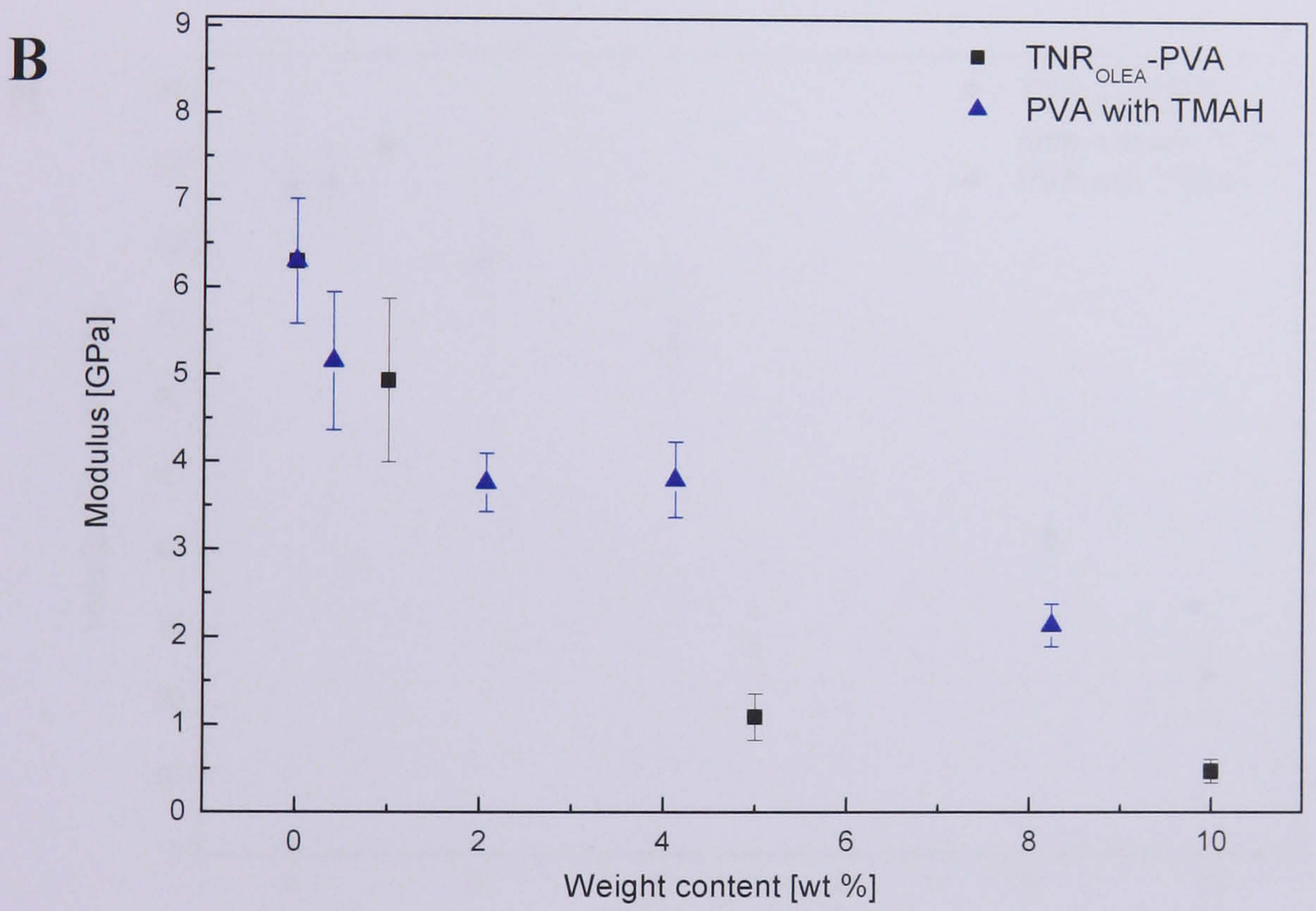
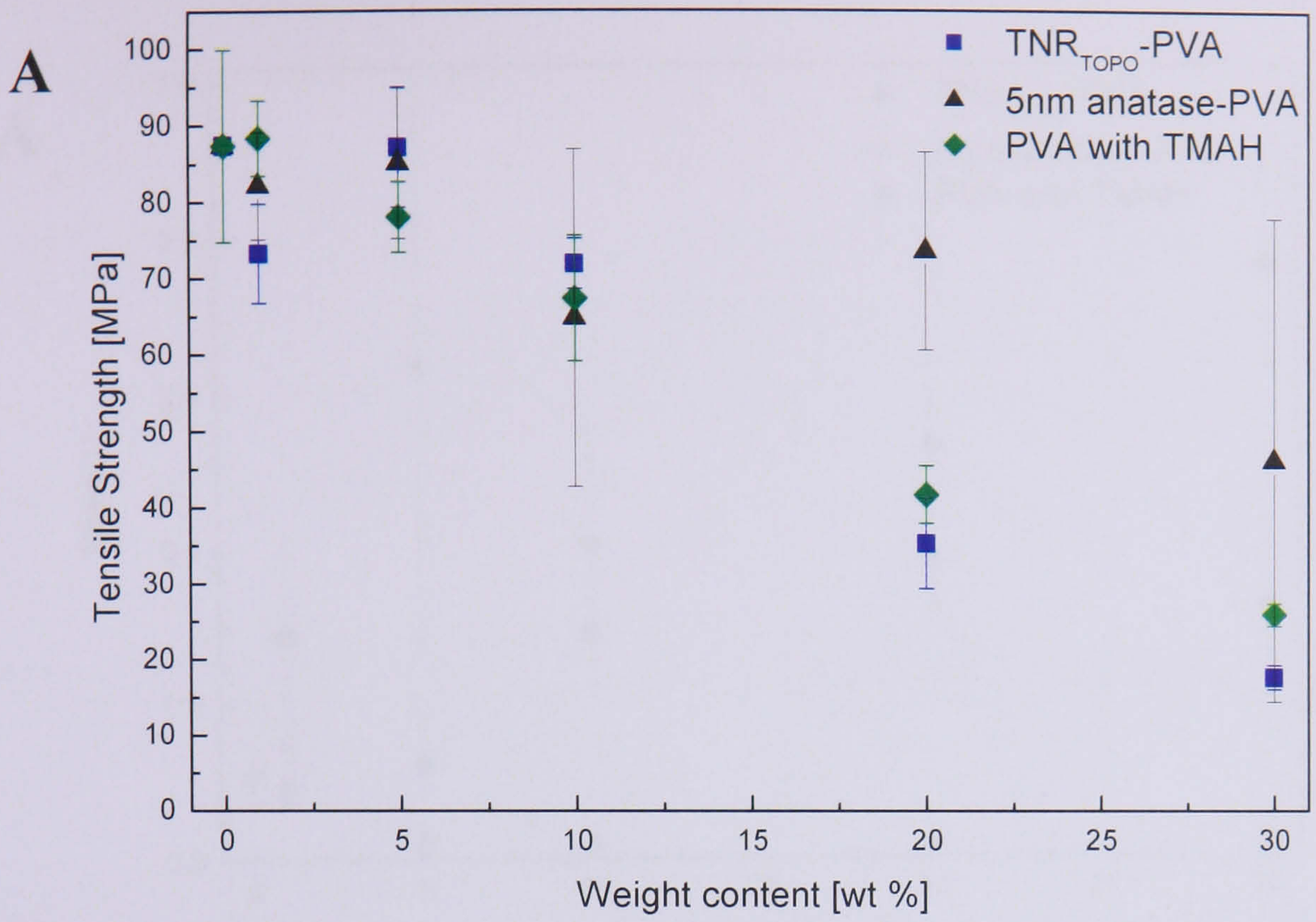


Figure 91 – Young's modulus of PVA and the composites: (a) PVA with TNR_{TOPO}, 5 nm anatase and TMAH*; (b) PVA with TNR_{OA} and TMAH*

---

* *Note: PVA with TMAH – pure polymer (no TiO_2) that contains the same amount of TMAH as the respective TNR composites, i.e. PVA with TMAH in Fig. 91-93A and 91-93B were adjusted to TMAH present in TNR_{TOPO} and TNR_{OA}, respectively. Superposition of PVA with TMAH data points onto the TiO_2 weight content x-axis is done for simplicity.*



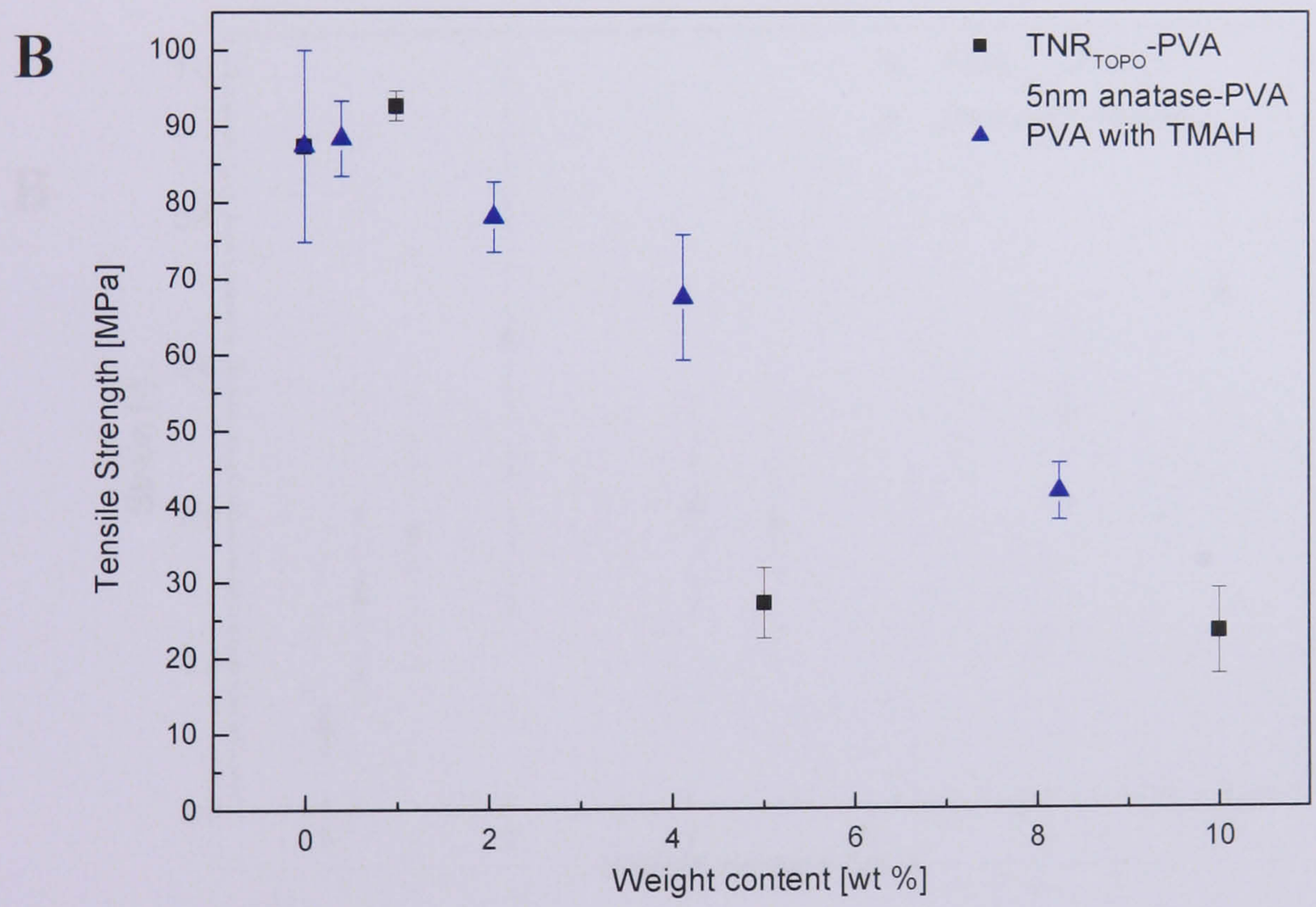
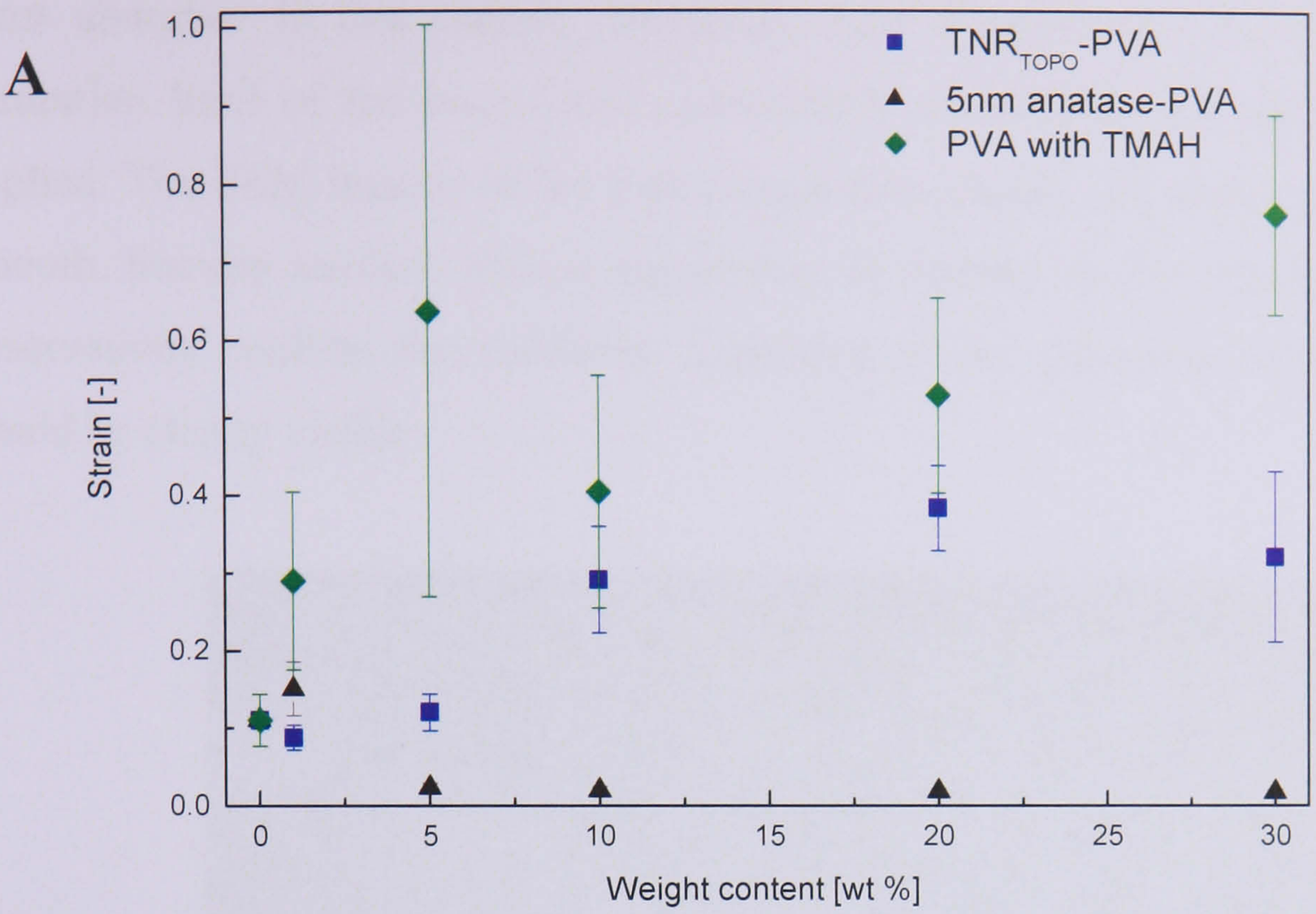


Figure 92 – Maximum tensile strength of PVA and the composites:
(a) PVA with TNR_{TOPO}, 5 nm anatase and TMAH*; (b) PVA with TNR_{OA} and TMAH*



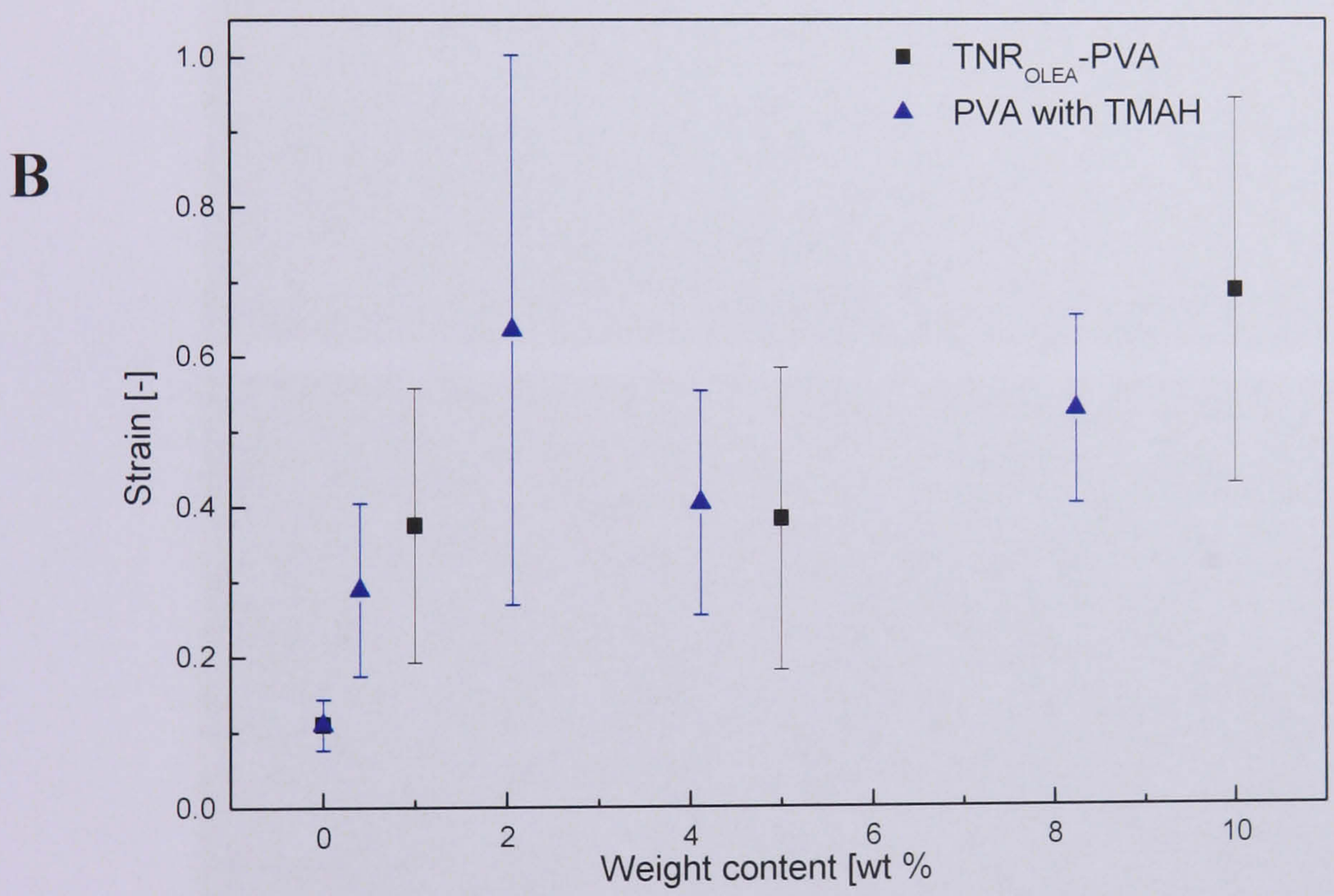


Figure 93 – Elongation at break of PVA and the composites: (a) PVA with TNR_{TOPO}, 5 nm anatase and TMAH*; (b) PVA with TNR_{OA} and TMAH*

The fracture surfaces of the composites were observed using SEM. Analysis was performed only on 10 wt% TNR_{OA}-PVA, since these rods are slightly longer and most abundant in this sample. However, their dimensions are still close to the resolution limit of the microscope, particularly considering the chromium coating applied. The SEM images of the nanocomposites (Figure 94) show only a relatively smooth fracture surface with a suggestion of texture at the 10 nm scale. These observations confirm the excellent dispersion of the nanorods as any aggregates would be clearly visible.

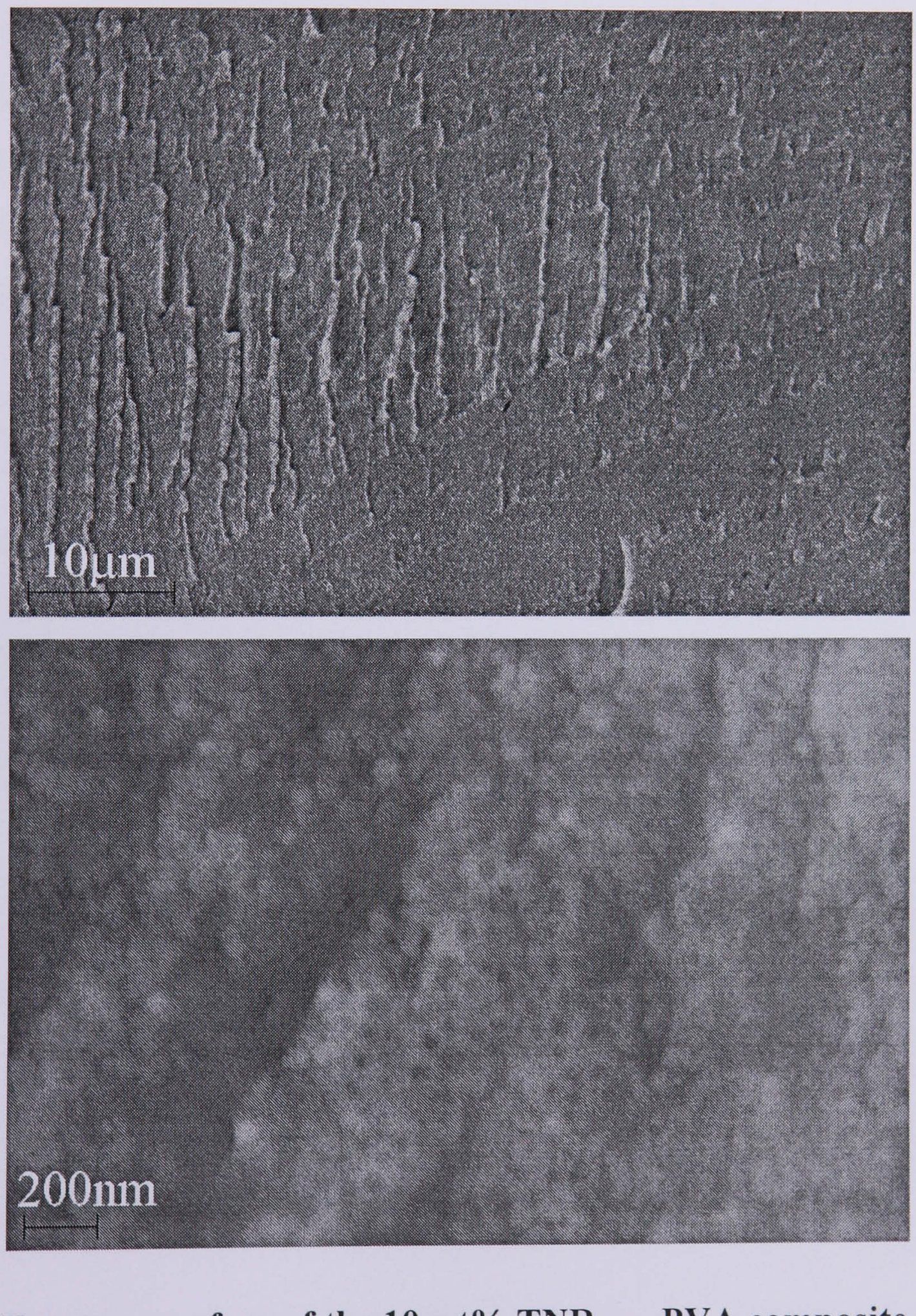


Figure 94 – Fracture surface of the 10 wt% TNR_{OA} - PVA composite under SEM

5.3.1 Photochemical degradation of composites

Photons with wavelengths in the UV range or lower, lead to excitation of TiO_2, which initiates, under ambient conditions, a series of photochemical reactions at the titania surface. Strong oxidative species are thus formed, which can react with organics and lead to their complete oxidation to CO_2 and water. Polymers are no exception and it is important to estimate the difference in photodegradation behaviour between the pure polymer, nanorod composite films and commercial TiO_2 composites. Exposing the composite films to UV-A for 300 h leads to their degradation as measured by fractional weight loss (Figure 95). A 4 wt% loss was observed for the pure polymer, whereas higher values were observed for composites with TiO_2. The fractional weight loss is different depending on the filler type; for instance, 1 and 5 wt% TNR_{TOPO} composite samples have a marginally higher weight loss than pristine PVA, while equivalent amounts of commercial TiO_2 show substantially higher values.

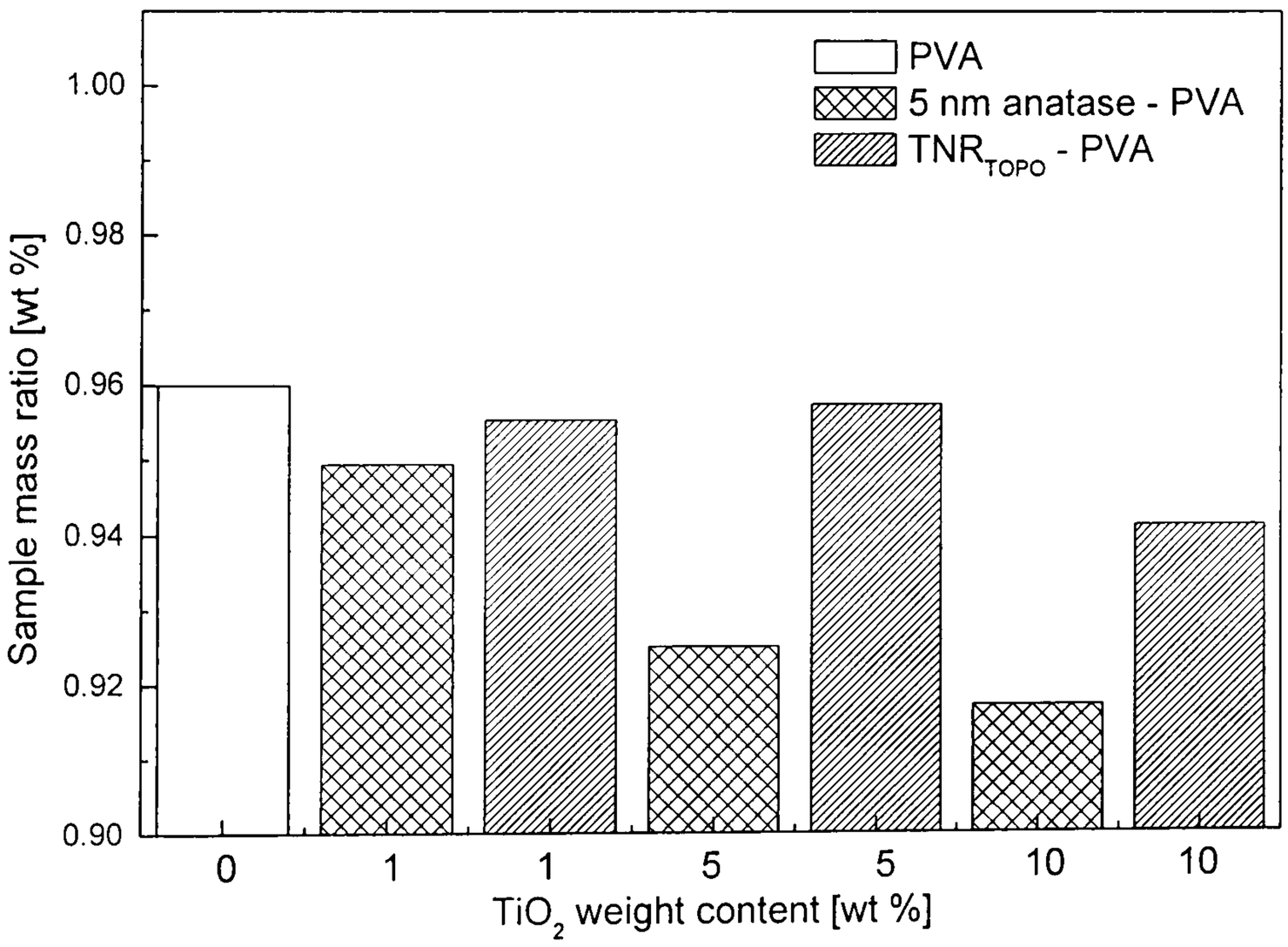


Figure 95 – Fractional weight loss of the pure PVA and the composites, after 300 h of UV (λ = 365 nm, power = 19 ± 1 $W \cdot m^{-2}$)

The effect of UV exposure on the optical properties was investigated using UV-Vis spectroscopy (Figure 96 and Figure 98). The optical quality of PVA irradiated by UV for 300 h remains almost unchanged (results not shown). Similar retention of optical quality was observed for 1 wt% TNR_{TOPO} (Figure 96A) and to some extent 5 wt% TNR_{TOPO} (Figure 96B). In the latter case, a "shoulder" observed around 380 – 420 nm arises due to thermal degradation of TMAH. UV degradation is carried out in an enclosure, with temperatures measured to be 50-55°C; heating pure PVA samples containing only TMAH, without UV irradiation, were separately shown to lead to similar changes in the absorption spectra (Figure 97), presumably due to thermal degradation of TMAH. Even greater changes were observed for the 10 wt% TNR_{TOPO} - PVA, presumably due to the greater TMAH content. For 5 nm anatase - PVA samples, which were not very transparent initially, degradation leads to rapid whitening and even greater light scattering / opacity of films (Figure 98).

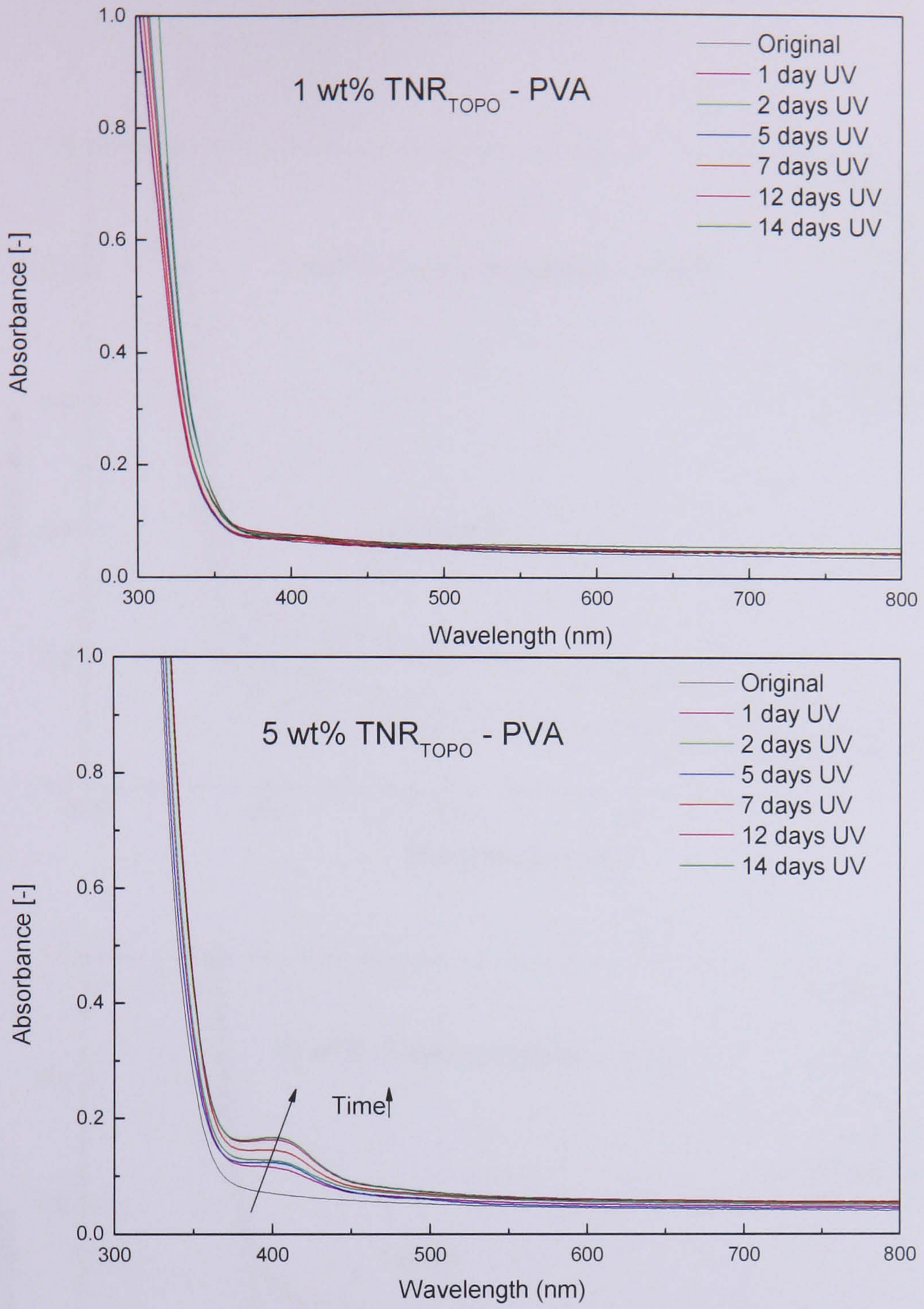


Figure 96 – UV-Vis spectra of PVA and the composites during UV degradation: (a) 1 wt% TNR_{TOPO} – PVA; (b) 5 wt% TNR_{TOPO} – PVA

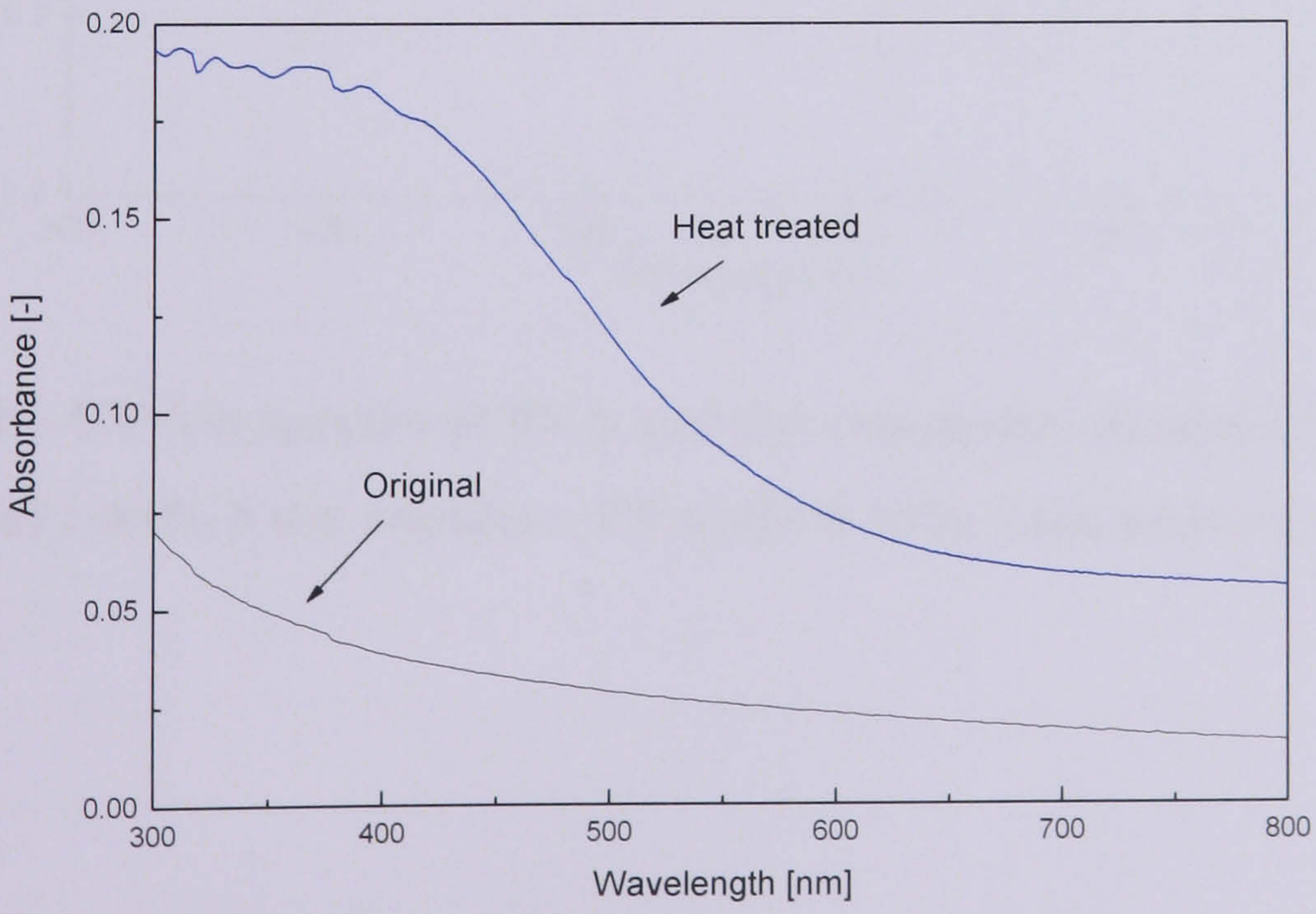
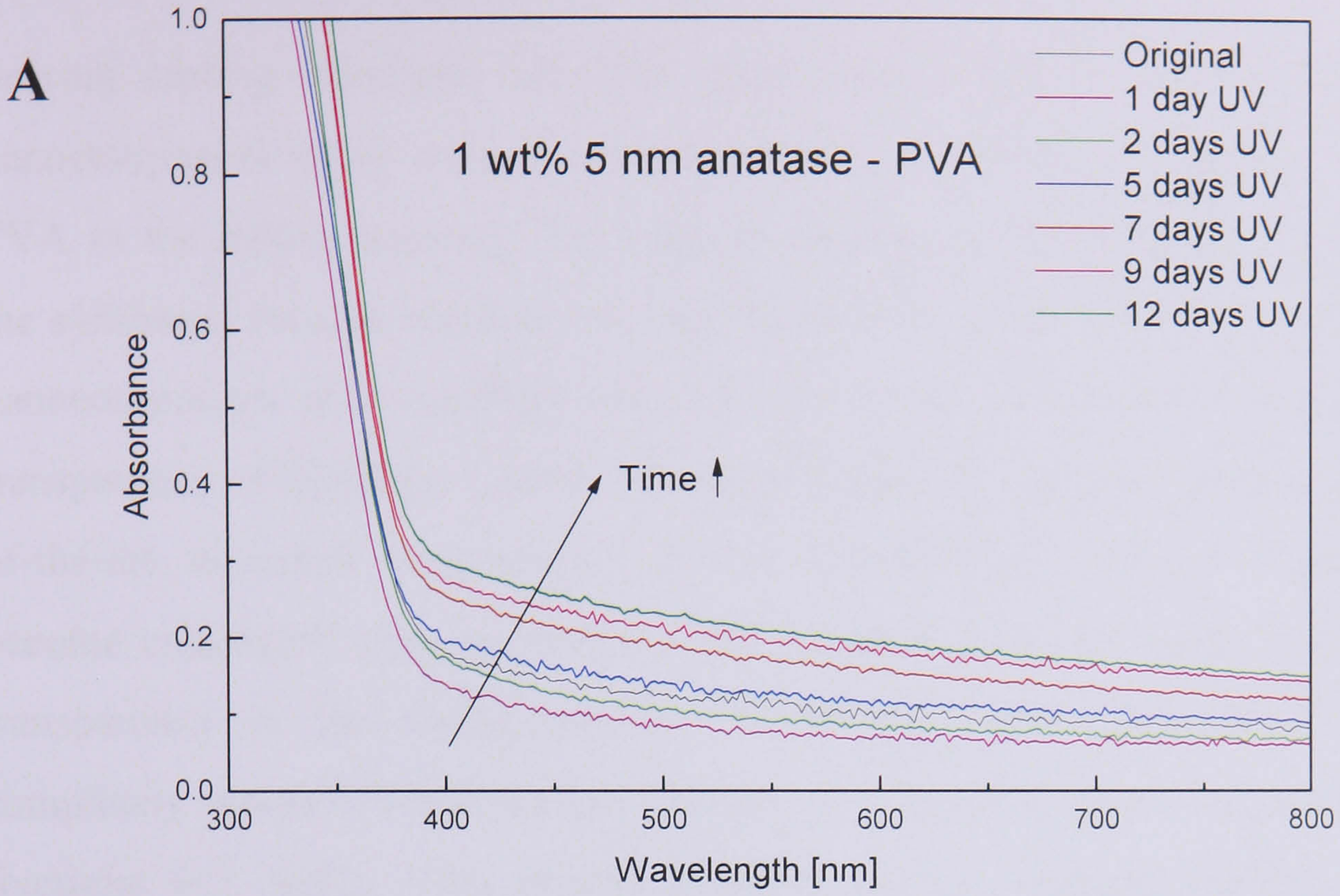


Figure 97 – UV-Vis spectra of PVA with 10 wt% TMAH, at room temperature and after heating at 70°C for 15 min [*no UV treatment*]



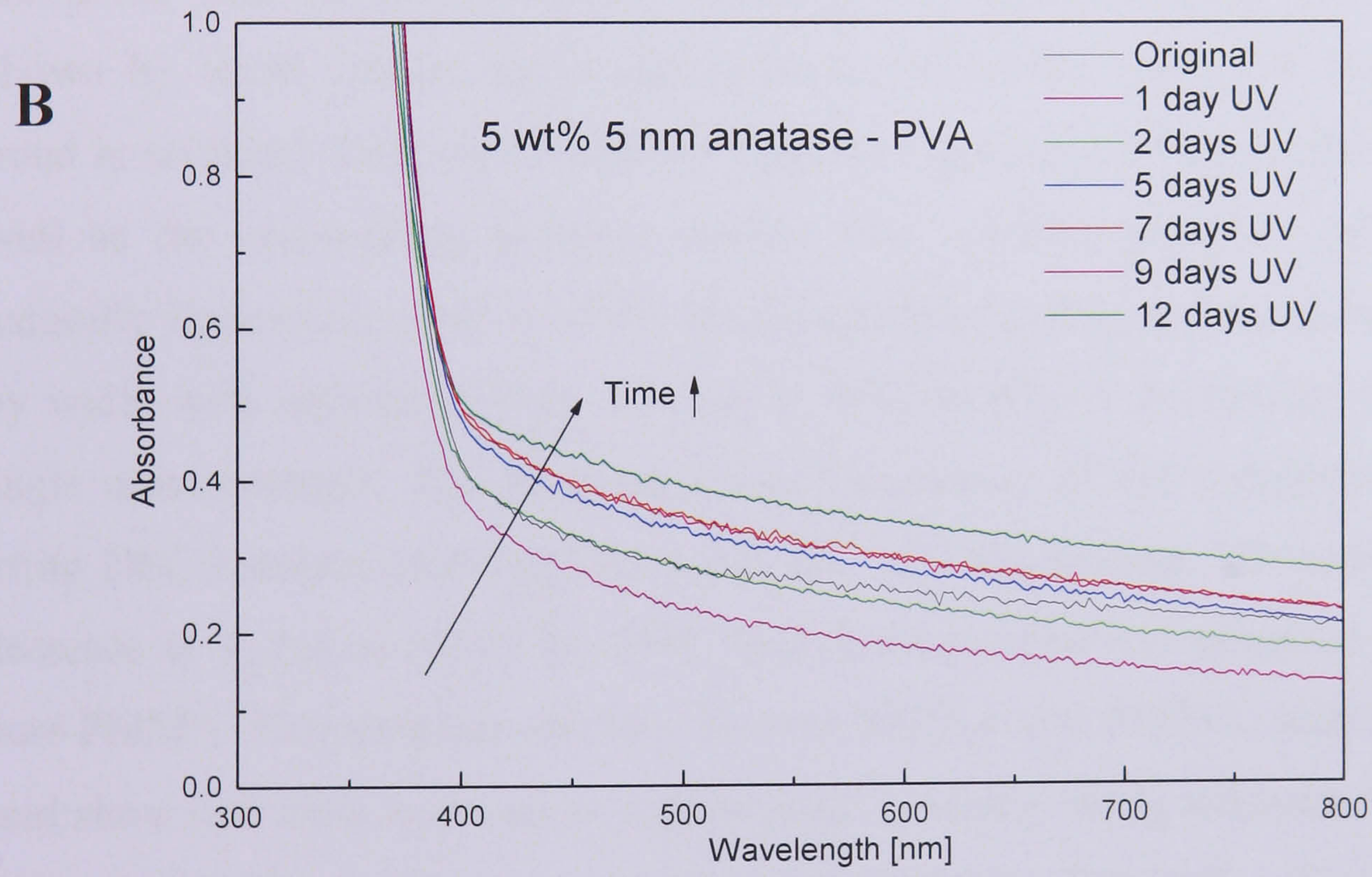


Figure 98 – UV-Vis spectra of PVA and the composites during UV degradation: (a) 1 wt% 5 nm anatase – PVA; (b) 5 wt% 5 nm anatase – PVA

5.4 Concluding remarks

Solvent casting technique has been successfully used to fabricate TNR polymer nanocomposites using organic-soluble PDLLA or PMMA, as well as water-soluble PVA as the matrix material. The organic capping on the nanorods, imparted during the synthesis, favours blending of TNR dispersions with PDLLA or PMMA to yield nanocomposites with excellent nanorod dispersion, evidenced by a high degree of transparency of the films. Controls fabricated using the commercially-available, state-of-the-art, equiaxed nanoparticles do not display good material transparency and become completely opaque, even for TiO_2 content above 2.5 wt%. Despite excellent transparency in the visible region, TNR-PDLLA and TNR-PMMA composites completely absorb UV light below 350 nm, even for very small TiO_2 nanorod loading fractions (<1 wt%). The organic capping on the nanorod surface renders the composite film surface increasingly hydrophobic, with increasing TNR content, as shown by water contact angle measurements. However, upon UV irradiation, the trend is reversed; TiO_2 photocatalysis leads to degradation of the organic-capping as well as the surrounding polymer matrix. The oxidised polymer surface and the naturally hydrophilic surface of the titania combine to display increasing wettability by water with increasing TNR loading as evidenced by a decreasing water contact angle measurements. The glass transition temperature of the composites, measured using DSC remains unchanged as a function of TNR loading. However, significant decrease in T_g (up to 20°C) for TNR-PMMA composites was observed compared to pure PMMA. Pure polymer controls, for both PDLLA and PMMA, with 10 wt% oleic acid show that oleic acid acts as a plasticizer, lowering the T_g substantially, by about 15°C and 30°C for the two polymers, respectively. Similarly, oleic acid at the nanorod-polymer interface in TNR-polymer nanocomposites has the same effect and prevents stronger immobilisation of the polymer chains by the titania nanorods. Due to the weakened nanorod-polymer interface, stiffness of the TNR-PDLLA and TNR-PMMA composites decreases with increasing TNR content; however, the nanocomposites retain sufficient structural integrity to be considered for applications where their excellent optical transparency and UV filtering can be exploited.

Removal of the organic capping achieved by UV-induced self-cleaning of the nanorods allows direct blending of aqueous TNR dispersions with water-soluble PVA. The nanorod dispersion is exceptional even for very high loading fraction in the nanocomposites (at least 30 wt%), while adding even 1 wt% of commercial titania nanoparticles to PVA starts to appreciably opacify the nanocomposites. Again strong UV absorption for TNR-PVA was observed; TiO_2 nanorods provide a strong and well-defined absorption edge around 350-400 nm. The extent can be varied by adjusting the nanorod content or the nanorod size, possibly leading to applications in optical limiting devices and transparent UV filters. Formation of aligned porous networks in polymers has been reported previously for carbon nanotubes[355], induced by electric fields. The thermal stability and mechanical properties such as the maximum tensile strength and stiffness of PVA are, perhaps surprisingly, inferior for the composite samples compared to the properties of pure PVA. The degradation is brought about by the presence of TMAH, which is essential for achieving excellent nanorod dispersion in the matrix, but tends to act as a plasticizer. Modifying the titania nanorod surface with siloxanes was investigated towards the end of the project, as an alternative to TMAH, with the aim of improving the adhesion at the nanorod-polymer interface and avoiding the undesirable plasticization, but the procedure still remains a task for future work. The photodegradation of the composites by the UV was simulated with an artificial UV source and the results suggest that for low nanorod content of up to 5 wt%, the extent of degradation (measured by weight loss and loss in transparency) does not differ significantly from pure PVA, which is desirable if durable composites are required.

6. Conclusions and future research

6.1 Summary of contributions

6.1.1 Synthesis and modification of TiO_2 nanorods

The synthesis of TiO_2 nanorods has been reported previously in the literature. The development of the synthesis procedures used during this project was carried out principally by a co-worker, Dr. Sabina Chyła. However, new results demonstrate that these methods are reproducible, yielding consistent products in terms of crystallinity, particle morphology and size distribution. Additionally, the reaction was successfully scaled up by a factor of 3 (on a molar basis), which is important for subsequent work if greater quantities are required.

The most novel development is the route to clean the titania nanorods of any organic ligands, such as those introduced during synthesis. The UV-assisted self-cleaning procedure, or stripping, exploits the photocatalytic activity of TiO_2 to oxidise the organic capping on the nanorod surface, whilst retaining the nanoparticles in dispersion. Importantly, the exceptional stability of TiO_2 to UV ensures that only the organics attached to the TNR surface are oxidised, while the nanorod morphology, size and crystalline phase remain unaffected. Conventional thermal oxidation of the organic ligands frequently leads to undesirable changes in morphology and crystal phase (i.e. agglomeration and sintering). The self-cleaning feature of TiO_2 has been used extensively for a number of applications (e.g. anti-fogging glass, self-cleaning surfaces), but this work provided first evidence that it can be used to control the nanoparticle surface character in dispersions. The stripping procedure appears to work equally well for nanorods of different sizes synthesised using different structure directing agents (oleic acid or TOPO and dodecylamine), and is likely to be a generally applicable approach.

The stripped TiO_2 nanorods can be stabilised, after processing, to form transparent dispersions, using alkyl ammonium hydroxides. Stabilisation using tetramethyl-ammonium cation (TMA^+) has been used previously *during* the hydrolytic syntheses of TiO_2 nanoparticles[6,54], where it was shown to act both as a catalyst and as a stabiliser in aqueous media. In the current organic-stripping procedure, it is used *after* the synthesis to produce good quality aqueous dispersions of particles that manifest the added advantages of the nonhydrolytic synthesis (e.g. higher synthesis temperature). In this sense, we utilise a known stabilisation mechanism in an innovative way to achieve good dispersion in solution, which is a prerequisite for many applications including polymer composites and homogeneous electrodes in photovoltaic applications. The mechanism of this stabilisation has been elucidated. The particles can be further treated chemically with functionalised siloxanes to adjust the surface character or to reduce photocatalytic activity; notably, the TNR particles coated with APTS remain fully dispersible to form transparent solutions.

6.1.2 TiO_2 nanorod – polymer nanocomposites

To date, TiO_2 *nanorod* – polymer composites have been rarely reported and, even in those cases, the focus is solely on applications in electronic devices. This thesis reports, for the first time, the successful fabrication of TNR – PDLLA, TNR – PMMA and TNR – PVA nanocomposites by solvent casting. Dispersions of TiO_2 nanorods were readily blended with organic-soluble (PDLLA and PMMA) and water-soluble (PVA) polymers to produce nanocomposite films with excellent optical properties, specifically a high degree of optical transparency and UV absorption. In most cases, the nanorod composites retain the transparency equal to that of the pure polymer, which is otherwise lost if commercial titania powders are used. This optical clarity is due to the quality of the dispersion; individually dispersed single-crystals do not scatter light or cause opacity of the films. Commercial nanoparticles, despite powerful ultrasonic treatment, cannot be individually dispersed and are present as large agglomerates. For pigment applications, opacity is desired but for optically transparent UV filters, the composites with exceptionally dispersed TiO_2 nanorods are particularly promising. Strong UV absorption was observed for TNR composites with as little as 1 wt% of nanorods. Quantum confinement effects were also observed; by

blending nanorods of different sizes into polymers it is possible to tune the absorption band edge, which offers yet another potential advantage for optical limiting devices.

Thermal and mechanical properties of the composites remain satisfactory for use in optical applications; however, these properties are somewhat lower than that of the pure polymer. Plasticization of the nanorod-polymer interface by the organics at the nanorod surface, either structure directing agents from synthesis or dispersing agents, was identified as the reason for this behaviour. Fabrication of TiO_2 nanorod – epoxy composites was also attempted, but with very limited results (brief summary is included in the Appendix 7.5).

6.2 Summary of collaboration work

During the course of this research, sample quantities of the as-prepared and / or stripped titania nanorods were provided to other researchers within Imperial College for use in nanocomposite foams and solar cells. This section will briefly summarise the most important findings of this work.

The fabrication of TNR-nanocomposite foams from high internal phase emulsions (HIPEs) is under current investigation[356]. Highly open, porous, polymer foams obtained via the polymerisation of the continuous monomer phase of concentrated emulsions are very attractive materials for a wide range of applications due to their low density and interconnected pore structure. For example, such materials could be useful for filtration applications, as ion exchange resins, monolithic micro-bioreactors and scaffolds for tissue engineering. However, greater application of polymerised HIPEs (polyHIPEs) is limited by their relatively poor mechanical performance and the expense of molecular surfactants required to stabilise the HIPEs. Adding TNR to polyHIPEs is an effective way to reinforce the nanocomposite foams. It has been shown[356] that adding only 1 wt% of TNR (Cozzoli-type synthesis, OA ligand) increases the compression modulus and the crush strength of the original polyHIPEs by approximately 100%. In comparison, similar level of reinforcement of polyHIPEs by commercially available TiO_2 nanopowder (P25) was observed only for a 4 wt% filler loading fraction. It is argued that the unsaturated character of the oleic acid on

the nanorod surface allows it to become covalently incorporated into the growing polymer network during the radical polymerisation reaction of the composites. In addition, the TNRs can act as particulate (a.k.a. Pickering) stabilisers allowing polyHIPE fabrication in the absence of molecular surfactants, even at low loadings.

TNR_{TOPO} were used for fabrication of polymer (poly ((3-hexyl) thiophene), P3HT) blend photovoltaic devices. A dense TiO_2 film (30 nm thick) was deposited on an indium-tin oxide substrate. The TiO_2 nanorod films (250 nm) were spin-coated onto dense titania layer, sintered and a 200 nm layer of P3HT was spin-coated on top of the nanorod film. Finally, poly (3,4-ethylenedioxythiophene):poly (styrene sulfonate) and a gold electrode are deposited on top of the P3HT layer. Current work is aimed at optimising the porosity of the devices, which greatly affects the photovoltaic performance. Preliminary measurements of the devices without the TNRs reveal significant leakage currents; this is most likely a problem with the device fabrication procedures, which need to be optimised. For the solar cells with TNR_{TOPO}, the results show a reduction in the leakage current and an increase in the device fill factor, which is directly proportional to the power conversion efficiency of the solar cell.

6.3 Future research

The addition sequence of TTIP is one aspect of the nonhydrolytic synthesis of TNR_{TOPO} that should be explored in order to understand its effect on the product properties (particle morphology, crystallinity, etc). It will be advantageous to have greater control over the aspect ratio of TNR_{TOPO} as it would allow fabrication of nanocomposites with different aspect ratio nanorods, which would, in turn, provide answers to the fundamental question – what is the effect of anisotropy on material properties? Adjusting the surface chemistry of titania nanorods is crucial for achieving good adhesion at the nanorod-polymer interface. Further research should be aimed at treating stripped TNR dispersions with different siloxanes in order to fine-tune the surface chemistry so that the functionalised nanorods strongly bind to the polymer matrix. Current state-of-the-art TNR polymer composite films do not display strong nanorod-polymer adhesion, which is prerequisite for alignment of nanorods within the matrix, which would, in turn, lead to materials with anisotropic properties. The likely effectiveness of this strategy is suggested by the polyHIPE results. Appropriate functionalisation of the stripped TNR dispersions will also allow transfer into organic solvents and subsequent processing of TNR – organic-soluble polymer (e.g. PMMA) composites as well as thermosets (epoxy).

Siloxane modification of TNR has been shown to be a viable way for the reduction of TNR photoactivity; however, it would be also interesting to consider alumina-type nanorod coatings. Another promising route would be to adapt the procedure developed by the Oxford research group[195] for Mn-doping of TiO_2 nanoparticles, which is the 'secret' behind fascinating reduction in photoactivity of the new Boots Soltan Once® sunscreen range.

7. Appendix

7.1 DMTA results for TNR – PDLLA and TNR – PMMA nanocomposite films, at 10 Hz

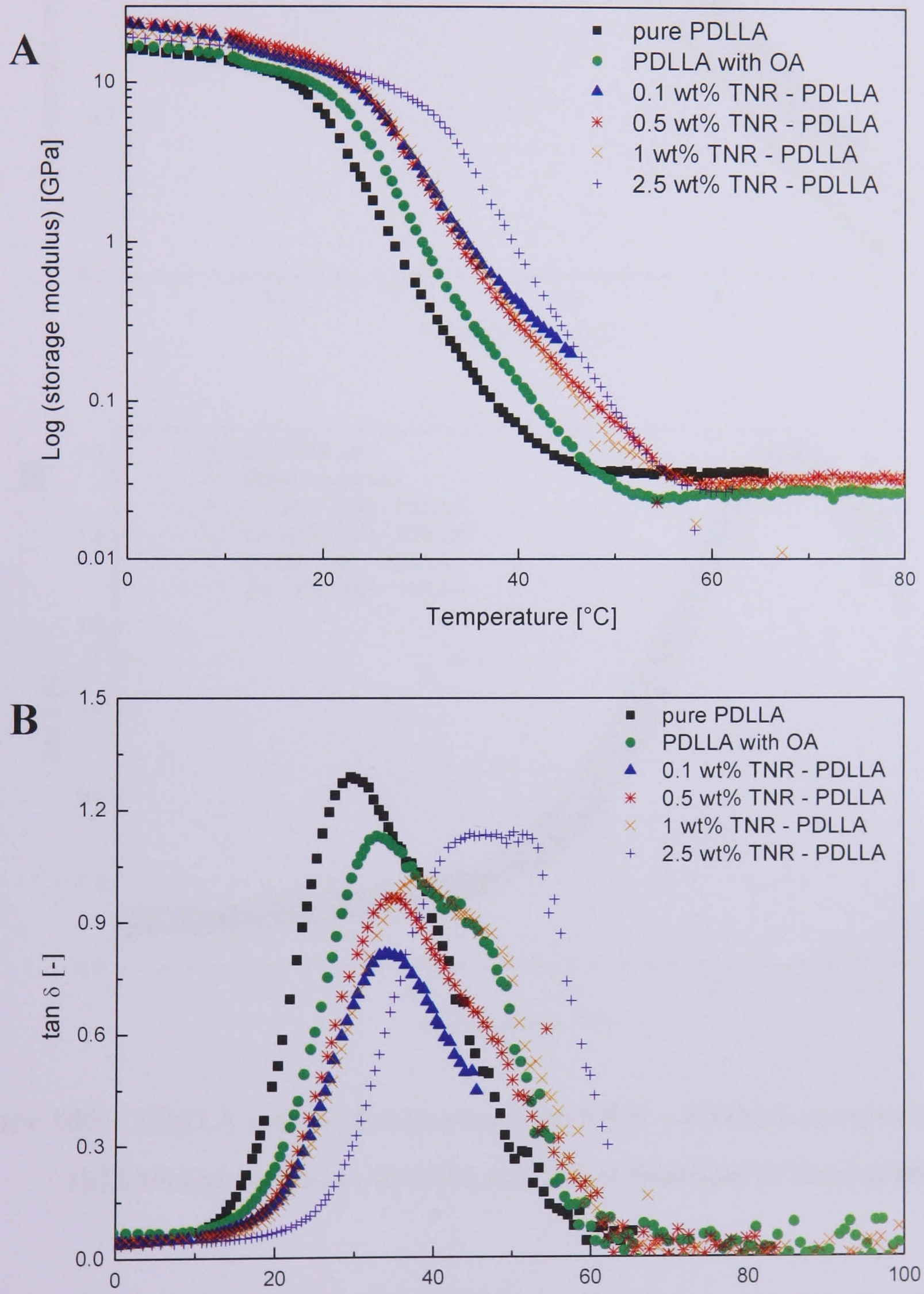
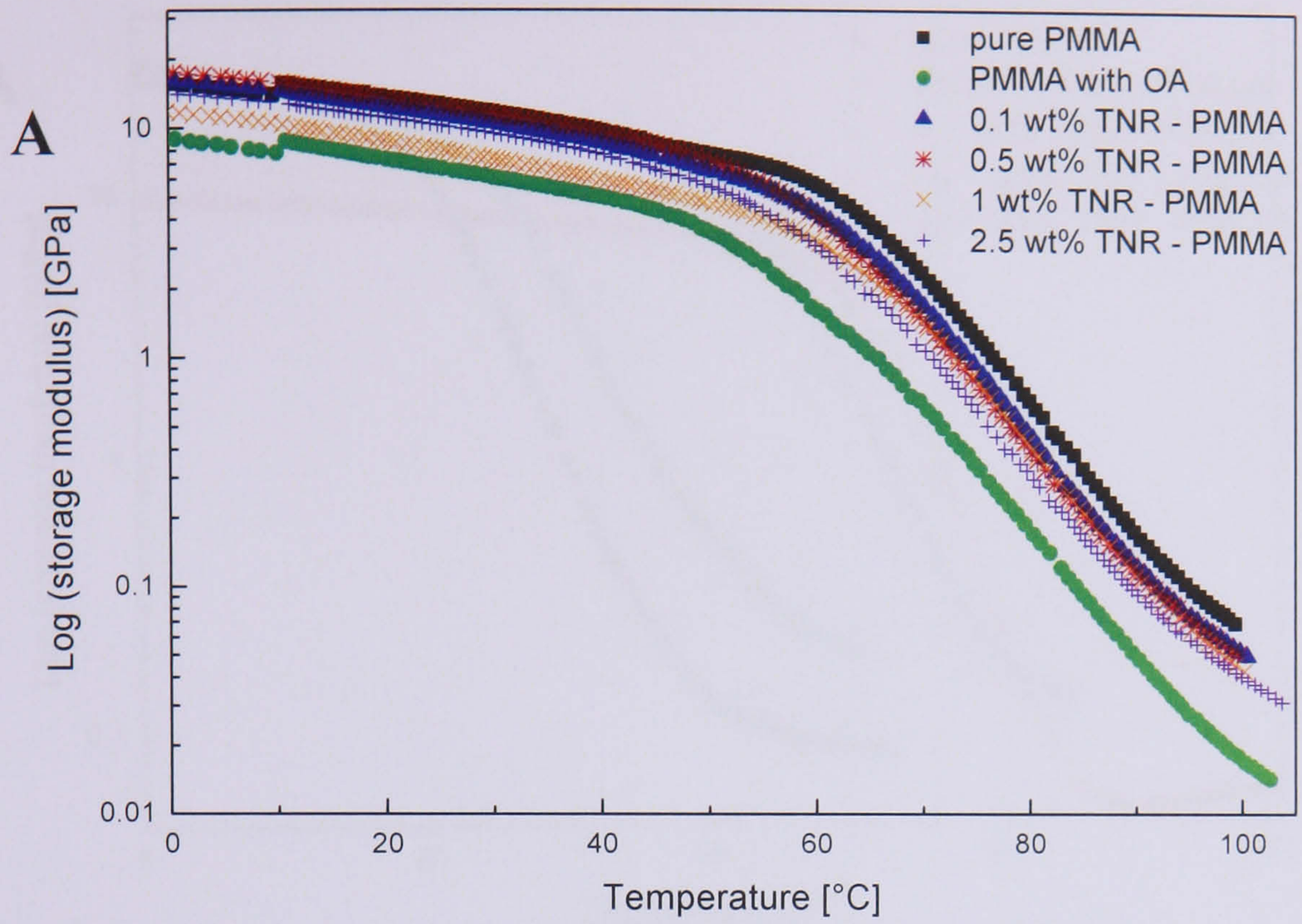


Figure 99 – DMTA results for low loading TNR – PDLLA composites at 10 Hz: (a) Storage modulus and (b) tan δ as a function of temperature



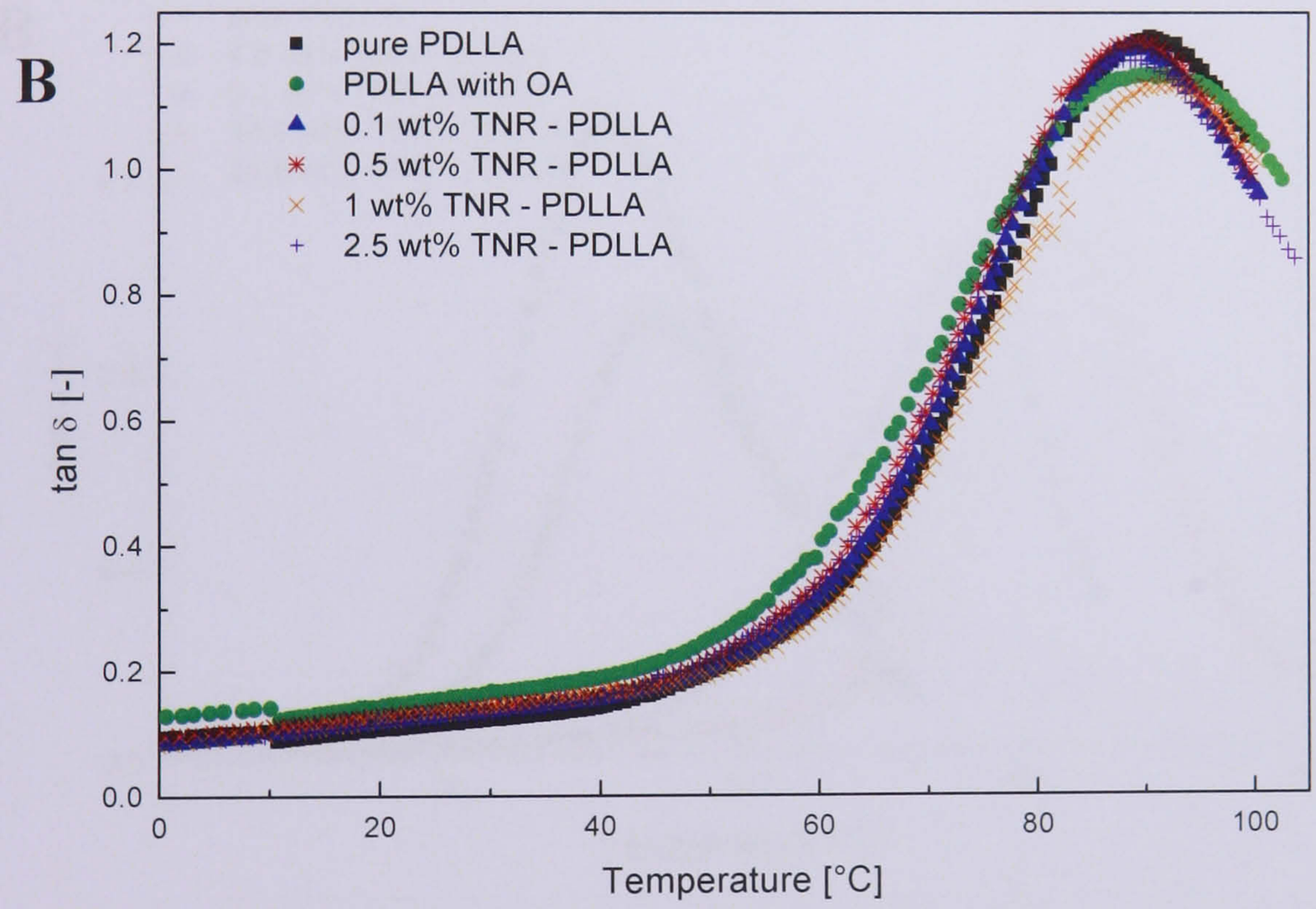
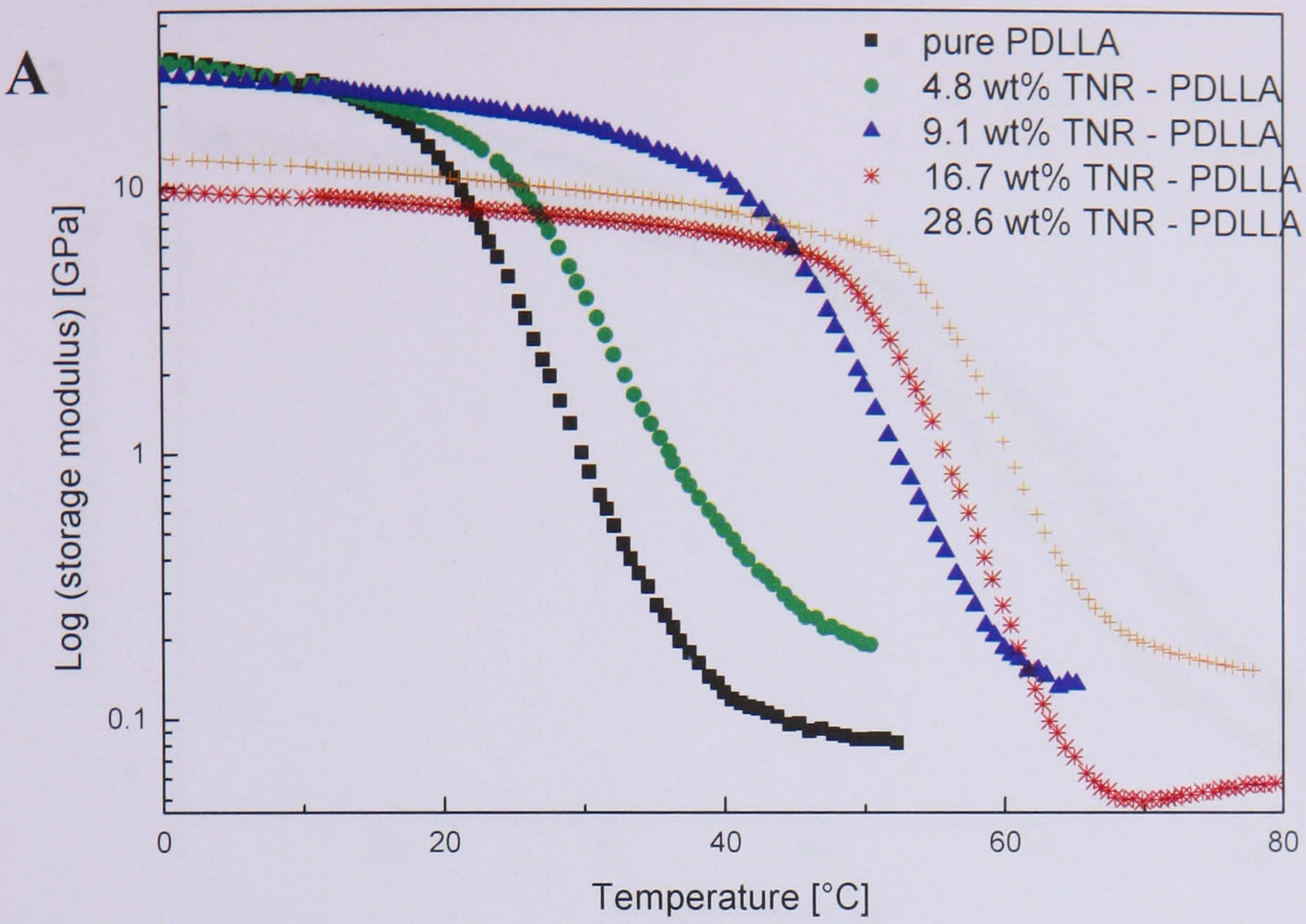


Figure 100 – DMTA results for low loading TNR – PMMA composites at 10 Hz:
(a) Storage modulus and (b) tan δ as a function of temperature



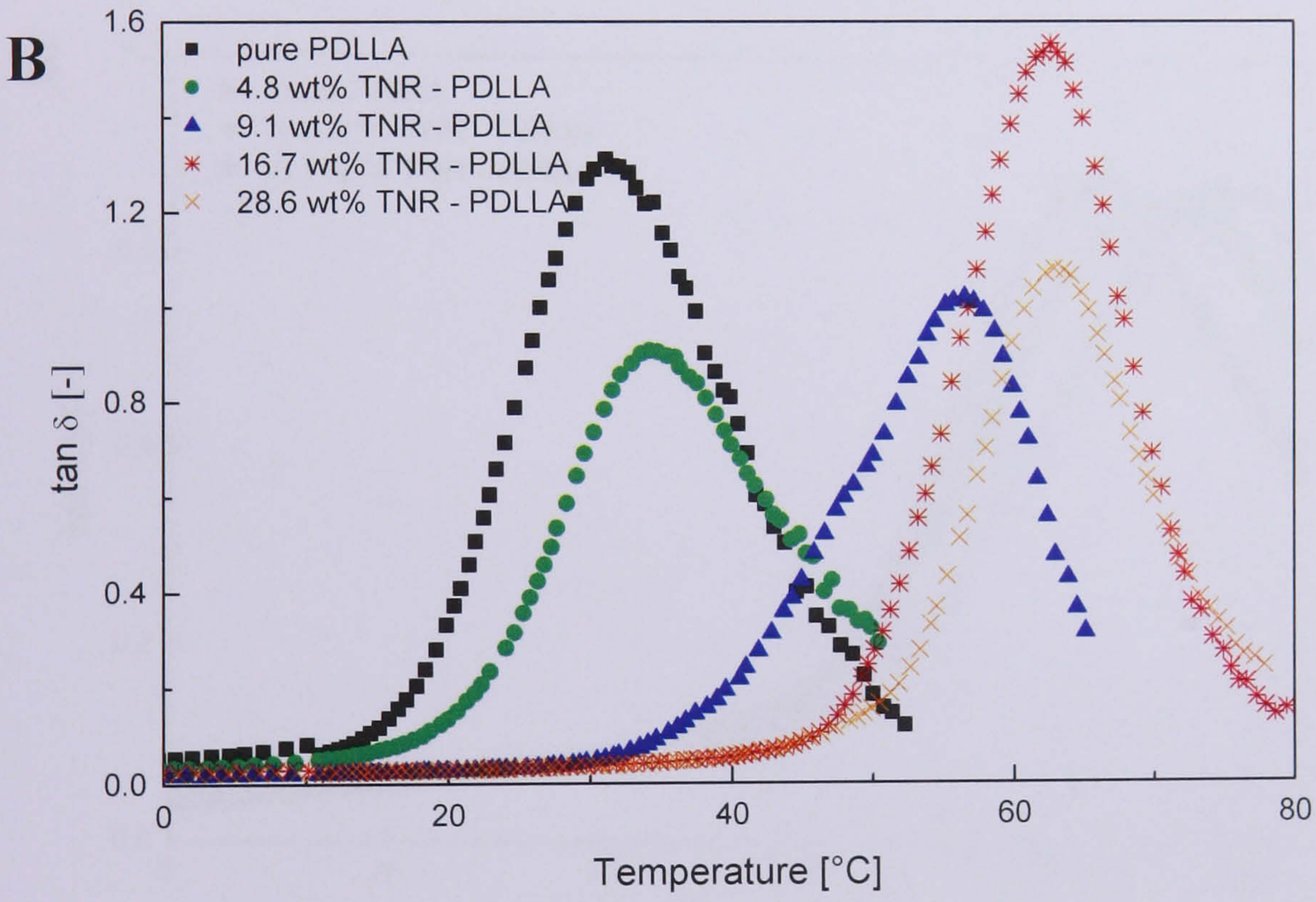
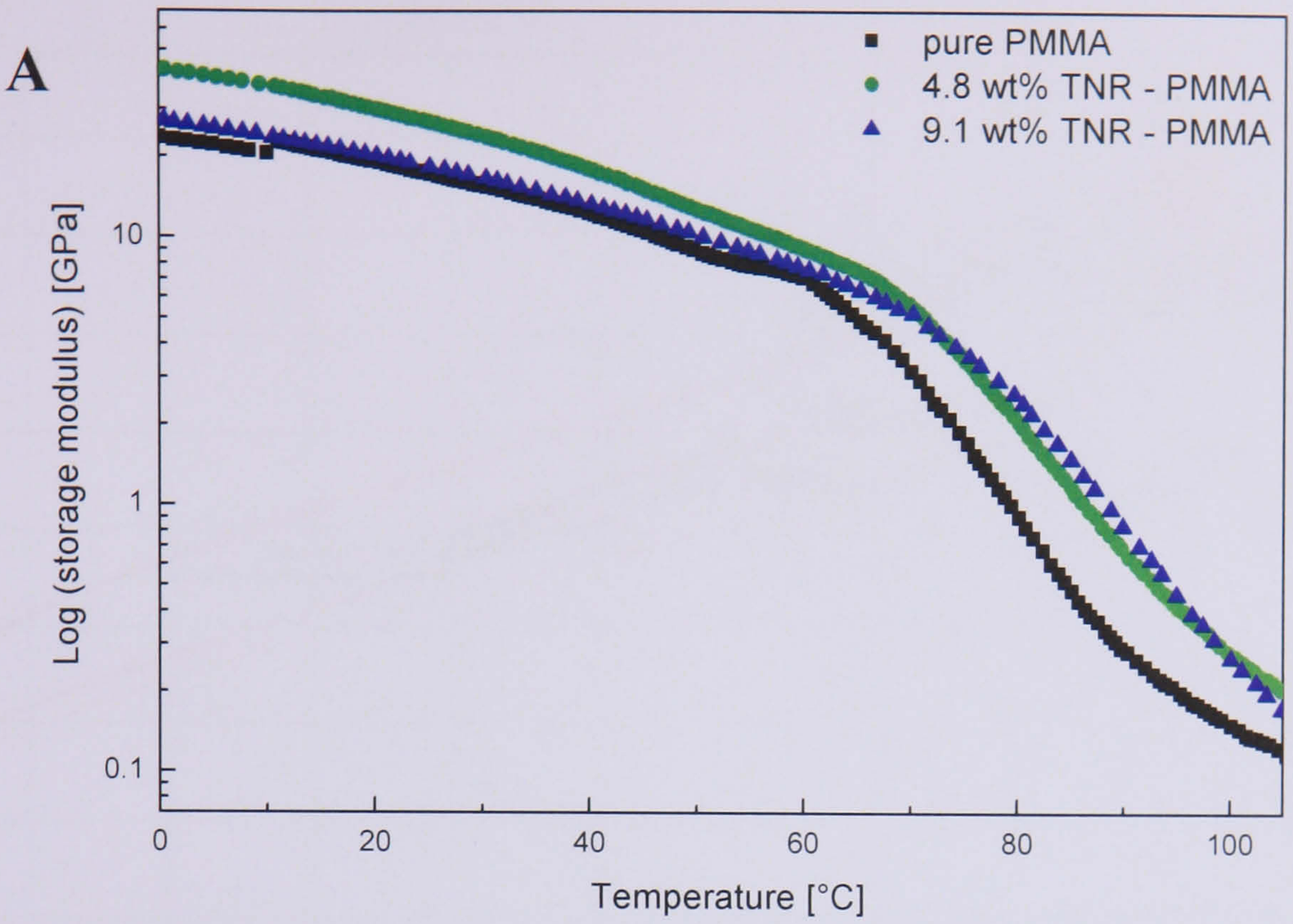


Figure 101 – DMTA results for high loading TNR–PDLLA composites at 10 Hz: (a) Storage modulus and (b) tan δ as a function of temperature



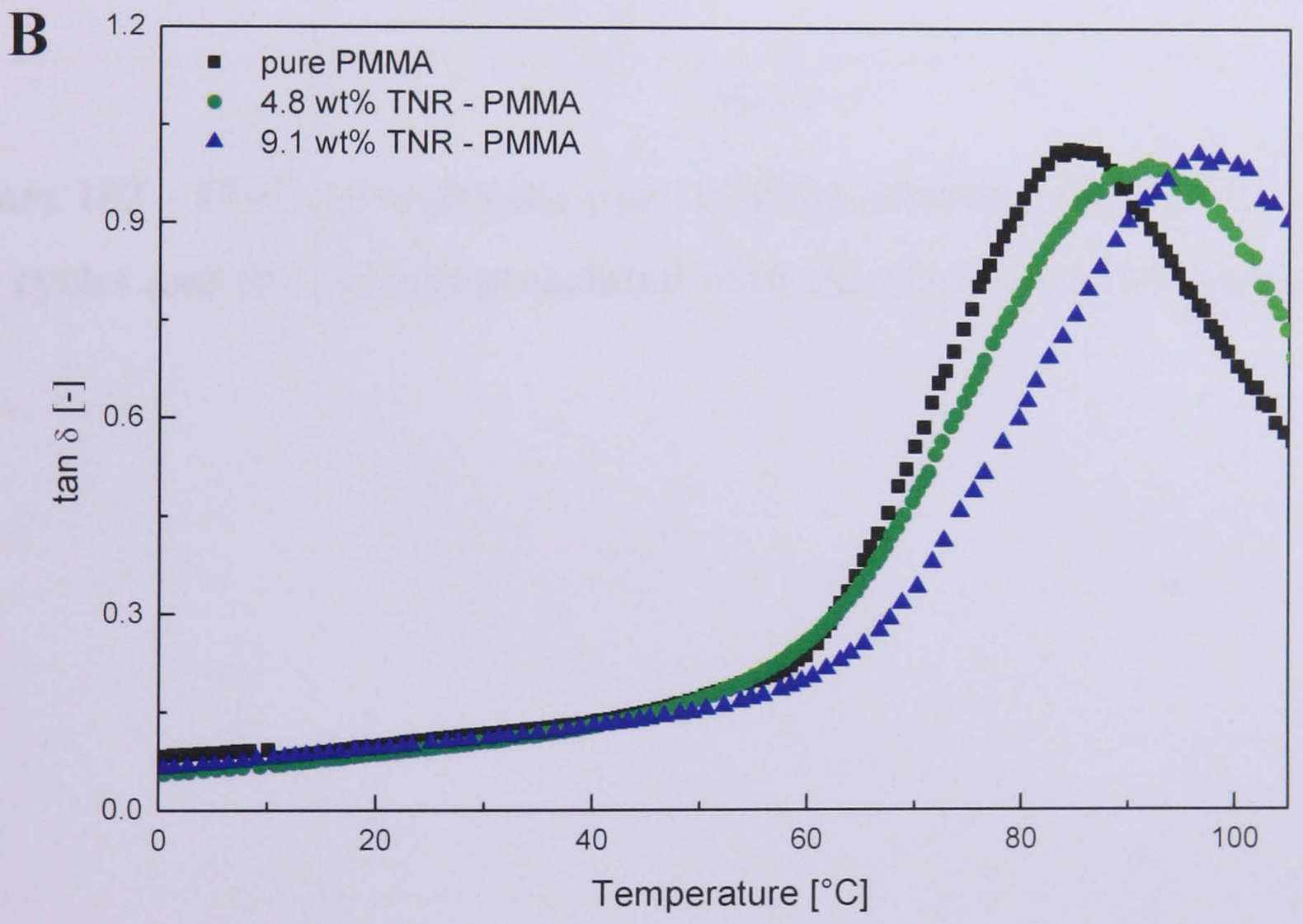


Figure 102 – DMTA results for high loading TNR – PMMA composites at 10 Hz: (a) Storage modulus and (b) tan δ as a function of temperature

7.2 Typical DSC scan

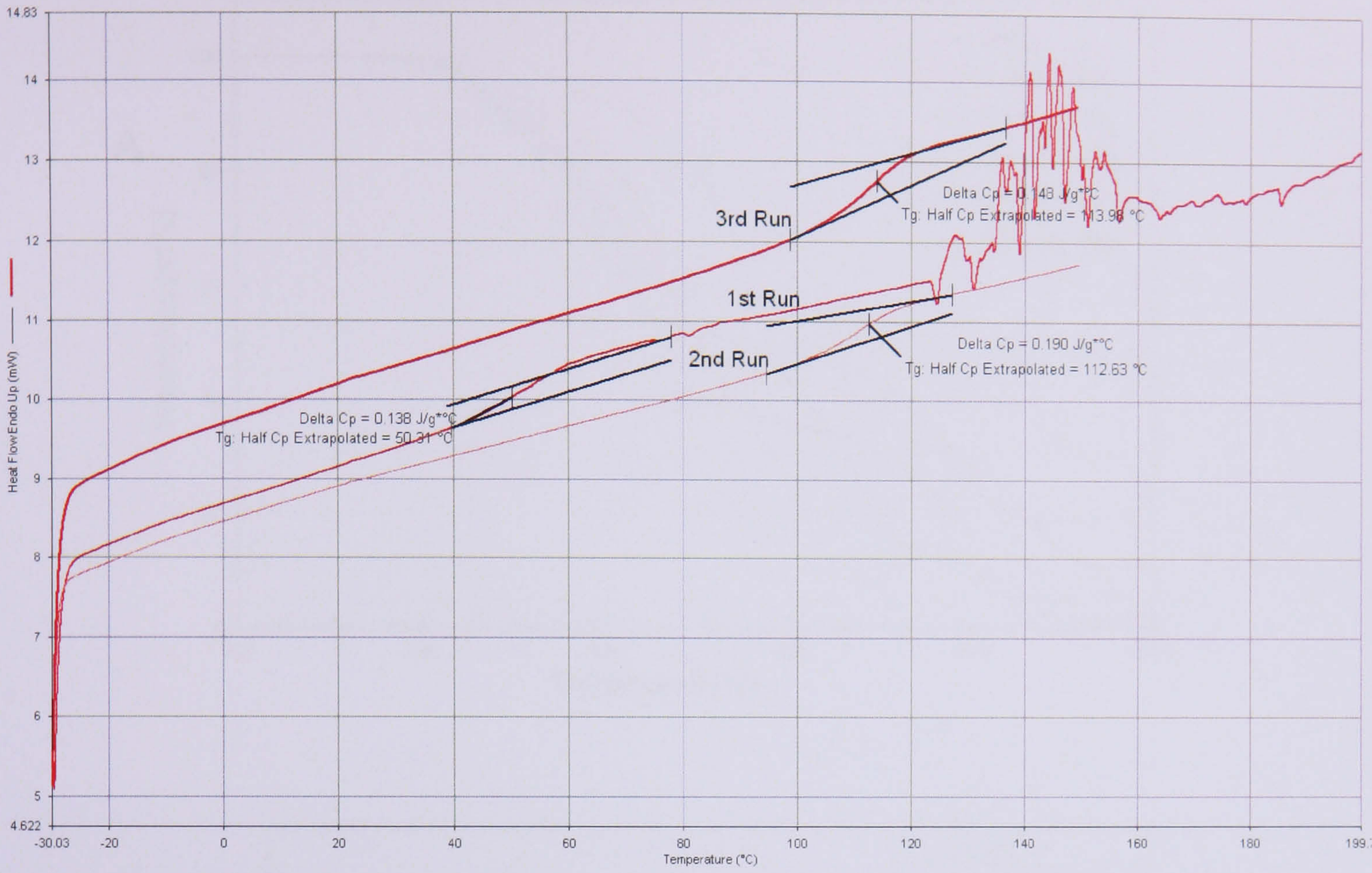
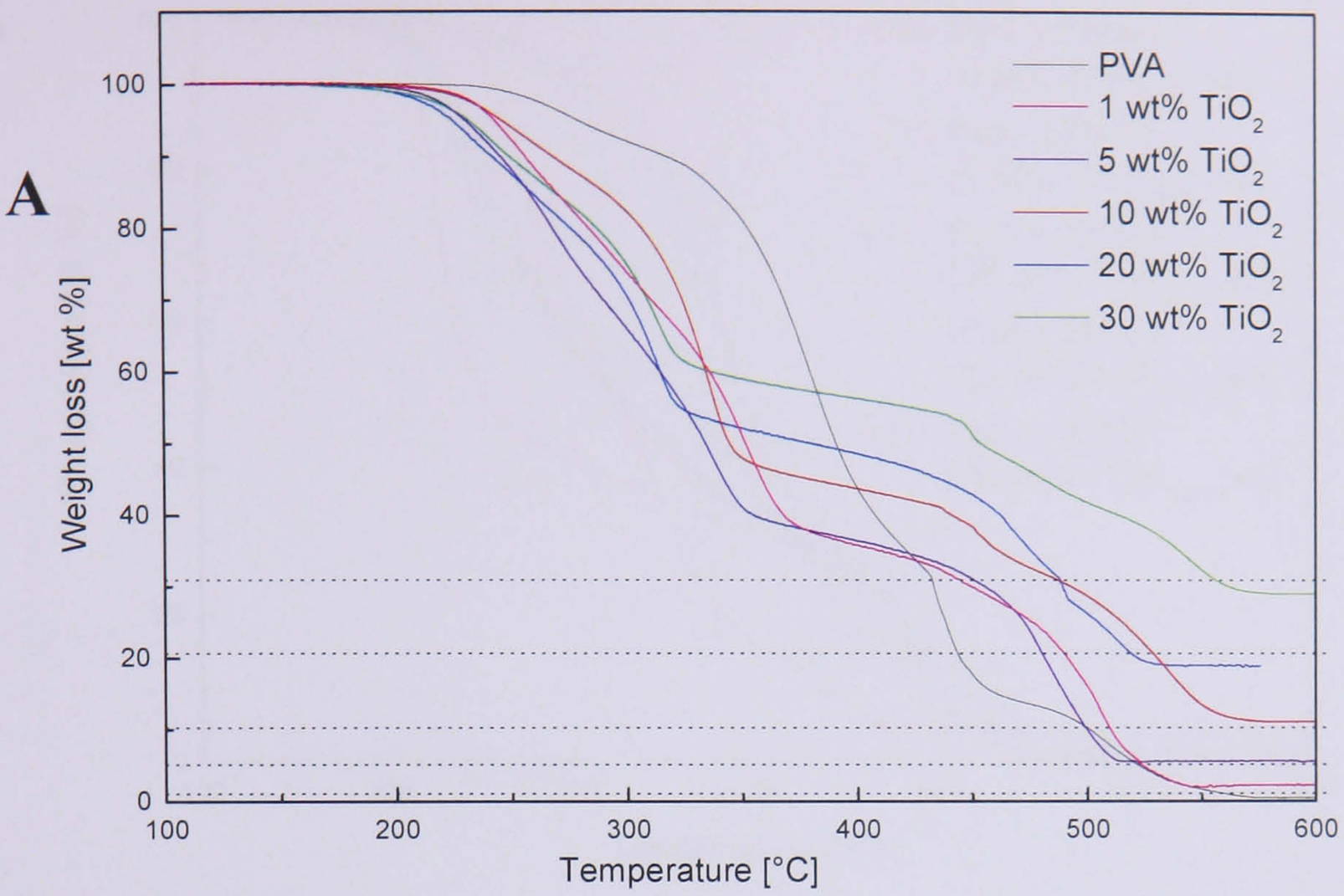


Figure 103 – DSC curve for the pure PMMA, showing three individual heating cycles and the regions associated with the glass transition temperature

7.3 TGA curves for PVA nanocomposite films



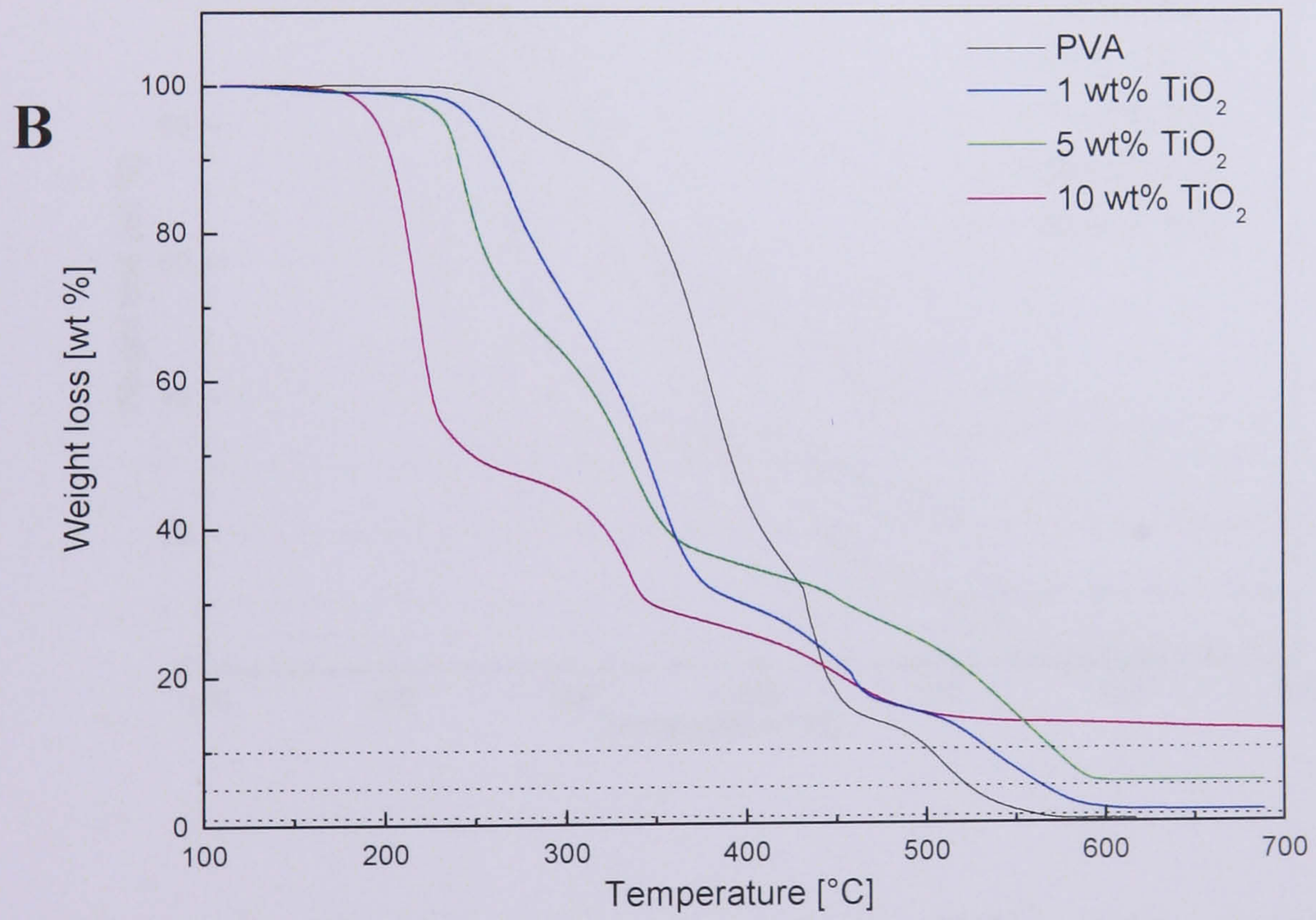
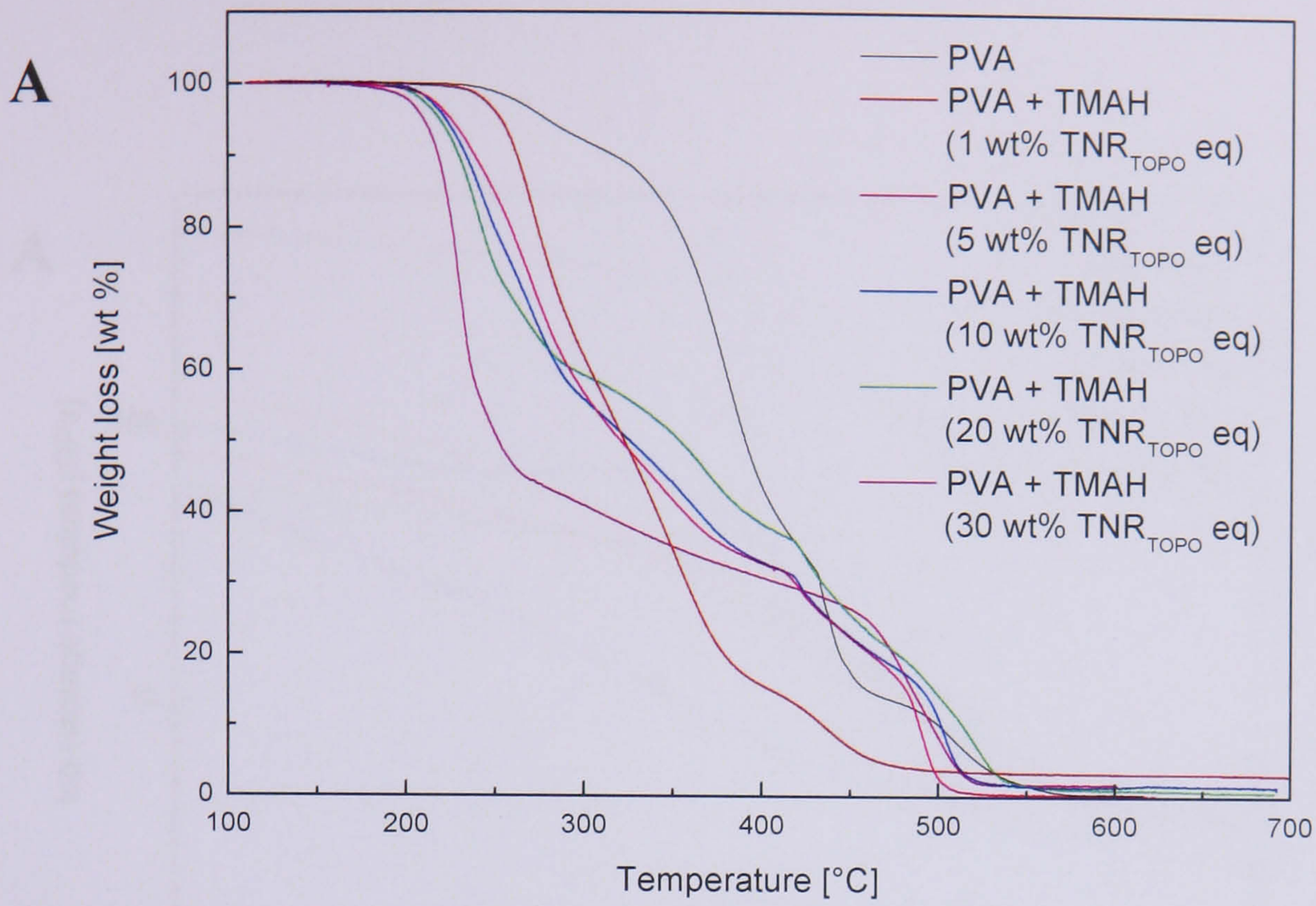


Figure 104 – Thermogravimetric analysis of PVA and the composites (a) TNR_{TOPO} – PVA (b) TNR_{OA} – PVA



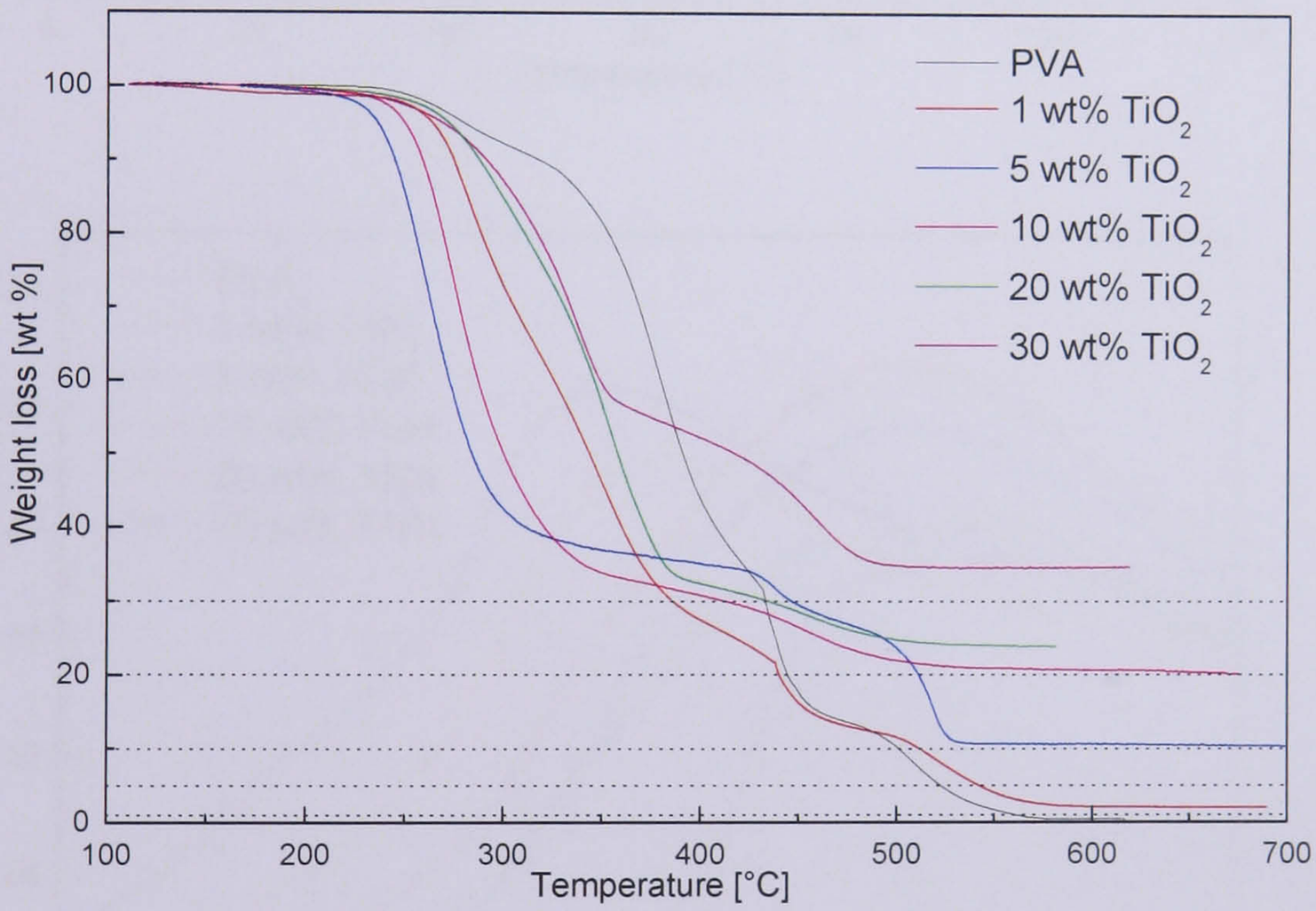
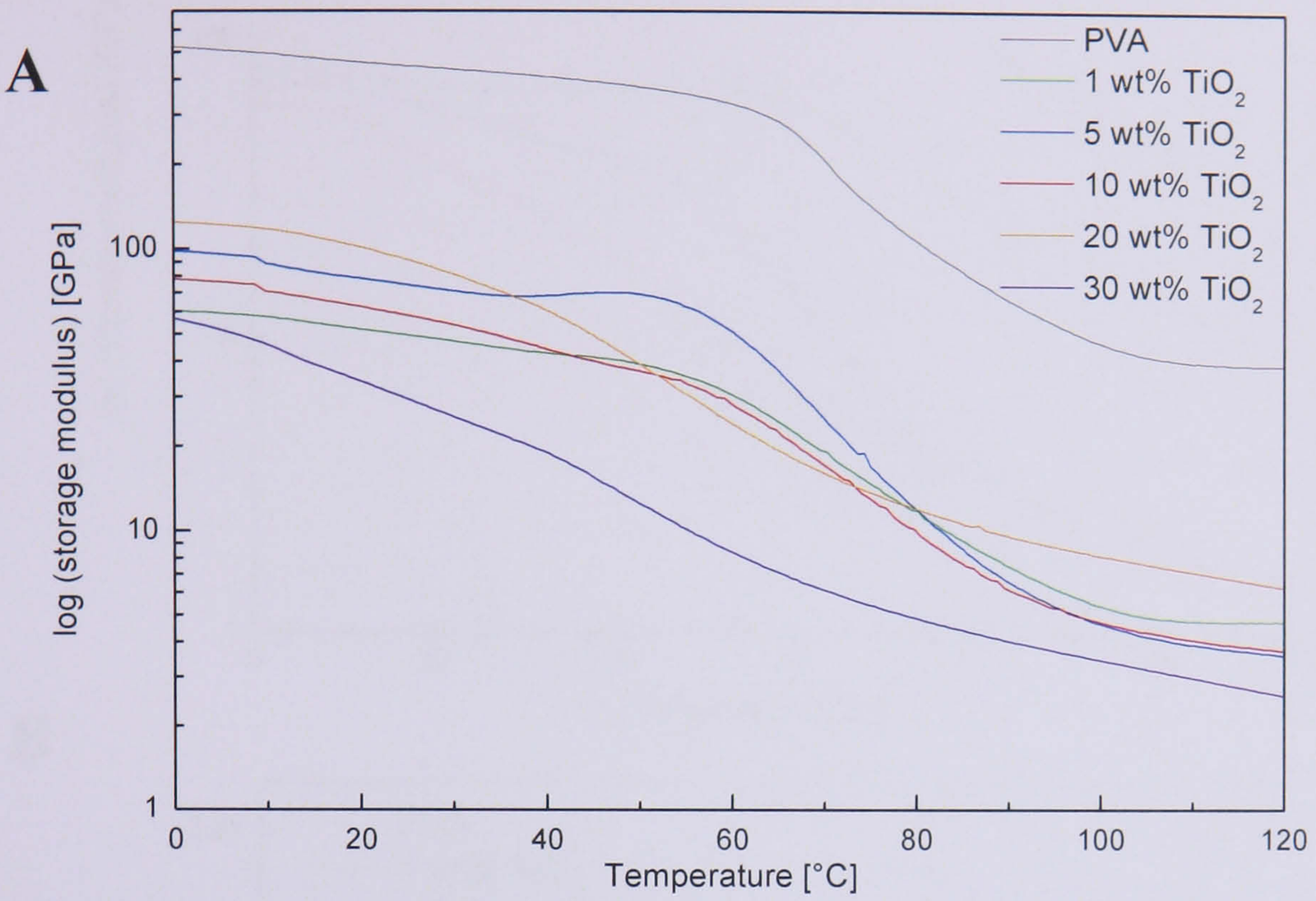


Figure 105 – Thermogravimetric analysis of PVA and composites (a) PVA with TMAH and (b) 5 nm anatase - PVA

7.4 DMTA results for PVA nanocomposite films, at 1 Hz



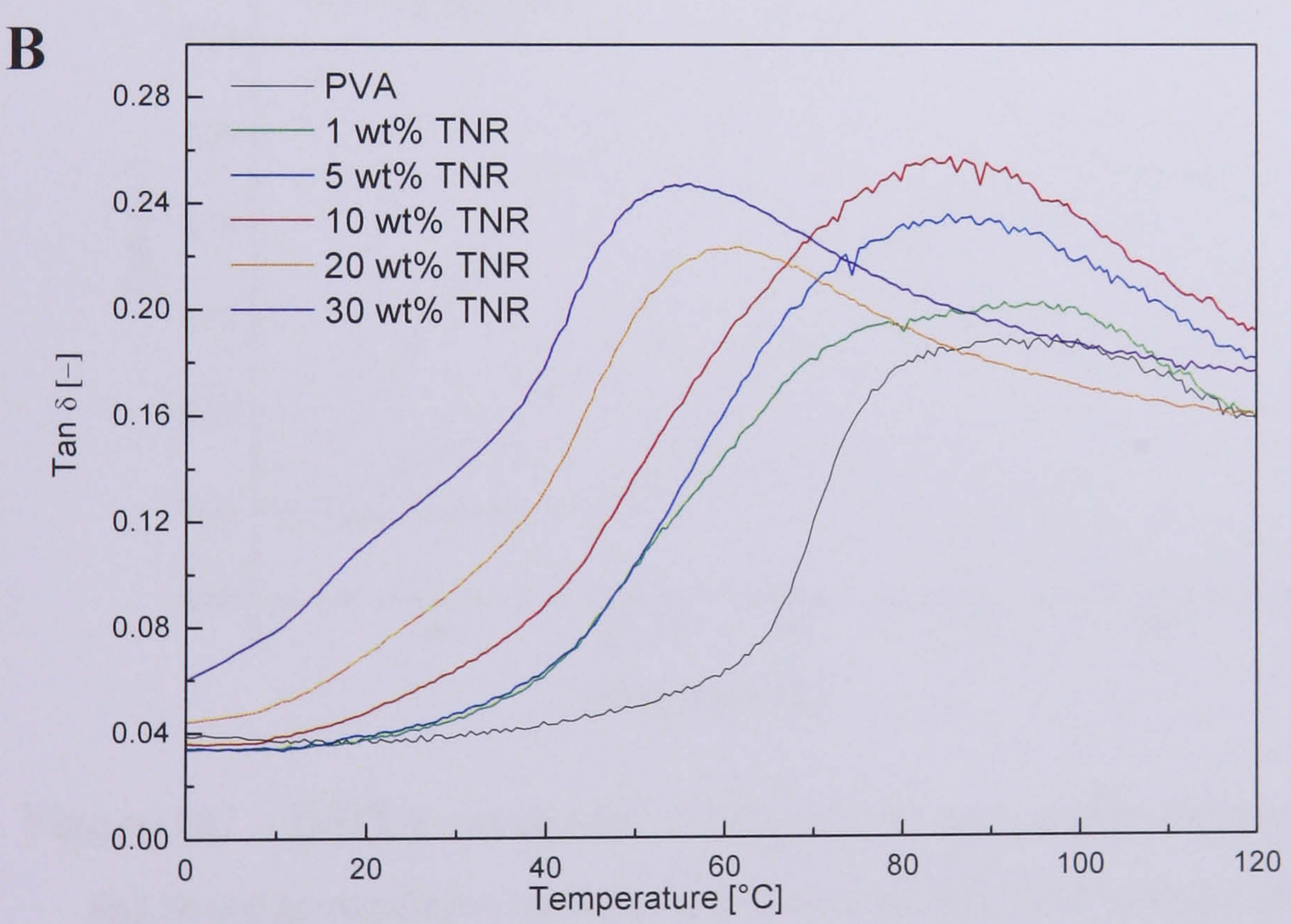
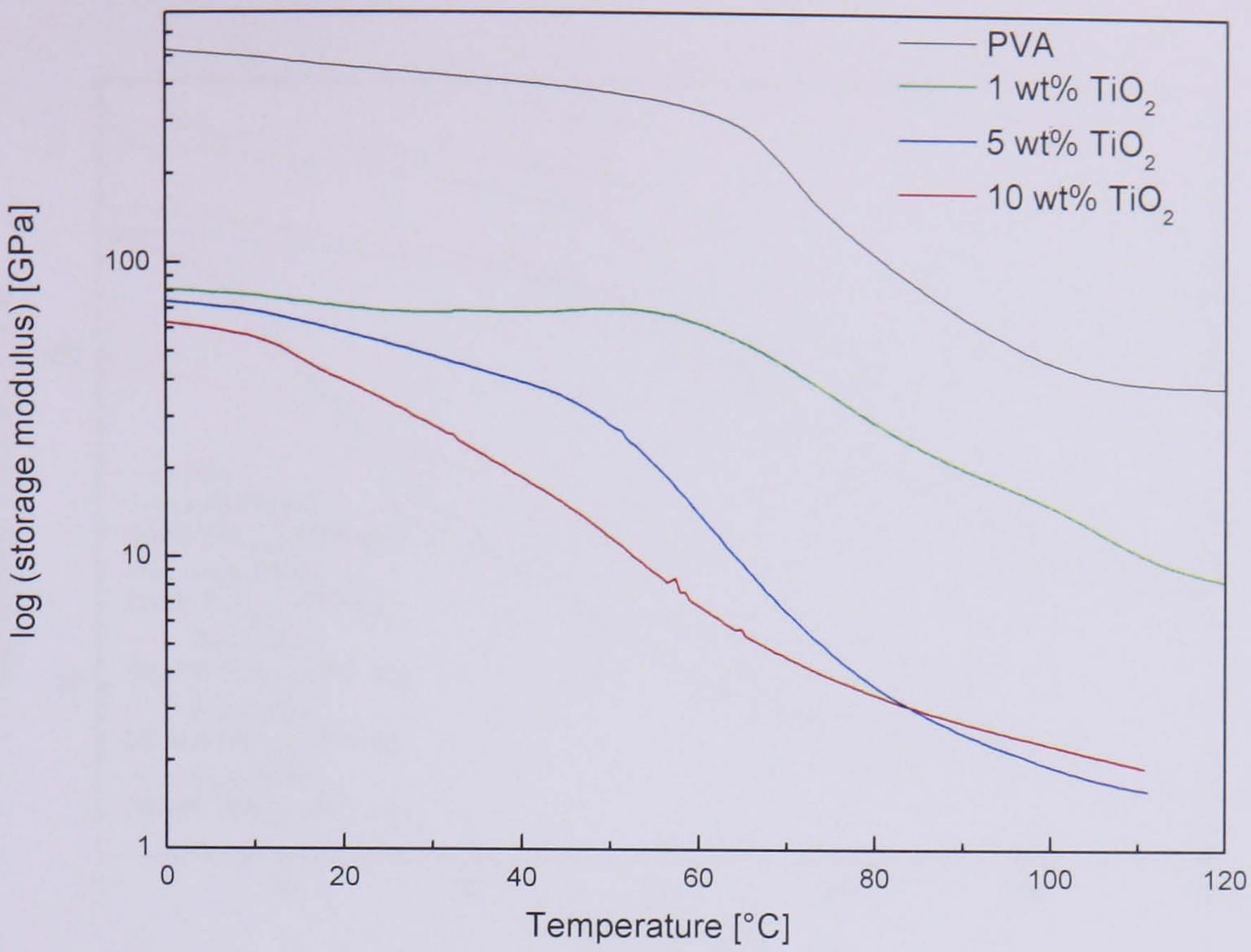


Figure 106 – DMTA results for TNR_{TOPO}-PVA nanocomposites at 1 Hz: (a) Storage modulus and (b) tan δ as a function of temperature

A



B

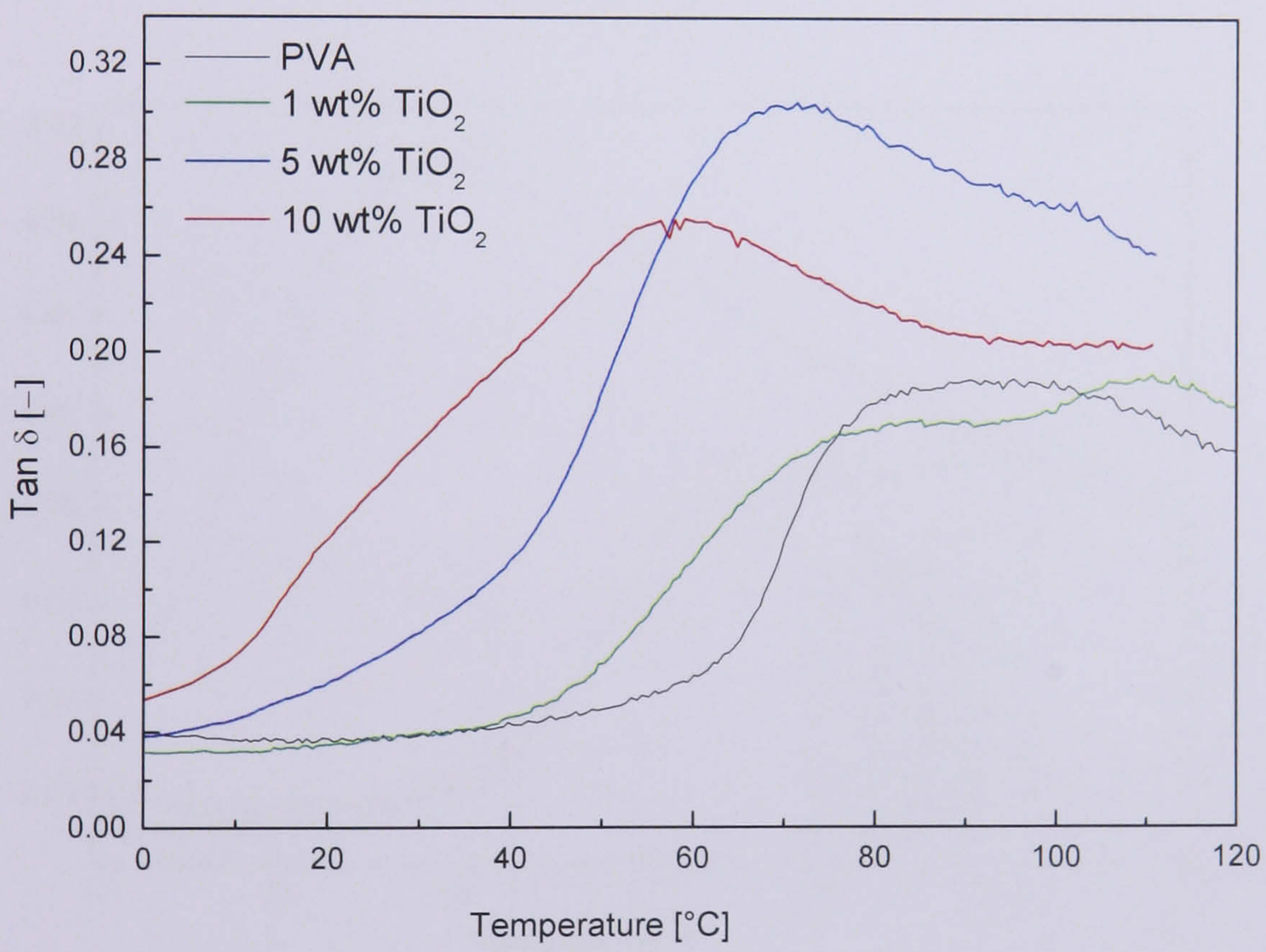
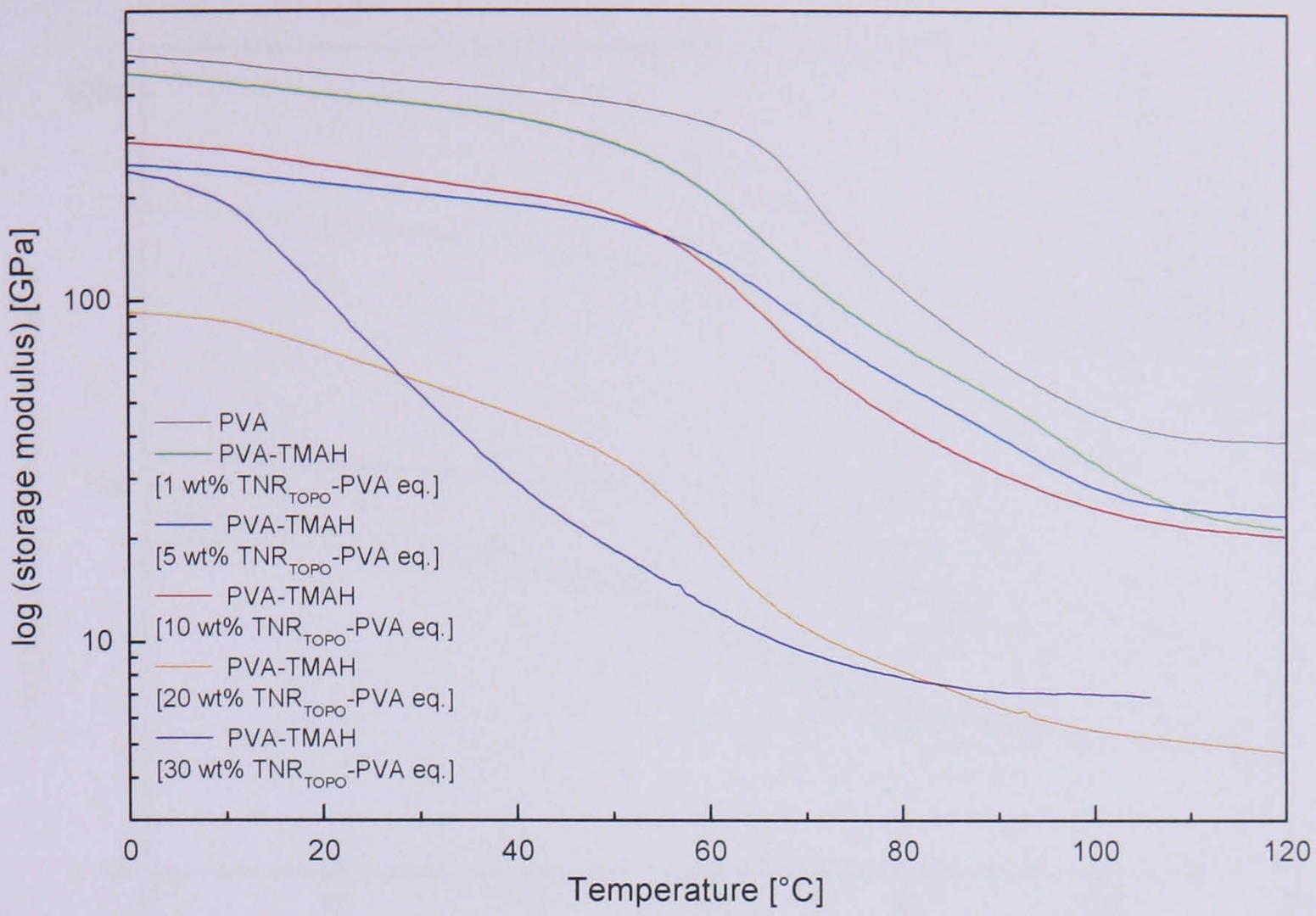


Figure 107 – DMTA results for TNR_{OA}-PVA nanocomposites at 1 Hz: (a) Storage modulus and (b) tan δ as a function of temperature



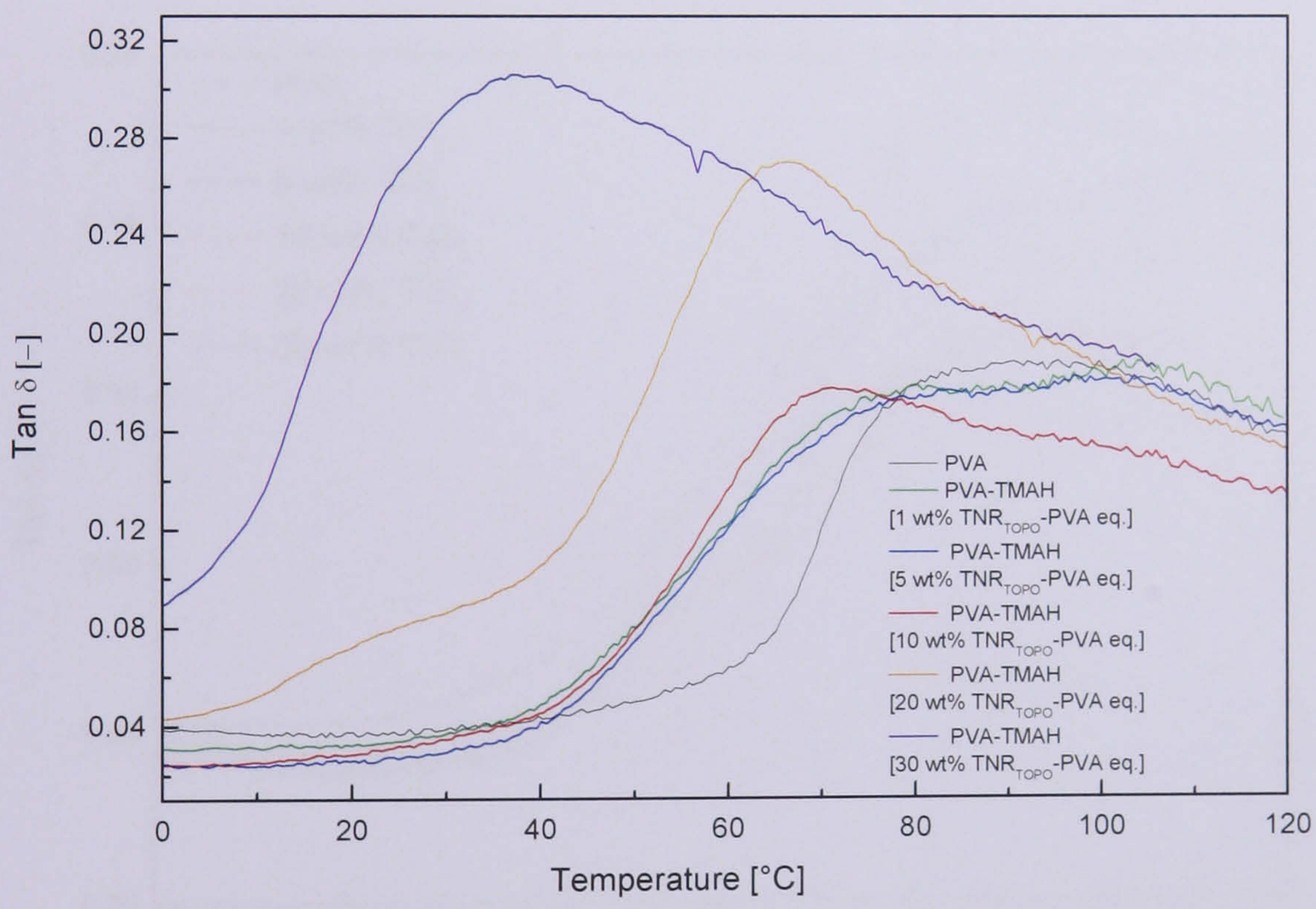
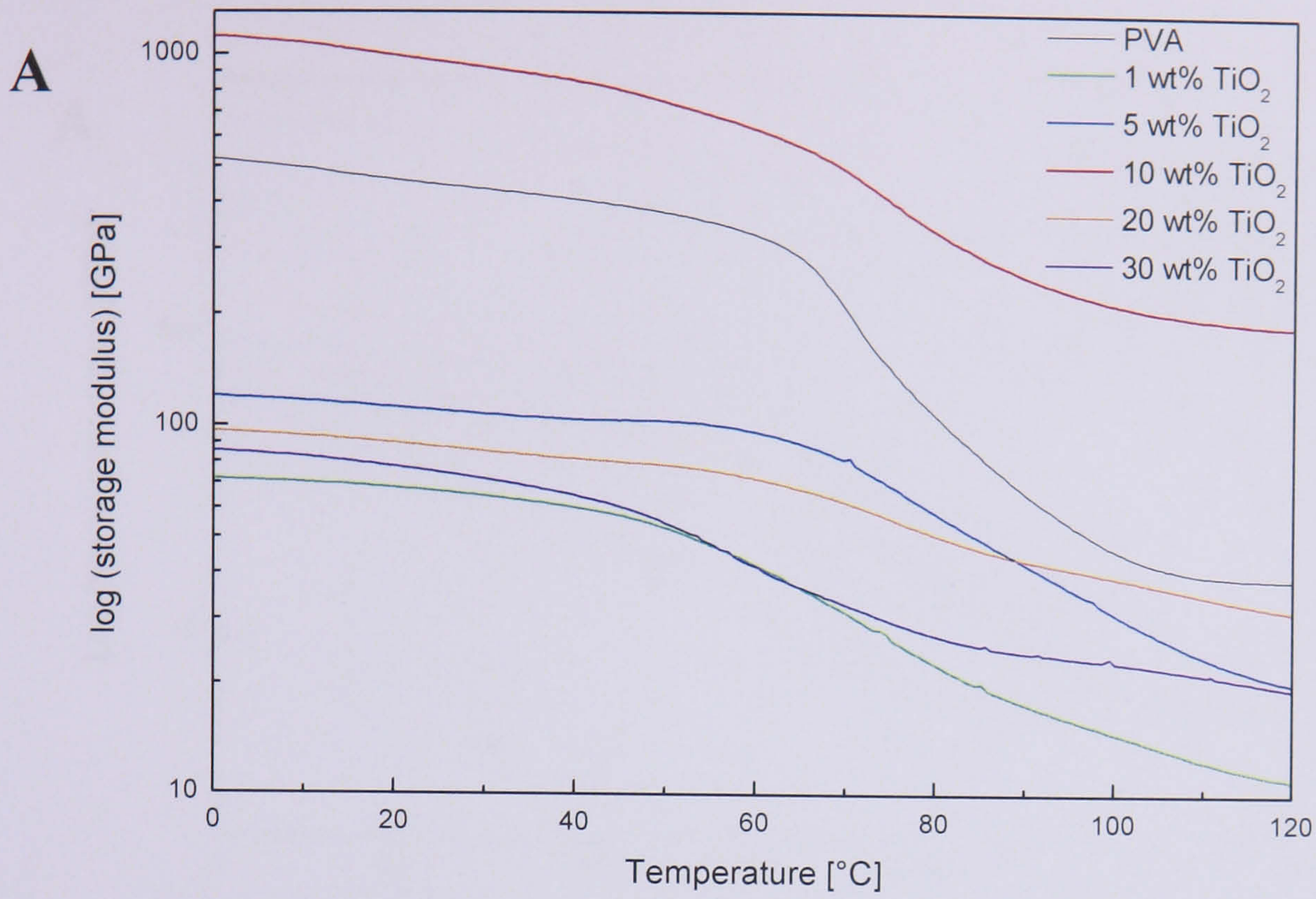


Figure 108 – DMTA results for PVA films with TMAH at 1 Hz: (a) Storage modulus and (b) tan δ as a function of temperature



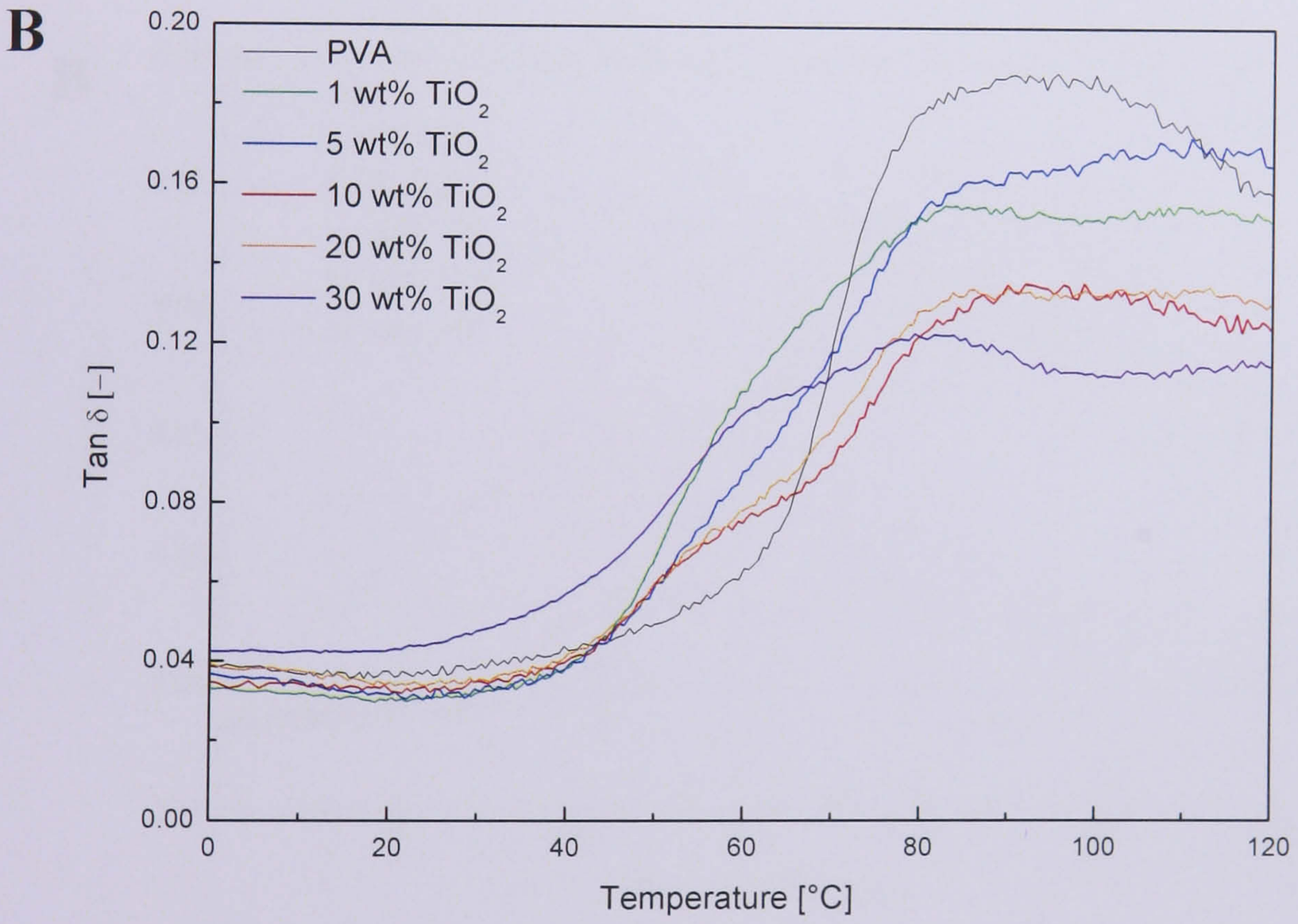


Figure 109 – DMTA results for 5 nm anatase-PVA nanocomposites at 1 Hz: (a) Storage modulus and (b) tan δ as a function of temperature

7.4 DMTA results for PVA nanocomposite films, at 10 Hz

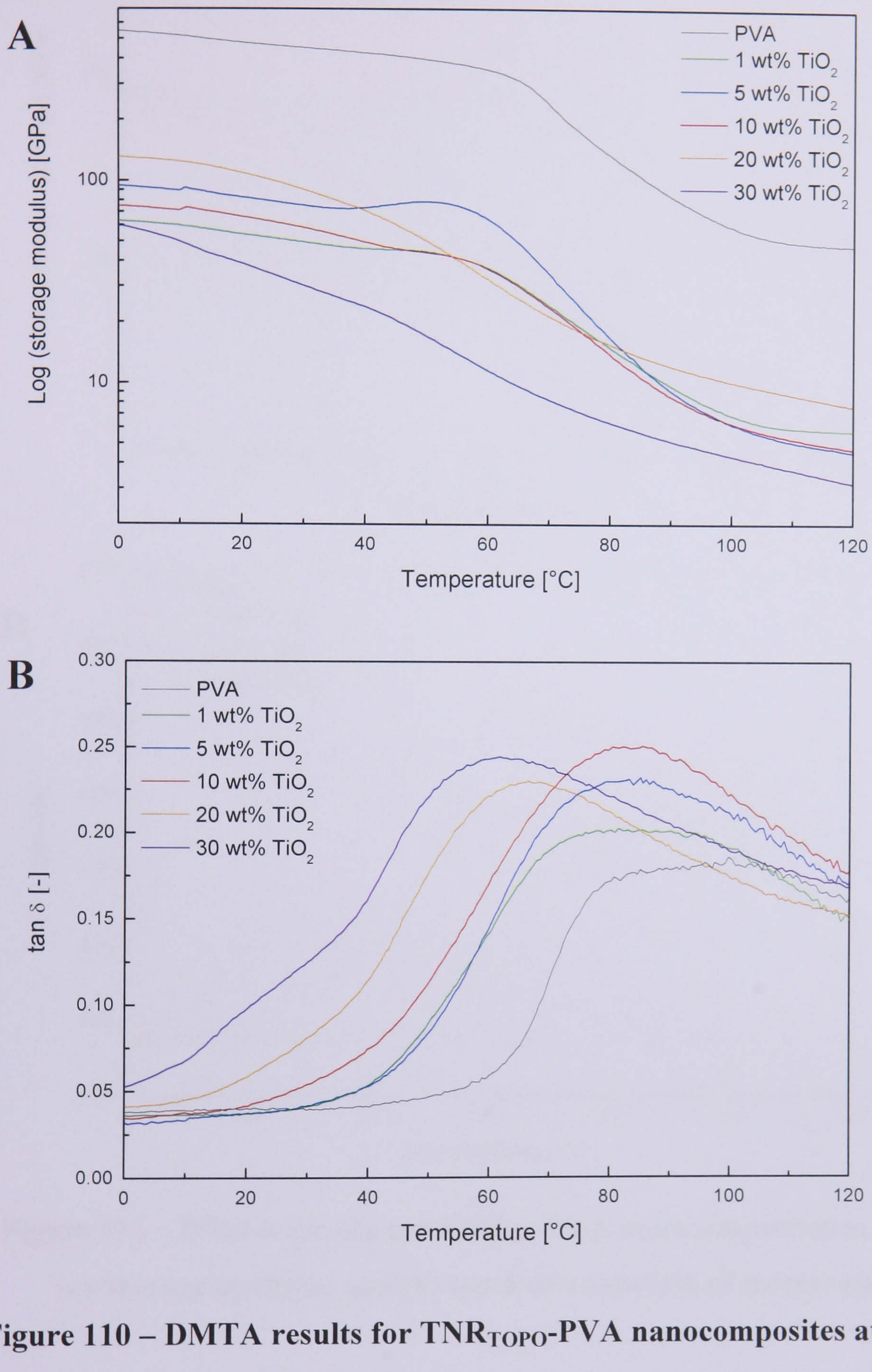
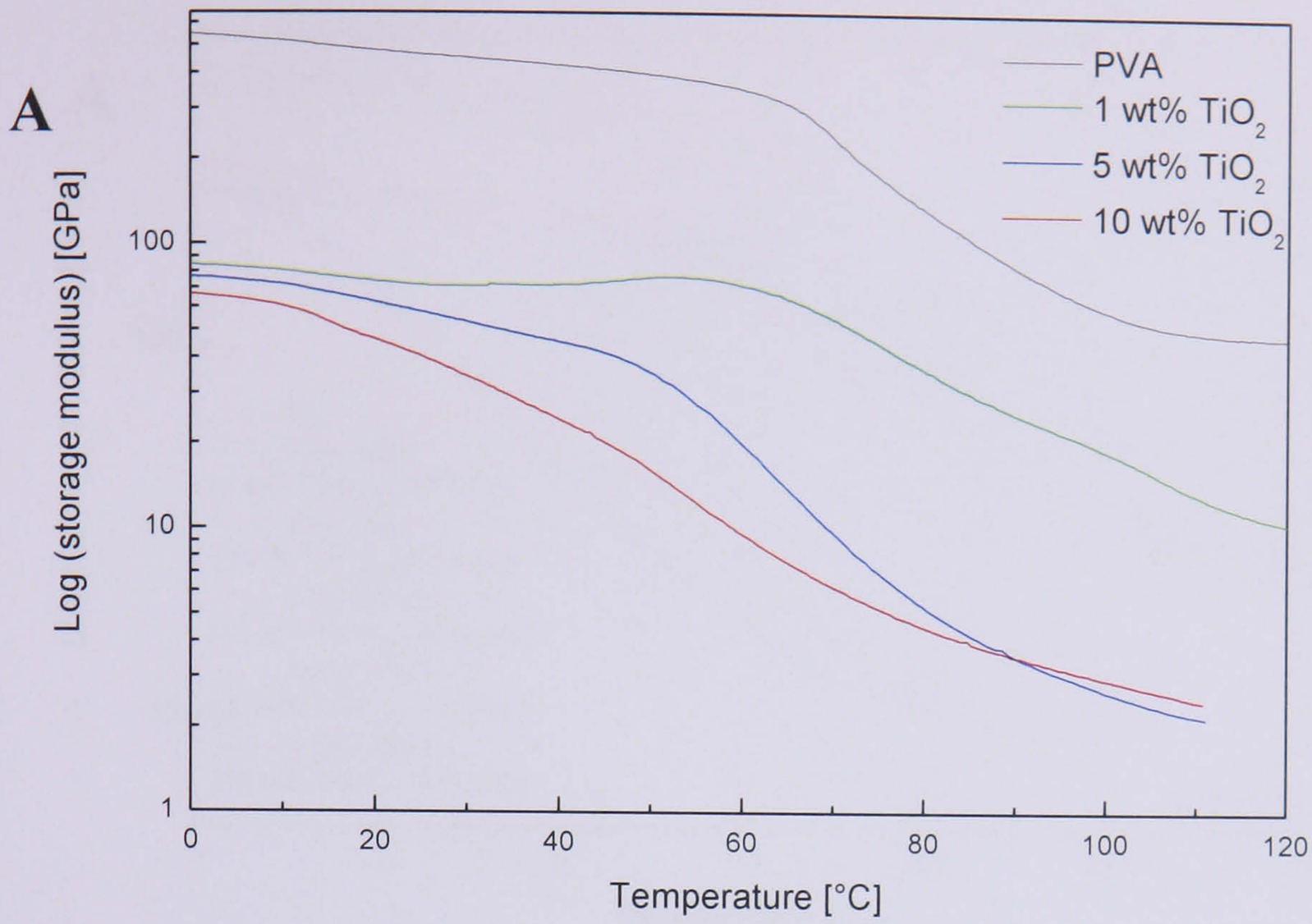


Figure 110 – DMTA results for TNR_{TOPO}-PVA nanocomposites at 10 Hz:
(a) Storage modulus and (b) tan δ as a function of temperature



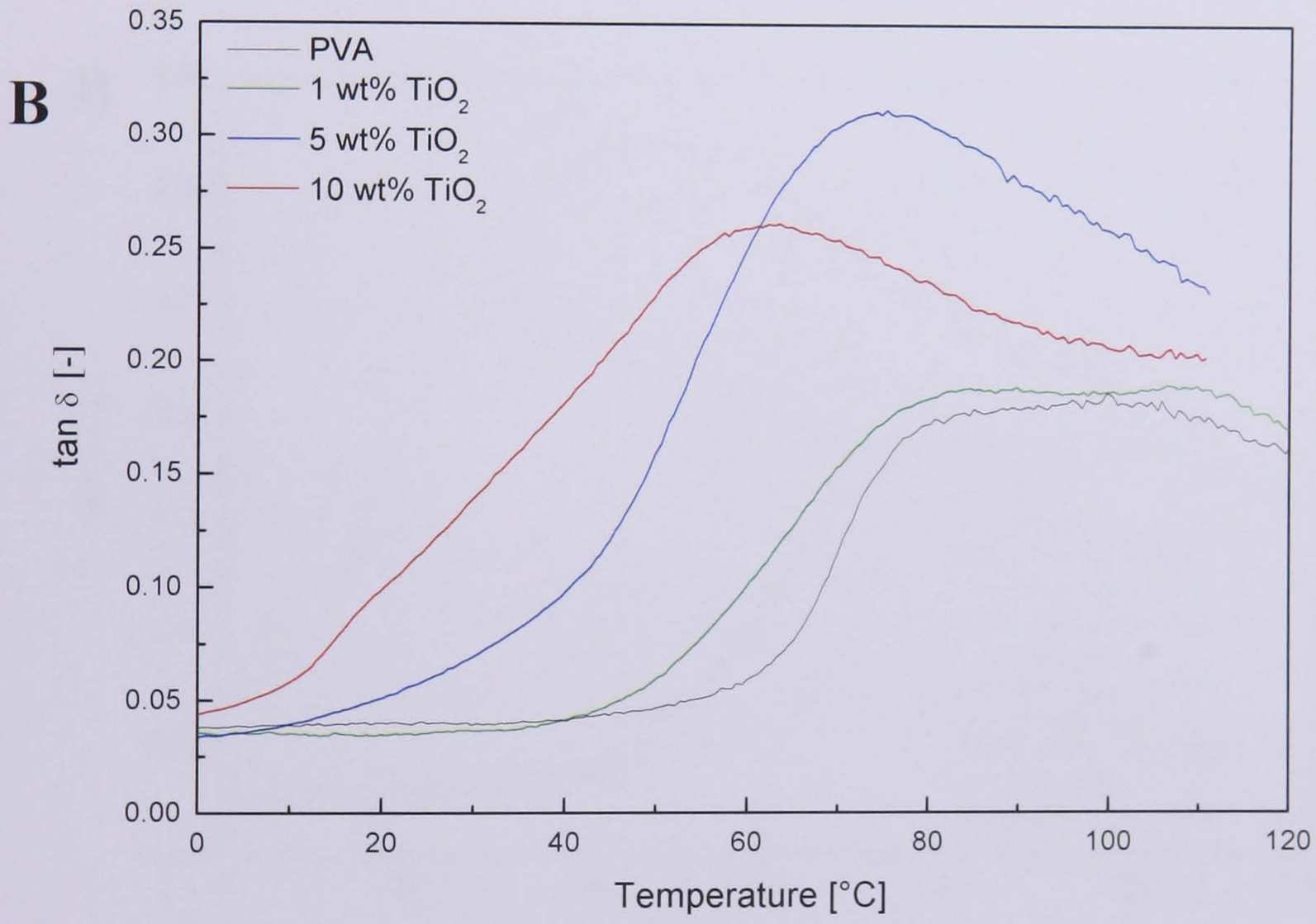
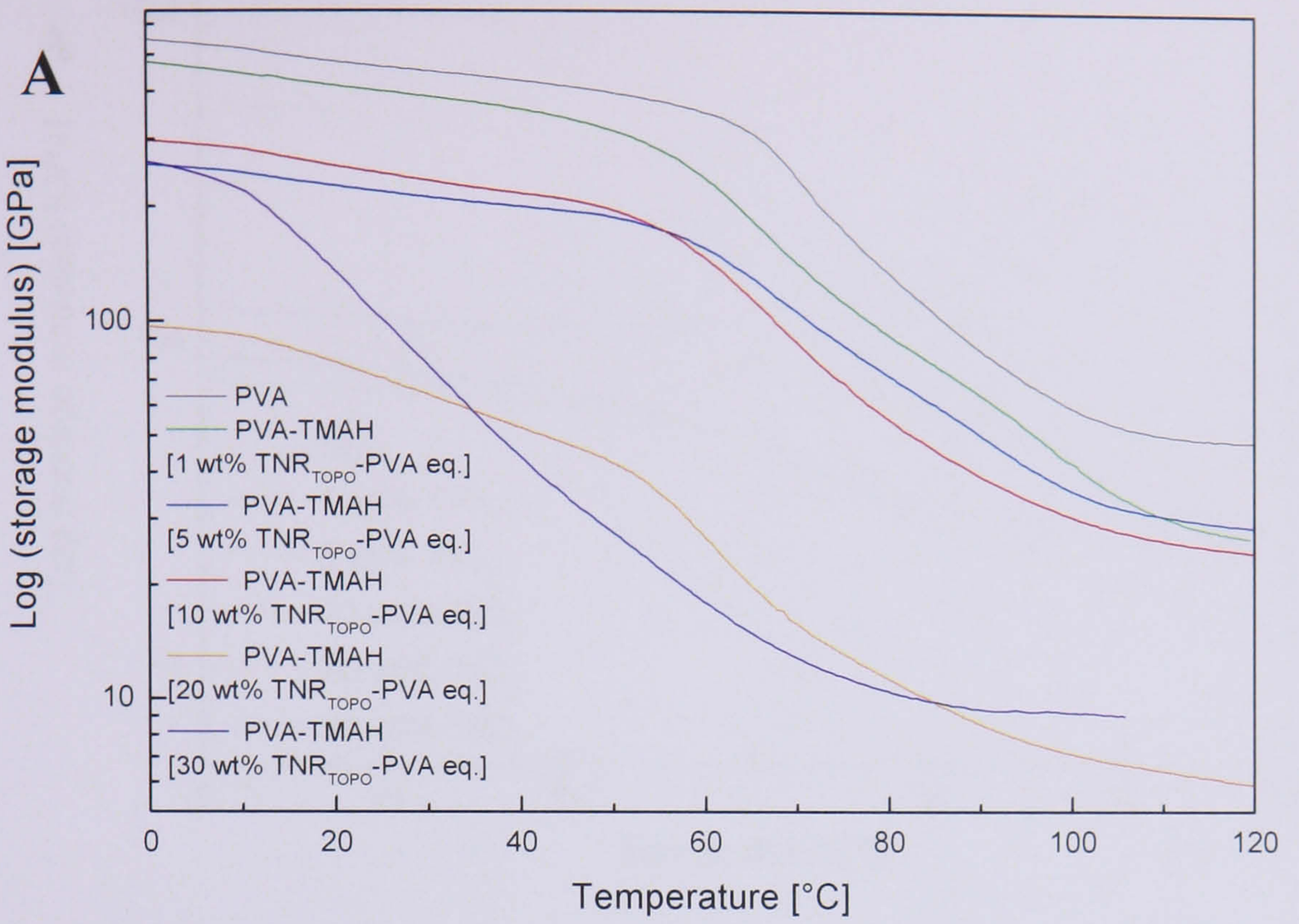


Figure 111 – DMTA results for TNR_{OA}-PVA nanocomposites at 10 Hz: (a) Storage modulus and (b) tan δ as a function of temperature



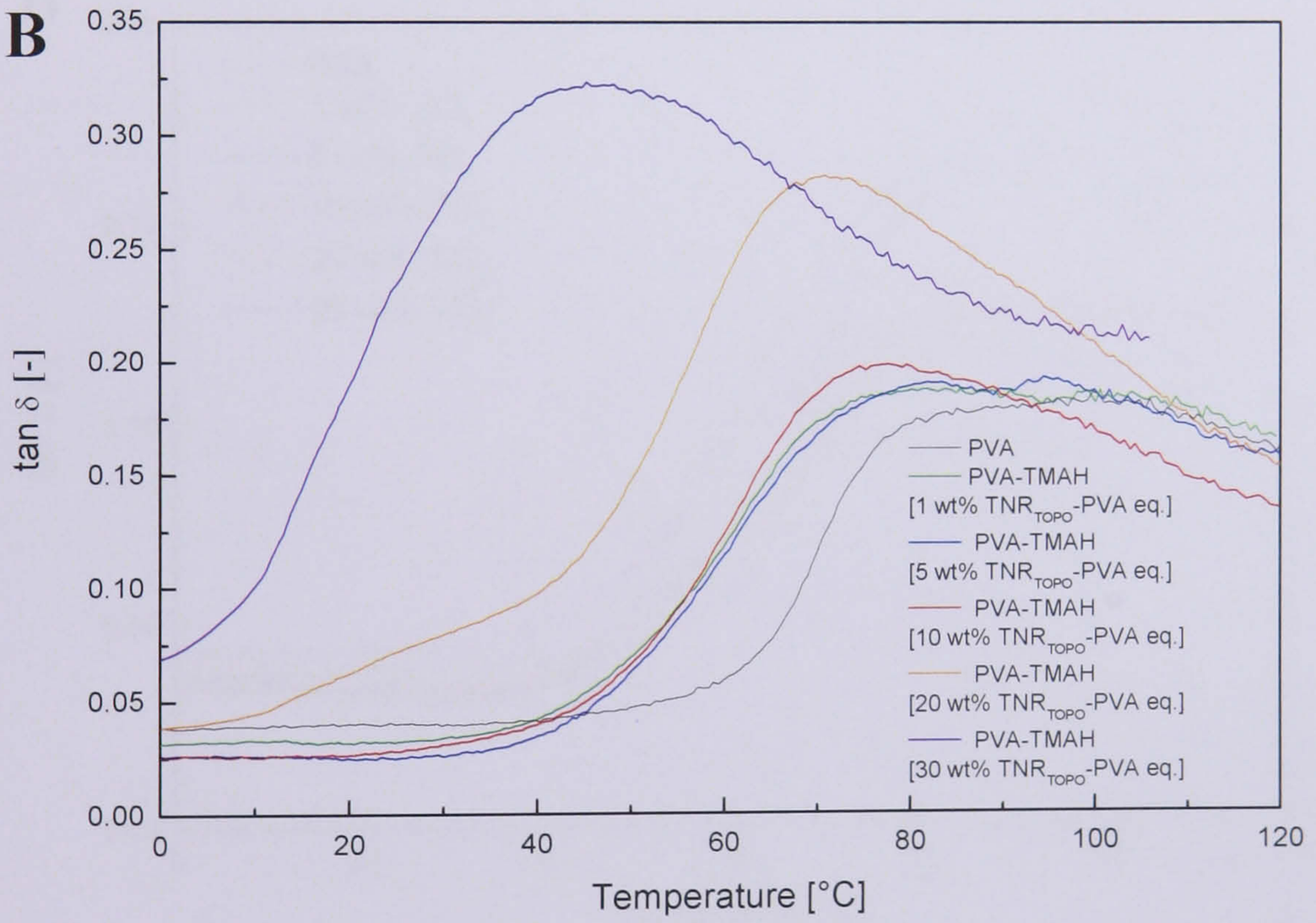
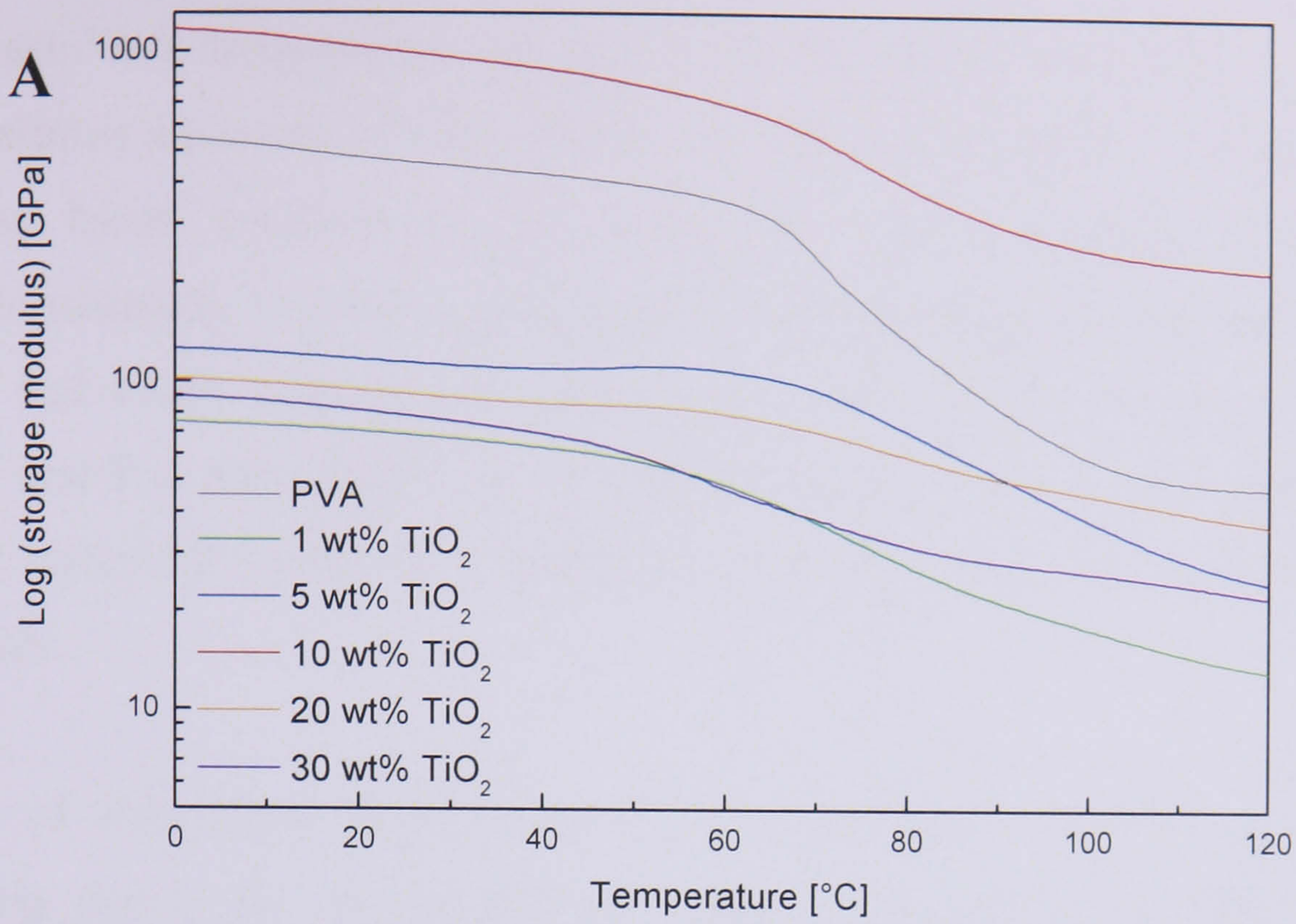


Figure 112 – DMTA results for PVA films with TMAH at 10 Hz: (a) Storage modulus and (b) tan δ as a function of temperature



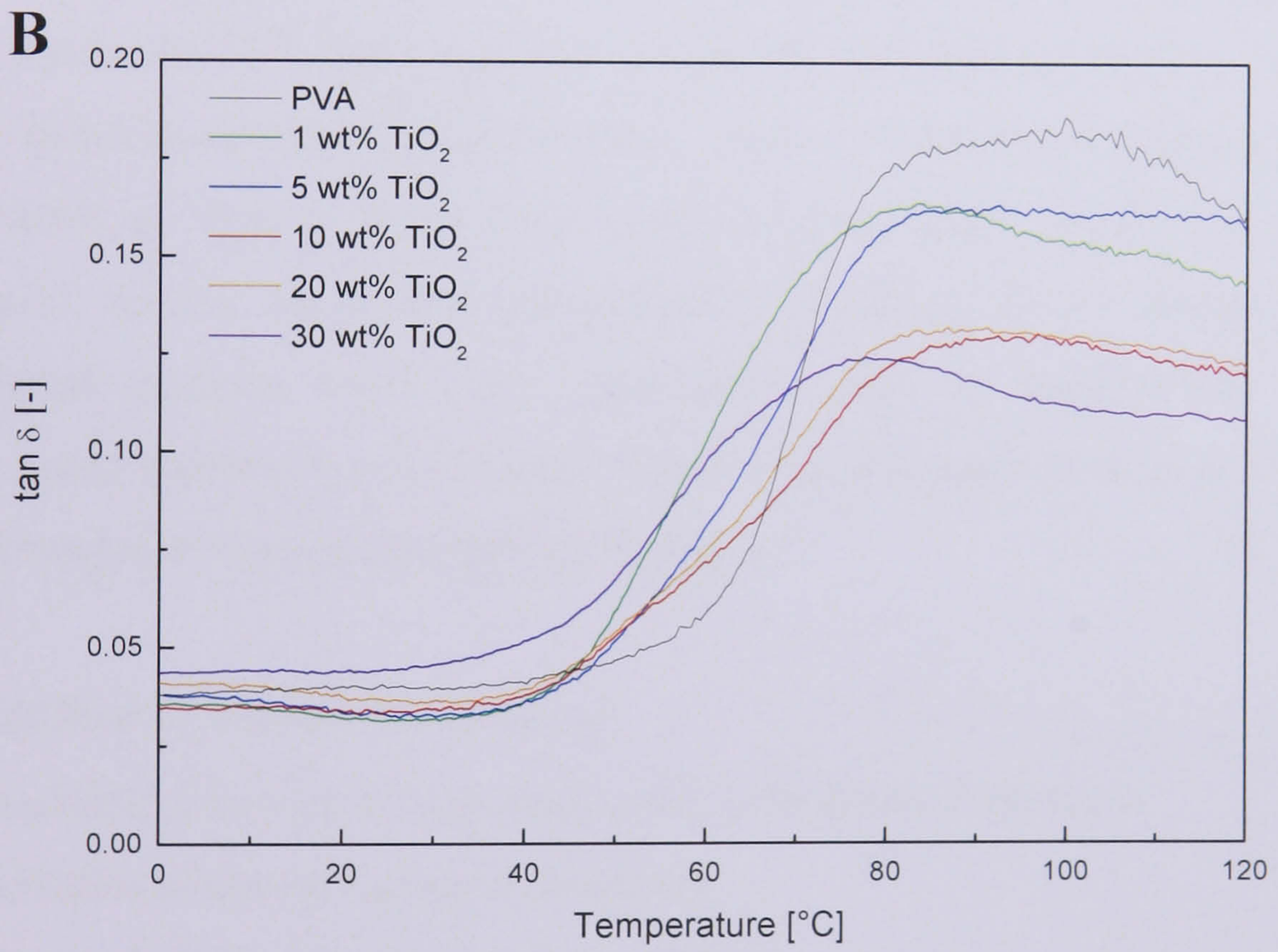


Figure 113 – DMTA results for 5 nm anatase - PVA nanocomposites at 10 Hz: (a) Storage modulus and (b) tan δ as a function of temperature

7.5 Work on thermosetting nanocomposites

'Epoxy resin' is a thermosetting epoxide-containing oligomer that cures (polymerises and crosslinks) when mixed with a catalyzing agent or "hardener". The applications for epoxy based materials are extensive and include coatings, adhesives and composite materials. In general, epoxies are known for their excellent adhesion, high modulus and failure strength, low creep, very good electrical insulating properties, chemical and heat resistance[357]. In contrast, the structure of such thermosets leads to one very undesirable property – brittleness, with poor resistance to crack initiation and growth.

The use of anisotropic titania nanorods in epoxy was explored as a potential toughening agent, for scratch-resistant coating applications in automotive and aerospace industry. Previous work on rigid fillers, initially micrometers in size[358-360] and now nanoscale[361,362], has suggested toughening mechanisms induced by the filler presence. In addition to plastic deformation, crack deflection and twisting around the rigid particles as well as crack-front pinning by the rigid particles are the main mechanisms behind toughness enhancement. Although both micron-sized and nanospherical particles have been successfully used to toughen the adhesives, nanorods could potentially offer further improvement through formation of networks. The nanocomposite preparation method involves:

1. Addition of titania filler to epoxy
2. Mechanical mixing at high-shear rates to facilitate dispersion
3. Addition of the curing agent (hardener)
4. Removal of dissolved gases under vacuum
5. Casting in release-coated steel mould
6. Curing cycle in an oven (2 h at 120°C; 2 h at 140°C; 2 h at 180°C)

Several samples with TiO_2 nanorods have been prepared together with pure polymer control (Figure 114).

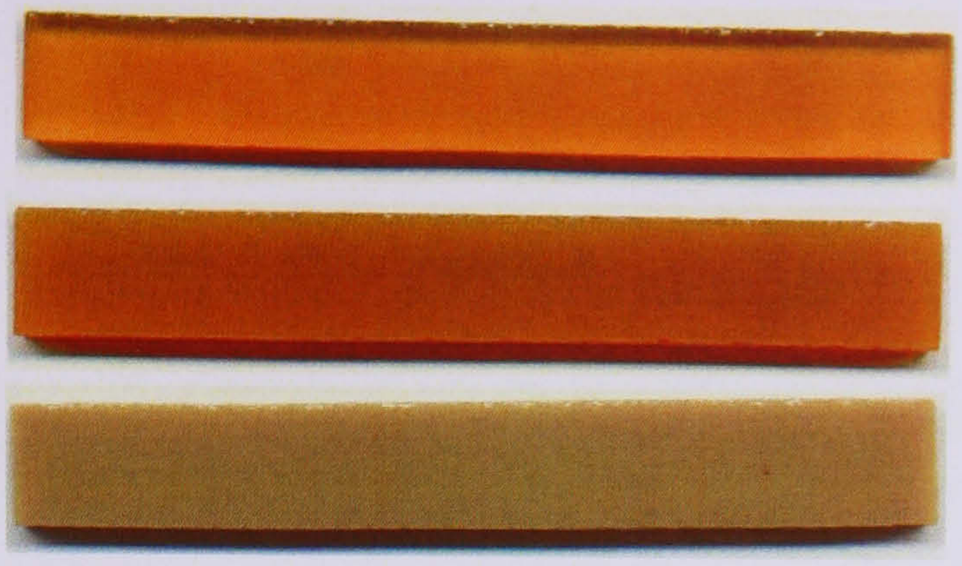


Figure 114 – TNR – epoxy samples (top to bottom): pure epoxy, 1 wt% TNR - epoxy (dried nanorod powder added), 1 wt% TNR - epoxy (nanorod dispersion in $CHCl_3$ added)

Initial toughness tests with notched samples did not provide any conclusive evidence that the nanorods successfully toughen the epoxy (Table 5). This is possibly due to poor dispersion, which could also be suggested from the images of the samples (Figure 114), which are significantly more opaque for the nanocomposites than for the pure epoxy.

Sample details	Fracture toughness (MPa√m)	Standard deviation
Pure epoxy	0.62	0.1
1wt% (dried) TNR	0.65	0.04
1wt% ($CHCl_3$ dispersion) TNR	0.61	0.06

Table 5 – Notched fracture toughness results for pure epoxy and TNR-epoxy nanocomposites

Further consideration of the epoxy system was not possible, since the aqueous dispersions could not be blended directly with the epoxy and the development of synthesis routes for stable nanorod dispersions in $CHCl_3$ (used for previously mentioned TNR-PMMA composites) was only completed at the end of the project. However, it is likely that excellent dispersion could be attained in this case, thus creating another composite system with excellent optical and UV-shielding properties. The presence of OA capping on the nanorods is likely to cause some loss in mechanical and thermal stability, but this would be greatly offset by the benefits offered in terms of optical features.

8. List of references

1. *http://www.goldmau.com/titanium.pdf*. (2008).

2. *http://www.huntsman.com/pigments/Media/Manufacture_and_Generals_Properties.pdf*. (2008).

3. *http://www.lyondell.com/investorpresentations/mch/2004/JPMorgan020404.pdf*. (2005).

4. Hoyer, P. Formation of a titanium dioxide nanotube array. *Langmuir* **12**, 1411-1413 (1996).

5. Kasuga, T., Hiramatsu, M., Hoson, A., Sekino, T. & Niihara, K. Titania nanotubes prepared by chemical processing. *Advanced Materials* **11**, 1307-+ (1999).

6. Cozzoli, P. D., Kornowski, A. & Weller, H. Low-temperature synthesis of soluble and processable organic-capped anatase TiO2 nanorods. *Journal of the American Chemical Society* **125**, 14539-14548 (2003).

7. Zhang, Z. H., Zhong, X. H., Liu, S. H., Li, D. F. & Han, M. Y. Aminolysis route to monodisperse titania nanorods with tunable aspect ratio. *Angewandte Chemie-International Edition* **44**, 3466-3470 (2005).

8. Armstrong, A. R., Armstrong, G., Canales, J. & Bruce, P. G. TiO2-B nanowires. *Angewandte Chemie-International Edition* **43**, 2286-2288 (2004).

9. Liu, S. Q. & Huang, K. L. Straightforward fabrication of highly ordered TiO2 nanowire arrays in AAM on aluminum substrate. *Solar Energy Materials and Solar Cells* **85**, 125-131 (2005).

10. Linsebigler, A. L., Lu, G. Q. & Yates, J. T. Photocatalysis on Tio2 Surfaces - Principles, Mechanisms, and Selected Results. *Chemical Reviews* **95**, 735-758 (1995).

11. Nussbaumer, R. J., Caseri, W. R., Smith, P. & Tervoort, T. Polymer-TiO2 nanocomposites: A route towards visually transparent broadband UV filters and high refractive index materials. *Macromolecular Materials and Engineering* **288**, 44-49 (2003).

12. Zhang, J. Z., Wang, X., Lu, L. D., Li, D. & Yang, X. J. Preparation and performance of high-impact polystyrene (HIPS)/Nano-Tio(2) nanocomposites. *Journal of Applied Polymer Science* **87**, 381-385 (2003).

13. Petrella, A. *et al.* Colloidal TiO2 nanocrystals/MEH-PPV nanocomposites: Photo(electro)chemical study. *Journal of Physical Chemistry B* **109**, 1554-1562 (2005).

14. Kang, S. H. *et al.* Nanorod-based dye-sensitized solar cells with improved charge collection efficiency. *Advanced Materials* **20**, 54-+ (2008).

15. Kislyuk, V. V. & Dimitriev, O. P. Nanorods and nanotubes for solar cells. *Journal of Nanoscience and Nanotechnology* **8**, 131-148 (2008).

16. Kroto, H. W., Heath, J. R., Obrien, S. C., Curl, R. F. & Smalley, R. E. C-60 - Buckminsterfullerene. *Nature* **318**, 162-163 (1985).

17. Iijima, S. Helical Microtubules of Graphitic Carbon. *Nature* **354**, 56-58 (1991).

18. Monthioux, M. & Kuznetsov, V. L. Who should be given the credit for the discovery of carbon nanotubes? *Carbon* **44**, 1621-1623 (2006).

19. Reibold, M. *et al.* Carbon nanotubes in an ancient Damascus sabre. *Nature* **444**, 286 (2006).

20. Rostrup-Nielsen, J. R. *Steam reforming catalysts : an investigation of catalysts for tubular steam reforming of hydrocarbons*. Teknisk Forlag A/S, (1975).

21. Rao, C. N. R. & Nath, M. Inorganic nanotubes. *Dalton Transactions* 1-24 (2003).

22. Tenne, R. & Rao, C. N. R. Inorganic nanotubes. *Philosophical Transactions of the Royal Society of London Series A-Mathematical Physical and Engineering Sciences* **362**, 2099-2125 (2004).

23. Remskar, M. Inorganic nanotubes. *Advanced Materials* **16**, 1497-1504 (2004).

24. Tenne, R., Margulis, L., Genut, M. & Hodes, G. Polyhedral and Cylindrical Structures of Tungsten Disulfide. *Nature* **360**, 444-446 (1992).

25. Feldman, Y., Wasserman, E., Srolovitz, D. J. & Tenne, R. High-Rate, Gas-Phase Growth of Mos2 Nested Inorganic Fullerenes and Nanotubes. *Science* **267**, 222-225 (1995).

26. Chopra, N. G. *et al.* Boron-Nitride Nanotubes. *Science* **269**, 966-967 (1995).

27. Nakamura, H. & Matsui, Y. Silica-Gel Nanotubes Obtained by the Sol-Gel Method. *Journal of the American Chemical Society* **117**, 2651-2652 (1995).

28. Spahr, M. E. *et al.* Redox-active nanotubes of vanadium oxide. *Angewandte Chemie-International Edition* **37**, 1263-1265 (1998).

29. Hacohen, Y. R., Grunbaum, E., Tenne, R., Sloan, J. & Hutchison, J. L. Cage structures and nanotubes of NiCl2. *Nature* **395**, 336-337 (1998).

30. Galvan, D. H., Kim, J. H., Maple, M. B. & Adem, E. Effect of electronic irradiation in the production of NbSe2 nanotubes. *Fullerene Science and Technology* **9**, 225-232 (2001).

31. Hulteen, J. C., Jirage, K. B. & Martin, C. R. Introducing chemical transport selectivity into gold nanotubule membranes. *Journal of the American Chemical Society* **120**, 6603-6604 (1998).

32. Tourillon, G., Pontonnier, L., Levy, J. P. & Langlais, V. Electrochemically synthesized Co and Fe nanowires and nanotubes. *Electrochemical and Solid State Letters* **3**, 20-23 (2000).

33. Rao, C. N. R., Govindaraj, A., Deepak, F. L., Gunari, N. A. & Nath, M. Surfactant-assisted synthesis of semiconductor nanotubes and nanowires. *Applied Physics Letters* **78**, 1853-1855 (2001).

34. Govindaraj, A., Deepak, F. L., Gunari, N. A. & Rao, C. N. R. Semiconductor nanorods: Cu, Zn, and Cd chalcogenides. *Israel Journal of Chemistry* **41**, 23-30 (2001).

35. Dloczik, L. *et al.* Hexagonal nanotubes of ZnS by chemical conversion of monocrystalline ZnO columns. *Applied Physics Letters* **78**, 3687-3689 (2001).

36. Jiang, X. C. *et al.* Synthesis of novel nickel sulfide layer-rolled structures. *Advanced Materials* **13**, 1278-1281 (2001).

37. Peng, Y. Y. *et al.* Cu5.5FeS6.5 nanotubes - a new kind of ternary sulfide nanotube. *New Journal of Chemistry* **25**, 1359-1361 (2001).

38. Pu, L., Bao, X. M., Zou, J. P. & Feng, D. Individual alumina nanotubes. *Angewandte Chemie-International Edition* **40**, 1490-+ (2001).

39. Cheng, B. & Samulski, E. T. Fabrication and characterization of nanotubular semiconductor oxides In2O3 and Ga2O3. *Journal of Materials Chemistry* **11**, 2901-2902 (2001).

40. Li, J. Y., Chen, X. L., Qiao, Z. Y., Cao, Y. G. & Li, H. Synthesis of GaN nanotubes. *Journal of Materials Science Letters* **20**, 1987-1988 (2001).

41. Nath, M. & Rao, C. N. R. Nanotubes of group 4 metal disulfides. *Angewandte Chemie-International Edition* **41**, 3451-3454 (2002).

42. Nath, M. & Rao, C. N. R. New metal disulfide nanotubes. *Journal of the American Chemical Society* **123**, 4841-4842 (2001).

43. Yada, M., Mihara, M., Mouri, S., Kuroki, M. & Kijima, T. Rare earth (Er, Tm, Yb, Lu) oxide nanotubes templated by dodecylsulfate assemblies. *Advanced Materials* **14**, 309-+ (2002).

44. Wu, J. J., Liu, S. C., Wu, C. T., Chen, K. H. & Chen, L. C. Heterostructures of ZnO-Zn coaxial nanocables and ZnO nanotubes. *Applied Physics Letters* **81**, 1312-1314 (2002).

45. Hernandez, B. A., Chang, K. S., Fisher, E. R. & Dorhout, P. K. Sol-gel template synthesis and characterization of BaTiO3 and PbTiO3 nanotubes. *Chemistry of Materials* **14**, 480-482 (2002).

46. Han, C. C., Bai, M. Y. & Lee, J. T. A new and easy method for making Ni and Cu microtubules and their regularly assembled structures. *Chemistry of Materials* **13**, 4260-4268 (2001).

47. Mayers, B. & Xia, Y. N. Formation of tellurium nanotubes through concentration depletion at the surfaces of seeds. *Advanced Materials* **14**, 279-+ (2002).

48. Brorson, M., Hansen, T. W. & Jacobsen, C. J. H. Rhenium(IV) sulfide nanotubes. *Journal of the American Chemical Society* **124**, 11582-11583 (2002).

49. Sha, J. *et al.* Silicon nanotubes. *Advanced Materials* **14**, 1219-+ (2002).

50. Chen, X. & Mao, S. S. Titanium dioxide nanomaterials: Synthesis, properties, modifications, and applications. *Chemical Reviews* **107**, 2891-2959 (2007).

51. Barringer, E. A. & Bowen, H. K. High-Purity, Monodisperse Tio2 Powders by Hydrolysis of Titanium Tetraethoxide .1. Synthesis and Physical-Properties. *Langmuir* **1**, 414-420 (1985).

52. Jean, J. H. & Ring, T. A. Nucleation and Growth of Monosized Tio2 Powders from Alcohol Solution. *Langmuir* **2**, 251-255 (1986).

53. Moritz, T., Reiss, J., Diesner, K., Su, D. & Chemseddine, A. Nanostructured crystalline TiO2 through growth control and stabilization of intermediate structural building units. *Journal of Physical Chemistry B* **101**, 8052-8053 (1997).

54. Chemseddine, A. & Moritz, T. Nanostructuring titania: Control over nanocrystal structure, size, shape, and organization. *European Journal of Inorganic Chemistry* 235-245 (1999).

55. Scolan, E. & Sanchez, C. Synthesis and characterization of surface-protected nanocrystalline titania particles. *Chemistry of Materials* **10**, 3217-3223 (1998).

56. Imai, H., Takei, Y., Shimizu, K., Matsuda, M. & Hirashima, H. Direct preparation of anatase TiO2 nanotubes in porous alumina membranes. *Journal of Materials Chemistry* **9**, 2971-2972 (1999).

57. Reddy, K. M., Reddy, C. V. G. & Manorama, S. V. Preparation, characterization, and spectral studies on nanocrystalline anatase TiO2. *Journal of Solid State Chemistry* **158**, 180-186 (2001).

58. Zhang, M., Bando, Y. & Wada, K. Sol-gel template preparation of TiO2 nanotubes and nanorods. *Journal of Materials Science Letters* **20**, 167-170 (2001).

59. Pottier, A., Chaneac, C., Tronc, E., Mazerolles, L. & Jolivet, J. P. Synthesis of brookite TiO2 nanoparticles by thermolysis of TiCl4 in strongly acidic aqueous media. *Journal of Materials Chemistry* **11**, 1116-1121 (2001).

60. Pottier, A. S. *et al.* Size tailoring of TiO2 anatase nanoparticles in aqueous medium and synthesis of nanocomposites. Characterization by Raman spectroscopy. *Journal of Materials Chemistry* **13**, 877-882 (2003).

61. Jung, J. H., Kobayashi, H., van Bommel, K. J. C., Shinkai, S. & Shimizu, T. Creation of novel helical ribbon and double-layered nanotube TiO2 structures using an organogel template. *Chemistry of Materials* **14**, 1445-1447 (2002).

62. Liu, S. M., Gan, L. M., Liu, L. H., Zhang, W. D. & Zeng, H. C. Synthesis of single-crystalline TiO2 nanotubes. *Chemistry of Materials* **14**, 1391-1397 (2002).

63. Zhang, H. Z. & Banfield, J. F. Kinetics of crystallization and crystal growth of nanocrystalline anatase in nanometer-sized amorphous titania. *Chemistry of Materials* **14**, 4145-4154 (2002).

64. Sugimoto, T., Zhou, X. P. & Muramatsu, A. Synthesis of uniform anatase TiO2 nanoparticles by gel-sol method - 1. Solution chemistry of Ti(OH)(n)((4-n)+) complexes. *Journal of Colloid and Interface Science* **252**, 339-346 (2002).

65. Sugimoto, T., Zhou, X. P. & Muramatsu, A. Synthesis of uniform anatase TiO2 nanoparticles by gel-sol method 4. Shape control. *Journal of Colloid and Interface Science* **259**, 53-61 (2003).

66. Huang, Q. & Gao, L. A simple route for the synthesis of rutile TiO2 nanorods. *Chemistry Letters* **32**, 638-639 (2003).

67. Oskam, G., Nellore, A., Penn, R. L. & Searson, P. C. The growth kinetics of TiO2 nanoparticles from titanium(IV) alkoxide at high water/titanium ratio. *Journal of Physical Chemistry B* **107**, 1734-1738 (2003).

68. Miao, L., Tanemura, S., Toh, S., Kaneko, K. & Tanemura, M. Fabrication, characterization and Raman study of anatase TiO2 nanorods by a heating-sol-gel template process. *Journal of Crystal Growth* **264**, 246-252 (2004).

69. Arnal, P., Corriu, R. J. P., Leclercq, D., Mutin, P. H. & Vioux, A. Preparation of anatase, brookite and rutile at low temperature by non-hydrolytic sol-gel methods. *Journal of Materials Chemistry* **6**, 1925-1932 (1996).

70. Arnal, P., Corriu, R. J. P., Leclercq, D., Mutin, P. H. & Vioux, A. A solution chemistry study of nonhydrolytic sol-gel routes to titania. *Chemistry of Materials* **9**, 694-698 (1997).

71. Vioux, A. Nonhydrolytic sol-gel routes to oxides. *Chemistry of Materials* **9**, 2292-2299 (1997).

72. Trentler, T. J., Denler, T. E., Bertone, J. F., Agrawal, A. & Colvin, V. L. Synthesis of TiO2 nanocrystals by nonhydrolytic solution-based reactions. *Journal of the American Chemical Society* **121**, 1613-1614 (1999).

73. Niederberger, M., Bartl, M. H. & Stucky, G. D. Benzyl alcohol and titanium tetrachloride - A versatile reaction system for the nonaqueous and low-temperature preparation of crystalline and luminescent titania nanoparticles. *Chemistry of Materials* **14**, 4364-4370 (2002).

74. Parala, H., Devi, A., Bhakta, R. & Fischer, R. A. Synthesis of nano-scale TiO2 particles by a nonhydrolytic approach. *Journal of Materials Chemistry* **12**, 1625-1627 (2002).

75. Jun, Y. W. *et al.* Surfactant-assisted elimination of a high energy facet as a means of controlling the shapes of TiO2 nanocrystals. *Journal of the American Chemical Society* **125**, 15981-15985 (2003).

76. Polleux, J., Pinna, N., Antonietti, M. & Niederberger, M. Ligand-directed assembly of preformed titania nanocrystals into highly anisotropic nanostructures. *Advanced Materials* **16**, 436-+ (2004).

77. Joo, J. *et al.* Large-scale synthesis of TiO2 nanorods via nonhydrolytic sol-gel ester elimination reaction and their application to photocatalytic inactivation of E. coli. *Journal of Physical Chemistry B* **109**, 15297-15302 (2005).

78. Tang, J. *et al.* An organometallic synthesis of TiO2 nanoparticles. *Nano Letters* **5**, 543-548 (2005).

79. Niederberger, M. & Garnweitner, G. Organic reaction pathways in the nonaqueous synthesis of metal oxide nanoparticles. *Chemistry-A European Journal* **12**, 7282-7302 (2006).

80. Hay, J. N. & Raval, H. M. Preparation of inorganic oxides via a non-hydrolytic sol-gel route. *Journal of Sol-Gel Science and Technology* **13**, 109-112 (1998).

81. Hay, J. N. & Raval, H. M. Synthesis of organic-inorganic hybrids via the non-hydrolytic sol-gel process. *Chemistry of Materials* **13**, 3396-3403 (2001).

82. Lin, J. *et al.* Hot-fluid annealing for crystalline titanium dioxide nanoparticles in stable suspension. *Journal of the American Chemical Society* **124**, 11514-11518 (2002).

83. Zhang, D. B., Qi, L. M., Ma, J. M. & Cheng, H. M. Formation of crystalline nanosized titania in reverse micelles at room temperature. *Journal of Materials Chemistry* **12**, 3677-3680 (2002).

84. Kasuga, T., Hiramatsu, M., Hoson, A., Sekino, T. & Niihara, K. Formation of titanium oxide nanotube. *Langmuir* **14**, 3160-3163 (1998).

85. Yang, J., Mei, S. & Ferreira, J. M. F. Hydrothermal synthesis of nanosized titania powders: Influence of peptization and peptizing agents on the

crystalline phases and phase transitions. *Journal of the American Ceramic Society* **83**, 1361-1368 (2000).

86. Seo, D. S., Lee, J. K. & Kim, H. Preparation of nanotube-shaped TiO2 powder. *Journal of Crystal Growth* **229**, 428-432 (2001).

87. Du, G. H., Chen, Q., Che, R. C., Yuan, Z. Y. & Peng, L. M. Preparation and structure analysis of titanium oxide nanotubes. *Applied Physics Letters* **79**, 3702-3704 (2001).

88. Chen, Q., Zhou, W. Z., Du, G. H. & Peng, L. M. Trititanate nanotubes made via a single alkali treatment. *Advanced Materials* **14**, 1208-+ (2002).

89. Wang, Y. Q., Hu, G. Q., Duan, X. F., Sun, H. L. & Xue, Q. K. Microstructure and formation mechanism of titanium dioxide nanotubes. *Chemical Physics Letters* **365**, 427-431 (2002).

90. Zhang, Y. X. *et al.* Hydrothermal synthesis and photoluminescence of TiO2 nanowires. *Chemical Physics Letters* **365**, 300-304 (2002).

91. Andersson, M., Osterlund, L., Ljungstrom, S. & Palmqvist, A. Preparation of nanosize anatase and rutile TiO2 by hydrothermal treatment of microemulsions and their activity for photocatalytic wet oxidation of phenol. *Journal of Physical Chemistry B* **106**, 10674-10679 (2002).

92. Yao, B. D. *et al.* Formation mechanism of TiO2 nanotubes. *Applied Physics Letters* **82**, 281-283 (2003).

93. Zhang, Q. H. & Gao, L. Preparation of oxide nanocrystals with tunable morphologies by the moderate hydrothermal method: Insights from rutile TiO2. *Langmuir* **19**, 967-971 (2003).

94. Tian, Z. R. R., Voigt, J. A., Liu, J., McKenzie, B. & Xu, H. F. Large oriented arrays and continuous films of TiO2-based nanotubes. *Journal of the American Chemical Society* **125**, 12384-12385 (2003).

95. Bavykin, D. V., Parmon, V. N., Lapkin, A. A. & Walsh, F. C. The effect of hydrothermal conditions on the mesoporous structure of TiO2 nanotubes. *Journal of Materials Chemistry* **14**, 3370-3377 (2004).

96. Yuan, Z. Y. & Su, B. L. Titanium oxide nanotubes, nanofibers and nanowires. *Colloids and Surfaces A-Physicochemical and Engineering Aspects* **241**, 173-183 (2004).

97. Wang, W. Z. *et al.* A study on the growth and structure of titania nanotubes. *Journal of Materials Research* **19**, 417-422 (2004).

98. Kim, C. S., Moon, B. K., Park, J. H., Chung, S. T. & Son, S. M. Synthesis of nanocrystalline TiO2 in toluene by a solvothermal route. *Journal of Crystal Growth* **254**, 405-410 (2003).

99. Kim, C. S., Moon, B. K., Park, J. H., Choi, B. C. & Seo, H. J. Solvotherinal synthesis of nanocrystalline TiO2 in toluene with surfactant. *Journal of Crystal Growth* **257**, 309-315 (2003).

100. Li, X. L., Peng, Q., Yi, J. X., Wang, X. & Li, Y. D. Near monodisperse TiO2 nanoparticles and nanorods. *Chemistry-A European Journal* **12**, 2383-2391 (2006).

101. Gong, D. *et al.* Titanium oxide nanotube arrays prepared by anodic oxidation. *Journal of Materials Research* **16**, 3331-3334 (2001).

102. Varghese, O. K., Gong, D. W., Paulose, M., Grimes, C. A. & Dickey, E. C. Crystallization and high-temperature structural stability of titanium oxide nanotube arrays. *Journal of Materials Research* **18**, 156-165 (2003).

103. Wu, J. M. Low-temperature preparation of titania nanorods through direct oxidation of titanium with hydrogen peroxide. *Journal of Crystal Growth* **269**, 347-355 (2004).

104. Peng, X. S. & Chen, A. C. Aligned TiO2 nanorod arrays synthesized by oxidizing titanium with acetone. *Journal of Materials Chemistry* **14**, 2542-2548 (2004).

105. Macak, J. M., Tsuchiya, H. & Schmuki, P. High-aspect-ratio TiO2 nanotubes by anodization of titanium. *Angewandte Chemie-International Edition* **44**, 2100-2102 (2005).

106. Wu, J. J. & Yu, C. C. Aligned TiO2 nanorods and nanowalls. *Journal of Physical Chemistry B* **108**, 3377-3379 (2004).

107. Wu, J. M., Shih, H. C., Wu, W. T., Tseng, Y. K. & Chen, I. C. Thermal evaporation growth and the luminescence property of TiO2 nanowires. *Journal of Crystal Growth* **281**, 384-390 (2005).

108. Huang, W. P., Tang, X. H., Wang, Y. Q., Koltypin, Y. & Gedanken, A. Selective synthesis of anatase and rutile via ultrasound irradiation. *Chemical Communications* 1415-1416 (2000).

109. Yu, J. C., Yu, J. G., Ho, W. K., Jiang, Z. T. & Zhang, L. Z. Effects of F-doping on the photocatalytic activity and microstructures of nanocrystalline TiO2 powders. *Chemistry of Materials* **14**, 3808-3816 (2002).

110. Zhu, Y. C., Li, H. L., Koltypin, Y., Hacohen, Y. R. & Gedanken, A. Sonochemical synthesis of titania whiskers and nanotubes. *Chemical Communications* 2616-2617 (2001).

111. Yamamoto, T. *et al.* Microwave-driven polyol method for preparation of TiO2 nanocrystallites. *Chemistry Letters* 964-965 (2002).

112. Uchida, S., Tomiha, M., Masaki, N., Miyazawa, A. & Takizawa, H. Preparation of TiO2 nanocrystalline electrode for dye-sensitized solar cells by

28 GHz microwave irradiation. *Solar Energy Materials and Solar Cells* **81**, 135-139 (2004).

113. Wu, X., Jiang, Q. Z., Ma, Z. F., Fu, M. & Shangguan, W. F. Synthesis of titania nanotubes by microwave irradiation. *Solid State Communications* **136**, 513-517 (2005).

114. LeBaron, P. C., Wang, Z. & Pinnavaia, T. J. Polymer-layered silicate nanocomposites: an overview. *Applied Clay Science* **15**, 11-29 (1999).

115. Ray, S. S. & Okamoto, M. Polymer/layered silicate nanocomposites: a review from preparation to processing. *Progress in Polymer Science* **28**, 1539-1641 (2003).

116. Okada, A. & Usuki, A. The chemistry of polymer-clay hybrids. *Materials Science & Engineering C-Biomimetic Materials Sensors and Systems* **3**, 109-115 (1995).

117. Giannelis, E. P. Polymer layered silicate nanocomposites. *Advanced Materials* **8**, 29-& (1996).

118. Ogawa, M. & Kuroda, K. Preparation of inorganic-organic nanocomposites through intercalation of organoammonium ions into layered silicates. *Bulletin of the Chemical Society of Japan* **70**, 2593-2618 (1997).

119. Fukushima, Y. & Inagaki, S. Synthesis of An Intercalated Compound of Montmorillonite and 6-Polyamide. *Journal of Inclusion Phenomena* **5**, 473-482 (1987).

120. Usuki, A. *et al.* Synthesis of Nylon 6-Clay Hybrid. *Journal of Materials Research* **8**, 1179-1184 (1993).

121. Kojima, Y. *et al.* Mechanical-Properties of Nylon 6-Clay Hybrid. *Journal of Materials Research* **8**, 1185-1189 (1993).

122. Vaia, R. A., Ishii, H. & Giannelis, E. P. Synthesis and Properties of 2-Dimensional Nanostructures by Direct Intercalation of Polymer Melts in Layered Silicates. *Chemistry of Materials* **5**, 1694-1696 (1993).

123. Harris, P. J. F. Carbon nanotube composites. *International Materials Reviews* **49**, 31-43 (2004).

124. Chen, C. C. *et al.* Magnetic and photoconductive properties of the CoxPt1-x-Pt-TiO2 nanocomposite films prepared by reactive sputter-deposition. *Vacuum* **80**, 265-271 (2005).

125. Kawahara, K., Suzuki, K., Ohka, Y. & Tatsuma, T. Electron transport in silver-semiconductor nanocomposite films exhibiting multicolor photochromism. *Physical Chemistry Chemical Physics* **7**, 3851-3855 (2005).

126. Kim, S. C., Heo, M. C., Hahn, S. H. & Kim, E. J. Photocatalytic activity of Pd-doped TiO2 thin films by using a RF magnetron co-sputtering method. *Journal of the Korean Physical Society* **47**, 700-704 (2005).

127. Liu, Z. H., Tang, X. H., Zhang, C. X. & Zhou, Q. A novel TiO2-pillared microporous manganese oxide. *Chemistry Letters* **34**, 1312-1313 (2005).

128. Li, D. L., Zhou, H. S., Honma, I. & Ichihara, M. Hexagonally ordered mesoporous ternary Li2O-TiO2-P2O5 oxides with high lithium content. *Chemical Communications* 5187-5189 (2005).

129. Yu, J. G., Xiong, J. F., Cheng, B. & Liu, S. W. Fabrication and characterization of Ag-TiO2 multiphase nanocomposite thin films with enhanced photocatalytic activity. *Applied Catalysis B-Environmental* **60**, 211-221 (2005).

130. Lana-Villarreal, T. & Gomez, R. Tuning the photoelectrochemistry of nanoporous anatase electrodes by modification with gold nanoparticles: Development of cathodic photocurrents. *Chemical Physics Letters* **414**, 489-494 (2005).

131. Cozzoli, P. D. *et al.* Photocatalytic synthesis of silver nanoparticles stabilized by TiO2 nanorods: A semiconductor/metal nanocomposite in homogeneous nonpolar solution. *Journal of the American Chemical Society* **126**, 3868-3879 (2004).

132. Jakob, M., Levanon, H. & Kamat, P. V. Charge distribution between UV-irradiated TiO2 and gold nanoparticles: Determination of shift in the Fermi level. *Nano Letters* **3**, 353-358 (2003).

133. Li, X. Z., Li, F. B., Yang, C. L. & Ge, W. K. Photocatalytic activity of WOx-TiO2 under visible light irradiation. *Journal of Photochemistry and Photobiology A-Chemistry* **141**, 209-217 (2001).

134. Yoon, J. W., Sasaki, T., Koshizaki, N. & Traversa, E. Preparation and characterization of M/TiO2 (M = Ag, Au, Pt) nanocomposite thin films. *Scripta Materialia* **44**, 1865-1868 (2001).

135. Dawson, A. & Kamat, P. V. Semiconductor-metal nanocomposites. Photoinduced fusion and photocatalysis of gold-capped TiO2 (TiO2/Gold) nanoparticles. *Journal of Physical Chemistry B* **105**, 960-966 (2001).

136. Wu, J. H., Uchida, S., Fujishiro, Y., Yin, S. & Sato, T. Synthesis and photocatalytic properties of HTaWO6/(Pt,TiO2) and HTaWO6/(Pt,Fe2O3) nanocomposites. *International Journal of Inorganic Materials* **1**, 253-258 (1999).

137. Fujishim, A. & Honda, K. Electrochemical Photolysis of Water at A Semiconductor Electrode. *Nature* **238**, 37-& (1972).

138. Fox, M. A. & Dulay, M. T. Heterogeneous Photocatalysis. *Chemical Reviews* **93**, 341-357 (1993).

139. Mills, A., Davies, R. H. & Worsley, D. Water-Purification by Semiconductor Photocatalysis. *Chemical Society Reviews* **22**, 417-425 (1993).

140. Hoffmann, M. R., Martin, S. T., Choi, W. Y. & Bahnemann, D. W. Environmental Applications of Semiconductor Photocatalysis. *Chemical Reviews* **95**, 69-96 (1995).

141. Linsebigler, A. L., Lu, G. Q. & Yates, J. T. Photocatalysis on Tio2 Surfaces - Principles, Mechanisms, and Selected Results. *Chemical Reviews* **95**, 735-758 (1995).

142. Mills, A. & LeHunte, S. An overview of semiconductor photocatalysis. *Journal of Photochemistry and Photobiology A-Chemistry* **108**, 1-35 (1997).

143. Peral, J., Domenech, X. & Ollis, D. F. Heterogeneous photocatalysis for purification, decontamination and deodorization of air. *Journal of Chemical Technology and Biotechnology* **70**, 117-140 (1997).

144. Agrios, A. G. & Pichat, P. State of the art and perspectives on materials and applications of photocatalysis over TiO2. *Journal of Applied Electrochemistry* **35**, 655-663 (2005).

145. Fujishima, A. & Zhang, X. T. Titanium dioxide photocatalysis: present situation and future approaches. *Comptes Rendus Chimie* **9**, 750-760 (2006).

146. *http://www.threebond.co.jp/en/technical/technicalnews/pdf/tech62.pdf*. (2005).

147. Wu, J. M. *et al.* Large-scale preparation of ordered titania nanorods with enhanced photocatalytic activity. *Langmuir* **21**, 6995-7002 (2005).

148. Ibusuki, T. & Takeuchi, K. Removal of Low Concentration Nitrogen-Oxides Through Photoassisted Heterogeneous Catalysis. *Journal of Molecular Catalysis* **88**, 93-102 (1994).

149. Matos, J., Laine, J. & Herrmann, J. M. Synergy effect in the photocatalytic degradation of phenol on a suspended mixture of titania and activated carbon. *Applied Catalysis B-Environmental* **18**, 281-291 (1998).

150. Takeda, N., Ohtani, M., Torimoto, T., Kuwabata, S. & Yoneyama, H. Evaluation of diffusibility of adsorbed propionaldehyde on titanium dioxide-loaded adsorbent photocatalyst films from its photodecomposition rate. *Journal of Physical Chemistry B* **101**, 2644-2649 (1997).

151. Uchida, H., Itoh, S. & Yoneyama, H. Photocatalytic Decomposition of Propyzamide Using Tio2 Supported on Activated Carbon. *Chemistry Letters* 1995-1998 (1993).

152. Sampath, S., Uchida, H. & Yoneyama, H. Photocatalytic Degradation of Gaseous Pyridine Over Zeolite-Supported Titanium-Dioxide. *Journal of Catalysis* **149**, 189-194 (1994).

153. Hu, Y., Tsai, H. L. & Huang, C. L. Effect of brookite phase on the anatase-rutile transition in titania nanoparticles. *Journal of the European Ceramic Society* **23**, 691-696 (2003).

154. Moret, M. P., Zallen, R., Vijay, D. P. & Desu, S. B. Brookite-rich titania films made by pulsed laser deposition. *Thin Solid Films* **366**, 8-10 (2000).

155. Zorn, M. E., Tompkins, D. T., Zeltner, W. A. & Anderson, M. A. Photocatalytic oxidation of acetone vapor on TiO2/ZrO2 thin films. *Applied Catalysis B-Environmental* **23**, 1-8 (1999).

156. Fu, X. Z., Clark, L. A., Yang, Q. & Anderson, M. A. Enhanced photocatalytic performance of titania-based binary metal oxides: TiO2/SiO2 and TiO2/ZrO2. *Environmental Science & Technology* **30**, 647-653 (1996).

157. Vinodgopal, K. & Kamat, P. V. Enhanced Rates of Photocatalytic Degradation of An Azo-Dye Using Sno2/Tio2 Coupled Semiconductor Thin-Films. *Environmental Science & Technology* **29**, 841-845 (1995).

158. Papp, J., Soled, S., Dwight, K. & Wold, A. Surface-Acidity and Photocatalytic Activity of Tio2, Wo3 Tio2, and Moo3 Tio2 Photocatalysts. *Chemistry of Materials* **6**, 496-500 (1994).

159. Shchukin, D., Poznyak, S., Kulak, A. & Pichat, P. TiO2-In2O3 photocatalysts: preparation, characterisations and activity for 2-chlorophenol degradation in water. *Journal of Photochemistry and Photobiology A-Chemistry* **162**, 423-430 (2004).

160. Cui, H., Dwight, K., Soled, S. & Wold, A. Surface-Acidity and Photocatalytic Activity of Nb2O5/Tio2 Photocatalysts. *Journal of Solid State Chemistry* **115**, 187-191 (1995).

161. Borgarello, E., Kiwi, J., Gratzel, M., Pelizzetti, E. & Visca, M. Visible-Light Induced Water Cleavage in Colloidal Solutions of Chromium-Doped Titanium-Dioxide Particles. *Journal of the American Chemical Society* **104**, 2996-3002 (1982).

162. Gratzel, M. & Howe, R. F. Electron-Paramagnetic Resonance Studies of Doped Tio2 Colloids. *Journal of Physical Chemistry* **94**, 2566-2572 (1990).

163. Soria, J. *et al.* Dinitrogen Photoreduction to Ammonia Over Titanium-Dioxide Powders Doped with Ferric Ions. *Journal of Physical Chemistry* **95**, 274-282 (1991).

164. Karakitsou, K. E. & Verykios, X. E. Effects of Altervalent Cation Doping of Tio2 on Its Performance As A Photocatalyst for Water Cleavage. *Journal of Physical Chemistry* **97**, 1184-1189 (1993).

165. Choi, W. Y., Termin, A. & Hoffmann, M. R. The Role of Metal-Ion Dopants in Quantum-Sized Tio2 - Correlation Between Photoreactivity and Charge-Carrier Recombination Dynamics. *Journal of Physical Chemistry* **98**, 13669-13679 (1994).

166. Martin, S. T., Morrison, C. L. & Hoffmann, M. R. Photochemical Mechanism of Size-Quantized Vanadium-Doped Tio2 Particles. *Journal of Physical Chemistry* **98**, 13695-13704 (1994).

167. Asahi, R., Morikawa, T., Ohwaki, T., Aoki, K. & Taga, Y. Visible-light photocatalysis in nitrogen-doped titanium oxides. *Science* **293**, 269-271 (2001).

168. Irie, H., Watanabe, Y. & Hashimoto, K. Carbon-doped anatase TiO2 powders as a visible-light sensitive photocatalyst. *Chemistry Letters* **32**, 772-773 (2003).

169. Diwald, O., Thompson, T. L., Goralski, E. G., Walck, S. D. & Yates, J. T. The effect of nitrogen ion implantation on the photoactivity of TiO2 rutile single crystals. *Journal of Physical Chemistry B* **108**, 52-57 (2004).

170. Gole, J. L., Stout, J. D., Burda, C., Lou, Y. B. & Chen, X. B. Highly efficient formation of visible light tunable TiO2-xNx photocatalysts and their transformation at the nanoscale. *Journal of Physical Chemistry B* **108**, 1230-1240 (2004).

171. Umebayashi, T., Yamaki, T., Itoh, H. & Asai, K. Band gap narrowing of titanium dioxide by sulfur doping. *Applied Physics Letters* **81**, 454-456 (2002).

172. Ohno, T., Mitsui, T. & Matsumura, M. Photocatalytic activity of S-doped TiO2 photocatalyst under visible light. *Chemistry Letters* **32**, 364-365 (2003).

173. Ohno, T. *et al.* Preparation of S-doped TiO2 photocatalysts and their photocatalytic activities under visible light. *Applied Catalysis A-General* **265**, 115-121 (2004).

174. Luo, H. M. *et al.* Photocatalytic activity enhancing for titanium dioxide by co-doping with bromine and chlorine. *Chemistry of Materials* **16**, 846-849 (2004).

175. Ohko, Y. *et al.* Multicolour photochromism of TiO2 films loaded with silver nanoparticles. *Nature Materials* **2**, 29-31 (2003).

176. Naoi, K., Ohko, Y. & Tatsuma, T. TiO2 films loaded with silver nanoparticles: Control of multicolor photochromic behavior. *Journal of the American Chemical Society* **126**, 3664-3668 (2004).

177. Spanhel, L., Weller, H. & Henglein, A. Photochemistry of Semiconductor Colloids .22. Electron Injection from Illuminated Cds Into Attached Tio2 and Zno Particles. *Journal of the American Chemical Society* **109**, 6632-6635 (1987).

178. Vogel, R., Hoyer, P. & Weller, H. Quantum-Sized Pbs, Cds, Ag2S, Sb2S3, and Bi2S3 Particles As Sensitizers for Various Nanoporous Wide-Bandgap Semiconductors. *Journal of Physical Chemistry* **98**, 3183-3188 (1994).

179. Robel, I., Subramanian, V., Kuno, M. & Kamat, P. V. Quantum dot solar cells. Harvesting light energy with CdSe nanocrystals molecularly linked to mesoscopic TiO2 films. *Journal of the American Chemical Society* **128**, 2385-2393 (2006).

180. Desilvestro, J., Gratzel, M., Kavan, L., Moser, J. & Augustynski, J. Highly Efficient Sensitization of Titanium-Dioxide. *Journal of the American Chemical Society* **107**, 2988-2990 (1985).

181. Haque, S. A. *et al.* Flexible dye sensitised nanocrystalline semiconductor solar cells. *Chemical Communications* 3008-3009 (2003).

182. Nazeeruddin, M. K. *et al.* Engineering of efficient panchromatic sensitizers for nanocrystalline TiO2-based solar cells. *Journal of the American Chemical Society* **123**, 1613-1624 (2001).

183. Allen, N. S. *et al.* Behaviour of nanoparticle (ultrafine) titanium dioxide pigments and stabilisers on the photooxidative stability of water based acrylic and isocyanate based acrylic coatings. *Polymer Degradation and Stability* **78**, 467-478 (2002).

184. Allen, N. S. *et al.* Degradation and stabilisation of polymers and coatings: nano versus pigmentary titania particles. *Polymer Degradation and Stability* **85**, 927-946 (2004).

185. Allen, N. S. *et al.* Photocatalytic coatings for environmental applications. *Photochemistry and Photobiology* **81**, 279-290 (2005).

186. Egerton, T. A. & Tooley, I. R. The surface characterisation of coated titanium dioxide by FTIR spectroscopy of adsorbed nitrogen. *Journal of Materials Chemistry* **12**, 1111-1117 (2002).

187. Li, Q. Y., Chen, Y. F., Zeng, D. D., Gao, W. M. & Wu, Z. J. Photocatalytic characterization of silica coated titania nanoparticles with tunable coatings. *Journal of Nanoparticle Research* **7**, 295-299 (2005).

188. El Toni, A. M., Yin, S. & Sato, T. Control of silica shell thickness and microporosity of titania-silica core-shell type nanoparticles to depress the photocatalytic activity of titania. *Journal of Colloid and Interface Science* **300**, 123-130 (2006).

189. Allen, N. S. *et al.* Interrelationship of spectroscopic properties with the thermal and photochemical behaviour of titanium dioxide pigments in metallocene polyethylene and alkyd based paint films: micron versus nanoparticles. *Polymer Degradation and Stability* **76**, 305-319 (2002).

190. Allen, N. S. *et al.* Factors affecting the interfacial adsorption of stabilisers on to titanium dioxide particles (flow microcalorimetry, modelling, oxidation and FTIR studies): Nano versus pigmentary grades. *Dyes and Pigments* **70**, 192-203 (2006).

191. Dransfield, G., Guest, P. J., Lyth, P. L., McGarvey, D. J. & Truscott, T. G. Photoactivity tests of TiO2-based inorganic sunscreens - Part 1: Non-aqueous dispersions. *Journal of Photochemistry and Photobiology B-Biology* **59**, 147-151 (2000).

192. Egerton, T. A., Everall, N. J. & Tooley, I. R. Characterization of TiO2 nanoparticles surface modified with aluminum stearate. *Langmuir* **21**, 3172-3178 (2005).

193. Yang, C. S. & Chen, C. J. Synthesis and characterization of silica-capped titania nanorods: An enhanced photocatalyst. *Applied Catalysis A-General* **294**, 40-48 (2005).

194. Alawi, M. A., Hasan, L. A. & Tanaka, K. Improved photocatalytic degradation of insecticide pirimicarb on SiO2-loaded TiO2. *Fresenius Environmental Bulletin* **16**, 403-407 (2007).

195. Wakefield, G., Lipscomb, S., Holland, E. & Knowland, J. The effects of manganese doping on UVA absorption and free radical generation of micronised titanium dioxide and its consequences for the photostability of UVA absorbing organic sunscreen components. *Photochemical & Photobiological Sciences* **3**, 648-652 (2004).

196. Wakefield, G., Green, M., Lipscomb, S. & Flutter, B. Modified titania nanomaterials for sunscreen applications - reducing free radical generation and DNA damage. *Materials Science and Technology* **20**, 985-988 (2004).

197. Wakefield, G. & Stott, J. Photostabilization of organic UV-absorbing and anti-oxidant cosmetic components in formulations containing micronized manganese-doped titanium oxide. *Journal of Cosmetic Science* **57**, 385-395 (2006).

198. Kemp, T. J. & McIntyre, R. A. Transition metal-doped titanium(IV) dioxide: Characterisation and influence on photodegradation of poly(vinyl chloride). *Polymer Degradation and Stability* **91**, 165-194 (2006).

199. Kemp, T. J. & McIntyre, R. A. Influence of transition metal-doped titanium(IV) dioxide on the photodegradation of polyethylene. *Polymer Degradation and Stability* **91**, 3020-3025 (2006).

200. Kemp, T. J. & McIntyre, R. A. Influence of transition metal-doped titanium(IV) dioxide on the photodegradation of polystyrene. *Polymer Degradation and Stability* **91**, 3010-3019 (2006).

201. Vianio H & Bianchini F *IARC handbooks of cancer prevention*. World Health Organisation (International Agency for Research), Geneva (2001).

202. Wang, R. *et al.* Light-induced amphiphilic surfaces. *Nature* **388**, 431-432 (1997).

203. Watanabe, T. *et al.* Photocatalytic activity and photoinduced hydrophilicity of titanium dioxide coated glass. *Thin Solid Films* **351**, 260-263 (1999).

204. Nakajima, A. *et al.* Transparent superhydrophobic thin films with self-cleaning properties. *Langmuir* **16**, 7044-7047 (2000).

205. Zhang, X. T. *et al.* Preparation and photocatalytic wettability conversion of TiO2-based superhydrophobic surfaces. *Langmuir* **22**, 9477-9479 (2006).

206. Zhang, X. T. *et al.* Superhydrophobic TiO2 surfaces: Preparation, photocatalytic wettability conversion, and superhydrophobic-superhydrophilic patterning. *Journal of Physical Chemistry C* **111**, 14521-14529 (2007).

207. Paz, Y., Luo, Z., Rabenberg, L. & Heller, A. Photooxidative Self-Cleaning Transparent Titanium-Dioxide Films on Glass. *Journal of Materials Research* **10**, 2842-2848 (1995).

208. Romeas, V., Pichat, P., Guillard, C., Chopin, T. & Lehaut, C. Degradation of palmitic (hexadecanoic) acid deposited on TiO2-coated self-cleaning glass: kinetics of disappearance, intermediate products and degradation pathways. *New Journal of Chemistry* **23**, 365-373 (1999).

209. Feng, X. J., Zhai, J. & Jiang, L. The fabrication and switchable superhydrophobicity of TiO2 nanorod films. *Angewandte Chemie-International Edition* **44**, 5115-5118 (2005).

210. Cho, S. M. & Choi, W. Y. Solid-phase photocatalytic degradation of PVC-TiO2 polymer composites. *Journal of Photochemistry and Photobiology A-Chemistry* **143**, 221-228 (2001).

211. Zan, L., Tian, L. H., Liu, Z. S. & Peng, Z. H. A new polystyrene-TiO2 nanocomposite film and its photocatalytic degradation. *Applied Catalysis A-General* **264**, 237-242 (2004).

212. Zan, L., Fa, W. J. & Wang, S. L. Novel photodegradable low-density polyethylene-TiO2 nanocomposite film. *Environmental Science & Technology* **40**, 1681-1685 (2006).

213. Bozzi, A., Yuranova, T., Guasaquillo, I., Laub, D. & Kiwi, J. Self-cleaning of modified cotton textiles by TiO2 at low temperatures under daylight irradiation. *Journal of Photochemistry and Photobiology A-Chemistry* **174**, 156-164 (2005).

214. Fu, G. F., Vary, P. S. & Lin, C. T. Anatase TiO2 nanocomposites for antimicrobial coatings. *Journal of Physical Chemistry B* **109**, 8889-8898 (2005).

215. *http://www. purifics. com.* (2006).

216. Konstantinou, I. K. & Albanis, T. A. TiO2-assisted photocatalytic degradation of azo dyes in aqueous solution: kinetic and mechanistic investigations - A review. *Applied Catalysis B-Environmental* **49**, 1-14 (2004).

217. Kim, S. H., Kwak, S. Y., Sohn, B. H. & Park, T. H. Design of TiO2 nanoparticle self-assembled aromatic polyamide thin-film-composite (TFC)

membrane as an approach to solve biofouling problem. *Journal of Membrane Science* **211**, 157-165 (2003).

218. Kwak, S. Y., Kim, S. H. & Kim, S. S. Hybrid organic/inorganic reverse osmosis (RO) membrane for bactericidal anti-fouling. 1. Preparation and characterization of TiO2 nanoparticle self-assembled aromatic polyamide thin-film-composite (TFC) membrane. *Environmental Science & Technology* **35**, 2388-2394 (2001).

219. Molinari, R., Grande, C., Drioli, E., Palmisano, L. & Schiavello, M. Photocatalytic membrane reactors for degradation of organic pollutants in water. *Catalysis Today* **67**, 273-279 (2001).

220. Molinari, R. *et al.* Study on a photocatalytic membrane reactor for water purification. *Catalysis Today* **55**, 71-78 (2000).

221. Molinari, R., Palmisano, L., Drioli, E. & Schiavello, M. Studies on various reactor configurations for coupling photocatalysis and membrane processes in water purification. *Journal of Membrane Science* **206**, 399-415 (2002).

222. Molinari, R., Grande, C., Drioli, E., Palmisano, L. & Schiavello, M. Photocatalytic membrane reactors for degradation of organic pollutants in water. *Catalysis Today* **67**, 273-279 (2001).

223. Bae, T. H. & Tak, T. M. Effect of TiO2 nanoparticles on fouling mitigation of ultrafiltration membranes for activated sludge filtration. *Journal of Membrane Science* **249**, 1-8 (2005).

224. Bae, T. H., Kim, I. C. & Tak, T. M. Preparation and characterization of fouling-resistant TiO2 self-assembled nanocomposite membranes. *Journal of Membrane Science* **275**, 1-5 (2006).

225. Prashantha, K. & Park, S. G. Nanosized TiO2-filled sulfonated polyethersulfone proton conducting membranes for direct methanol fuel cells. *Journal of Applied Polymer Science* **98**, 1875-1878 (2005).

226. Kubota, Y. *et al.* Photokilling of T-24 Human Bladder-Cancer Cells with Titanium-Dioxide. *British Journal of Cancer* **70**, 1107-1111 (1994).

227. Kubota, Y., Hosaka, M., Hashimoto, K. & Fujishima, A. A study of the application of photoexcited TiO2 particle to cancer treatment. *Chemical Journal of Chinese Universities-Chinese* **16**, 56-62 (1995).

228. Huang, N. P., Xu, M. H., Yuan, C. W. & Yu, R. R. The study of the photokilling effect and mechanism of ultrafine TiO2 particles on U937 cells. *Journal of Photochemistry and Photobiology A-Chemistry* **108**, 229-233 (1997).

229. Kubota, Y. *et al.* Protective effect of TiO2 particles on UV light induced pyrimidine dimer formation. *Journal of Photochemistry and Photobiology A-Chemistry* **141**, 225-230 (2001).

230. Ohko, Y. *et al.* Self-sterilizing and self-cleaning of silicone catheters coated with TiO2 photocatalyst thin films: A preclinical work. *Journal of Biomedical Materials Research* **58**, 97-101 (2001).

231. Zhang, J. *et al.* Study on the optical properties of PPV/TiO2 nanocomposites. *Synthetic Metals* **118**, 181-185 (2001).

232. Zhang, J., Wang, B. J., Ju, X., Liu, T. & Hu, T. D. New observations on the optical properties of PPV/TiO2 nanocomposites. *Polymer* **42**, 3697-3702 (2001).

233. Zhang, J. *et al.* The interfacial structure of PPV/TiO2 nanocomposite. *Optical Materials* **21**, 573-578 (2003).

234. Breeze, A. J., Schlesinger, Z., Carter, S. A. & Brock, P. J. Charge transport in TiO2/MEH-PPV polymer photovoltaics. *Physical Review B* **6412**, (2001).

235. Yang, B. D., Yoon, K. H. & Chung, K. W. Dispersion effect of nanoparticles on the conjugated polymer-inorganic nanocomposites. *Materials Chemistry and Physics* **83**, 334-339 (2004).

236. Yang, S. H., Nguyen, T. P., Le Rendu, P. & Hsu, C. S. Optical and electrical investigations of poly(p-phenylene vinylene)/silicon oxide and poly(p-phenylene vinylene)/titanium oxide nanocomposites. *Thin Solid Films* **471**, 230-235 (2005).

237. Qian, L. *et al.* Study of blue electroluminescence from titania nanotubes doped into a polymeric matrix. *Nanotechnology* **17**, 100-104 (2006).

238. Lu, M. D. & Yang, S. M. Syntheses of polythiophene and titania nanotube composites. *Synthetic Metals* **154**, 73-76 (2005).

239. Vu, Q. T. *et al.* Nanocomposites based on titanium dioxide and polythiophene: Structure and properties. *Reactive & Functional Polymers* **65**, 69-77 (2005).

240. Vu, Q. T. *et al.* Electrophoretic deposition of nanocomposites formed from polythiophene and metal oxides. *Electrochimica Acta* **51**, 1117-1124 (2005).

241. Kwong, C. Y. *et al.* Poly(3-hexylthiophene): TiO2 nanocomposites for solar cell applications. *Nanotechnology* **15**, 1156-1161 (2004).

242. Feng, W., Feng, Y. Y. & Wu, Z. G. Ultrasonic-assisted synthesis of poly(3-hexylthiophene)/TiO2 nanocomposite and its photovoltaic characteristics. *Japanese Journal of Applied Physics Part 1-Regular Papers Brief Communications & Review Papers* **44**, 7494-7499 (2005).

243. Lin, Y. Y., Chu, T. H., Chen, C. W. & Su, W. F. Improved performance of polymer/TiO2 nanorod bulk heterojunction photovoltaic devices by interface modification. *Applied Physics Letters* **92**, (2008).

244. Boucle, J. *et al.* Hybrid bulk heterojunction solar cells based on blends of TiO2 nanorods and P3HT. *Comptes Rendus Physique* **9**, 110-118 (2008).

245. Boucle, J. *et al.* Hybrid solar cells from a blend of poly(3-hexylthiophene) and ligand-capped TiO2 nanorods. *Advanced Functional Materials* **18**, 622-633 (2008).

246. Huisman, C. L., Goossens, A. & Schoonman, J. Preparation of a nanostructured composite of titanium dioxide and polythiophene: a new route towards 3D heterojunction solar cells. *Synthetic Metals* **138**, 237-241 (2003).

247. Su, S. J. & Kuramoto, N. Processable polyaniline-titanium dioxide nanocomposites: effect of titanium dioxide on the conductivity. *Synthetic Metals* **114**, 147-153 (2000).

248. Xia, H. S. & Wang, Q. Ultrasonic irradiation: A novel approach to prepare conductive polyaniline/nanocrystalline titanium oxide composites. *Chemistry of Materials* **14**, 2158-2165 (2002).

249. Li, X. W. *et al.* Surface modification of TiO2 nanoparticles by polyanifine. *Applied Surface Science* **217**, 16-22 (2003).

250. Sui, X. M., Chu, Y., Xing, S. X., Yu, M. & Liu, C. Z. Self-organization of spherical PANI/TiO2 nanocomposites in reverse micelles. *Colloids and Surfaces A-Physicochemical and Engineering Aspects* **251**, 103-107 (2004).

251. Xu, J. C., Liu, W. M. & Li, H. L. Titanium dioxide doped polyaniline. *Materials Science & Engineering C-Biomimetic and Supramolecular Systems* **25**, 444-447 (2005).

252. Lee, I. S., Lee, J. Y., Sung, J. H. & Choi, H. J. Synthesis and electrorheological characteristics of polyaniline-titanium dioxide hybrid suspension. *Synthetic Metals* **152**, 173-176 (2005).

253. Li, X. W., Wang, G. C., Li, X. X. & Lu, D. M. Surface properties of polyaniline/nano-TiO2 composites. *Applied Surface Science* **229**, 395-401 (2004).

254. Min, S. X., Wang, F. & Han, Y. Q. An investigation on synthesis and photocatalytic activity of polyaniline sensitized nanocrystalline TiO2 composites. *Journal of Materials Science* **42**, 9966-9972 (2007).

255. Tai, H. L., Jiang, Y. D., Xie, G. Z. & Zhao, M. J. Fabrication and gas sensitivity study of polypyrrole/titanium oxide composite thin films. *Journal of Inorganic Materials* **22**, 524-528 (2007).

256. Roux, S., Soler-Illia, G. J. A. A., moustier-Champagne, S., Audebert, P. & Sanchez, C. Titania/polypyrrole hybrid nanocomposites built from in-situ generated organically functionalized nanoanatase building blocks. *Advanced Materials* **15**, 217-+ (2003).

257. Tai, H. L., Jiang, Y. D., Xie, G. Z., Yu, J. S. & Zhao, M. J. Self-assembly of TiO2/polypyrrole nanocomposite ultrathin films and application for an NH3 gas sensor. *International Journal of Environmental Analytical Chemistry* **87**, 539-551 (2007).

258. Su, P. G. & Huang, L. N. Humidity sensors based on TiO2 nanoparticles/polypyrrole composite thin films. *Sensors and Actuators B-Chemical* **123**, 501-507 (2007).

259. Vlachopoulos, N., Liska, P., Augustynski, J. & Gratzel, M. Very Efficient Visible-Light Energy Harvesting and Conversion by Spectral Sensitization of High Surface-Area Polycrystalline Titanium-Dioxide Films. *Journal of the American Chemical Society* **110**, 1216-1220 (1988).

260. Oregan, B. & Gratzel, M. A Low-Cost, High-Efficiency Solar-Cell Based on Dye-Sensitized Colloidal Tio2 Films. *Nature* **353**, 737-740 (1991).

261. Savenije, T. J., Warman, J. M. & Goossens, A. Visible light sensitisation of titanium dioxide using a phenylene vinylene polymer. *Chemical Physics Letters* **287**, 148-153 (1998).

262. van Hal, P. A., Christiaans, M. P. T., Wienk, M. M., Kroon, J. M. & Janssen, R. A. J. Photoinduced electron transfer from conjugated polymers to TiO2. *Journal of Physical Chemistry B* **103**, 4352-4359 (1999).

263. Arango, A. C., Carter, S. A. & Brock, P. J. Charge transfer in photovoltaics consisting of interpenetrating networks of conjugated polymer and TiO2 nanoparticles. *Applied Physics Letters* **74**, 1698-1700 (1999).

264. Boucle, J., Ravirajan, P. & Nelson, J. Hybrid polymer-metal oxide thin films for photovoltaic applications. *Journal of Materials Chemistry* **17**, 3141-3153 (2007).

265. Burroughes, J. H. *et al.* Light-Emitting-Diodes Based on Conjugated Polymers. *Nature* **347**, 539-541 (1990).

266. Zeng, T. W. *et al.* A large interconnecting network within hybrid MEH-PPV/TiO2 nanorod photovoltaic devices. *Nanotechnology* **17**, 5387-5392 (2006).

267. Gratzel, M. Dye-sensitized solar cells. *Journal of Photochemistry and Photobiology C-Photochemistry Reviews* **4**, 145-153 (2003).

268. Li, Y. X., Hagen, J. & Haarer, D. Novel photoelectrochromic cells containing a polyaniline layer and a dye-sensitized nanocrystalline TiO2 photovoltaic cell. *Synthetic Metals* **94**, 273-277 (1998).

269. Croce, F., Appetecchi, G. B., Persi, L. & Scrosati, B. Nanocomposite polymer electrolytes for lithium batteries. *Nature* **394**, 456-458 (1998).

270. Croce, F., Fiory, F. S., Persi, L. & Scrosati, B. A high-rate, long-life, lithium nanocomposite polymer electrolyte battery. *Electrochemical and Solid State Letters* **4**, A121-A123 (2001).

271. Kumar, B. & Scanlon, L. G. Polymer-Ceramic Composite Electrolytes. *Journal of Power Sources* **52**, 261-268 (1994).

272. Quartarone, E., Mustarelli, P. & Magistris, A. PEO-based composite polymer electrolytes. *Solid State Ionics* **110**, 1-14 (1998).

273. Croce, F. *et al.* Role of the ceramic fillers in enhancing the transport properties of composite polymer electrolytes. *Electrochimica Acta* **46**, 2457-2461 (2001).

274. Wieczorek, W., Florjanczyk, Z. & Stevens, J. R. Composite Polyether Based Solid Electrolytes. *Electrochimica Acta* **40**, 2251-2258 (1995).

275. Wieczorek, W., Lipka, P., Zukowska, G. & Wycislik, H. Ionic interactions in polymeric electrolytes based on low molecular weight poly(ethylene glycol)s. *Journal of Physical Chemistry B* **102**, 6968-6974 (1998).

276. Best, A. S., Adebahr, J., Jacobsson, P., MacFarlane, D. R. & Forsyth, M. Microscopic interactions in nanocomposite electrolytes. *Macromolecules* **34**, 4549-4555 (2001).

277. Adebahr, J. *et al.* Ion transport in polymer electrolytes containing nanoparticulate TiO2: The influence of polymer morphology. *Physical Chemistry Chemical Physics* **5**, 720-725 (2003).

278. Chiang, C. Y., Reddy, M. J. & Chu, P. P. Nano-tube TiO2 composite PVdF/LiPF6 solid membranes. *Solid State Ionics* **175**, 631-635 (2004).

279. Ikeda, A., Tsuchiya, Y., Konishi, T., Ogasawara, S. & Kikuchi, J. I. Photocurrent-boosting by intramembrane electron mediation between titania nanoparticles dispersed into Nafion-porphyrin composites. *Chemistry of Materials* **17**, 4018-4022 (2005).

280. Karlsson, C., Best, A. S., Swenson, J., Kohlbrecher, J. & Borjesson, L. A SANS study of 3PEG-LiClO4-TiO2 nanocomposite polymer electrolytes. *Macromolecules* **38**, 6666-6671 (2005).

281. Kim, K. M., Ko, J. M., Park, N. G., Ryu, K. S. & Chang, S. H. Characterization of poly(vinylidenefluoride-co-hexafluoropropylene)-based polymer electrolyte filled with rutile TiO2 nanoparticles. *Solid State Ionics* **161**, 121-131 (2003).

282. Tang, W. P. Preparation of anatase-type TiO2 nanocrystal/acetylene black composites by a dry process, and their electrochemical lithium insertion. *Journal of Materials Chemistry* **14**, 3457-3461 (2004).

283. Lee, L. H. & Chen, W. C. High refractive-index thin films prepared from trialkoxysilane-capped poly(methyl methacrylate)-titania materials. *Chemistry of Materials* **13**, 1137-1142 (2001).

284. Wang, Z. B., Li, G. C., Xie, G. G. & Zhang, Z. K. Dispersion behavior of TiO2 nanoparticles in LLDPE/LDPE/TiO2 nanocomposites. *Macromolecular Chemistry and Physics* **206**, 258-262 (2005).

285. Han, K. Q. & Yu, M. H. Study of the preparation and properties of UV-blocking fabrics of a PET/TiO2 nanocomposite prepared by in situ

polycondensation. *Journal of Applied Polymer Science* **100**, 1588-1593 (2006).

286. Chen, X. C. Preparation and property of TiO2 nanoparticle dispersed polyvinyl alcohol composite materials. *Journal of Materials Science Letters* **21**, 1637-1639 (2002).

287. Nussbaumer, R. J., Caseri, W. R. & Smith, P. Reversible photochromic properties of TiO2-polymer nanocomposites. *Journal of Nanoscience and Nanotechnology* **6**, 459-463 (2006).

288. Wang, S. X., Wang, M. T., Lei, Y. & Zhang, L. D. "Anchor effect" in poly(styrene maleic anhydride)/TiO2 nanocomposites. *Journal of Materials Science Letters* **18**, 2009-2012 (1999).

289. Su, H. W. & Chen, W. C. High refractive index polyimide-nanocrystalline-titania hybrid optical materials. *Journal of Materials Chemistry* **18**, 1139-1145 (2008).

290. Xiong, M. N., Zhou, S. X., You, B. & Wu, L. M. Trialkoxysilane-capped acrylic resin/titania organic-inorganic hybrid optical films prepared by the sol-gel process. *Journal of Polymer Science Part B-Polymer Physics* **43**, 637-649 (2005).

291. Lu, C. L. *et al.* Research on preparation, structure and properties of TiO2/polythiourethane hybrid optical films with high refractive index. *Macromolecular Materials and Engineering* **288**, 717-723 (2003).

292. Guan, C., Lu, C. L., Liu, Y. F. & Yang, B. Preparation and characterization of high refractive index thin films of TiO2/epoxy resin nanocomposites. *Journal of Applied Polymer Science* **102**, 1631-1636 (2006).

293. Chau, J. L. H. *et al.* Transparent high refractive index nanocomposite thin films. *Materials Letters* **61**, 2908-2910 (2007).

294. Renz, C. *Helv. Chim. Acta* **4**, 961 (1921).

295. Wang, H. M., Tao, X. M. & Newton, E. Optical properties of titanium dioxide nanoparticles/3-(2-benzothiazolyl)-7-N,N-diethylaminocoumarin/polymethyl methacrylate composite films. *Optical Materials* **27**, 161-166 (2004).

296. Dessombz, A. *et al.* Design of liquid-crystalline aqueous suspensions of rutile nanorods: Evidence of anisotropic photocatalytic properties. *Journal of the American Chemical Society* **129**, 5904-5909 (2007).

297. Chen, L. F., Hong, Y. P., Zhang, Y. & Qiu, J. L. Fabrication of polymer matrix composites reinforced with controllably oriented whiskers. *Journal of Materials Science* **35**, 5309-5312 (2000).

298. Hao, X. Y. *et al.* Dynamic mechanical properties of whisker/PA66 composites at high strain rates. *Polymer* **46**, 3528-3534 (2005).

299. Qu, M. J., Jian, X. G., He, W. & Liao, G. X. Performance of potassium titanate whisker reinforced PPESK composites. *Journal of Materials Science & Technology* **20**, 445-447 (2004).

300. Yu, D. M., Wu, J. S., Zhou, L. M., Xie, D. R. & Wu, S. Z. The dielectric and mechanical properties of a potassium-titanate-whisker-reinforced PP/PA blend. *Composites Science and Technology* **60**, 499-508 (2000).

301. Liu, G. *et al.* Effect of nanoscale SiO2 and TiO2 as the fillers on the mechanical properties and aging behavior of linear low-density polyethylene/low-density polyethylene blends. *Journal of Polymers and the Environment* **13**, 339-348 (2005).

302. Ma, D. L., Akpalu, Y. A., Li, Y., Siegel, R. W. & Schadler, L. S. Effect of Titania nanoparticles on the morphology of low density polyethylene. *Journal of Polymer Science Part B-Polymer Physics* **43**, 488-497 (2005).

303. Tong, Y. J., Li, Y. S., Xie, F. C. & Ding, M. X. Preparation and characteristics of polyimide-TiO2 nanocomposite film. *Polymer International* **49**, 1543-1547 (2000).

304. Chiang, P. C., Whang, W. T., Tsai, M. H. & Wu, S. C. Physical and mechanical properties of polyimide/titania hybrid films. *Thin Solid Films* **447**, 359-364 (2004).

305. Xian, G. J., Zhang, Z. & Friedrich, K. Tribological properties of micro- and nanoparticles-filled poly(etherimide) composites. *Journal of Applied Polymer Science* **101**, 1678-1686 (2006).

306. Chang, L., Zhang, Z., Zhang, H. & Friedrich, K. Effect of nanoparticles on the tribological behaviour of short carbon fibre reinforced poly(etherimide) composites. *Tribology International* **38**, 966-973 (2005).

307. Rong, Y., Chen, H. Z., Wu, G. & Wang, M. Preparation and characterization of titanium dioxide nanoparticle/polystyrene composites via radical polymerization. *Materials Chemistry and Physics* **91**, 370-374 (2005).

308. Wang, Z. B., Li, G. C., Peng, H. R., Zhang, Z. K. & Wang, X. Study on novel antibacterial high-impact polystyrene/TiO2 nanocomposites. *Journal of Materials Science* **40**, 6433-6438 (2005).

309. Wang, Z. B., Xie, G. W., Wang, X. & Zhang, Z. K. Rheology and dispersion behavior of high-impact polystyrene/ethylene-vinyl acetate copolymer/TiO2 nanocomposites. *Journal of Applied Polymer Science* **100**, 4434-4438 (2006).

310. Yang, Y. N. & Wang, P. Preparation and characterizations of a new PS/TiO2 hybrid membranes by sol-gel process. *Polymer* **47**, 2683-2688 (2006).

311. Chen, W. C., Lee, S. J., Lee, L. H. & Lin, J. L. Synthesis and characterization of trialkoxysilane-capped poly(methyl methacrylate)-titania hybrid optical thin films. *Journal of Materials Chemistry* **9**, 2999-3003 (1999).

312. Khaled, S. M., Sui, R., Charpentier, P. A. & Rizkalla, A. S. Synthesis of TiO2-PMMA nanocomposite: Using methacrylic acid as a coupling agent. *Langmuir* **23**, 3988-3995 (2007).

313. Dzunuzovic, E., Jeremic, K. & Nedeljkovic, J. M. In situ radical polymerization of methyl methacrylate in a solution of surface modified TiO2 and nanoparticles. *European Polymer Journal* **43**, 3719-3726 (2007).

314. Zhu, M. F. *et al.* Preparation of PA6/nano titanium dioxide (TiO2) composites and their spinnability. *Macromolecular Symposia* **210**, 251-261 (2004).

315. Yang, J. L., Zhang, Z. & Zhang, H. The essential work of fracture of polyamide 66 filled with TiO2 nanoparticles. *Composites Science and Technology* **65**, 2374-2379 (2005).

316. Zhang, H., Zhang, Z., Yang, J. L. & Friedrich, K. Temperature dependence of crack initiation fracture toughness of various nanoparticles filled polyamide 66. *Polymer* **47**, 679-689 (2006).

317. Evora, V. M. F. & Shukla, A. Fabrication, characterization, and dynamic behavior of polyester/TiO2 nanocomposites. *Materials Science and Engineering A-Structural Materials Properties Microstructure and Processing* **361**, 358-366 (2003).

318. Chen, Y. C., Zhou, S. X., Gu, G. X. & Wu, L. M. Microstructure and properties of polyester-based polyurethane/titania hybrid films prepared by sol-gel process. *Polymer* **47**, 1640-1648 (2006).

319. Nakane, K., Kurita, T., Ogihara, T. & Ogata, N. Properties of poly(vinyl butyral)/TiO2 nanocomposites formed by sol-gel process. *Composites Part B-Engineering* **35**, 219-222 (2004).

320. Li, C., Tang, A. B., Zou, Y. B. & Liu, X. B. Preparation and dielectric properties of polyarylene ether nitriles/TiO2 nanocomposite film. *Materials Letters* **59**, 59-63 (2005).

321. Wetzel, B., Haupert, F., Friedrich, K., Zhang, M. Q. & Rong, M. Z. Impact and wear resistance of polymer nanocomposites at low filler content. *Polymer Engineering and Science* **42**, 1919-1927 (2002).

322. Zhang, Z., Breidt, C., Chang, L., Haupert, F. & Friedrich, K. Enhancement of the wear resistance of epoxy: short carbon fibre, graphite, PTFE and nano-TiO2. *Composites Part A-Applied Science and Manufacturing* **35**, 1385-1392 (2004).

323. Lu, S. R., Zhang, H. L., Zhao, C. X. & Wang, X. Y. New epoxy/silica-titania hybrid materials prepared by the sol-gel process. *Journal of Applied Polymer Science* **101**, 1075-1081 (2006).

324. Sangermano, M. *et al.* Preparation and characterization of nanostructured TiO2/epoxy polymeric films. *Macromolecular Materials and Engineering* **291**, 517-523 (2006).

325. *http://www.guardian.co.uk/science/2008/may/21/nanotechnology.controversiesinscience*. (2008).

326. Sayes, C. M. *et al.* Correlating nanoscale titania structure with toxicity: A cytotoxicity and inflammatory response study with human dermal fibroblasts and human lung epithelial cells. *Toxicological Sciences* **92**, 174-185 (2006).

327. Kay, S., Thapa, A., Haberstroh, K. M. & Webster, T. J. Nanostructured polymer/nanophase ceramic composites enhance osteoblast and chondrocyte adhesion. *Tissue Engineering* **8**, 753-761 (2002).

328. Savaiano, J. K. & Webster, T. J. Altered responses of chondrocytes to nanophase PLGA/nanophase titania composites. *Biomaterials* **25**, 1205-1213 (2004).

329. Sato, M., Slamovich, E. B. & Webster, T. J. Enhanced osteoblast adhesion on hydrothermally treated hydroxyapatite/titania/poly(lactide-co-glycolide) sol-gel titanium coatings. *Biomaterials* **26**, 1349-1357 (2005).

330. Webster, T. J. & Smith, T. A. Increased osteoblast function on PLGA composites containing nanophase titania. *Journal of Biomedical Materials Research Part A* **74A**, 677-686 (2005).

331. Liu, H. N., Slamovich, E. B. & Webster, T. J. Increased osteoblast functions on nanophase titania dispersed in poly-lactic-co-glycolic acid composites. *Nanotechnology* **16**, S601-S608 (2005).

332. Boccaccini, A. R., Gerhardt, L. C., Rebeling, S. & Blaker, J. J. Fabrication, characterisation and assessment of bioactivity of poly(D,L lactid acid) (PDLLA)/TiO2 nanocomposite films. *Composites Part A-Applied Science and Manufacturing* **36**, 721-727 (2005).

333. El Fray, M. & Boccaccini, A. R. Novel hybrid PET/DFA-TiO2 nanocomposites by in situ polycondensation. *Materials Letters* **59**, 2300-2304 (2005).

334. Wu, C. S. In situ polymerization of titanium isopropoxide in polycaprolactone: Properties and characterization of the hybrid nanocomposites. *Journal of Applied Polymer Science* **92**, 1749-1757 (2004).

335. Goto, K. *et al.* Bioactive bone cements containing nano-sized titania particles for use as bone substitutes. *Biomaterials* **26**, 6496-6505 (2005).

336. Kormann, C., Bahnemann, D. W. & Hoffmann, M. R. Photolysis of Chloroform and Other Organic-Molecules in Aqueous Tio2 Suspensions. *Environmental Science & Technology* **25**, 494-500 (1991).

337. Lu, K. L. *et al.* Mechanical damage of carbon nanotubes by ultrasound. *Carbon* **34**, 814-816 (1996).

338. Williams, D. B. & Carter, B. C. *Transmission Electron Microscopy: A Textbook for Materials Science*. Kluwer Academic / Plenum Publishers, (1996).

339. Zhou, W. & Wang, ZL. *Scanning Microscopy for Nanotechnology*. Springer, (2007).

340. Massa, W. *Crystal Structure Determination*. Springer, (2000).

341. Giacovazzo, C. *et al. Fundamentals of Crystallography*. Oxford University Press, (2002).

342. Atkins, P. *Physical Chemistry*. Oxford University Press, (2001).

343. Qian, L., Du, Z. L., Yang, S. Y. & Jin, Z. S. Raman study of titania nanotube by soft chemical process. *Journal of Molecular Structure* **749**, 103-107 (2005).

344. Gearing, J. *Handbook of Polymer Testing*. CRC Press, (1999).

345. Berg, J. *Wettability*. CRC Press, (1993).

346. Cottam BF *The synthesis of one-dimensional titanium dioxide nanostructures - PhD Thesis*. (2008).

347. Gumy, D. *et al.* Catalytic activity of commercial of TiO2 powders for the abatement of the bacteria (E-coli) under solar simulated light: Influence of the isoelectric point. *Applied Catalysis B-Environmental* **63**, 76-84 (2006).

348. Laaksonen, T., Ahonen, P., Johans, C. & Kontturi, K. Stability and electrostatics of mercaptoundecanoic acid-capped gold nanoparticles with varying counterion size. *Chemphyschem* **7**, 2143-2149 (2006).

349. Myers, D. Surfaces, Interfaces, and Colloids - Principles and Applications. *in Surfaces, Interfaces, and Colloids - Principles and Applications* 2nd edn, p.76 (1990).

350. Shi, W., Zhang, J., Shi, X. M. & Jiang, G. D. Different photodegradation processes of PVC with different average degrees of polymerization. *Journal of Applied Polymer Science* **107**, 528-540 (2008).

351. Maquet, V. *et al.* Poly(D,L-lactide) foams modified by poly(ethylene oxide)-block-poly(D,L-lactide) copolymers and a-FGF: in vitro and in vivo evaluation for spinal cord regeneration. *Biomaterials* **22**, 1137-1146 (2001).

352. Grimmett, G. *Percolation*. Springer, (1999).

353. *http://www.ptli.com/testlopedia/tests/DMA-D4440.asp*. (2008).

354. Ray, S. S. & Okamoto, M. Polymer/layered silicate nanocomposites: a review from preparation to processing. *Progress in Polymer Science* **28**, 1539-1641 (2003).

355. Martin, C. A. *et al.* Electric field-induced aligned multi-wall carbon nanotube networks in epoxy composites. *Polymer* **46**, 877-886 (2005).

356. Menner, A., Salgueiro, M., Shaffer, M. S. P. & Bismarck, A. Nanocomposite foams obtained by polymerisation of high internal phase emulsions. *unpublished work* (2008).

357. Matthews, F. & Rawlings, R. *Composite Materials: Engineering and Science*. CRC, (1999).

358. Kinloch, A. J., Maxwell, D. L. & Young, R. J. The Fracture of Hybrid-Particulate Composites. *Journal of Materials Science* **20**, 4169-4184 (1985).

359. Kinloch, A. J. & Taylor, A. C. The toughening of cyanate-ester polymers - Part I - Physical modification using particles, fibres and woven-mats. *Journal of Materials Science* **37**, 433-460 (2002).

360. Faber, K. T. & Evans, A. G. Crack Deflection Processes .1. Theory. *Acta Metallurgica* **31**, 565-576 (1983).

361. Kinloch, A. J. & Taylor, A. C. Mechanical and fracture properties of epoxy/inorganic micro- and nano-composites. *Journal of Materials Science Letters* **22**, 1439-1441 (2003).

362. Kinloch, A. J. *et al.* The effect of silica nano particles and rubber particles on the toughness of multiphase thermosetting epoxy polymers. *Journal of Materials Science* **40**, 5083-5086 (2005).

BIBL. LONDON UNIV.